University of California,
Irvine

N-glycosylation Branching and Neural Stem Cell Fate Potential

DISSERTATION

submitted in partial satisfaction of the requirements for the degree of

DOCTOR OF PHILOSOPHY

in Anatomy & Neurobiology

by

Andrew Richard Yale

Dissertation Committee:
Professor Lisa A. Flanagan, Chair
Professor Michael Demetriou
Professor Robert F. Hunt

2020

DEDICATION

To my father, Richard Yale, for being a pillar of motivation for your family and a role model for achieving your dreams, no matter how hard it gets.

To my mother, Evelyn Yale, for your unending love and dedication to provide for your family.

To my older brother, Steven Yale, for being an inspiration that anyone could always look toward to better themselves.

To my younger brothers, Justin and Jacob Yale, for your unconditional love and for being a source of humor and happiness throughout my life.

To my uncle and aunt, Robert and Remy Yale, for being a second set of parents and for your endless encouragement and support.

To my paternal grandparents, Gary and Junie Cooper, for always providing unconditional sanctuary throughout my life and for your unwavering confidence.

To my maternal grandma, Gertrude Manalansan, for always being a source of joy and positivity and for the strength and resilience you display every day.

TABLE OF CONTENTS

LIST OF FIGURES

LIST OF TABLES

ACKNOWLEDGEMENTS

Firstly, I would like to thank my advisor Dr. Lisa Flanagan for providing me the opportunity to work in her lab. I cannot thank her enough as she offered her time and mentorship during a period of self doubt. She is a font of wisdom to whom I did not take enough advantage of. She genuinely cares about the health and well being of all the individuals who work in her lab. Though I have fumbled many times, she has always been there to steer me into the right direction. Thank you, Lisa, for being patient and believing in me.

I would like to thank my doctoral committee members Dr. Michael Demetriou and Dr. Robert Hunt for providing guidance and advice throughout this project. Even despite issues that arose, you still were patient with me and provided direction to see this project through. In addition, I would also thank Dr. Matthew Blurton-Jones and Dr. Richard Robertson for serving on my advancement committee.

To my lab members Alan Jiang and Brenda Gutierrez, the time we were forced to spend together underground was both stressful and exciting, and I believe our collective trauma has bound us together more strongly. I will never forget the stress and work we overcame together and the incredible friendship that developed. Alan, you are an incredibly hard worker and have truly carried our lab over the past couple years. Brenda, your enthusiasm and joy was something to look forward to every day. I am also incredibly grateful for Dr. Shubha Tiwari as she has been both mentor and one of my closest confidants to whom I share my utmost trust with. While she knows how to press my buttons, she has always successfully drawn out the best through constructive antagonism. Thank you for being the devil's advocate. I will never forget the endless times we all have gotten coffee together to satisfy my love of coffee, and I hope our friendship will never end.

There are many previous members of the Flanagan lab that I also must thank and recognize. Dr. Tayloria Adams, your dedication to provide scientific opportunities for all is an inspiration and beacon to all students who want to pursue research. Dr. Jamison Nourse, I want to thank you for your mentorship when I first joined the lab. Your extensive work on this project served as my platform, and I can only hope I honored the passing of the torch. Dr. Janahan Arulmoli, you have been a great friend and research mate. Despite being years since you have left, your legacy still resonates throughout the lab. Rylan Kautz, you are not just recognized as an honorary Flanagan lab member, but you have also been a great friend whom I can always grab a beer with and discuss the latest in pop television and movie culture. Clarissa Ro, thank you for being the glue that held our lab together when I first started. Estelle Kim, you have been a great friend, and your contribution to the *in vivo* work for the MGAT5 project will not go unnoticed. I must also thank the undergraduates who worked with me throughout my dissertation, Loise Cho and Lakshay Verma. These two were instrumental for helping me develop and carry out a multitude of experiments that helped shape this project. Your incredible dedication and self-motivation will carry you far through your future endeavors.

I would also like to thank those who have provided their expertise to this project or other work that I have been a part of within this lab. Dr. Paul Gershon, thank you and your student Junsung Im for helping us perform our mass spectrometry studies. Dr. Michael Sy and Dr. Michael Demetriou for providing invaluable information and points of discussion regarding N-glycosylation. Dr. Leonid Groysman and Rebecca Nishi for providing mentorship for the stroke and stem cell transplantation project that we were lucky to be a part of. I would also offer special thanks to Dr. Alison Miyamoto from CSU Fullerton, Dr. Edwin Monuki and Dr. Basam Barkho, former postdoctoral fellow in the Monuki lab. Dr. Miyamoto and Dr. Monuki offered research

opportunities within their labs when I was part of the CIRM undergraduate research program, and Dr. Barkho acted as a direct mentor for me within the Monuki lab. These three people inspired me to pursue research.

I would like to thank all my friends that I have met here at UC Irvine. Watching all of us dedicate our time and sanity to our work allowed us to empathically connect to each other so we never felt alone in our struggle. I am grateful for our brief moments of reprieve, whether it be hiking, traveling, brunch, birthdays, baby showers, KBBQ, or celebrating our accomplishments at the Anteater Pub. I would also like to thank my childhood and college friends who have constantly stuck by me. Even when we have long moments of absence, you still find a way to connect as if a day has not been skipped. I can not be any happier to have you in my life.

Lastly, to my entire family. Thank you to my three brothers whom each inspire me to try to be the best that I can be and to always look for the bright side. To my grandparents, whom have never faltered in their love, confidence, and encouragement. Thank you to my aunt and uncle who have been second parents to me throughout my life. Lastly but surely not least, my parents who have always been there for me and my three brothers no matter the circumstance. My parents have made incredible sacrifices and have dedicated so much of their time to see us achieve great heights. They have always encouraged the pursuit of an education, but more importantly the pursuit of happiness. So, my only goal is to make them proud, to make them happy; and I can only hope I have accomplished that. I love you.

CURRICULUM VITAE

Andrew Richard Yale

Education

2020 Ph.D. in Biomedical Sciences - University of California, Irvine – School of Medicine

2013 B.S. in Cellular & Molecular Biology - California State University, Fullerton

Awards/Honors

2018 Dr. Lorna Carlin-sponsored Stanley Behrens Fellows in Medicine Honorable Mention Award
2018 Bio-Techne-sponsored research travel award
2018 UC Irvine – Associated Graduate Students' Annual Travel Award
2018 UC Irvine School of Medicine research travel award
2017 UC Irvine School of Medicine *Grad Day* – Dean's special recognition for outstanding poster presentation
2017 San Diego Glycobiology Symposium 2017 – selected for oral presentation
2011 Howell-CSUPERB Research Scholar Award (CSU-wide)
2009 – 2013 Dean's Honor List (CSU Fullerton) (all semesters inclusive)

Grants/Fellowships

2017 – 2018 UC Irvine - Brython Davis Fellowship recipient
2015 – 2017 UC Irvine - NIH/NINDS T32 Training fellowship for translational stem cell research for neurological disorders and stroke (NS082174)
2011 – 2012 CSU Fullerton - CIRM Bridges to Stem Cell Research Scholarship-Internship

Research Experience

2014 – 2020
Graduate Student Researcher: Department of Anatomy & Neurobiology, University of California, Irvine – School of Medicine (research advisor: Dr. Lisa A. Flanagan)

- Investigation into whether N-glycosylation of surface proteins can underly electrophysiological properties of neural stem cells (Yale *et al*, 2018)
- Investigation into how remodeling of N-glycans can impact neurogenesis and neurodevelopment using transgenic animal models deficient in N-glycan processing enzymes
- Characterization of potential molecular mechanisms that underly N-glycosylation-mediated control on neural stem cell differentiation
- Help test novel microfluidic, DEP-based platforms for label-free characterization and separation of neural stem cells (Jiang *et al*, 2019)
- Help test the applicability of carbon nanofibrous scaffolds for the growth and characterization of neural stem cells and for dopamine detection (Perebikovsky *et al* 2020)
- Test whether biomaterial scaffolds can aid in neural stem cell survivability during transplant and recovery in an animal model for stroke

2012
Undergraduate Research Assistant (CIRM-funded internship): Department of Developmental and Cell Biology, University of California, Irvine (research advisor: Dr. Edwin S. Monuki)

- Generation of choroid plexus epithelial cells from embryonic and induced pluripotent stem cells
- Characterization of pluripotent cell-derived choroid plexus epithelial cells by qRT-PCR, immunocytochemistry, and *in situ* hybridization

2011 – 2013
Undergraduate Research Assistant: Department of Biological Sciences, California State University, Fullerton (research advisor: Dr. Alison Miyamoto)

- Identification of a functional cleavage site on the extracellular matrix protein microfibril-associated glycoprotein 2 (MAGP2) (Donovan *et al*, 2013)
- Identified the functional necessity for glycosylation of MAGP2 for secretion and deposition into the extracellular space

Publications

Perebikovsky A, Hwu AT, **Yale AR**, Ghazinejad M, Madou M. 2020. Nanofibrous carbon multifunctional smart scaffolds for simultaneous cell differentiation and dopamine detection. *ACS Biomater. Sci. Eng.*, 6(1):225-234

Jiang AYL, **Yale AR**, Aghaamoo M, Lee D, Lee AP, Adams TNG, Flanagan LA. 2019. High-throughput continuous dielectrophoretic separation of neural stem cells. *Biomicrofluidics*, 13(6):064111

Yale AR, Nourse JL, Lee KR, Ahmed SN, Arulmoli SN, Jiang AYL, McDonnell LP, Botten GA, Lee AP, Monuki ES, Demetriou M, Flanagan LA. 2018. Cell surface N-glycans influence electrophysiological properties and fate potential of neural stem cells. *Stem Cell Reports*, 11(4):869-882

Donovan, L.J., Cha, S.E., **Yale, A.R.**, Dreikorn, S., and Miyamoto, A. 2012. Identification of a functional proprotein convertase cleavage site in microfibril-associated glycoprotein 2. *Matrix Biology*, 32(2):117-22

Manuscripts in preparation
Yale AR, Kim E, Monuki ES, Flanagan LA. 2019. Regulatio of neural stem cells and neural development by MGAT5-mediated N-glycosylation. *In preparation*.

Abstracts/Presentations

Oral Presentations

National & International

Yale AR, Nourse JL, Lee KR, Flanagan LA. Cell surface glycosylation alters electrophysiological properties and fate potential of mouse neural stem cells. *2017 San Diego Glycobiology Symposium (SDGS) NextGen*, San Diego, CA, US (January 2017)

State & Local

Yale *AR.* Cell surface N-glycans influence electrophysiological properties and fate potential of neural stem cells. UC Irvine, Anatomy & Neurobiology Annual Grad Day Symposium (Annually 2014-2019)

Yale AR, Nourse JL, Lee KR, Flanagan LA. Complex N-glycans influence stem cell fate in the neural lineage. *UC Irvine, NIH T32 Training Grant Retreat* (August 2015, June 2016, September 2016)

Yale AR, Nourse JL, Lee KR, Flanagan LA. Glycosylation and Neural Stem Cell Fate. *UC Irvine, Anatomy & Neurobiology: Progress in Neuroscience* (April 2016)

Poster Presentations

National & International

Yale AR, Kim E, Reeves C, Monuki ES, Demetriou M, Flanagan LA. Highly-branched N-glycans generated by MGAT5 control neural stem cell differentiation and cell surface protein expression. *2018 Society for Neuroscience annual research conference*, San Diego, CA, US (November 2018)

Yale AR, Kim E, Reeves C, Monuki ES, Demetriou M, Flanagan LA. Highly-branched N-glycans generated by MGAT5 control neural stem cell differentiation and cell surface protein expression. *2018 International Society for Stem Cell Research annual research conference*, Melbourne, Victoria, AUS (June 2018)

Yale AR, Nourse JL, Lee KR, Ahmed SN, Arulmoli SN, McDonnell LP, Jiang AYL, Botten GA, Lee AP, Monuki ES, Demetriou M, Flanagan LA. The N-glycan branching pathway alters neural stem cell biophysical properties and shifts fate potential towards astrogenesis. *2017 Society for Neuroscience (SFN) annual research conference*, Washington, DC, US (November 2017)

Yale AR, Nourse JL, Lee KR, Ahmed SN, Arulmoli SN, McDonnell LP, Jiang AYL, Botten GA, Lee AP, Monuki ES, Demetriou M, Flanagan LA. The N-glycan branching pathway alters neural stem cell biophysical properties and shifts fate potential towards astrogenesis. *2017 International Society for Stem Cell Research annual research conference*, Boston, MA, US (June 2017)

Yale AR, Nourse JL, Lee KR, Flanagan LA. Cell surface glycosylation alters electrophysiological properties and fate potential of mouse neural stem cells. *2017 San Diego Glycobiology annual research symposium*, San Diego, CA, US (January 2017)

Yale AR, Nourse JL, Lee KR, Ahmed SN, Flanagan LA. Cell surface glycosylation alters electrophysiological properties and fate potential of mouse neural stem cells. *2016 ISSCR annual research conference*, San Francisco, CA, US (June 2016)

Yale AR, Barkho BZ, Watanabe M, Monuki ES. Derivation of choroid plexus epithelial cells from mouse induced pluripotent stem cells. *2013 CIRM Grantee Meeting*, San Francisco, CA, US (March 2013)

Yale AR, Barkho BZ, Watanabe M, Monuki ES. Derivation of choroid plexus epithelial cells from mouse induced pluripotent stem cells. *2012 CIRM Bridges Fellowship Trainee Meeting*, San Francisco, CA, US (July 2012)

State & Local

Yale AR, Nourse JL, Lee KR, Ahmed SN, Arulmoli SN, McDonnell LP, Jiang AYL, Botten GA, Lee AP, Monuki ES, Demetriou M, Flanagan LA. The N-glycan branching pathway alters neural stem cell biophysical properties and shifts fate potential towards astrogenesis. *2017 UC Irvine, School of Medicine Grad Day* (October 2017)

Yale AR, Nourse JL, Lee KR, Flanagan LA. N-linked glycosylation influences neural stem cell fate. *2015 UC Irvine, Anatomy & Neurobiology Annual Grad Day Symposium* (June 2015)

Yale AR, Nourse JL, Lee KR, Flanagan LA. N-linked glycosylation influences neural stem cell fate. *2015 UC Irvine, Stem Cell Awareness Day Annual Symposium* (October 2015)

Yale AR, Barkho BZ, Watanabe M, Monuki ES. Generation of BMP4-sensitive neuroepithelial cells from mouse induced pluripotent stem cells. *2012 CSU Fullerton, Annual Stem Cell Symposium*, Fullerton, CA (March 2012)

Mentoring

University of California, Irvine

Undergraduate Students

2018 – 2020 Lakshay Verma (Professor Lisa Flanagan Laboratory)*
2016 – 2018 Loise Cho (Professor Lisa Flanagan Laboratory)*
2016 – 2017 Jerrica Sabino (Professor Lisa Flanagan Laboratory)
2015 – 2016 Jordan Edmunds (Professor Lisa Flanagan Laboratory)
2013 Jesus Ayala (Professor Lisa Flanagan Laboratory)

High School Students

2017 – 2018 Kevin Mazo (Professor Lisa Flanagan Laboratory)
2017 – 2018 Mitchell Rogers (Professor Lisa Flanagan Laboratory)
2017 – 2018 Samuel Salib (Professor Lisa Flanagan Laboratory)
2017 Jacob Umans (Professor Lisa Flanagan Laboratory)

*Received funding through Undergraduate Research Opportunities Program (UROP) and the Summer Undergraduate Research Program (SURP)

California State University, Fullerton

Undergraduate Students

2012 – 2013 Khang Lai (Professor Alison Miyamoto Laboratory)
2011 – 2012 Richard Cervantes (Professor Alison Miyamoto Laboratory)
2011 – 2012 Gordon Withers (Professor Alison Miyamoto Laboratory)
2011 – 2012 Various students through HHMI Summer Research Experience (Professor Alison Miyamoto Laboratory)

Professional Memberships

2015 – present International Society for Stem Cell Research (ISSCR) Member
2017 – present Society for Neuroscience (SFN) Member

Additional Volunteer and Outreach

2006 – 2008
Boys and Girls Club of America, Camarillo, CA
I volunteered to tutor students from K-6th grade, particularly those with learning disabilities.

2006 – 2008
Ventura County Medical Center, Ventura, CA
I assisted nurses with preparing examination rooms, transport, and helped the hospital lab take inventory and analyze blood samples.

2015 – 2016
UC Irvine, Stem Cell Research Center high school summer research program
I helped plan, organize, and present research to high school students within UC Irvine's Gross Hall Stem Cell Research Center to promote interest in stem cell science.

2015 – present
Girls, Inc., after-school teaching program
I helped plan, organize, and teach elementary and middle school students (originally just girls, but now expanded to boys) about the central nervous system, diseases, and the importance of scientific research.

ABSTRACT OF THE DISSERTATION

N-glycosylation Branching and Neural Stem Cell Fate Potential

By

Andrew Richard Yale

Doctor of Philosophy in Anatomy & Neurobiology

University of California, 2020

Professor Lisa A. Flanagan, Chair

Neural stem/progenitor cells (NSPCs) generate all the differentiated cell types in the central nervous system. However, mechanisms controlling differentiation into specific cell types, such as neurons and astrocytes, and how differentiation is regulated by extracellular cues must be identified. Gaining a better understanding of how NSPC differentiation is affected by their environment will be essential for developing these cells as therapeutics for brain repair. Our lab identified a novel biophysical signature, membrane capacitance, that indicates neuron- or astrocyte-bias of NSPCs. I found that N-glycosylation, specifically the N-glycan branching pathway, differs between astrocyte- and neuron-biased NSPCs. My studies showed that N-acetylglucosamine (GlcNAc) treatment to enhance N-glycan branching shifted membrane capacitance and altered fate of NSPCs. I identified the MGAT5 branching enzyme as a critical regulator of NSPC differentiation in vitro and in vivo. My studies showed that loss of MGAT5 significantly impacted neural development, causing enhanced neuron differentiation but depletion of the NSPC pool that led to a reduction in neurons in the MGAT5 cortex in vivo. I found that MGAT5 null NSPCs in vitro formed more neurons and fewer astrocytes than their WT counterparts. To identify a potential mechanism for how branching impacts fate, I used a proteomic screen to identify cell surface proteins regulated by branching and found a reduction

in cell adhesion proteins in GlcNAc-treated NSPCs. My functional assays probing cell-cell and cell-ECM adhesion showed that cellular adhesion is diminished when NSPC N-glycan branching is enhanced. Taken together, my studies identified N-glycan branching as a critical component of fate-specific membrane capacitance, a novel regulator of NSPC differentiation, and a means by which NSPC differentiation can be affected by the extracellular environment.

CHAPTER 1

Introduction

Neural stem/progenitor cells (NSPCs) are multipotent cells capable of differentiating into the vast number of neurons, astrocytes, and oligodendrocytes found throughout the central nervous system (CNS) and are thus exciting candidates for use in regenerative therapies for neurological disease and trauma. The identification of progenitor cells and the lineages they produce is key to our understanding of how the enormous diversity of cell types is produced in the brain, and this information will guide future attempts to harness stem cells for brain repair.

NSPCs arise from the neural epithelium, a layer of cells formed by the invagination and closure of the primitive ectodermal layer during neurulation. These neuroepithelial cells rapidly divide and thicken the neural tube and transition into radial glial cells (RGCs), in other terms – NSPCs. The generation of neurons, astrocytes, and oligodendrocytes occurs from this single pool of NSPCs in a tightly regulated temporal and spatial manner. Early in corticogenesis, NSPCs generate the neurons that occupy the cortical plate in an inside-out manner – deep layer 6 is formed first with superficial layer 2 being formed last. During late embryogenesis, the fate potential of NSPCs switches as the neuron-producing machinery is suppressed by glial producing mechanisms (*1*).

How NSPCs generate the wide variety of neurons in the cortex and switch fate potential to glia are not fully understood. NSPCs must integrate multiple external signals that impact cell fate decision to control differentiation, and how a cell translates these signals to a set of instructions can change depending on other contextual signals it receives at the same time.. An example of this is illustrated by the bone morphogenetic protein (BMP) signaling pathway

during cortical development. BMP2/4 is pro-neurogenic early in development (*2*), but strongly promotes astrocyte formation during late cortical development (*3, 4*). This switch in signaling may be driven by activity of a co-factor, leukemia inhibitory factor (LIF), during periods of astrogenesis (*5*). However, LIF is also present during neurogenic periods early in cortical development, and LIF can stimulate NSPCs to generate neurons (*6*). EGF receptor (EGFR) may be involved in shifting the effects of BMP since EGFR expression increases during astrogenic stages and appears to change the signaling mechanism of both BMP and LIF from pro-neurogeneic to pro-gliogenic (*7*). Furthermore, dividing NSPCs distribute EGFR unevenly between the daughter cells, generating cells that either display glial/astrocyte markers or not depending on the amount of EGFR the cell inherited during division (*8*). This complex signaling at the cell membrane is compounded *in vitro* by the fact that NSPC cultures are typically maintained in EGF-containing growth medium, a process necessary to maintain and expand the large number of cells necessary for prospective transplantation therapies.

Despite the fact that NSPCs may change cell surface protein expression when making the switch from neurogenesis to astrogenesis, identifying neurogenic and astrogenic NSPCs remains a challenge. Common NSPC markers such as nestin, PSA-NCAM, and A2B5 have been in place for many years but are insufficient to resolve neurogenic-astrogenic bias. Other methods to characterize the behavior and fate potential of NSPCs might prove useful for understanding the heterogeneity of NSPCs.

1.1 LABEL-FREE APPROACHES TO DISTINGUISH CELL CHARACTERISTICS

Label-free approaches to cell characterization may be useful for distinguishing alternative properties exhibited by cells. Dielectrophoresis (DEP), a technique that induces cell movement in a non-uniform electric field, is of particular interest since it can probe a number of

electrophysiological properties of a cell in suspension and without the use of any labels. The compartment of the cell that is being assessed by DEP is dependent on the frequency of the applied electric field, and thus analysis of cells with DEP is provides information on specific cellular compartments. At low frequencies, movement is dependent on properties of the plasma membrane, and this technique is sensitive enough to discern even minute differences in the plasma membrane (*9*). Some notable examples include utilizing DEP to detect differences in normal and malaria-infected red blood cells (*10*), neu-oncogene expression in tumorigenic cells (*11*), or stimulated vs unstimulated Jurkat cells (*12*).

Electrophysiological characteristics distinguish cells from one another in a variety of cell types. One property, membrane capacitance, differs between the different leukocyte subpopulations (*13*), and dynamic changes to membrane biophysical properties have been described during mesenchymal stem cell (MSC) differentiation towards adipogenesis or osteogenesis (*14*). We previously found that DEP can distinguish NSPCs and their differentiated progeny (*15*). DEP is sufficient to discern the fate potential of NSPCs from both human and rodent NSPCs based on membrane capacitance alone, providing a novel means to distinguish neuron- and astrocyte-biased NSPCs (*16*). DEP is non-toxic to NSPCs (*17*), and we have developed multiple DEP-based devices that sort NSPCs on the basis of their membrane capacitance signature (*18-22*). As will be discussed in Chapter 2, we have increased the throughput and fidelity of DEP sorting by developing a continuous, flow-based sorter that can simultaneously separate neuron-biased and astrocyte-biased NSPCs (*19*). Furthermore, Chapter 3 will discuss the use of this sorter to study the membrane properties of NSPCs and identify a biological component of the plasma membrane that distinguishes neuron-biased and astrocyte-biased NSPCs (*23*).

1.2 THE BIOLOGICAL LINK TO MEMBRANE CAPACITANCE

Prior to the studies presented in Chapter 3, it remained unclear what components of the plasma membrane could underly changes in membrane capacitance. The frequencies used in DEP are not the same that are used to detect resting membrane potential (*15, 24*). Multiple theories arose including questions regarding protein abundance on the plasma membrane, cell size, or plasma membrane folding. Expression of a G protein-coupled receptor in yeast did not alter capacitance (*25*), but the expression of channelrhodopsin-2 in HEK293 cells did (*26*), suggesting that perhaps certain proteins could impact membrane capacitance although it would be difficult to distinguish which proteins. Cell membrane microdomains, such as ruffles or microvilli, increase cell surface area and are theorized to alter membrane capacitance (*27*). While NSPCs with distinct membrane capacitance differences do not differ in cell size (*16, 20*), they may have different membrane microdomains and membrane folds that are not visible through phase contrast microscopy. Interestingly, a study found modification of phospholipid bilayers with polyethelene glycol in artificial vesicles significantly altered membrane capacitance (*28*), suggesting that cell surface modifications could contribute to membrane capacitance.

A cellular process that modifies the plasma membrane surface and impacts membrane microdomains is glycosylation. During glycosylation, carbohydrates able to store charge are added to plasma membrane proteins and lipids. Domains of glycosylated cell surface molecules generate surface undulations to increase surface area (*29*), create large membrane structures extending up to 200 nm from the cell surface (*30*), and influence the protein makeup of the plasma membrane (*31, 32*). We tested whether glycosylation could impact NSPC behavior within DEP by treating NSPCs with the N-glycosylation inhibitor, swainsonine. The reduction in complex N-glycans on the cell surface resulted in a significant shift in cell behavior in DEP,

providing the first link between N-glycosylation and cell behavior in DEP (*20*). My work in Chapter 3 takes these studies a step further by comparing the expression profiles of various glycosylation processing enzymes between DEP-sorted or developmentally isolated NSPCs that differ in fate potential. We ultimately identify a complex N-glycan remodeling process known as N-glycan branching as a molecular component impacting fate-specific membrane capacitance (*23*).

1.3 N-LINKED GLYCOSYLATION AND THE CORE BRANCHING PATHWAY

Almost all proteins entering the endoplasmic reticulum (ER) are post-translationally modified by N-glycosylation. This process covalently links a sugar polymer (glycan) to an asparagine (Asn, N) residue of the consensus site N-X-S/T on an immature peptide. N-glycosylation of proteins within the cell is canonically known to aid in the folding and trafficking of proteins as they pass through the ER and the Golgi. As these proteins transit from the ER to the Golgi, the N-glycans are constantly processed and remodeled *en route* to the cell surface (Haltiwanger 2004). This remodeling involves the trimming of mannose residues on the terminal ends of an immature N-glycan by the enzymes mannosidase 1 and 2 (MAN1, MAN2) followed by the sequential addition of N-acetylglucosamine (GlcNAc) by the N-acetylglucosaminyltransferases I, II, IV, and V (MGAT1-5) to generate mono-, bi-, tri-, and tetra-antennary N-glycans (*33*). This process, known as N-glycan branching, is responsible for the vast diversity of N-glycans that pattern the cell surface.

The biosynthesis of the donor substrate, UDP-GlcNAc, which is utilized to generate the N-glycan branches, competes with metabolic processes for energy production (*34-36*). The enzymes MGAT1 and MGAT2, which add the first two branches to N-glycans, are limited by the availability of the acceptor N-glycan. However, MGAT4 and MGAT5 are limited by the

availability of UDP-GlcNAc (*33, 37, 38*) resulting in decreased activity and limited production of tri- and tetra-antennary (highly branched) N-glycans (*35, 37*). This leaves these enzymes in a state of hypersensitivity. Indeed, when cells are supplemented with exogenous GlcNAc, the activities of MGAT4 and MGAT5 are selectively upregulated and a spike in the production of highly branched N-glycans is observed (*23, 37*). In Chapter 3, we utilize this paradigm to test whether the stimulation of N-glycan branching impacts DEP-measured biophysical properties. We not only find that a shift in N-glycan branching could account for the differences in fate-specific membrane capacitance, but could also regulate NSPC fate potential along the neuron-astrocyte axis (*23*).

1.4 N-GLYCOSYLATION IN NSPC FATE POTENTIAL AND NEURAL DEVELOPMENT

Changes in glycans expressed throughout the brain coincide with the shift from neurogenesis to gliogenesis during cortical development (*39, 40*). Defects in N-glycosylation biosynthesis can be embryonic lethal (*41-43*), and improper N-glycan processing during early steps in the N-glycan branching pathway leads to severe developmental disorders known as congenital disorders of glycosylation (CDGs), which present symptoms of neural abnormalities (*44*). A study aiming to dissect the roles of N-glycan branching in development found that silencing MGAT1 resulted in failed closure and fusion of the neural tube (*42*). Furthermore, neuron-specific deletion of MGAT1 results in severe psychomotor retardation, tremors, and paralysis (*45*), mimicking symptoms seen in the human disease CDG-IIa caused by insufficient N-glycan remodeling due to dysfunctional MGAT2 (*44*). Taken together, these findings highlight the importance for N-glycan branching for proper neural development.

However, the impact N-glycan branching has on cortical NSPCs and their fate potential has not been described. We show that expression of highly-branched N-glycans is significantly upregulated in the ventricular zone, a niche where NSPCs reside, of the developing cortex starting at E16 – the embryonic date at which NSPCs begin to switch from neurogenesis to gliogenesis (*23*) (Chapter 3). Furthermore, GlcNAc supplementation, which enhances N-glycan branching, shifts the fate potential of NSPCs to generate more astrocytes at the expense of neurons *in vitro* (*23*)(Chapter 3). Therefore, we sought to study the impact N-glycan branching could have on early cortical development.

Since GlcNAc drives the formation of highly branched N-glycans, we utilized a transgenic mouse model lacking MGAT5 to assess the contribution of highly-branched N-glycans to NSPCs *in vivo*. This mouse model has been described as being grossly normal, but more recent studies have identified that knockout animals have decreased depression-like behavior (*46, 47*) and females sometimes fail to nurture their pups. While these are mild neurological symptoms, a closer inspection of the brain during development has not been performed. In Chapter 4, we find that loss of MGAT5 enhances neuronal maturation but depletes upper-layer neurogenic progenitors during embryonic development. When the cortex was assessed at postnatal day 7 (P7), we found a significant reduction in both upper and deep layer neurons in the MGAT5 knockout mice, leading to significant cortical thinning. These studies highlight the functional relevance of MGAT5 to neurogenesis in the developing cortex.

1.5 N-GLYCOSYLATION AND THE MOLECULAR MECHANISMS THAT GOVERN NSPC BEHAVIOR

Since N-glycan branching complexity can significantly alter the function of many plasma membrane proteins, it can control and coordinate many different sensors of external cues and

therefore dictates a cell's response to its surroundings. Identifying which cell responses are most susceptible to changes in glycosylation patterns on the surface will be key to understanding how N-glycosylation can direct NSPC behavior.

Changes in N-glycan branching impact ligand-receptor sensitivity for a number of growth factor systems such as EGF, PDGF, bFGF, and IGF (*37, 48*). These effects are due in part to the binding of cell surface N-glycans by galectins, molecules whose ligands are galactose residues found on the terminal ends of complex N-glycan branches. The lattice of galectins and bound N-glycans opposes endocytosis (*37, 49*), an effect that is amplified when a galectin is bound to the MGAT5-modified N-glycan branch (*50*). N-glycan branching and binding to galectins can control receptor residence time at the cell surface, ligand affinity, and protein distribution and clustering for proteins including growth factor and morphogen receptors, ECM binding integrins, and cell adhesion molecules (*51*). While N-glycan branching control of receptors is well described for cancer cells, these functions have yet to be assessed for NSPCs.

We performed an unbiased screen of cell surface proteins by mass spectrometry and found that adhesion proteins were highly susceptible to changes in N-glycan branching (described in Chapter 5). E12 NSPCs treated with GlcNAc to increase branching had a lower cell surface abundance of several cell-cell and cell-ECM adhesion proteins including cadherins and integrins. The studies described in Chapter 5 include a number of functional assays to test cell-cell and cell-ECM adhesion. We found that N-glycosylation branching negatively impacts cellular adhesion. Furthermore, we found that Yap, a downstream effector in the Hippo signaling pathway that is tied to cellular adhesion and mechanotransduction, is redistributed to the nucleus, providing the first step in a potential mechanism for how N-glycan branching regulates NSPC fate potential.

1.6 SUMMARY

NSPCs show great promise as therapeutics for neural disease and trauma. However, the heterogeneity of cells in the lineage and unpredictability of cell behavior hampers the development of consistent and efficient regenerative therapies. Understanding the mechanisms that govern NSPC fate potential will improve our understanding of the development and differentiation of NSPCs and help guide future research for regenerative medicine. The work presented here highlights the development of a label-free sorting tool based on an innate electrophysiological property, membrane capacitance (Chapter 2). Sorting NSPCs on the basis of fate-specific membrane capacitance enabled the discovery of a novel link between membrane capacitance, N-glycosylation branching, and NSPC fate potential (Chapter 3). We further explored how N-glycosylation branching could impact neurogenesis *in vivo* and provide new evidence that branched N-glycans generated by MGAT5 regulate neuronal production and maturation during cortical development (Chapter 4). Lastly, we utilized a proteomic screen comparing control and GlcNAc-treated NSPCs to identify cellular adhesion as a potential mechanism for how N-glycan branching impacts NSPC fate potential (Chapter 5). In Chapter 6, we summarize these findings and discuss future directions of the research.

1.7 REFERENCES

1. H. Okano, S. Temple, Cell types to order: temporal specification of CNS stem cells. *Curr Opin Neurobiol* **19**, 112-119 (2009).
2. W. Li, C. A. Cogswell, J. J. LoTurco, Neuronal differentiation of precursors in the neocortical ventricular zone is triggered by BMP. *J Neurosci* **18**, 8853-8862 (1998).
3. W. A. Gomes, M. F. Mehler, J. A. Kessler, Transgenic overexpression of BMP4 increases astroglial and decreases oligodendroglial lineage commitment. *Dev Biol* **255**, 164-177 (2003).
4. K. Nakashima *et al.*, BMP2-mediated alteration in the developmental pathway of fetal mouse brain cells from neurogenesis to astrocytogenesis. *Proc Natl Acad Sci U S A* **98**, 5868-5873 (2001).
5. K. Nakashima *et al.*, Synergistic signaling in fetal brain by STAT3-Smad1 complex bridged by p300. *Science* **284**, 479-482 (1999).
6. M. Molne *et al.*, Early cortical precursors do not undergo LIF-mediated astrocytic differentiation. *J Neurosci Res* **59**, 301-311 (2000).
7. J. Viti, A. Feathers, J. Phillips, L. Lillien, Epidermal growth factor receptors control competence to interpret leukemia inhibitory factor as an astrocyte inducer in developing cortex. *J Neurosci* **23**, 3385-3393 (2003).
8. Y. Sun, S. K. Goderie, S. Temple, Asymmetric distribution of EGFR receptor during mitosis generates diverse CNS progenitor cells. *Neuron* **45**, 873-886 (2005).
9. A. Lee, M. Aghaamoo, T. Adams, L. Flanagan. (Current Stem Cell Reports, 2018), vol. 4, pp. 116-126.
10. P. Gascoyne, R. Pethig, J. Satayavivad, F. Becker, M. Ruchirawat, Dielectrophoretic detection of changes in erythrocyte membranes following malarial infection. *Biochimica Et Biophysica Acta-Biomembranes* **1323**, 240-252 (1997).
11. M. Cristofanilli *et al.*, Automated electrorotation to reveal dielectric variations related to HER-2/neu overexpression in MCF-7 sublines. *Clin Cancer Res* **8**, 615-619 (2002).
12. R. Pethig *et al.*, Dielectrophoretic studies of the activation of human T lymphocytes using a newly developed cell profiling system. *Electrophoresis* **23**, 2057-2063 (2002).
13. D. M. Vykoukal, P. R. Gascoyne, J. Vykoukal, Dielectric characterization of complete mononuclear and polymorphonuclear blood cell subpopulations for label-free discrimination. *Integr Biol (Camb)* **1**, 477-484 (2009).
14. M. Angstmann, I. Brinkmann, K. Bieback, D. Breitkreutz, C. Maercker, Monitoring human mesenchymal stromal cell differentiation by electrochemical impedance sensing. *Cytotherapy* **13**, 1074-1089 (2011).
15. L. A. Flanagan *et al.*, Unique dielectric properties distinguish stem cells and their differentiated progeny. *Stem Cells* **26**, 656-665 (2008).
16. F. H. Labeed *et al.*, Biophysical characteristics reveal neural stem cell differentiation potential. *PLoS One* **6**, e25458 (2011).
17. J. Lu *et al.*, Advancing practical usage of microtechnology: a study of the functional consequences of dielectrophoresis on neural stem cells. *Integr Biol (Camb)* **4**, 1223-1236 (2012).
18. T. N. G. Adams, A. Y. L. Jiang, P. D. Vyas, L. A. Flanagan, Separation of neural stem cells by whole cell membrane capacitance using dielectrophoresis. *Methods* **133**, 91-103 (2018).

19. A. Y. L. Jiang *et al.*, High-throughput continuous dielectrophoretic separation of neural stem cells. *Biomicrofluidics* **13**, 064111 (2019).
20. J. L. Nourse *et al.*, Membrane biophysics define neuron and astrocyte progenitors in the neural lineage. *Stem Cells* **32**, 706-716 (2014).
21. J. L. Prieto, J. Lu, J. L. Nourse, L. A. Flanagan, A. P. Lee, Frequency discretization in dielectrophoretic assisted cell sorting arrays to isolate neural cells. *Lab Chip* **12**, 2182-2189 (2012).
22. M. G. Simon *et al.*, Increasing label-free stem cell sorting capacity to reach transplantation-scale throughput. *Biomicrofluidics* **8**, 064106 (2014).
23. A. R. Yale *et al.*, Cell Surface N-Glycans Influence Electrophysiological Properties and Fate Potential of Neural Stem Cells. *Stem Cell Reports* **11**, 869-882 (2018).
24. E. Gheorghiu, The resting potential in relation to the equivalent complex permittivity of a spherical cell-suspension. *Physics in Medicine and Biology* **38**, 979-988 (1993).
25. M. Stoneman *et al.*, Protein influence on the plasma membrane dielectric properties: In vivo study utilizing dielectric spectroscopy and fluorescence microscopy. *Bioelectrochemistry* **70**, 542-550 (2007).
26. D. Zimmermann *et al.*, Effects on capacitance by overexpression of membrane proteins. *Biochem Biophys Res Commun* **369**, 1022-1026 (2008).
27. X. Wang *et al.*, Changes in friend murine erythroleukemia cell-membranes during induced-differentiation determined by electrorotation. *Biochimica Et Biophysica Acta-Biomembranes* **1193**, 330-344 (1994).
28. S. Desai, M. Vahey, J. Voldman, Electrically Addressable Vesicles: Tools for Dielectrophoresis Metrology. *Langmuir* **25**, 3867-3875 (2009).
29. F. T. Zhao, J. Li, G. X. Shi, Y. Liu, L. P. Zhu, Modification of glycosylation reduces microvilli on rat liver epithelial cells. *Cell Biol Int* **26**, 627-633 (2002).
30. M. J. Paszek *et al.*, The cancer glycocalyx mechanically primes integrin-mediated growth and survival. *Nature* **511**, 319-325 (2014).
31. I. R. Nabi, J. Shankar, J. W. Dennis, The galectin lattice at a glance. *J Cell Sci* **128**, 2213-2219 (2015).
32. P. Lajoie, J. G. Goetz, J. W. Dennis, I. R. Nabi, Lattices, rafts, and scaffolds: domain regulation of receptor signaling at the plasma membrane. *J Cell Biol* **185**, 381-385 (2009).
33. J. W. Dennis, I. R. Nabi, M. Demetriou, Metabolism, cell surface organization, and disease. *Cell* **139**, 1229-1241 (2009).
34. A. Grigorian *et al.*, Control of T Cell-mediated autoimmunity by metabolite flux to N-glycan biosynthesis. *J Biol Chem* **282**, 20027-20035 (2007).
35. H. Schachter, Biosynthetic controls that determine the branching and microheterogeneity of protein-bound oligosaccharides. *Biochem Cell Biol* **64**, 163-181 (1986).
36. K. O. Broschat *et al.*, Kinetic characterization of human glutamine-fructose-6-phosphate amidotransferase I: potent feedback inhibition by glucosamine 6-phosphate. *J Biol Chem* **277**, 14764-14770 (2002).
37. K. S. Lau *et al.*, Complex N-glycan number and degree of branching cooperate to regulate cell proliferation and differentiation. *Cell* **129**, 123-134 (2007).
38. K. Sasai, Y. Ikeda, T. Fujii, T. Tsuda, N. Taniguchi, UDP-GlcNAc concentration is an important factor in the biosynthesis of beta1,6-branched oligosaccharides: regulation

based on the kinetic properties of N-acetylglucosaminyltransferase V. *Glycobiology* **12**, 119-127 (2002).
39. N. Flaris *et al.*, Developmentally-regulated lectin-binding in the embryonic mouse telencephalon. *Brain Research* **678**, 99-109 (1995).
40. A. Ishii *et al.*, Developmental changes in the expression of glycogenes and the content of N-glycans in the mouse cerebral cortex. *Glycobiology* **17**, 261-276 (2007).
41. E. Ioffe, P. Stanley, Mice lacking N-acetylglucosaminyltransferase I activity die at mid-gestation, revealing an essential role for complex or hybrid N-linked carbohydrates. *Proc Natl Acad Sci U S A* **91**, 728-732 (1994).
42. M. Metzler *et al.*, Complex asparagine-linked oligosaccharides are required for morphogenic events during postimplantation development. *Embo Journal* **13**, 2056-2065 (1994).
43. R. S. Haltiwanger, J. B. Lowe, Role of glycosylation in development. *Annu Rev Biochem* **73**, 491-537 (2004).
44. H. H. Freeze, E. A. Eklund, B. G. Ng, M. C. Patterson, Neurology of inherited glycosylation disorders. *Lancet Neurol* **11**, 453-466 (2012).
45. Z. Ye, J. D. Marth, N-glycan branching requirement in neuronal and postnatal viability. *Glycobiology* **14**, 547-558 (2004).
46. L. Feldcamp *et al.*, Mgat5 modulates the effect of early life stress on adult behavior and physical health in mice. *Behav Brain Res* **312**, 253-264 (2016).
47. L. Soleimani, J. C. Roder, J. W. Dennis, T. Lipina, Beta N-acetylglucosaminyltransferase V (Mgat5) deficiency reduces the depression-like phenotype in mice. *Genes Brain Behav* **7**, 334-343 (2008).
48. E. A. Partridge *et al.*, Regulation of cytokine receptors by Golgi N-glycan processing and endocytosis. *Science* **306**, 120-124 (2004).
49. K. S. Lau, J. W. Dennis, N-Glycans in cancer progression. *Glycobiology* **18**, 750-760 (2008).
50. J. Hirabayashi *et al.*, Oligosaccharide specificity of galectins: a search by frontal affinity chromatography. *Biochim Biophys Acta* **1572**, 232-254 (2002).
51. S. S. Pinho, C. A. Reis, Glycosylation in cancer: mechanisms and clinical implications. *Nat Rev Cancer* **15**, 540-555 (2015).

CHAPTER 2

High-throughput Continuous Dielectrophoretic Separation of Neural Stem Cells

Authors: Alan Y.L. Jiang[a,b,c], **Andrew R. Yale[b,c]**, Mohammad Aghaamoo[a], Do-Hyun Lee[a], Abraham P. Lee[a], Tayloria N.G. Adams[c,d]*, Lisa A. Flanagan[a,b,c,e]*

[a] Department of Biomedical Engineering, University of California, Irvine

[b] Department of Neurology, University of California, Irvine

[c] Sue & Bill Gross Stem Cell Research Center, University of California, Irvine

[d] Department of Chemical and Biomolecular Engineering, University of California, Irvine

[e] Department of Anatomy & Neurobiology, University of California, Irvine

*Co-corresponding authors

Key Words: Cell sorting, dielectrophoresis, membrane capacitance, microfluidic, hydrophoresis, neural stem and progenitor cell, astrocyte

2.1 ABSTRACT

We created an integrated microfluidic cell-separation system that incorporates hydrophoresis and dielectrophoresis modules to facilitate high-throughput continuous cell separation. The hydrophoresis module consists of a serpentine channel with ridges and trenches to generate a diverging fluid flow that focuses cells into two streams along the channel edges. The dielectrophoresis module is composed of a chevron-shaped electrode array. Separation in the dielectrophoresis module is driven by inherent cell electrophysiological properties and does not require cell-type specific labels. The chevron shape of the electrode array couples with fluid flow in the channel to enable continuous sorting of cells to increase throughput. We tested the new system with mouse neural stem cells since their electrophysiological properties reflect their differentiation capacity (e.g. whether they will differentiate into astrocytes or neurons). The goal of our experiments was to enrich astrocyte-biased cells. Sorting parameters were optimized for each batch of neural stem cells to ensure effective and consistent separations. The continuous sorting design of the device significantly improved sorting throughput and reproducibility. Sorting yielded two cell fractions and we found astrocyte-biased cells were enriched in one fraction and depleted from the other. This is an advantage of the new continuous sorting device over traditional dielectrophoresis-based sorting platforms that target a subset of cells for enrichment but do not provide a corresponding depleted population. The new microfluidic dielectrophoresis cell-separation system improves label-free cell sorting by increasing throughput and delivering enriched and depleted cell subpopulations in a single sort.

2.2 INTRODUCTION

The subtle phenotypic differences between cells can be difficult to detect but have big consequences for cell behavior. Separating cells based on their phenotypic differences enables critical experiments aimed at deciphering their biological functions and determining their relevance in disease. Cell separation systems that do not require cell type-specific labels have a number of advantages. Labels can be limiting since many cells of interest for biological or biomedical applications do not have sufficient markers that distinguish them from other cell types. Labeling of cells could change their biological function, and since this is rarely screened for or tested, incorrect assumptions may be made about the function of labeled cells. Antibodies or labels used for traditional flow cytometry methods bind to cell surface components and could stimulate intracellular signaling cascades. Labeling of intracellular components requires modification of the cell to introduce foreign material that may interfere with normal cellular function. Unlabeled and unmodified cells are also ideal for therapeutic purposes since they require less manipulation that could affect cell phenotype prior to introduction into a patient. Continued development of label-free cell separation technologies will provide much needed alternatives to label-based separation systems.

Many different microfluidic cell separation devices have been developed (Hyun and Jung 2013). Combining multiple separation modalities in microfluidic devices can have advantages over any single approach. Label-free systems include hydrophoresis, in which fluid flow is used to direct cell location in a microfluidic channel, and dielectrophoresis (DEP) in which non-uniform electric fields induce cell movement due to inherent cellular properties (Pethig 2010, Hyun and Jung 2013). Hydrophoresis may not have sufficient resolving power to separate cells that are quite similar to each other, particularly cells that are of similar size. DEP can distinguish

cells of similar size as long as the cells have distinct electrophysiological properties. For example, similarly sized cells that significantly differ in membrane capacitance can be separated by alternating current (AC) DEP in the frequency range of approximately 1-1000 kHz (Martinsen et al. 2002, Chen and Pohl 1974, Labeed et al. 2011, Nourse et al. 2014, Simon et al. 2014, Adams et al. 2018). A limitation to DEP-based sorting is that many DEP devices rely on trapping of cells along electrode arrays and release of the isolated cells after washing away non-trapped cells. This "trap and release" mechanism is low throughput due to spatial limits on the number of trapping sites in a device. Combining methodologies such as hydrophoresis and DEP may provide advantages over those of either technique alone.

We developed a microfluidic separation device combining hydrophoretic and DEP modules to create a continuous cell sorter that overcomes the limited throughput of DEP trapping devices. The hydrophoretic module directs all cells to the outer edges of the microfluidic channel. This positions cells for separation by the DEP module, in which the induced DEP force directs targeted cells to the middle of the channel. Channel outlets separately collect two cell populations, those remaining along the outer edges of the channel and those focused to the middle of the channel. Our goal was to create a continuous, rapid, and label-free cell separation system to overcome limitations of sorters using a single separation modality.

2.3 DEVICE DESIGN PRINCIPLES

Integration of Hydrophoretic and DEP Modules

We created a hydrodynamic oblique angle parallel electrode sorter (HOAPES) that incorporates hydrophoresis and DEP in a single platform with single-step operation. The integrated system performs better than the trap and release methods used in previous DEP

devices by continuously sorting cells, minimizing cell-cell interactions and manual operation, and eliminating residual flow. The microfluidic HOAPES device incorporates a filter to remove cell clumps, a hydrophoretic module, a DEP module, and a set of 3 outlet channels (Fig. 2.1A).

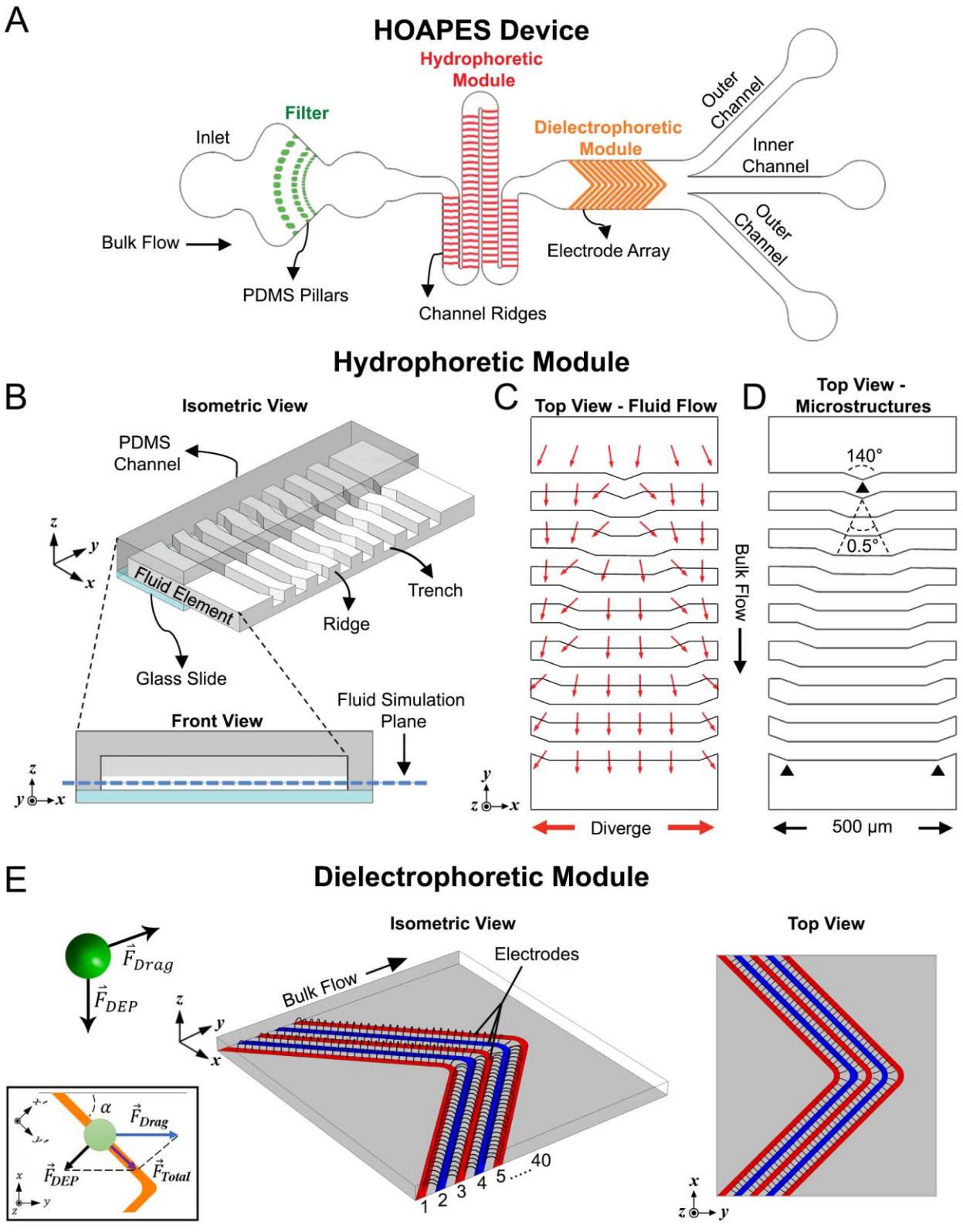

Figure 2.1: Schematic of HOAPES device with hydrophoretic and DEP modules. (A) A simplified schematic of the HOAPES device shows fluid inlet, PDMS pillars (green) that create a

filter to remove cell clumps, the hydrophoretic module (red), DEP module (orange), and set of 3 outlets (not to scale). (B) An isometric view shows a portion of the hydrophoretic module with PDMS channel (gray), glass slide (blue) and the fluid volume of the channel. Half of the PDMS and glass that make up the channel were removed to depict the details of the fluid within the channel. PDMS microstructures on the ceiling of the channel create fluidic ridges and trenches. A projected front view shows the PDMS channel (light gray), glass slide (blue), PDMS ceiling microstructures that create fluid trenches (dark gray), and fluid (white). The plane used for fluid simulation in panel C is denoted by the dashed blue line. (C) A top view of a portion of the hydrophoretic module shows a COMSOL simulation of the diverging fluid flow (red arrows) at the fluid simulation plane. A 10 times scaling factor was applied to the x component of the velocity vector to emphasize the direction of the transverse flow. (D) Top view of a portion of the hydrophoretic module shows the ceiling PDMS microstructures, depicting their gradual change in dimension along the channel based on defined diverging angles. (E) A simplified representation of the electric field profile from the 40 electrode array in the DEP module. The isometric view illustrates the electric field distribution in the z direction while the top view illustrates the distribution in the x, y direction. The green sphere represents a biological cell and the arrows denote the direction of the drag force and induced DEP force. The inset shows a free body diagram illustrating a cell (green circle) moving along an electrode. The drag force acts in the y-direction, the DEP force perpendicular to the electrode, and the combination of the two creates a total force directing cells along the electrodes.

Hydrophoresis is the manipulation of suspended particles using microstructure-induced hydrodynamic pressure gradients. Hydrophoresis can be used to direct cells to specific locations in a microfluidic channel without sheath flow. This simplifies device operation since multiple fluidic inlets with balanced flow rates are not needed to create sheath flow to direct cell position in the channel. We utilized a hydrophoretic sheathless aligner working in the laminar flow regime that directs cell location across a wide range of flow rates. This enables efficient and reproducible direction of cells within the channel without costly high-precision instrumentation (Song et al. 2015a). The goal of the hydrophoretic module was to push cells to the channel edges so that all cells would be at a similar position in the channel when encountering the DEP module. The hydrophoretic module working mechanism was evaluated with computational flow simulations while the microstructure design of the channel was determined with dimensional analysis (also known as the factor label method)(Song and Choi 2014). Briefly, the hydrophoretic module contains a series of slanted ridged microstructures on the channel ceiling

that create a pressure gradient to push cells toward the channel edges. The relationship between cell movement and the dimensionless physical parameters was defined by the following equation (Song and Choi 2014):

$$L_p \propto f\left(\frac{w}{D}, \frac{d}{D}, Re\right), (1)$$

where L_p is the hydrophoretic equilibrium position of the cell, w is the width of the fluid channel, D is the diameter of the cell, d is the depth of the fluid trench and Re is the Reynolds number (all dimensions listed in equations are depicted in Supplemental Figure 2.S1). The design constraints for optimal hydrophoretic focusing were reported as (Song and Choi 2014):

$$\frac{d}{D} \leq 2 \text{ and } (h - d) < d, (2)$$

where h is the channel height. Following these design constraints, a simplified CAD model with 7 slanted ridged microstructures was designed in Solidworks and imported into COMSOL Multiphysics to evaluate the flow pattern of the fluid element (Fig. 2.1B). Fluid flow in the hydrophoretic module was evaluated at a fluid simulation plane 15 μm from the bottom of the channel (blue dashed line in Fig. 2.1B, front view). The height of the fluid simulation plane was set at 15 um from the bottom of the channel since the diverging fluid flow directing cell movement in the channel was maximal at this location (Supplemental Fig. 2.S2 and Movie 2.1). The maximum transverse flow occurred at every slanted region of the ridged microstructures, generating an overall diverging flow profile that carries the cells toward the channel edges (Fig. 2.1C). A 10 times scaling factor was applied to the x component of the velocity vector in Figure 2.1C to emphasize the direction of the transverse flow. To take advantage of the maximum transverse flow, we designed a 0.5° angle (Fig. 2.1D) to gradually shift the slanted region toward the channel edges to achieve two focused streams of suspended cells. This design avoided stepwise movement of cells in the hydrophoretic module. Full dimensions of the hydrophoretic

module are depicted in Supplemental Figure 2.S1 and videos show that fluid flow in the module directs cells to the channel edges (Supplemental Fig. 2.S3 and Movie 2.2).

DEP is one of the most widely used label-free techniques to manipulate cells in microfluidic systems. The induced movement for each cell is highly dependent on the strength and frequency of the applied AC electric field. The specific response of a cell to the applied electric field can be estimated by the complex Clausius-Mossotti (CM) factor. The CM factor describes the relationship between the cell and the suspension medium that is defined as:

$$CM = \frac{(\varepsilon^*_{cell} - \varepsilon^*_{media})}{(\varepsilon^*_{cell} + 2\varepsilon^*_{media})}; \varepsilon^* = \varepsilon + j\sigma/\omega \quad (3)$$

Here, the term ε^* is the complex permittivity, ε is the permittivity, $j = \sqrt{-1}$ (imaginary unit), σ is the electrical conductivity, and ω is the angular frequency of the AC electric field. The CM factor can be positive or negative, depending on the relative difference between the polarizability of the cell and the surrounding medium. Since the complex permittivity is a function of the frequency of the applied electric field, different cells with distinct electrical properties may exhibit different responses to the electric field at a particular applied frequency. Further, the DEP force, $\vec{F}_{DEP}$, induced on a cell can be estimated by the following equation:

$$\vec{F}_{DEP} = 2\pi R^3 \varepsilon_{media} Re(CM) \nabla \left|\vec{E}\right|^2, \quad (4)$$

where R is the radius of the cell, ε_{media} is the permittivity of the medium, $Re(CM)$ is the real part of the CM factor, and $\nabla \left|\vec{E}\right|^2$ is the gradient of the electric field squared. Hence, when the surrounding medium has greater complex permittivity than the cells, the real part of the CM factor will be less than zero ($Re(CM) < 0$) and the cells will move from high to low electric field regions (negative DEP, nDEP). In contrast, when cells have greater permittivity than the

surrounding medium ($Re(CM) > 0$), they will move from low to high field regions of the electric field (positive DEP, pDEP).

We created the DEP module with angled planar interdigitated electrodes in a chevron pattern (Fig. 2.1E). The goal of the pattern was to pull cells experiencing pDEP to the center of the channel, where they would exit via the inner channel outlet. Cells not in pDEP would remain at the channel edges and exit through the outer channel outlets. The high electric field regions are typically along the electrode edges for planar interdigitated electrodes (Fig. 2.1E). Therefore, cells experiencing pDEP feel an induced DEP force ($\vec{F}_{DEP}$) perpendicular to the electrodes that pulls the cells toward the electrodes. The pDEP force must be sufficiently strong to attract cells to the electrodes in the presence of the fluid flow. Cells that experience sufficiently strong pDEP to reach the electrodes experience a DEP force perpendicular to the electrode angle (Fig. 2.1E inset). Hereafter, this force is referred to as $\vec{F}_{DEP,xy}$. Coupling the induced DEP force with the viscous drag force ($\vec{F}_{drag}$) parallel to the bulk fluid flow causes the cells to migrate along the electrodes and progressively move down the channel toward the outlets (Fig. 2.1E, Supplemental Fig. 2.S3 and Movie 2.3). Under normal sorting conditions, the cell's velocity ($\vec{v}_p$) is less than or equal to the fluid velocity ($\vec{u}_f$); hence the only drag force acting on the cell is in the y-direction from the fluid flow and can be defined by the Stokes drag equation for a spherical cell in laminar flow:

$$\vec{F}_{drag} = 6\pi\eta\vec{v}R;\ \vec{v} = \vec{u}_f - \vec{v}_p \quad (5)$$

where η is the dynamic viscosity of the fluid, and $\vec{v}$ is the flow velocity relative to the cell. Thus, the motion of the cells in the x-y plane is dictated by the vector sum of $\vec{F}_{DEP,xy}$ and $\vec{F}_{drag}$, and the resultant force (F_{total}) in the xy coordinate is defined as:

$$(F_{total})_x = \vec{F}_{DEP,xy}.\cos(\alpha) \quad (6)$$

$$(F_{total})_y = \vec{F}_{drag} - \vec{F}_{DEP,xy}.\sin(\alpha) \quad (7)$$

where α is the angle of the electrode relative to the wall of the fluid channel. For the cells to move along the electrodes, $\vec{F}_{DEP,xy}$ should cancel out the perpendicular component of $\vec{F}_{drag}$ with respect to the electrodes. For these calculations we do not consider additional forces, such as friction from the electrodes or channel surface or gravity or buoyancy. In the $x'y'$ coordinates (inset Fig. 2.1E):

$$\sum F_{x'} = 0 \quad (8)$$

$$\vec{F}_{DEP,xy} - \vec{F}_{drag}.\sin(\alpha) = 0 \rightarrow \vec{F}_{DEP,xy} = \vec{F}_{drag}.\sin(\alpha) \quad (9)$$

In equation (6), if we replace $\vec{F}_{DEP,xy}$ with $\vec{F}_{drag}.\sin(\alpha)$ derived from equation (9), we have

$$(F_{total})_x = \vec{F}_{drag}.\sin(\alpha).\cos(\alpha) \quad (10)$$

The angle of the electrode relative to the channel sidewall was optimized to yield the maximum focusing force ($(F_{total})_x$) toward the center of the channel. Using equation (10) to solve for α that yields maximum $(F_{total})_x$, gives:

$$(F_{total})_x = \frac{sin2\alpha}{2} \cdot \vec{F}_{drag} \quad (11)$$

$$\frac{2(F_{total})_x}{\vec{F}_{Drag}} = sin2\alpha \quad (12)$$

$$2\alpha = \frac{\pi}{2}; \alpha = \frac{\pi}{4}\ or\ 45° \quad (13)$$

The result indicates that the maximum focusing occurs when the angle of the electrode is 45° relative to the channel sidewall.

Once we determined that the optimal angle of the electrode relative to the sidewall for cell focusing was 45°, we created a symmetric chevron electrode design resulting in a 90° angle at the electrode tip. The symmetric design doubles the electrode area for focusing cells, thus

increasing throughput. The electrode tips were designed to allow release of cells so they could travel further down the channel. This was accomplished by rounding the tips at the points of the chevron pattern (Supplemental Fig. 2.S1), which effectively decreased the electrode width and increased the gap between the electrodes at the points. The electrodes are 35 μm wide with 35 μm gaps between electrodes (Supplemental Fig. 2.S1). If the electrode points were not rounded, the electrode width at the point would be 50 μm. By rounding the points, the width was decreased to 35 μm, matching the width at the slanted region. The radius of curvature for the inner electrode edge on the rounded tips was 50 μm while the radius of curvature for the outer edge of the electrode was 85 μm (Supplemental Fig. 2.S1). This differential curvature of the inner and outer electrode edges creates a larger gap of 65 μm between electrodes at the curves. Thus, the slanted electrodes are 35 μm wide with 35 μm gaps but at the points the electrodes are 35 μm wide with 65 μm gaps (Supplemental Fig. 2.S1). The electric field strength is lessened at the electrode tips by increasing the gap between electrodes to 65 μm (Fig. 2.1E, top view). The weakened electric field strength at the electrode tips allows cells to release from one electrode to the next and move down the channel. Overall, cells that experience an induced pDEP force will be focused toward the middle of the channel by migrating along the electrodes toward the tips, where they then release to travel further down the channel and exit via the inner channel outlet.

2.4 RESULTS

2.4.1 Cells for Testing the HOAPES Device

We tested cell sorting in the new HOAPES device with mouse neural stem and progenitor cells (NSPCs). These cells form distinct differentiated cell types in the central nervous system, particularly astrocytes and neurons. Cultures of mouse NSPCs contain cells that are biased

toward forming astrocytes and others that are neuron-biased (Flanagan et al. 2008, Labeed et al. 2011). These astrocyte- and neuron-biased cells do not differ significantly in size and express similar markers, making them difficult to separate from each other using traditional means (Flanagan et al. 2008, Labeed et al. 2011). However, astrocyte- and neuron-biased cells do differ in the electrophysiological property membrane capacitance (Flanagan et al. 2008, Labeed et al. 2011). Differences in membrane capacitance are sufficient to enable separation of astrocyte-biased and neuron-biased cells without the use of cell type-specific labels (Nourse et al. 2014, Simon et al. 2014, Adams et al. 2018, Yale et al. 2018). DEP is generally not toxic for mouse NSPCs (Lu et al. 2012). But, cells exposed to certain frequencies in DEP for times longer than 5 minutes show a decrease in viability (Lu et al. 2012). Thus, a continuous DEP sorting system in which cells are exposed to electric fields for seconds rather than minutes (as needed for DEP trapping devices) would be advantageous. The specific properties of mouse NSPCs and the desire to decrease their exposure to electric fields make them an ideal test case for continuous label-free DEP sorting.

2.4.2 Functional Analysis of the HOAPES Hydrophoretic and DEP Modules

We tested functional operation of the HOAPES device by flowing through mouse NSPCs. The HOAPES device was mounted on a microscope stage to enable visualization of cell behavior during sorting (Fig. 2.2A). Cells were loaded into the inlet port of the channel as described in Methods. The flow rate was first calibrated using a low cell concentration (1 million cells/ml), an applied voltage of 6 Vpp (Simon et al. 2014, Lu et al. 2012), and a frequency at which more than 95% of the cells experienced pDEP and were focused to the inner channel (such as 1 MHz). Starting with a flow rate of 1 µl/min, we gradually increased the flow rate and found that 3.5 µl/min was the maximum rate that maintained more than 95% of the cells focused to the

inner channel. We next optimized the cell concentration by switching to a lower frequency that could be used for sorting (such as 150 kHz) and gradually increasing the cell concentration starting at 1 million cells/ml. We found that a cell concentration of 3 million cells/ml could be effectively sorted while maintaining the purity (percentage of cells focused to the inner channel) obtained with lower cell concentrations. Based on these optimizations we used a concentration of $3x10^6$ cells/ml and a flow rate of 3.5 µl/min.

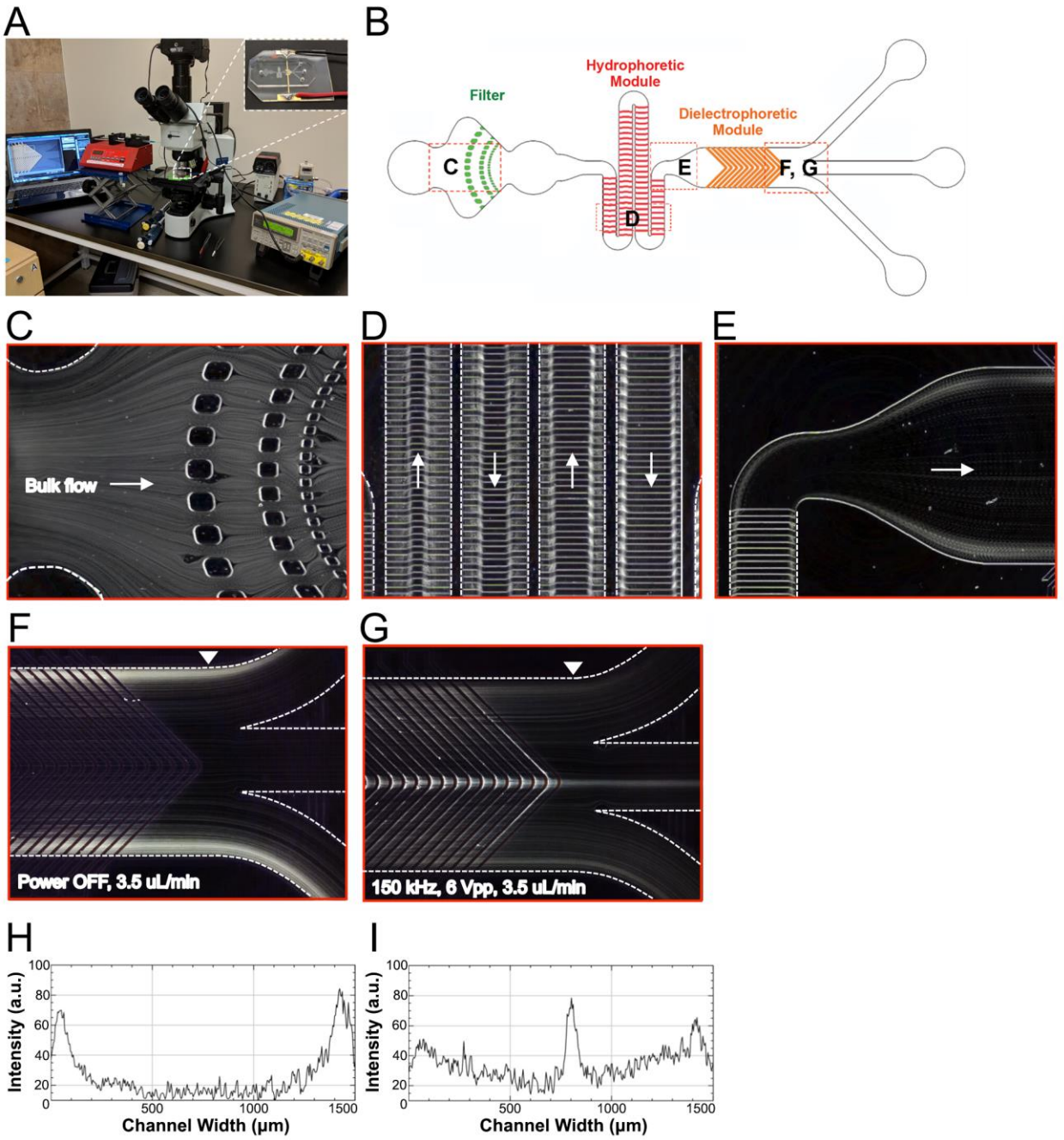

Figure 2.2: Functional analysis of the HOAPES device. (A) For sorting cells, the HOAPES device (inset) is mounted on the stage of an upright microscope to enable visualization of cells in the channel. The device is connected to a function generator for DEP and syringe pump for constant fluid flow. (B) Red dashed boxes on the HOAPES device schematic show the locations where images in C-G were taken. (C) The trajectories of mouse NSPCs in the HOAPES device were obtained from Z-projections (see Methods). Individual cells easily pass the PDMS pillars of the filter region designed to prevent cell clumps from entering the channel. (D) In the hydrophoretic module, cell trajectories show that cells are gradually directed into 2 streams along the channel edges. Arrows indicate the direction of fluid flow. (E) At the end of the

hydrophoretic module, cells are in 2 streams along the channel edges as they enter the DEP module. Arrow indicates the direction of fluid flow. (F) When power to the DEP module is off, the cells remain in 2 streams along the channel edges and exit the two outer channels. (G) When power to the DEP module is on and electrodes are actuated at 150 kHz and 6 Vpp, a subset of cells are focused to the middle of the channel and exit via the inner channel. (H) Plot shows the signal intensity of cell trajectories across the channel width when power to the DEP module is off (image in F). Arrowhead in F indicates the region of the channel across which the signal intensity was measured. Two peaks are evident along the channel edges. (I) Plot shows the signal intensity of cell trajectories across the channel width when power to the DEP module is on (image in G). Arrowhead in G indicates the region of the channel across which the signal intensity was measured. A peak is evident in the center of the channel and the two peaks along the channel edges are lower than those in H. Flow rate in C-G was 3.5 µl/min.

Cells entered the channel via bulk flow and encountered the filter region (Fig. 2.2B, C), which was designed to prevent entry of large cell clumps that could clog the downstream channel. The filter effectively trapped large debris and cell aggregates but allowed fluid flow to continue through the channel so sorting was not disrupted, increasing the utility of the sorter. Rarely, small cell clumps not trapped by the filter disrupted the function of the hydrophoretic module or the flow distribution at the channel outlets. The flow profile in the channel before and after the DEP module was closely monitored and any runs with irregular flow due to these small cell clumps were discarded.

After passing the filter region, cells continued to spread across the channel width as they entered the hydrophoretic module. Cells in the hydrophoretic module were gradually directed to the outer edges of the channel through the action of PDMS microstructures on the channel ceiling that create hydrodynamic pressure gradients directing cell movement (Fig. 2.2D, Supplemental Fig. 2.S3, Movie 2.2). The location of the angles in the PDMS microstructures changes along the channel length, becoming successively further apart to direct cells toward channel edges (Fig. 2.2D, Fig. 2.1, Fig. 2.3, Supplemental Fig. 2.S1). At the end of the hydrophoretic module, the NSPCs were localized to two streams along the outer edges of the channel (Fig. 2.2E).

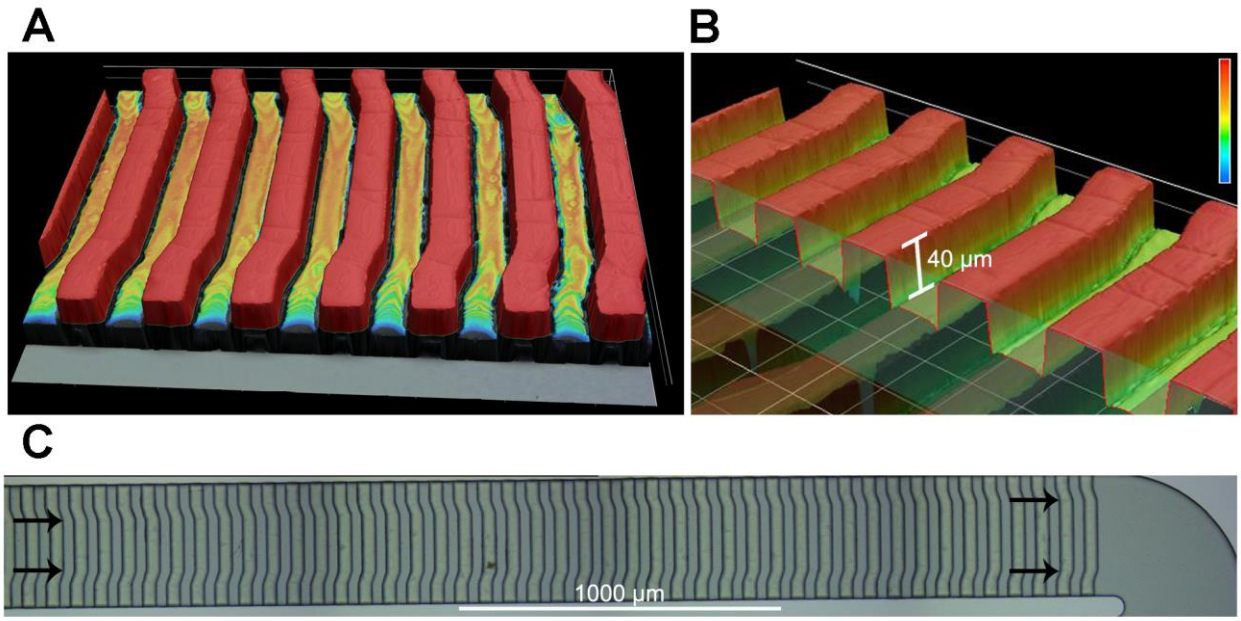

Figure 2.3: Detail of PDMS microstructures in the hydrophoretic module. Images are from laser scanning confocal microscopy of the silicone mold used to create the PDMS channel for the hydrophoretic module. (A) Raised structures on the silicone mold are highlighted red. (B) A cut away image shows the measured height of the raised structures on the mold. (C) Images of a section of the mold show the gradual change in the angle of the structures (angles indicated by arrows).

Cells enter the DEP module in two streams along the channel edges. The electrodes in the DEP region are 35 µm wide with 35 µm gaps and are chevron shaped, creating an angled electrode array pointing toward the center of the channel (Fig. 2.1, Supplemental Fig. 2.S1). When the electrodes in the DEP module were not energized, the NSPCs remained along the channel edges and exited via the outer channels (Fig. 2.2 F, H). In contrast, when the electrodes were energized at an AC frequency at which a percentage of the cells experienced pDEP (150 kHz), the induced DEP force directed those cells along the electrodes, bringing them to the center of the channel (Fig. 2.2 G, I). Videos of NSPCs in the channel show their movement along the slanted electrodes (Fig. 2.4, Supplemental Fig. 2.S3, Movie 2.3). When cells reach the angled tips of the chevron electrode array, the reduction in induced DEP force allows them to be released from the electrode and travel down the channel (see Device Design Principles). The

cells experiencing sufficient pDEP exit via the inner outlet. Varying the frequency of the applied electric field changes the percentage of cells in pDEP, enabling selection of subpopulations of cells.

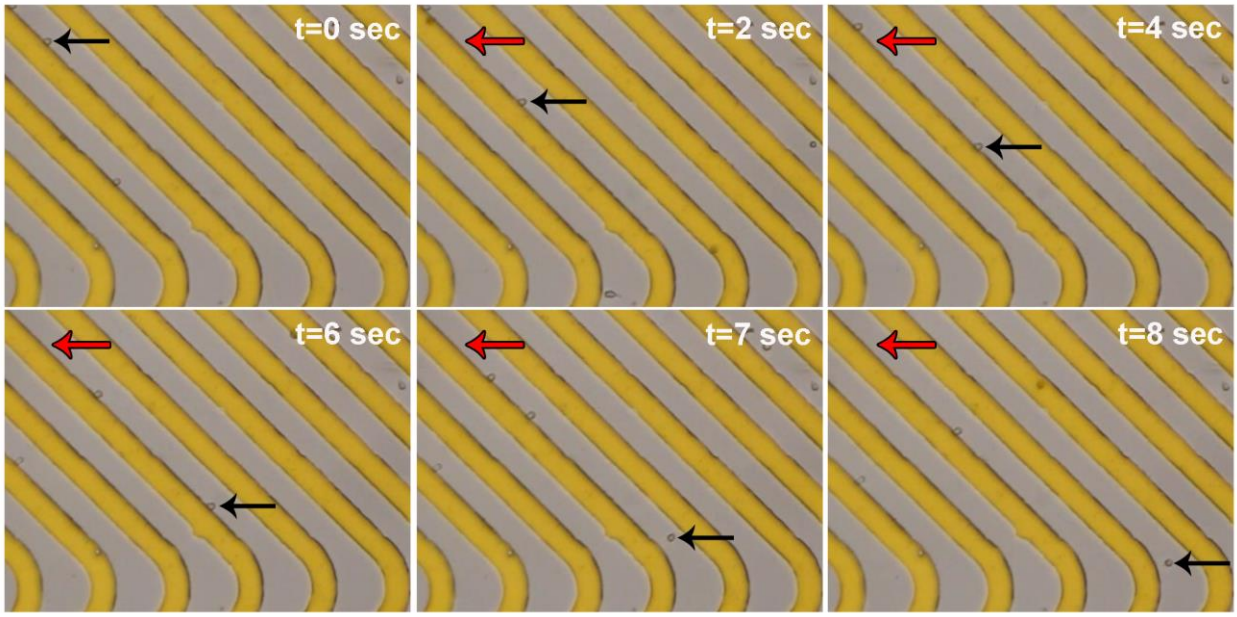

Figure 2.4: Movement of cells along electrodes in the DEP module. A time series of phase contrast images (10x) show cells moving along the slanted electrodes (gold) in the DEP module when electrodes were actuated at 150 kHz, 6 Vpp. One cell's position at each time point is shown by black arrows while red arrows mark the starting position of that cell in the first panel. The last two panels (t=7 sec and t=8 sec) show the cell releasing from the electrode at the rounded tip and moving further down the channel.

2.4.3 Experimental Strategy for Cell Sorting in the HOAPES Device

We utilized a standard workflow for each sorting experiment with the HOAPES device (Fig. 2.5). Mouse NSPCs are routinely grown in suspension and generate large clusters of cells termed neurospheres. Individual cells were dissociated from neurospheres for sorting in the HOAPES device (Fig. 2.5A). Dissociated NSPCs were resuspended in a low conductivity DEP buffer solution for sorting, which we found previously does not harm NSPCs or alter their behavior (Flanagan et al. 2008, Lu et al. 2012). A focusing curve was generated for each batch of NSPCs to determine the appropriate sorting frequency since we find that the optimal frequency

can vary slightly from batch to batch (Fig. 2.5B). NSPCs were loaded into the HOAPES device and the desired frequency for sorting set such that approximately one third of the cells were focused to the inner outlet through pDEP (see Determining Optimal Sorting Frequency). The focused cells were collected from the inner outlet and the unfocused cells along the channel edges were collected from the two outer channels and pooled (Fig. 2.5C). Sorted cells were compared to several types of control cells: NSPCs grown in regular culture conditions (media control), NSPCs incubated in DEP buffer but not sorted (DEP buffer control), and NSPCs exposed to electric fields but not sorted (1 MHz control). The latter group was generated by setting a high frequency (1 MHz) at which all cells in the population experience pDEP and are focused to the inner channel. Since the goal of the sort was to enrich astrocyte-biased cells, we analyzed the fate of sorted cells and controls by differentiating the cells and quantifying astrocyte formation (Fig. 2.5D-F).

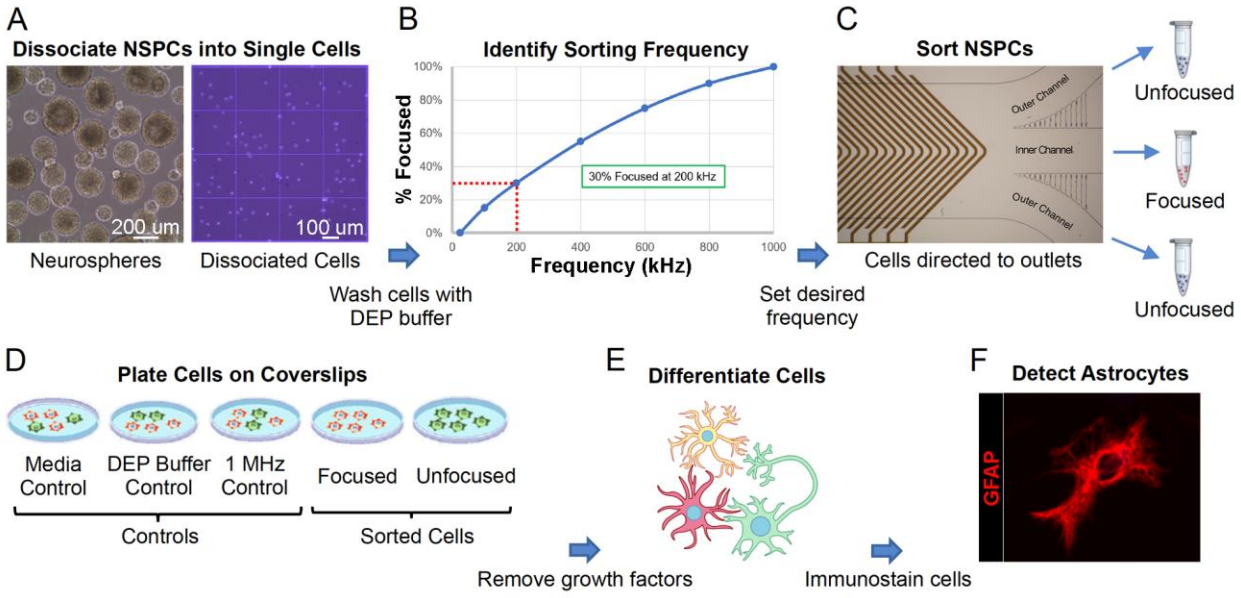

Figure 2.5: Experimental strategy for sorting mouse NSPCs with the HOAPES device. (A) Mouse NSPCs grow in suspension and form clusters of cells known as neurospheres (left). Neurospheres were dissociated to form single cells (right) and cells washed with DEP buffer. (B) Cells in DEP buffer were loaded into the HOAPES device and the percentage of cells focused to the inner channel quantified across a range of frequencies. The resultant focusing curve (shown

here as a schematic) was used to determine a sorting frequency targeting ~30% of the cells. (C) Mouse NSPCs were sorted in the HOAPES device at the determined frequency and two populations of cells collected: those focused to the inner channel and those that remained unfocused and tracked to the outer channels. The unfocused cells from the two outer channels were pooled for further analysis. (D) Sorted cells (focused and unfocused) and controls (media, DEP buffer, and 1 MHz) were plated on glass coverslips for cellular differentiation and further analysis. (E) Cell differentiation was induced by removal of growth factors from the culture media. Cells were differentiated for 3 days to allow formation of astrocytes. (F) Astrocytes in the differentiated cell samples were detected by immunostaining with antibodies that detect the astrocyte marker glial fibrillary acidic protein (GFAP, red). Image shows a differentiated astrocyte.

2.4.4 Determining Optimal Sorting Frequency

We found previously that astrocyte-biased cells in NSPC populations experience pDEP at lower frequencies than do neuron-biased cells (Flanagan et al. 2008, Labeed et al. 2011, Nourse et al. 2014). Using a trap and release DEP-based sorting scheme, we determined that sorting cells at a frequency at which ~30% of the cells experience pDEP led to enrichment of astrocyte-biased cells (Simon et al. 2014). We therefore tested a similar approach here, aiming to collect 30% of the cells experiencing pDEP at low frequencies. Since the HOAPES device incorporates fluid flow and continuous movement of cells along the electrode array, we experimentally determined the frequency needed to focus ~30% of the cells to the inner channel outlet. We generated focusing curves for each batch of mouse NSPCs by measuring the percentage of cells focused to the inner channel outlet at a range of frequencies from 10-1000 kHz (example shown in Fig. 2.6). We found the frequency needed to target 30% of the cells ranged from 136-250 kHz across 4 batches of mouse NSPCs, with an average of 184 kHz.

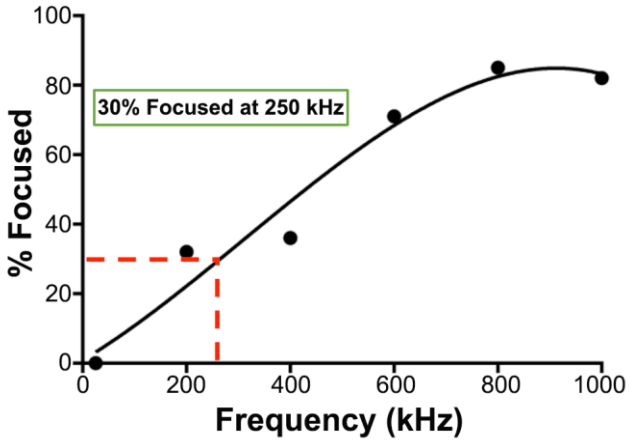

Figure 2.6: Representative focusing curve. A focusing curve from a mouse NSPC sorting experiment shows the gradual increase in the percentage of cells focused to the inner channel across increasing frequency. A best fit line was used to determine 250 kHz as the appropriate sorting frequency for this population.

2.4.5 Sorting NSPCs in HOAPES Yielded Both Enriched and Depleted Cell Populations

We sorted mouse NSPCs in the HOAPES device at frequencies determined by focusing curves and differentiated the cells to assess astrocyte formation. Imaging of the differentiated cells showed robust astrocyte formation by cells focused to the inner channel (Fig. 2.7A). We found no significant difference in the formation of astrocytes by the control cells (percentage GFAP-positive cells: 28.7 +/- 1.6 Media, 23.9 +/- 1.7 DEP Buffer, 26.1 +/-2.5 1 MHz, SEM; one way ANOVA $p=0.25$) (Fig. 2.7B). Thus, cells incubated in DEP buffer or exposed to 1 MHz electric fields did not differ from cells in regular NSPC media in their ability to form astrocytes. These data corroborate our previous findings that DEP sorting of NSPCs does not change their fate potential (Lu et al. 2012).

We found significant differences in astrocyte formation by the sorted cells (percentage GFAP-positive cells: 23.9 +/- 1.7 DEP Buffer Control, 33.9 +/- 2.2 Focused, 12.05 +/- 1.7 unfocused, SEM; one way ANOVA $p<0.0001$) (Fig. 2.7C). Astrocyte-biased NSPCs were significantly enriched in the focused sample, showing a 1.4-fold increase in cells forming

astrocytes compared to control cells (p=0.0015)(Fig. 2.7C). Interestingly, astrocyte-biased cells were correspondingly depleted from unfocused samples collected from the outer exit channels (Fig. 2.7C). Astrocyte-biased cells were reduced by half compared to controls (2-fold reduction)(p=0.0001). The focused, enriched cells and unfocused, depleted cells differed from each other by 2.8-fold, providing two populations that differed more from each other than either population did from controls (p<0.0001). The focused and unfocused cells give a higher degree of separation than that obtained with our previous sorting platforms. Thus, a significant advantage of the HOAPES device over other DEP sorting platforms is the generation of enriched and depleted cell populations in a single sort.

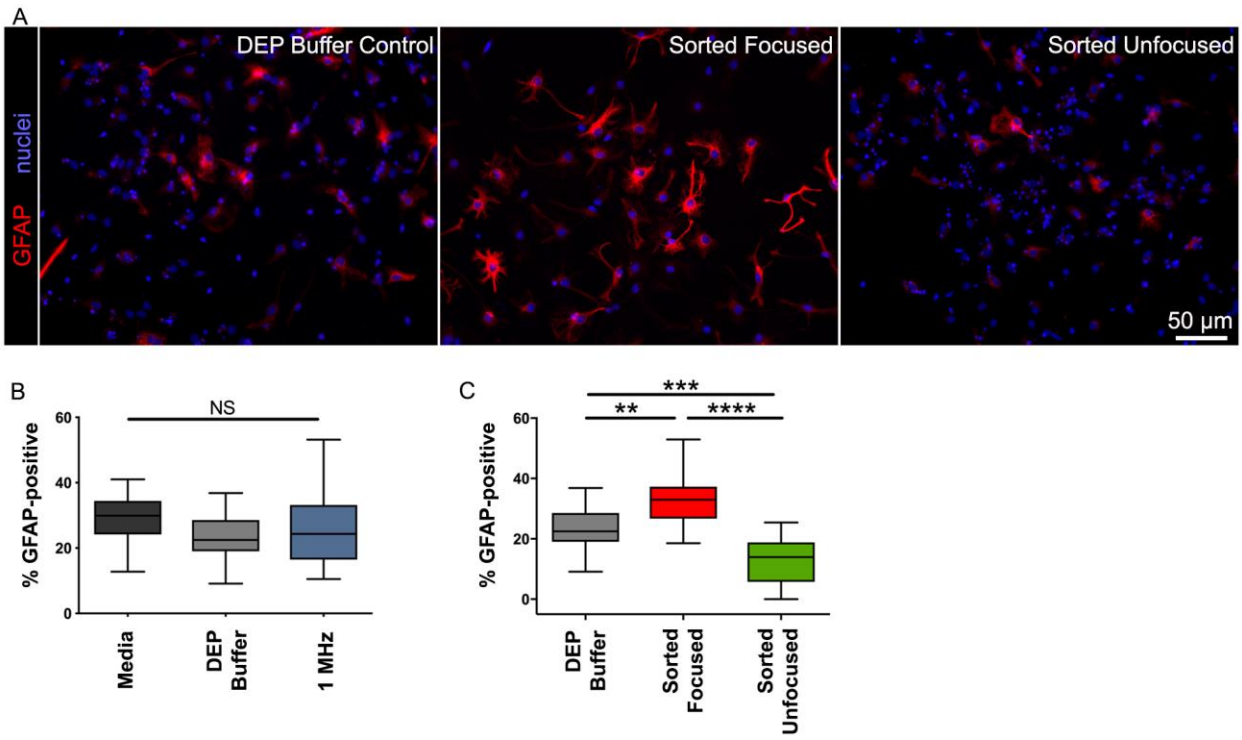

Figure 2.7: Astrocyte-biased cells are increased in focused and decreased in unfocused fractions. (A) Images of differentiated cells stained with antibody to GFAP (red) show that more cells in the focused population generated astrocytes. All cell nuclei were stained with Hoechst (blue). Scale bar 50 µm. (B) Control cell populations did not differ in the percentage of cells that generated astrocytes. Controls included cells in regular culture media (Media), cells incubated in DEP buffer for the duration of the sorting experiment (DEP buffer), and cells sorted in HOAPES

at a high frequency so that all cells are focused to the inner channel (1 MHz). (C) The percentage of cells forming astrocytes was significantly higher for focused cells and lower for unfocused cells. N=4 independent biological repeats (one way ANOVA with Tukey *post-hoc* for multiple comparisons, **p< 0.01, ***p<0.001, ****p<0.0001, and NS, not significant).

2.4.6 Device Reproducibility and Throughput

A goal of the continuous sorting HOAPES device was to increase reproducibility and throughput of cell sorting. Sorting with the HOAPES device was more reproducible than sorting with our previous trap and release DEP-based sorters (Simon et al. 2014). This is likely due to the fact that the continuous sorter minimizes cell-cell interactions, eliminates residual flow, and reduces manual operation. The throughput of the HOAPES device is much higher than that of our previous DEP-based devices: the DACS device (Nourse et al. 2014), Well device (Simon el al. 2014), and LCEA device (Simon et al. 2014) (Fig. 2.8). Compared to our first generation trap and release DEP-based sorting device (DACS device) (Nourse et al. 2014), the HOAPES device delivers a 40-fold increase in the throughput of sorted cells.

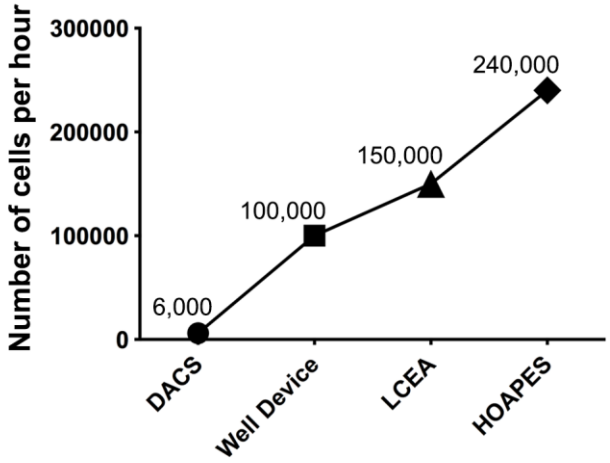

Figure 2.8: DEP-based sorting device throughput comparison. The actual throughput (# cells/hour) is shown for several devices used to sort NSPCs.

2.5 DISCUSSION

We created a microfluidic cell separation device incorporating hydrophoresis and DEP to continuously and rapidly sort cells. The hydrophoretic module efficiently directs cells to the edges of a microfluidic channel, lining up the cells for separation by the DEP module. The DEP module utilizes an array of slanted electrodes to target cells experiencing pDEP toward the channel center. Outlet channels separately collect cells focused by pDEP and those that remained unfocused. By providing two populations after sorting, focused and unfocused cells, the device generated enriched and depleted cell populations in a single sort. This was shown by sorting mouse NSPCs and determining that astrocyte-biased cells were increased in the focused fraction and decreased in the unfocused. The continuous sorting design greatly increased throughput over other DEP-based sorters. In sum, the new HOAPES device greatly improves label-free cell sorting by providing enriched and depleted cell samples in a single sort and increasing sorted cell throughput.

Professor Hsueh-Chia Chang has been a pioneer in the field of microfluidics and an inspiration to many who followed behind. Professor Chang's studies in the area of electrokinetics and microfluidic devices laid the groundwork for many of the design elements we incorporated into our device. In our previous DEP-based cell sorting devices the cells enter the device as a disperse population spanning the channel width. However, in designing a continuous DEP-based sorter we realized that directing cells to a particular starting point along the channel width would enable us to use the directed movement of cells along the channel width as a means of separation. Professor Chang's group used a similar strategy to separate microbial samples and red blood cells (Cheng et al. 2007, Cheng et al. 2009). Their devices used electrodes to induce nDEP to direct cells to the channel center. In our case, we hoped to direct cells to the channel

outer edges so employed a sheathless hydrophoretic cell aligner (Song and Choi 2014, Song et al. 2015a, Lee et al. 2018b). We improved upon previous device designs by incorporating a gradual increase in the angle of the PDMS microstructures on the channel ceiling. This created a gradual movement of cells and, coupled with the length of the hydrophoretic module, resulted in seamless direction of cells to the outer edges of the channel (Figs. 2.1, 2.2 and Movie 2.2). From there, the cells had a common starting point as they entered the DEP-based cell separation module of the device.

Electrodes for DEP-based cell sorting can be patterned in a wide array of geometries. When developing a DEP device for continuous cell sorting, our goal was to design electrodes to direct cell movement without trapping the cells in the channel. Toward a similar end, Professor Chang's group used a slanted electrode design to separate distinct cell populations in a continuous fashion. Cell movement was directed by induced nDEP forces, and the angle of the electrodes (and the frequency applied to the electrodes) determined whether each distinct cell type would track along the electrode or not (Kuczenski et al. 2011). The orientation of the electrodes in the x-y direction created "DEP gates" (electrode pairs at different orientations along the channel) that moved different cell types in different directions (Cheng et al. 2007, Kuczenski et al. 2011). This provided the basis of separation for distinct cell types. Negative DEP from slanted electrodes has also been combined with hydrophoresis to separate beads of different sizes or live and dead CHO cells (Yan et al., 2015). We sought to develop a continuous sorting system based on pDEP that could separate stem cells on the basis of fate potential (Flanagan et al. 2008, Labeed et al. 2011, Simon et al. 2014, Nourse et al. 2014).

We used a slanted electrode design for continuous sorting, but employed an array of parallel electrodes rather than a series of electrode pairs at different orientations along the

channel. We created a chevron design of parallel electrodes since this design directs cells to the center of the channel (Hu et al. 2005). We found previously that pDEP forces effectively separate mammalian cells that are very similar to each other, particularly in terms of cell size and shape, so we designed our system around pDEP (Flanagan et al. 2008, Labeed et al. 2011, Simon et al. 2014, Nourse et al. 2014). Other designs have used slanted electrodes with pDEP to direct cell movement in a channel (Song et al. 2015b). However, in these devices it was necessary to turn the electric field on and off in order for cells to detach from electrode edges and proceed down the channel. We designed a chevron pattern with release points at the tips. This accomplished two goals - increasing the throughput by doubling the separation region and enabling cell release without the need to turn off the electric field. Observation of cells in the HOAPES device confirmed that induced pDEP forces were sufficient to direct cells along the slanted electrodes toward the channel center and that cells were released from electrode tips to continue moving down the channel (Figs. 2.2G, 2.4 and Movie 2.3). Our design facilitates continuous device operation, reduces possible error since the electric field need not be turned off at specific points in the separation, and increases throughput of DEP-based sorting.

The continuous cell sorting afforded by the HOAPES device overcomes several limitations of our earlier DEP-based sorting devices. The HOAPES device has only a single inlet, making fluid flow easier to control since it does not need to be balanced across multiple inlets. The filter in the HOAPES device prevents clogging by large cell clusters and debris, enabling continuous operation since experiments need not be stopped to remove channel blockages. Since cells are not trapped along electrodes, we avoid cell-cell interactions that might adversely impact the induced DEP forces acting on each cell. The lack of trapping also means that cells are exposed to electric fields for much shorter times (seconds rather than minutes), avoiding any potential

toxicity in DEP electric fields (Lu et al. 2012). Additionally, DEP trap and release devices require turning the fluid pump on and off, which can result in residual fluid flow that can increase cell contamination in samples. In the HOAPES continuous flow design residual flow is eliminated.

The HOAPES device increases throughput since the hydrodynamic forces acting on the cell aid separation by moving cells along the slanted electrodes. We optimized cell density and flow rate for mouse NSPCs in the device ($3x10^6$ cells/ml and 3.5 µl/min) and determined an actual throughput of 240,000 cells/hour. This is a significant increase in throughput compared to our previous devices, which yielded a maximum actual throughput of 150,000 cells/hour (Simon et al. 2014). This higher throughput, coupled with the fact that NSPCs can be expanded after sorting while maintaining enrichment, means that we can generate sufficient numbers of cells for most downstream applications, including stem cell transplantation (Simon et al. 2014). The theoretical maximum throughput of the HOAPES device operating at $3x10^6$ cells/ml cell concentration, 3.5 µl/min flow rate, and 6 Vpp with no cell losses or cell clumping and assuming a steady state separation would be 630,000 cells/hour. Increasing the voltage during separation could potentially increase this throughput by allowing an increase in flow rate or cell concentration, as long as the voltage increase does not harm the cells.

The HOAPES device utilizes AC DEP for cell separation, which provides flexibility for targeting different cell populations by varying the frequency of the applied electric field. We found previously that astrocyte-biased cells can be enriched from mouse NSPCs in low frequency DEP bands while neuron-biased cells are in high frequency bands (Nourse et al. 2014). We set the sorting frequency for the experiments in the current study to target approximately one third of the cells in the population that experience pDEP at low frequencies.

At those frequencies we were able to generate cell populations enriched for and depleted of astrocyte-biased cells. The sorting frequency can be varied to target different cells in the population, resulting in changes to the percentage of cells directed to the inner channel outlet of the device. Thus, sorting can be performed at a wide range of frequencies to test for enrichment or depletion of cells of interest.

A significant improvement of the HOAPES device is the generation of enriched and depleted cell populations in a single sort. Many biological applications require comparison of cells that may be quite similar to each other but differ in a key aspect. For stem cells, that key aspect can be fate, or what type of differentiated cell will be formed. Cells that are biased to form astrocytes are similar in size to other cell populations in NSPC cultures (Labeed et al. 2011, Nourse et al. 2014), but have very specific functions. Astrocyte-biased cells are of interest for transplantation in neurological diseases such as Amyotrophic Lateral Sclerosis (ALS), in which defective astrocyte function contributes to disease progression (Lepore et al., 2008; Yamanaka and Komine, 2018). The fact that the HOAPES device generates enriched and depleted cells enables experiments in which control, unsorted cells can be directly compared to populations making both more and fewer astrocytes. Comparison across a range of cells such as these, all derived from the same starting population of cells, reduces random sources of variation and allows analysis of cell properties directly related to the function of interest, in this case the ability to form astrocytes.

Cells in a heterogeneous population, such as stem cells, display a spectrum of inherent electrical properties. Our current device design generates two populations at the end of separation, but the distribution of electrical properties in stem cell populations suggests that separation into more bins, corresponding to tighter grouping of cells by electrical properties,

could increase purity of the separated cells. Future devices should take advantage of the full range of properties displayed by the cell population and collect more fractions to create finer separation.

DEP-based cell sorters are becoming increasingly relevant for a variety of cell biology and biomedical applications. We found previously that astrocyte- and neuron-biased cells do not differ significantly in cell size, but do differ in electrophysiological properties, namely whole cell membrane capacitance (Labeed et al. 2011, Nourse et al. 2014). Thus, the HOAPES device is capable of separating cell types that are remarkably similar to each other, in this case subsets of NSPCs that are fated to different lineages and differ in membrane capacitance but not size. Recent studies demonstrate that the correlation of stem cell fate with cell electrophysiological properties and cell behavior in DEP is not limited to the neural stem cell lineage. Similar patterns hold true for embryonic/pluripotent stem cells, mesenchymal and adipose-derived stem cells, hematopoietic stem cells, and cancer stem cells (Lee et al. 2018a). Consequently, DEP-based sorting devices are relevant for isolation of cells destined to form particular types of differentiated cells from many starting populations of stem cells.

Sorting by DEP is applicable across a wide swath of biological and medical applications. DEP has sufficient resolution to distinguish similar populations of cells, including stimulated versus nonstimulated Jurkat cells (Pethig et al. 2002), subpopulations of human leukocytes (Yang et al. 1999, Vykoukal et al. 2009), red blood cells on the basis of ABO type (Srivastava et al. 2008), and breast cancer cells transfected with the neu oncogene (Cristofanilli et al. 2002). DEP analysis is capable of identifying apoptotic cells before traditional markers are expressed (Chin et al. 2006, Labeed et al. 2006, Mulhall et al. 2015), the efficacy of cancer treatments (Mahabadi et al. 2018), and the status of intracellular mitochondria (Rohani et al. 2017). The

pathogenicity of microbes can be detected by DEP, enabling rapid detection of dangerous organisms (Fernandez et al. 2017). Further development of label-free DEP-based sorting devices will be critical for many areas of cell biology and medicine.

2.6 MATERIALS AND METHODS

Hydrophoretic Oblique Angle Parallel Electrode Sorting (HOAPES) Fabrication:

The HOAPES device is comprised of three main sections: filter, sheathless hydrophoretic cell aligner, and DEP module with oblique parallel electrodes adapted from an earlier design (Lee et al. 2018b). For full dimensions of the HOAPES device see Supplemental Figure S1. The channel height is 70 µm, except in the hydrophoretic module where the height varies due to PDMS microstructures on the channel ceiling (see Device Design Principles). The device has a single inlet directly followed by an array of 70 µm tall PDMS posts that create a filter to capture cell clumps. In the first row, the posts are 150 µm wide with 100 µm gaps between posts. The second row is 350 µm downstream from the first row and the posts are 112 µm wide with 75 µm gaps between posts. The third row is 170 µm downstream from the second row and the posts are 60 µm wide with 40 µm gaps between posts. Details of the hydrophoretic and DEP modules are in the Device Design Principles section. At the end of the DEP module there are 3 outlet microchannels (one inner and two outer) with 8 µm wide perforations between them to decrease disruption of fluid flow in the event of clogging at the outlets.

The structure of the microchannels was created with two-step photolithography (Choi and Park 2010). In the first step, a 30 µm thick layer of SU-8 2025 photoresist (MicroChem Corp., Newton, MA, USA) was spin coated onto a silicon substrate, the first layer photomask was manually aligned, and UV cured. In the second step, a 40 µm thick layer of photoresist was spin

coated onto the first layer of photoresist and a second photomask was aligned to the first layer and cured using a mask aligner (Karl Suss MA6 Mask Aligner). Since the PDMS microstructures on the channel ceiling of the hydrophoretic module are critical for cell alignment, we assessed the shape and dimensions of the silicon mold for the hydrophoretic module by laser confocal microscopy (Fig. 2.3). Laser scanning confocal microscopy was carried out on a 3D laser scanning microscope (Keyence VK-250), which has nanometer resolution to show surface topology. This analysis confirmed the microstructure shape, gradual change in angle of the structures along the channel, and 40 μm dimension. PDMS was cast onto the mold, cured, and cut to the desired size. Inlet and outlets were punched in the PDMS using a 1.5 mm diameter biopsy punch.

The electrodes were fabricated using standard photolithography techniques previously described (Simon et al. 2014). Briefly, 200 Å titanium followed by 1000 Å gold were coated on standard 25 mm x 75 mm glass slides using electron-beam physical vapor deposition. The electrode features were transferred onto the gold-coated slide using Shipley 1827 positive photoresist (Shipley Company, Marlborough, MA, USA). To assemble the device, the PDMS substrate and the electrode slide were irreversibly bonded after a two-minute oxygen plasma treatment. Finally, 22-gauge solid copper wires were soldered onto the electrode pads for electrical connection.

Fluid Flow and Electric Field Simulations

A finite element computer program (Student Version 5.0, COMSOL Multiphysics, http://comsol.com) was used to simulate both the fluid flow characteristic in the hydrophoretic module and the electric field profile in the DEP module. In both modules, a simplified 3D computer-aided design (CAD) model with fewer repeating elements was created using

Solidworks (2018 student version, http://solidworks.com) and then imported into COMSOL to reduce the processing power required for the simulation (Fig. 2.1); however, all dimensions of the channel and microstructures were kept consistent with the original design to enable accurate predictions of the fluid flow and electric field distribution.

Hydrophoretic module simulation: The simulation assumed steady state and non-slip boundary conditions at the channel walls. The Navier-Stokes equations for momentum were solved assuming laminar (Reynolds number <2100) and incompressible Newtonian fluid flow (constant density and viscosity). The governing equations in the hydrophoretic module are the continuity and Navier-Stokes equations:

$$\nabla \cdot u = 0 \quad (14)$$

$$\frac{\partial u}{\partial t} + u\nabla u = -\frac{1}{\rho}\nabla P + \frac{\mu}{\rho}\nabla^2 u \quad (15)$$

Where u is the velocity vector (m/s), P is the pressure (Pa) and μ/ρ is the kinematic viscosity (m^2/s). The DEP buffer calculated density was 1.03 g/cm^3 and viscosity was 1.1 cP at 25°C. The flow direction was evaluated at the fluid simulation plane (15 μm from the bottom of the channel)(Fig. 2.1B, Supplemental Fig. 2.S2, Movie 2.1).

Electric field simulation: The electric field was simulated using the AC/DC module in COMSOL Multiphysics. The DEP buffer conductivity was set to 100 □S/cm and electric potential was set to +3V or -3V for each electrode pair.

Mouse Neural Stem and Progenitor Cell (NSPC) Culture:

CD-1 mice (Charles River) were purchased, selected randomly, and bred as approved by the University of California, Irvine Institutional Animal Care and Use Committee. Dorsal forebrain cortical tissue was dissected from the cerebral cortices of embryonic day 12.5 (E12)

mice and placed in dissection buffer: PBS, 0.6% glucose, 50 U/mL Pen/Strep. Cortical tissue from multiple embryos within the same litter was pooled, and a subsequent culture from a single litter was considered a biological repeat. The tissue was dissociated using 0.05% Trypsin-EDTA at 37^{o} C for 10 min. Afterward, trypsin was inhibited using soybean trypsin inhibitor (Life Technologies) and dissociated cells were re-suspended in proliferation medium containing DMEM, 1x B27, 1x N2, 1 mM sodium pyruvate, 2 mM L-glutamine, 1 mM N-acetylcysteine, 20 ng/ml EGF, 10 ng/ml bFGF, and 2 µg/ml heparin. Cells were seeded at 150,000 cells/ml into non-tissue culture treated plastic plates and grown as non-adherent spheres. Cell cultures were passaged approximately every 3 days using enzyme-free NeuroCult Chemical Dissociation Kit (Mouse) (StemCell Technologies). All NSPC cultures were passaged at least once prior to experimental use. Mouse NSPCs were dissociated prior to sorting with non-enzymatic NeuroCult. Dissociated cells were resuspended in DEP buffer, an iso-osmotic solution consisting of 8.5% (w/v) sucrose, 0.3% (w/v) glucose, and adjusted to a final conductivity of 100 +/- 5 □S/cm via addition of RPMI-1640 medium (Flanagan et al. 2008, Lu et al. 2012). DEP buffer conductivity was measured with a conductivity meter (Thermo Orion, Beverly, MA). The final cell concentration was adjusted to $3x10^6$ cells/ml for all experiments.

NSPC Sorting with HOAPES Device:

The HOAPES device was placed on a hot plate set at 150°C for 30 minutes to sterilize and remove moisture. Fluid flow to the device was driven by a syringe pump (Harvard Apparatus PicoPlus, Holliston, MA) pushing a 1 mL syringe with 1.5 mm outer diameter Tygon® tubing connected to the device inlet. To remove bubbles from the microchannels and sterilize, 70% ethanol was pumped into the device at 20 µl/min. Filtered MQ H2O was then flowed into the device at 20 µl/min for 15 minutes to wash away all ethanol. Bovine serum albumin (BSA, 5%)

diluted in filtered MQ H2O was then washed through the device for 15 minutes at 10 µl/min to coat the walls of the microchannels, preventing cell sticking. BSA was washed away with 100 □S/cm DEP buffer at 20 µl/min for 15 minutes. The device was then mounted on an upright Olympus microscope (model BX41) with bright field objectives and connected to a function generator (AFG320, Tektronic, Beaverton, OR). A commercial dSLR camera (Canon model EOS Rebel T2i) was attached to the microscope to record videos and monitor sorting.

The appropriate sorting frequency was optimized for each batch of cells by generating a pre-sort focusing curve. NSPCs were loaded into the HOAPES device at 3.5 µl/min flow rate and the DEP module was actuated at 6 volts peak-to-peak (Vpp) and the frequency swept from 10 kHz to 1000 kHz. The number of cells focused to the center, inner outlet channel and unfocused to the outer channels was determined for each frequency. The number of cells in the inner channel was divided by the total number of cells to determine the percentage of cells focused at each frequency. The focusing curve (percentage of cells focused at each frequency) was then used to determine the appropriate frequency for sorting in order to collect the desired percentage of focused cells.

NSPC sorting was carried out in batches to minimize cell settling. Cells were loaded into the device by attaching Tygon tubing to the end of a 1 ml syringe. Cells were not directly loaded into the syringe since this resulted in cell settling. The syringe was primed with DEP buffer then 30 µl of cells in DEP buffer was drawn into the tubing. The tubing was attached to the channel inlet, with care taken to avoid air bubbles by merging the droplet at the end of the tubing with a convex droplet of fluid at the channel inlet. The tubing was mounted vertically to minimize the effects of cell settling. The process was repeated to load additional 30 µl batches of cell solution into the device as needed. The electrodes were actuated at the sorting frequency and the syringe

pump turned on to induce flow of cells into the channel. In all sorts cells were exposed to electric fields for less than 1 minute. At the end of each run, focused cells from the inner outlet and unfocused cells from the outer outlets were collected and placed in separate Eppendorf tubes. Additional runs were completed at a control frequency (1 MHz) in which the majority of the cells focused to the inner outlet. If some cells remained unfocused, they were collected from the outer outlets and mixed with the focused cells, creating an unsorted control sample. Two other control samples were collected: cells that remained in proliferation media (media control) and cells that were incubated in the DEP buffer until the end of the sort (DEP buffer control). At the end of each sort, 50K cells from each condition (controls, focused, unfocused) were evenly plated onto 12 mm laminin-coated coverslips in proliferation media. Cells were then differentiated and immunostained to assess astrocyte formation (described below). Actual device throughput was calculated from cell recovery data from sorting experiments while theoretical device throughput was calculated from the flow rate in the device and cell concentration used for sorting and assumed no cell losses and steady state separation.

Z-projections of Cells in the Device:

Videos were used to highlight trajectories of mouse NSPCs moving through the device to determine cell locations across multiple frequencies. Videos were stacked in ImageJ using standard deviation of the intensity (maps the change in intensity from one frame to another) to create images. Each stacked Z-projection image was generated from 30 seconds of video, and the signal intensity across the channel in each image was measured using ImageJ.

NSPC Differentiation and Immunostaining:

NSPCs were plated as adherent cultures for differentiation. HCl-washed German glass coverslips (Assistant/Carolina Biological Supply, Burlington, NC) were pretreated with poly-D-

lysine (40 µg/mL in milliQ H_20) for 5 minutes then coated with laminin (20 µg/mL in EMEM) at 37^o C for 4-24 hours prior to cell adhesion. NSPCs were seeded onto the laminin-coated coverslips in proliferation medium. After 24 hours, proliferation medium was removed and replaced with differentiation medium (same components as proliferation medium but excluding EGF, bFGF, and heparin) to induce differentiation. NSPCs were differentiated into astrocytes in these conditions for 3 days. After differentiation, cells were immunostained with anti-glial fibrillary acidic protein (anti-GFAP) monoclonal (Sigma Aldrich, Cat # G3893, clone GA5) at 1:200 and stained with secondary antibody (Alexa 488, Jackson ImmunoResearch) at 1:200 as previously described (Flanagan et al. 2008, Labeed et al. 2011). Cells counted as astrocytes exhibited typical astrocyte morphologies and a filamentous pattern of GFAP reactivity in the cytoplasm. Controls included cells stained with secondary antibodies only (negative controls) and appropriate subcellular localization of antibody signal (cytoskeletal for GFAP intermediate filament protein). Cells were imaged with an inverted Nikon-TE fluorescence microscope. Three to 5 randomly selected fields for each 12 mm coverslip were selected for quantitation. From these fields, the number of GFAP+ cells and the number of nuclei were counted using ImageJ. The percent GFAP+ cells were calculated for each collected sample.

Statistical Analysis:

Statistical analysis was completed using one-way ANOVA with Tukey post hoc test for multiple comparisons for samples with n=3 or more biological repeats. Biological repeats are listed as “n” in figure legends.

2.7 ACKNOWLEDGEMENTS:

This work was supported in part by NSF Postdoctoral Research Fellowship in Biology DBI-1612261 (TNGA), University of California President's and Chancellor's Postdoctoral Fellowship (TNGA), NSF CAREER Award IOS-1254060 (LAF), the California Institute of Regenerative Medicine (CIRM) RB5-07254 (LAF), NIH NINDS T32 NS082174 (predoctoral fellowship to AYLJ), the Brython Davis Fellowship (ARY), and the NSF and the industrial members of the Center for Advanced Design and Manufacturing of Integrated Microfluidics (NSF I/UCRC award number 1841509, APL).

2.8 SUPPLEMENTAL MATERIAL:

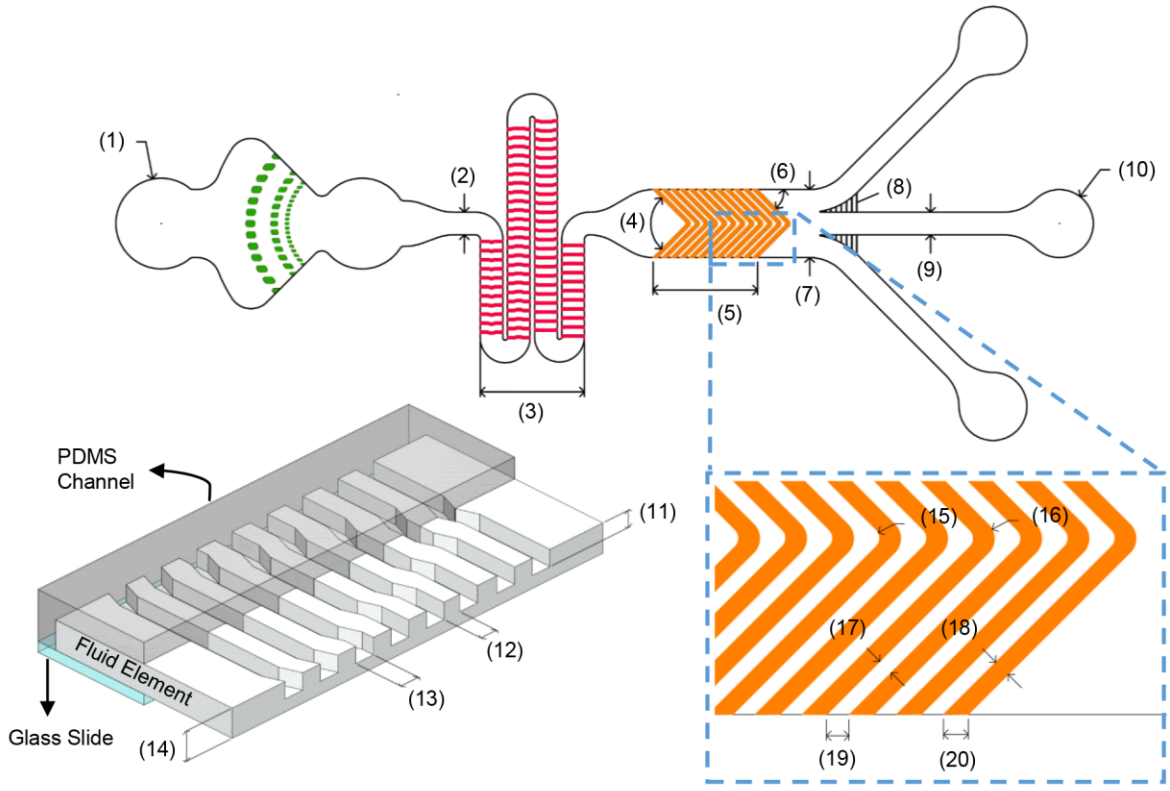

Location	Name	Symbol	Dimension
(1)	Inlet Diameter	-	2000 μm
(2)	Hydrophoresis Channel Width	w	500 μm
(3)	Number of Ridges	-	240
(4)	Electrode Tip Angle (degrees)	2α	90
(5)	Number of Electrodes	-	40
(6)	Electrode Sidewall Angle (degrees)	α	45
(7)	DEP Channel Width	-	1500 μm
(8)	Perforation Channel Width	-	8 μm
(9)	Outlet Channel Width	-	500 μm
(10)	Outlet Diameter	-	1500 μm
(11)	Trench Depth	d	40 μm
(12)	Ridge Width	-	50 μm
(13)	Trench Width	-	50 μm
(14)	Channel Height	h	70 μm
(15)	Electrode Tip Inner Radius of Curvature	-	50 μm
(16)	Electrode Tip Outer Radius of Curvature	-	85 μm
(17)	Electrode Gap	-	35 μm
(18)	Electrode Width	-	35 μm
(19)	Angled Electrode Gap	-	50 μm
(20)	Angled Electrode Width	-	50 μm

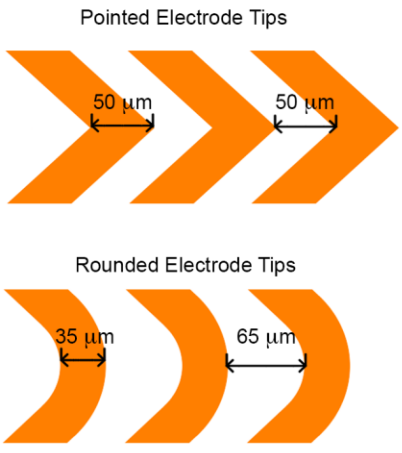

Figure 2.S1: HOAPES device dimensions. Schematics of the HOAPES device are labeled with numbers to show each regions for which dimensions are included in the table. Symbols in the

table correspond to dimensions for equations in the main text. Schematics of pointed and rounded tips show differences in electrode and gap dimensions.

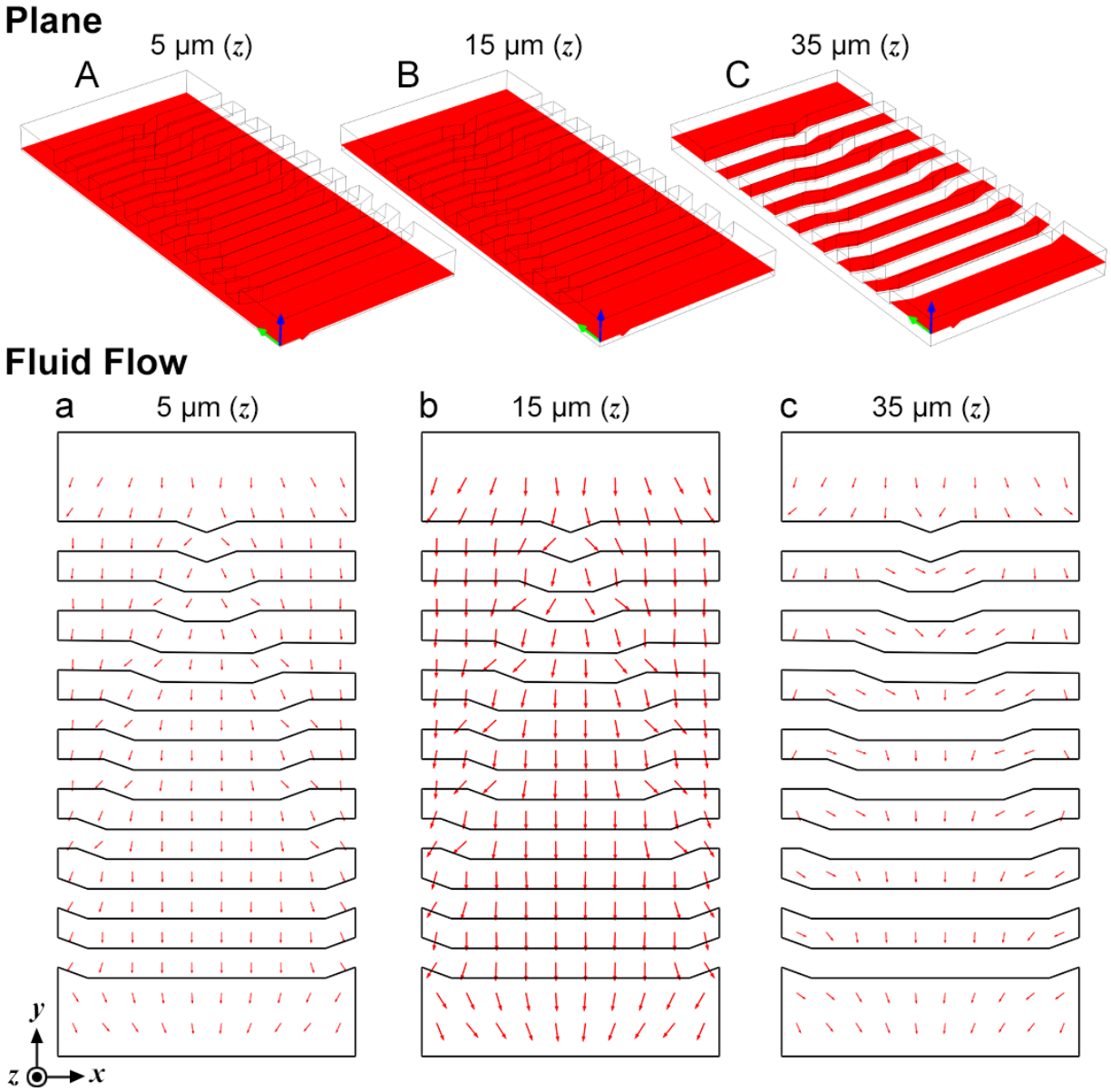

Figure 2.S2: Simulation of fluid flow at different heights in the channel. Fluid flow was simulated at 14 locations, 5 μm apart, along the height of the channel (70 μm) and images show simulations at 5 μm (A, a), 15 μm (B, b), and 35 μm (C, c) from the bottom of the channel. (A-C) Visual representations of the fluid simulation plane in red indicate the location of the plane along the height of the channel. (a-c) Red arrows indicate the direction of fluid flow and the size of the arrows shows the velocity vector of the fluid flow at each location. The plane 15 μm from the channel bottom (B, b) gave maximal fluid divergence. Still images correspond to Movie 2.1.

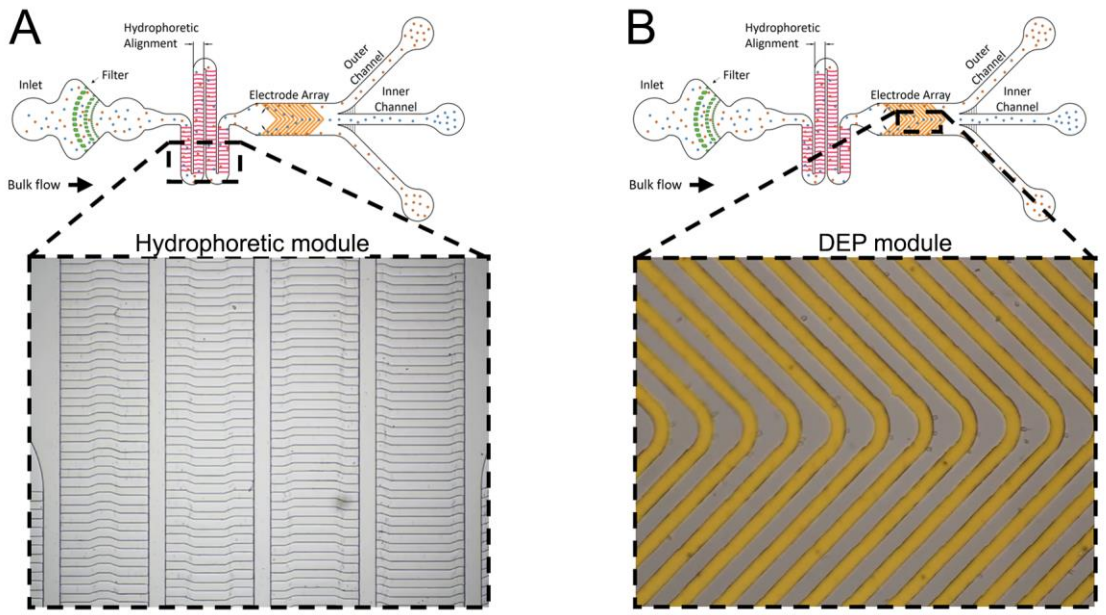

Figure 2.S3: Cell movement through the hydrophoretic and DEP modules of the HOAPES device. Blue and orange circles in the device schematics signify two distinct populations of cells. (A) Schematic shows the region of the hydrophoretic module corresponding to Movie 2.2. (B) Schematic shows the region of the DEP module corresponding to Movie 2.3.

Movie 2.1: Video showing fluid simulation at various planes in the hydrophoretic module. Video shows fluid simulation at 14 planes, 5 µm apart, in the hydrophoretic module. Left panel shows velocity vectors (red arrows), with size reflecting velocity. Right panel shows the plane corresponding to the simulation in the left panel.

Movie 2.2: Video showing movement of NSPCs through the hydrophoretic module. Video shows suspended mouse NSPCs in the hydrophoretic module being directed toward the channel edges. Cells form two distinct streams of cells at the channel edges at the end of the hydrophoretic module.

Movie 2.3: Video showing movement of NSPCs through the DEP module. Video shows suspended mouse NSPCs in the DEP module as the electrodes are actuated at 150 kHz, 6 V_{pp}. Cells in pDEP are visible tracking along the electrode edges and moving from one electrode to the next as they move down the channel towards the outlets. Cells moving along the slanted electrodes are focused to the middle of the channel and exit through the inner outlet channel. After sorting, cells are collected from inner and outer channel ports for further analysis.

2.9 REFERENCES:

Adams, T. N. G., A. Y. L. Jiang, P. D. Vyas and L. A. Flanagan (2018). "Separation of neural stem cells by whole cell membrane capacitance using dielectrophoresis." Methods **133**: 91-103.

Chen, C. S. and H. A. Pohl (1974). "Biological dielectrophoresis: the behavior of lone cells in a nonuniform electric field." Ann N Y Acad Sci **238**: 176-185.

Cheng, I.F., H.C. Chang, D. Hou, H.C. Chang (2007). "An integrated dielectrophoretic chip for continuous bioparticle filtering, focusing, sorting, trapping, and detecting." Biomicrofluidics **1**: 021503.

Cheng, I. F., V. E. Froude, Y. Zhu, H. C. Chang and H. C. Chang (2009). "A continuous high-throughput bioparticle sorter based on 3D traveling-wave dielectrophoresis." Lab Chip **9**(22): 3193-3201.

Chin, S., L. M. Broche, H. M. Coley, H. Thomas, M. P. Hughes and F. H. Labeed (2006). "Rapid detection of early apoptosis events by dielectrophoresis." International Journal of Nanomedicine(1): 333-337.

Choi, S. and J. K. Park (2010). "Two-step photolithography to fabricate multilevel microchannels." Biomicrofluidics **4**: 46503.

Cristofanilli, M., G. De Gasperis, L. Zhang, M. C. Hung, P. R. Gascoyne and G. N. Hortobagyi (2002). "Automated electrorotation to reveal dielectric variations related to HER-2/neu overexpression in MCF-7 sublines." Clin Cancer Res **8**(2): 615-619.

Fernandez, R. E., A. Rohani, V. Farmehini and N. S. Swami (2017). "Review: Microbial analysis in dielectrophoretic microfluidic systems." Anal Chim Acta **966**: 11-33.

Flanagan, L. A., J. Lu, L. Wang, S. A. Marchenko, N. L. Jeon, A. P. Lee and E. S. Monuki (2008). "Unique dielectric properties distinguish stem cells and their differentiated progeny." Stem Cells **26**: 656-665.

Flanagan, L. A., J. Lu, L. Wang, S. A. Marchenko, N. L. Jeon, A. P. Lee and E. S. Monuki (2008). "Unique dielectric properties distinguish stem cells and their differentiated progeny." Stem Cells **26**(3): 656-665.

Hu, X., P. H. Bessette, J. Qian, C. D. Meinhart, P. S. Daugherty and H. T. Soh (2005). "Marker-specific sorting of rare cells using dielectrophoresis." Proc Natl Acad Sci USA **102**(44): 15757-15761.

Hyun, K. A. and H. I. Jung (2013). "Microfluidic devices for the isolation of circulating rare cells: a focus on affinity-based, dielectrophoresis, and hydrophoresis." Electrophoresis **34**(7): 1028-1041.

Kuczenski, R. S., H. C. Chang and A. Revzin (2011). "Dielectrophoretic microfluidic device for the continuous sorting of Escherichia coli from blood cells." Biomicrofluidics **5**(3): 32005-3200515.

Labeed, F. H., H. M. Coley and M. P. Hughes (2006). "Differences in the biophysical properties of membrane and cytoplasm of apoptotic cells revealed using dielectrophoresis." Biochim Biophys Acta **1760**(6): 922-929.

Labeed, F. H., J. Lu, H. J. Mulhall, S. A. Marchenko, K. F. Hoettges, L. C. Estrada, A. P. Lee, M. P. Hughes and L. A. Flanagan (2011). "Biophysical characteristics reveal neural stem cell differentiation potential." PLoS One **6**(9): e25458.

Labeed, F. H., J. T. Lu, H. J. Mulhall, S. A. Marchenko, K. F. Hoettges, L. C. Estrada, A. P. Lee, M. P. Hughes and L. A. Flanagan (2011). "Biophysical characteristics reveal neural stem cell differentiation potential." PLOS One **6**: e25458.

Lee, A. P., M. Aghaamoo, T. N. G. Adams and L. A. Flanagan (2018a). "It's electric: when technology gives a boost to stem cell science." Current Stem Cell Reports **4**(2): 116-126.

Lee, D. H., X. Li, A. Jiang and A. P. Lee (2018b). "An integrated microfluidic platform for size-selective single-cell trapping of monocytes from blood." Biomicrofluidics **12**: 054104.

Lepore, A. C., B. Rauck, C. Dejea, A. C. Pardo, M. S. Rao, J. D. Rothstein and N. J. Maragakis (2008). "Focal transplantation-based astrocyte replacement is neuroprotective in a model of motor neuron disease." Nat Neurosci **11**(11): 1294-1301.

Lu, J., C. A. Barrios, A. R. Dickson, J. L. Nourse, A. P. Lee and L. A. Flanagan (2012). "Advancing practical usage of microtechnology: a study of the functional consequences of dielectrophoresis on neural stem cells." Integr Biol (Camb) **4**(10): 1223-1236.

Mahabadi, S., F. H. Labeed and M. P. Hughes (2018). "Dielectrophoretic analysis of treated cancer cells for rapid assessment of treatment efficacy." Electrophoresis **39**(8): 1104-1110.

Martinsen, O.G., S. Grimnes, H.P. Schwan (2002). "Interface phenomena and dielectric properties of biological tissue." Encycl. Surf. Colloid. Sci. **20**: 2643–2652.

Mulhall, H. J., A. Cardnell, K. F. Hoettges, F. H. Labeed and M. P. Hughes (2015). "Apoptosis progression studied using parallel dielectrophoresis electrophysiological analysis and flow cytometry." Integr Biol (Camb) **7**(11): 1396-1401.

Nourse, J. L., J. L. Prieto, A. R. Dickson, J. Lu, M. M. Pathak, F. Tombola, M. Demetriou, A. P. Lee and L. A. Flanagan (2014). "Membrane biophysics define neuron and astrocyte progenitors in the neural lineage." Stem Cells **32**(3): 706-716.

Pethig, R. (2010). "Review Article—Dielectrophoresis: Status of the theory, technology, and applications." Biomicrofluidics **4**(2): 022811.

Pethig, R., V. Bressler, C. Carswell-Crumpton, Y. Chen, L. Foster-Haje, M. E. Garcia-Ojeda, R. S. Lee, G. M. Lock, M. S. Talary and K. M. Tate (2002). "Dielectrophoretic studies of the activation of human T lymphocytes using a newly developed cell profiling system." Electrophoresis **23**(13): 2057-2063.

Rohani, A., J. H. Moore, J. A. Kashatus, H. Sesaki, D. F. Kashatus and N. S. Swami (2017). "Label-Free Quantification of Intracellular Mitochondrial Dynamics Using Dielectrophoresis." Anal Chem **89**(11): 5757-5764.

Simon, M. G., Y. Li, J. Arulmoli, L. P. McDonnell, A. Akil, J. L. Nourse, A. P. Lee and L. A. Flanagan (2014). "Increasing label-free stem cell sorting capacity to reach transplantation-scale throughput." Biomicrofluidics **8**(6): 064106.

Song, S., S. Choi (2014). "Inertial modulation of hydrophoretic cell sorting and focusing." Applied Physics Letters **104**: 074106.

Song, S., M. S. Kim, J. Lee, S. Choi (2015a). "A continuous-flow microfluidic syringe filter for size-based cell sorting." Lab Chip **15**: 1250-1254.

Song, H., J. M. Rosano, Y. Wang, C. J. Garson, B. Prabhakarpandian, K. Pant, G. J. Klarmann, A. Perantoni, L. M. Alvarez and E. Lai (2015b). "Continuous-flow sorting of stem cells and differentiation products based on dielectrophoresis." Lab Chip **15**(5): 1320-1328.

Srivastava, S. K., P. R. Daggolu, S. C. Burgess and A. R. Minerick (2008). "Dielectrophoretic characterization of erythrocytes: positive ABO blood types." Electrophoresis **29**(24): 5033-5046.

Vykoukal, D. M., P. R. Gascoyne and J. Vykoukal (2009). "Dielectric characterization of complete mononuclear and polymorphonuclear blood cell subpopulations for label-free discrimination." Integr Biol (Camb) **1**(7): 477-484.

Yale, A. R., J. L. Nourse, K. R. Lee, S. N. Ahmed, J. Arulmoli, A. Y. L. Jiang, L. P. McDonnell, G. A. Botten, A. P. Lee, E. S. Monuki, M. Demetriou and L. A. Flanagan (2018). "Cell Surface N-Glycans Influence Electrophysiological Properties and Fate Potential of Neural Stem Cells." Stem Cell Reports **11**(4): 869-882.

Yamanaka, K. and O. Komine (2018). "The multi-dimensional roles of astrocytes in ALS." Neurosci Res **126**: 31-38.

Yan, S., J. Zhang, Y. Yuan, G. Lovrecz, G. Alici, H. Du, Y. Zhu and W. Li (2015). "A hybrid dielectrophoretic and hydrophoretic microchip for particle sorting using integrated prefocusing and sorting steps." Electrophoresis **36**(2): 284-291.

Yang, J., Y. Huang, X. Wang, X. B. Wang, F. F. Becker and P. R. Gascoyne (1999). "Dielectric properties of human leukocyte subpopulations determined by electrorotation as a cell separation criterion." Biophys J **76**(6): 3307-3314.

CHAPTER 3

Cell surface N-glycans influence electrophysiological properties and fate potential of neural stem cells

Authors: **Andrew R. Yale[1,2,3]***, Jamison L. Nourse[2,3]*, Kayla R. Lee[2,3], Syed N. Ahmed[2,3], Janahan Arulmoli[3,4], Alan Y.L. Jiang[3,4], Lisa P. McDonnell[2,3], Giovanni A. Botten[5], Abraham P. Lee[4], Edwin S. Monuki [3,6], Michael Demetriou[2,7], and Lisa A. Flanagan[1,2,3,4]

[1] Department of Anatomy & Neurobiology, University of California, Irvine

[2] Department of Neurology, University of California, Irvine

[3] Sue & Bill Gross Stem Cell Research Center, University of California, Irvine

[4] Department of Biomedical Engineering, University of California, Irvine

[5] Department of Microbiology, Immunology & Molecular Genetics, University of California, Los Angeles

[6] Department of Pathology and Laboratory Medicine, University of California, Irvine

[7] Department of Microbiology and Molecular Genetics, University of California, Irvine

*Equal contribution

Keywords: Neural stem cell; neuron progenitor; astrocyte progenitor; glycosylation; biophysical properties; electrophysiological properties; dielectrophoresis; membrane capacitance

3.1 ABSTRACT:

Understanding the cellular properties controlling neural stem and progenitor cell (NSPC) fate choice will improve their therapeutic potential. The electrophysiological measure whole cell membrane capacitance reflects fate bias in the neural lineage but the cellular properties underlying membrane capacitance are poorly understood. We tested the hypothesis that cell surface carbohydrates contribute to NSPC membrane capacitance and fate. We found NSPCs differing in fate potential express distinct patterns of glycosylation enzymes. Screening several glycosylation pathways revealed that the one forming highly-branched N-glycans differs between neurogenic and astrogenic populations of cells *in vitro* and *in vivo*. Enhancing highly-branched N-glycans on NSPCs significantly increases membrane capacitance and leads to the generation of more astrocytes at the expense of neurons with no effect on cell size, viability, or proliferation. These data identify the N-glycan branching pathway as a significant regulator of membrane capacitance and fate choice in the neural lineage.

3.2 INTRODUCTION

Neural stem cells (NSCs) develop into neurons, astrocytes, and oligodendrocytes and understanding how choices are made among these different fates will improve the use of these cells in transplantation therapies (*1*). NSCs expanded *in vitro* for therapeutic purposes generate a heterogeneous population of neural stem and progenitor cells (NSPCs) with varying ratios of progenitors linked to distinct cell fates. The cell biological characteristics that distinguish cells biased toward forming neurons from those that will generate astrocytes are ill-defined and current cell surface markers for these cells are limited. Understanding the intrinsic properties of neuron- and astrocyte-biased cells and the mechanisms that govern their fate will improve the ability to predict or control the differentiation potential of transplanted cells, enhancing the reproducibility and effectiveness of NSPC therapeutics.

A cell biological characteristic shown to predict fate in multiple stem cell lineages is whole cell membrane capacitance, which is an electrophysiological property of the plasma membrane. Whole cell membrane capacitance can be used to identify and enrich cells at distinct stages of differentiation and is measured for living cells, non-invasively, without labels by dielectrophoresis (DEP) or impedance sensing. Membrane capacitance and cell behavior in DEP distinguish cells with subtle differences, including normal and malaria infected red blood cells (*2*), stimulated and unstimulated Jurkat cells (*3*), and breast cancer cells expressing different amounts of the neu oncogene (*4*). Analysis or sorting of NSPCs by DEP is not toxic since the short-term DEP exposure needed for these applications does not alter cell survival, proliferation, or differentiation (*5*). Membrane capacitance discriminates between undifferentiated cells and their differentiated progeny in multiple stem cell lineages. NSPCs are distinguished from differentiated neurons and astrocytes and prospectively sorted from neurons by membrane

capacitance using DEP (*6, 7*). Membrane capacitance defines and enables the enrichment of undifferentiated cells from differentiated progeny in the hematopoietic stem cell (HSC), mesenchymal/adipose-derived stem cell (MSC, ADSC), and embryonic stem (ES) cell lineages, indicating the relevance of biophysical properties to fate across multiple stem cell types (for a recent review see (*8*)). In the neural and mesenchymal stem cell lineages, inherent electrophysiological properties of the undifferentiated cells predict their differentiated fate. The neurogenic and astrogenic fate potential of NSPC populations (both human and mouse) are reflected in distinct membrane capacitance values and membrane capacitance dynamically reflects declining neurogenic potential of human NSPCs (*9*). Importantly, the sufficiency of membrane capacitance as a marker of fate in the neural lineage is shown by the enrichment of neurogenic or astrogenic cells from a mixed population of undifferentiated mouse NSPCs by DEP (*10, 11*). Similarly, the osteogenic fate potential of undifferentiated MSCs is detected by DEP (*12*). Since the biophysical property whole cell membrane capacitance is linked to fate, determining the molecular components contributing to this measure may reveal novel insights into processes governing cell differentiation.

The cellular and molecular components contributing to membrane capacitance are not well understood. The DEP frequencies used for stem cell analysis are not in a range that can be used to detect cell resting membrane potential (*6, 13*). Expression of a G protein-coupled receptor in yeast did not alter capacitance (*14*) although expression of channelrhodopsin-2 in HEK-293 cells did (*15*), suggesting the possibility that certain membrane proteins can affect membrane capacitance. Based on biophysical theory, membrane capacitance should be impacted by plasma membrane surface area and thickness. While NSPCs that have distinct membrane capacitance values do not differ in size as measured by phase contrast microscopy (*9, 10*), they may differ in

membrane microdomains not visible at that level of resolution. Cell membrane microdomains such as ruffles, microvilli, or other morphologies that increase membrane roughness are expected to alter membrane capacitance by increasing cell surface area (*16*). Membrane thickness affected by the lipid composition of the plasma membrane has been proposed to influence whole cell membrane capacitance although there are constraints on the absolute thickness of the lipid bilayer set by the size of phospholipid head groups and fatty acid tails (*17*). Modification of vesicle phospholipid bilayers with polyethylene glycol (PEG) altered membrane capacitance (*18*), suggesting cell surface modifications could contribute to membrane capacitance of cells.

A cellular process that modifies the surface of the plasma membrane and impacts membrane microdomains is glycosylation, by which carbohydrates able to store charge are added to plasma membrane proteins and lipids. Domains of glycosylated cell surface molecules generate surface undulations to increase surface area (*19, 20*), create structures extending up to 200 nm from the cell surface so make "thickened" membrane structures (*21, 22*), and influence the protein makeup of the plasma membrane (*23*). Glycosylation is critical for normal nervous system development (*24*) and changes in glycosylation patterns during cortical brain development correlate with developmental periods of increased neuron or astrocyte production (*25-27*). Treatment of NSPCs with agents that modify cell surface carbohydrates alters their behavior in DEP (*10*), raising the possibility that whole cell membrane capacitance is affected by glycosylation. We hypothesized glycosylation may impact membrane capacitance and fate of NSPCs.

3.3 RESULTS

3.3.1 E12 neurogenic and E16 astrogenic mouse NSPCs exhibit differences in glycosylation enzyme expression

In the developing cerebral cortex, neurons are formed early (starting in mice at approximately embryonic day 10, E10) and neurogenesis decreases as astrocyte generation commences (around E16). Both neurons and astrocytes differentiate from NSPCs in the developing dorsal telencephalon cortical stem cell niche (the ventricular zone/subventricular zone). In contrast, most oligodendrocytes in the cortex are generated ventrally in the ganglionic eminence and these cells migrate into the cortex at later developmental stages (*28*). In order to test whether glycosylation patterns vary with fate potential, we isolated NSPCs from embryonic dorsal forebrain cerebral cortices at stages of development when either more neurons (E12) or astrocytes (E16) are formed (*29*). E12 (neuron-biased population) and E16 (astrocyte-biased population) cells differ in fate-specific membrane capacitance, making these cells reasonable tests for the contribution of glycosylation to this biophysical property (*9*).

Glycosylation is controlled by a series of enzymes in the endoplasmic reticulum (ER) and Golgi that sequentially add and remodel sugars (glycans) attached to proteins and lipids destined for expression on the cell surface or secretion into the extracellular space. To identify glycosylation pathways potentially relevant to capacitance and fate of NSPCs, we compared RNA levels of glycosylation enzymes in E12 and E16 NSPCs. Multiple genes involved in glycosylation were differentially expressed between E12 and E16 NSPCs (Tables 3.S1, 3.S2, 3.S3). Since membrane capacitance reflects characteristics of the plasma membrane, we prioritized enzymes expected to generate cell surface glycans so enzymes involved in ER quality control, targeting of enzymes to lysosomes, or lysosomal degradation of glycans were not

considered further. We focused on N-glycosylation for the following reasons. Virtually all cell surface proteins are N-glycosylated, and N-glycosylation controls function of membrane receptors mediating responses to extracellular cues. Loss of N-glycosylation enzymes causes defects in neural development (*30*). N-glycosylation of cell surface components can lead to formation of membrane microdomains affecting cell surface area, which is thought to impact capacitance (*19, 20*). Most O-glycosylated proteins are secreted and many become components of the ECM, but some, such as the heparan sulfate proteoglycans glypican and syndecan can be membrane bound. Contributions of O-glycosylation to membrane capacitance and the combined effects of N- and O-glycosylation will be the focus of future studies.

N-glycosylation enzymes exhibiting at least a 1.2-fold or greater change in expression between E12 and E16 NSPCs can be broadly grouped by function (Fig. 3.1). The *Mgat* genes code for N-acetylglucosaminyltransferases that work in parallel with mannosidase II (MAN2A1 and MAN2A2) to sequentially determine the degree of N-glycan branching. Sialyltransferases include ST6GAL1 that generates a terminal sialic acid on glycans and ST8SIA2 and ST8SIA4 that work together to form polysialic acid. FUT8 and FUT11 are fucosyltransferases that add fucose residues to the core or terminal ends of N-glycans, respectively. B4GALT2 and B4GALT5 are galactosyltransferases that add galactose to N-glycans. B3GNT2 is an acetylglucosaminyltransferase that adds GlcNAc to N-glycans. The N-glycan branching, sialic acid, and fucose pathways were assessed further to test their association with fate in the neural lineage since multiple members of these pathways were identified in the screen and enzymes that perform different functions were associated with either E12 or E16 NSPCs.

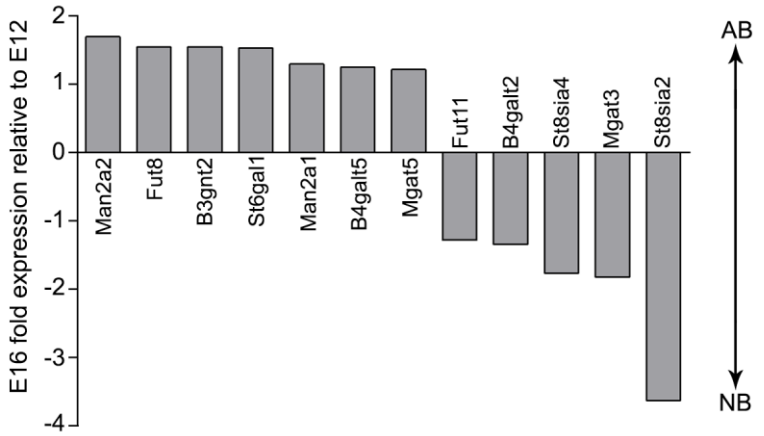

Figure 3.1. Differences in N-glycosylation enzyme gene expression between E12 and E16 mouse NSPCs. A total of 32 N-glycosylation enzyme genes were screened in E12 and E16 mouse NSPCs and transcripts that differed by more than 1.2-fold between the samples are depicted in the bar graph. Positive expression represents genes more highly expressed in E16 NSPCs, which is a more astrocyte-biased population (AB), while negative expression indicates genes more highly expressed in E12 NSPCs containing a more neuron-biased population (NB).

3.3.2 Complex branching but not sialylation or fucosylation correlates with NSPC fate

The N-glycan branching pathway utilizes enzymes that cleave excess mannose residues and initiate a new N-glycan branch by attaching N-acetylglucosamine (GlcNAc)(Fig. 3.2A)(*31*). High mannose N-glycans contain mannose but no GlcNAc branches while hybrid N-glycans contain both mannose and GlcNAc and complex N-glycans have lost all the excess mannose residues. Analysis of NSPCs by RNA-seq revealed high expression of genes important for N-glycan branching, including *Man1* isoforms, *Man2* isoforms, *Mgat1, Mgat2, Mgat3, Mgat4* isoforms, and *Mgat5* (Fig. 3.2B). NSPCs also express galectins, which are proteins that bind N-glycans and modulate the activities of several N-glycan containing cell surface proteins. RNA-seq analysis revealed that NSPCs express galectins 1, 4, 5, and 8 but little to no 2, 3, 7, 9, or 12 (Fig. 3.2B).

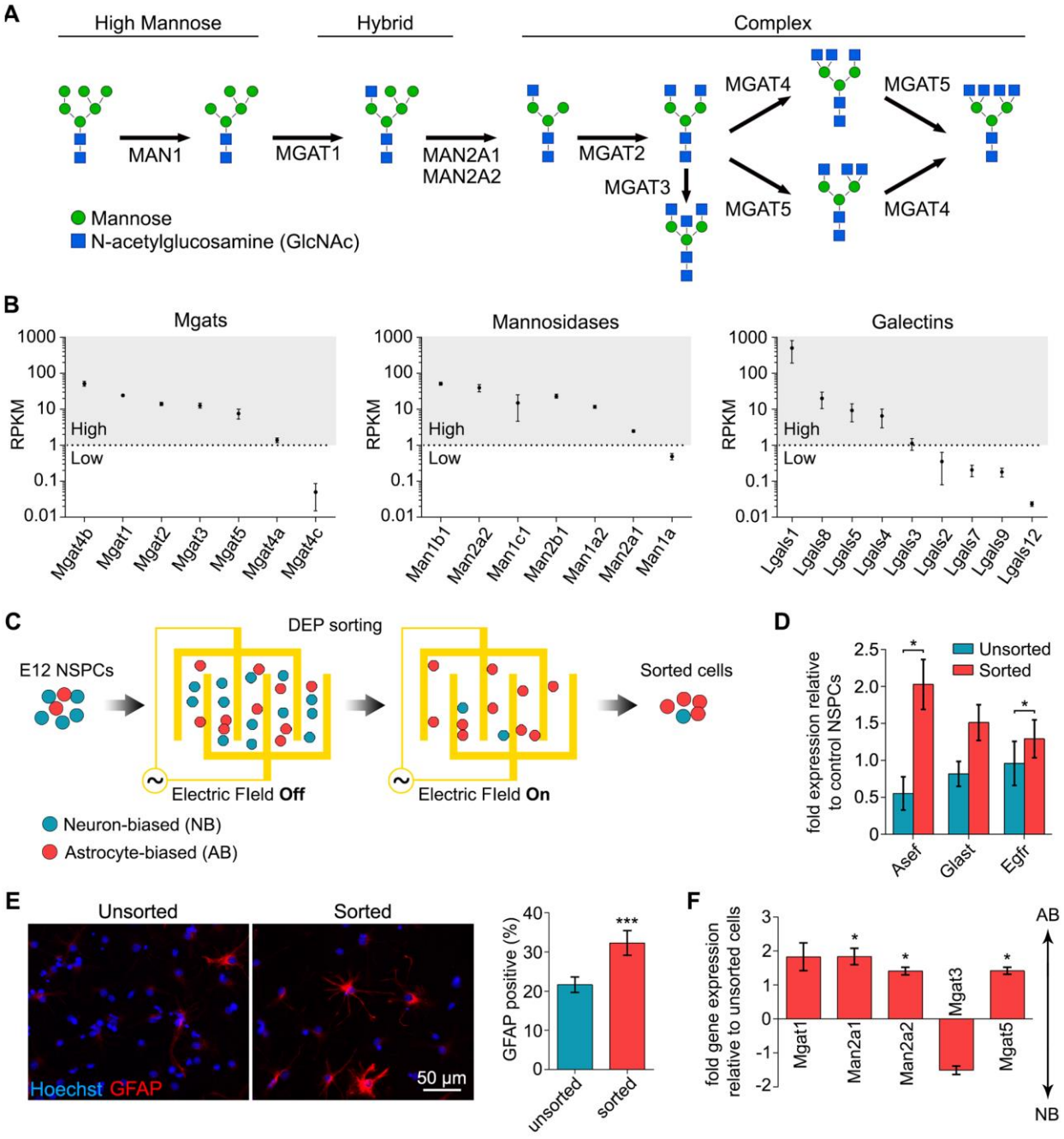

Figure 3.2. N-glycan branching correlates with NSPC fate. (A) Schematic representation of the N-glycans formed by glycosylation enzymes, culminating in the formation of highly-branched, complex N-glycans. (B) RNA-seq analysis of E12 NSPCs reveals expression levels of transcripts encoding N-glycan branching enzymes and galectins. Scatterplots display average RPKM (reads per kilobase of transcript per million mapped reads) values organized from high (>1 RPKM) to low (<1 RPKM) expression (mean ± SEM).(C) Schematic illustrating sorting of E12 NSPCs by DEP to create an enriched astrocyte-biased population. E12 NSPCs are randomly distributed when the electric field is off. When the electric field is on, astrocyte-biased cells are attracted to the electrode edges and the neuron-biased cells are removed by flow, leaving an

astrocyte biased population of sorted cells. (D) qRT-PCR analysis of astrocyte progenitor marker expression indicates sorted cells have significantly increased *Asef* (p=0.0239) and *Egfr* (p=0.0273) expression (paired Student's t-test). (E) Increased GFAP-positive cells after differentiation in the sorted sample compared to unsorted cells confirms enrichment of an astrocyte-biased population. (p=0.0002, paired Student's t-test). (F) qRT-PCR analysis of glycosylation enzymes shows that sorted cells express higher levels of enzymes whose activity lead to the formation of highly branched N-glycans (*Man2a1*, p=0.0433, *Man2a2*, p=0.0474, *Mgat5*, p=0.0314; paired Student's t-test sorted vs. unsorted), while *Mgat3* that prevents branching appears decreased. All error bars represent standard error of the mean. N=3 or more independent biological repeats (*p<0.05, ***p<0.001).

Gene expression analysis by qRT-PCR of *Mgat1*, the initial N-acetylglucosaminyltransferase in the pathway, and *Man2a1, Man2a2*, and *Mgat5* identified in the initial screen (Fig. 3.1) revealed significantly higher levels of *Mgat1* in E16 compared to E12 NSPCs (Fig. 3.S1A). Matrix-assisted laser desorption/ionization time of flight (MALDI-TOF) mass spectrometry analysis suggested that E12 NSPCs had more N-glycans with 1 or 2 GlcNAc residues whereas E16 cells had more N-glycans with 3 or 4 GlcNAc residues (Fig. 3.S1B). Lectin flow cytometry with fluorescein-conjugated leukocyte-phytohaemagglutinin (L-PHA), a plant lectin highly specific for MGAT5-generated highly-branched N-glycans (*32*), detected slightly higher but not significantly different L-PHA binding on E16 NSPCs compared to E12 cells (Fig. 3.S1C).

We enriched cells from E12 NSPCs using DEP to generate a control and astrocyte-biased population from the same developmental stage since variation between E12 and E16 NSPCs could be due to their different ages independent of fate (Fig. 3.2C). We showed previously that DEP sorting yields enriched astrocyte-biased populations from E12 NSPCs (*10, 11*). We tested enrichment in the current study by analyzing undifferentiated cells for markers of astrocyte progenitors (*33-36*) and differentiated cells for the formation of GFAP-positive astrocytes. We measured the expression of astrocyte progenitor markers in undifferentiated E12 and E16 NSPCs and found that *Asef* (*Arghgef4*), *Glast* (*Slc1a3*), and *Egfr* were more highly expressed in E16

astrogenic cells (Fig. 3.S1D). Analysis of these markers in undifferentiated cells after DEP sorting showed significant increases in astrocyte progenitor marker expression in sorted cells compared to controls (Fig. 3.2D). More GFAP-positive astrocytes were generated from sorted cells than control NSPCs after differentiation (Fig. 3.2E). While some undifferentiated NSPCs express GFAP, control and sorted undifferentiated E12 cortical NSPCs do not express GFAP (Fig. 3.S1E) (*6*), confirming that this marker can be used to detect differentiation of astrocytes from these cells. Thus, the expression of astrocyte progenitor markers by undifferentiated cells and expression of GFAP by differentiated cells both indicate that sorting generated a more astrocyte biased population of cells.

We used qRT-PCR to screen for differences in glycosylation enzyme expression between control and sorted astrocyte-biased NSPCs. Sorted cells express significantly higher levels of *Man2a1, Man2a2*, and *Mgat5* and a trend toward higher *Mgat1* compared to unsorted E12 NSPCs (Fig. 3.2E). Notably, sorted cells appeared deficient in *Mgat3*, which prevents formation of highly-branched N-glycans and was higher in E12 NSPCs than E16 NSPCs in the initial screen (Figs. 3.1, 3.2E). Furthermore, highly-branched N-glycans detected by L-PHA were significantly elevated in sorted cells (MFI 19423 ± 2023) compared to unsorted control E12 NSPCs (MFI 18101 ± 2092) (paired Student's t-test, p=0.0157). Together with the analysis of E12 and E16 NSPCs, the sorted cell data indicate a correlation between highly-branched N-glycans and fate of the cell population, suggesting this pathway may affect membrane capacitance and fate in the neural lineage.

The three enzymes that add sialic acid to N-glycans identified in the original screen of E12 and E16 NSPCs were *St6gal1*, which had higher expression in E16 NSPCs, and *St8sia2* and *St8sia4*, which were more highly expressed in E12 NSPCs (Fig. 3.1). Analysis by qRT-PCR

indicated significantly higher levels of both *St8sia2* and *St8sia4* in E12 NSPCs compared to E16 NSPCs but no difference in *St6gal1* expression between E12 and E16 NSPCs (Fig S2A). Total sialic acid residues detected by MALDI-TOF suggested higher levels of sialic acid containing N-glycans on E12 compared to E16 NSPCs (Fig. 3.S2B). Using the lectin *Sambucus nigra* agglutinin (SNA), we found no difference in terminal sialic acid residues generated by ST6GAL1 between E12 and E16 NSPCs (Fig. 3.S2C). The enzymes encoded by *St8sia2* and *St8sia4* form long polysialic acid (PSA) chains, most notably on the neural cell adhesion molecule (NCAM) to generate PSA-NCAM. Flow cytometric analysis for PSA-NCAM indicated lower levels on E16 NSPCs compared to E12 cells, but the difference was not significant (Fig. 3.S2D). Gene expression of *St8sia2* did not differ between the sorted astrocyte-biased population and unsorted NSPCs, and analysis of cell surface PSA-NCAM indicated no difference in PSA expression between the cells (Fig. 3.S2E, F). While there appears to be more sialic acid on E12 than E16 NSPCs, potentially via the activities of ST8SIA2 and ST8SIA4 and not ST6GAL1, the lack of a difference in *St8sia2* and PSA expression in the sorted cells suggests this may not directly relate to fate. We previously found that enrichment of PSA-NCAM positive cells from E12 NSPCs did not enrich for neuron-generating cells (*10*). Furthermore, earlier studies showed that treatment of blood cells with neuraminidase to remove sialic acid did not change the responses of the cells in DEP frequency ranges that probe the plasma membrane, indicating that the loss of sialic acid did not affect membrane capacitance (*37, 38*). Collectively, E12 NSPCs have an increased ability to create polysialic acid compared to E16 NSPCs, but there is not a clear link between polysialic acid and fate-specific membrane capacitance.

Fucosylation of N-glycans occurs through the activity of fucosyltransferases (FUT). In the original screen, *Fut8* gene expression was higher in E16 NSPCs while *Fut11* was higher in

E12 NSPCs (Fig. 3.1). We further analyzed FUT8 that attaches a core fucose since the expression of this enzyme showed a greater difference between the E12 and E16 samples than FUT11. Analysis of E12 and E16 NSPCs by qRT-PCR showed slightly higher but not significantly different levels of *Fut8* in the E16 sample compared to the E12 (Fig 3.S3A), and core-fucosylated N-glycans were slightly elevated in E16 NSPC membranes compared to those from E12 as indicated by MALDI-TOF (Fig. 3.S3B). However, lectin flow cytometry with *Lens culinaris* agglutinin (LCA), which detects core-fucosylated N-glycans, indicated similar or slightly lower levels of core fucose on E16 NSPCs compared to E12 NSPCs (Fig. 3.S3C). Additionally, expression of *Fut8* did not differ between the unsorted control NSPCs and the sorted astrocyte-biased population (Fig. 3.S3D). Thus, the analysis of *Fut8* expression and activity in NSPCs did not provide evidence of a significant association between core fucosylation and fate in the neural lineage.

3.3.3 Complex, highly-branched N-glycans increase in the brain stem cell niche as fate shifts from neurogenesis to astrogenesis

Development of the mammalian cerebral cortex proceeds in a stepwise pattern with neurons formed first (~E10) followed by astrocytes (~E16). The sequential generation of neurons and astrocytes at early developmental stages provides a means to test association of glycosylation with fate *in vivo*. Cortical NSPCs are found within the ventricular zone/subventricular zone (VZ/SVZ) of the embryonic cerebral cortex, and differentiated cells migrate away from this region and toward the pial surface to form the cortical plate (CP). We analyzed sagittal brain sections from E10-E18 embryos and used the NSPC markers Sry-box (SOX) 1 and SOX2 to mark the VZ/SVZ and microtubule associated protein 2 (MAP2) or doublecortin (DCX) as markers of differentiated neurons to define the CP (Fig. 3.S4).

Oligodendrocytes are not primarily generated in the cortex; most form ventrally in the ganglionic eminence and migrate to inhabit the cortex (dorsal telencephalon) at later embryonic stages, ~E18 (*28*). Thus, very few oligodendrocyte progenitors would be present in the cortical stem cell niche.

We used L-PHA lectin staining to assess highly-branched N-glycans in the VZ/SVZ stem cell niche and found significantly more L-PHA binding at E16 than at E12 (Fig. 3.3). There was no difference in staining of the CP at E12 and E16, showing that the differences observed in the NSPC-containing VZ/SVZ were not due to general increases in highly-branched N-glycans in all regions of the cortex over time. The levels of highly-branched N-glycans continued to increase in the VZ/SVZ NSPC niche at E18 as astrogenesis continues to peak (Figs. 3.3C, D). Representative images of L-PHA stained brain sections at all developmental stages quantified in Figure 3.3 are shown in Figure 3.S5. Together with the results from cell culture studies, these data show that highly-branched, complex N-glycans are associated with astrogenic NSPC populations both *in vitro* and *in vivo*.

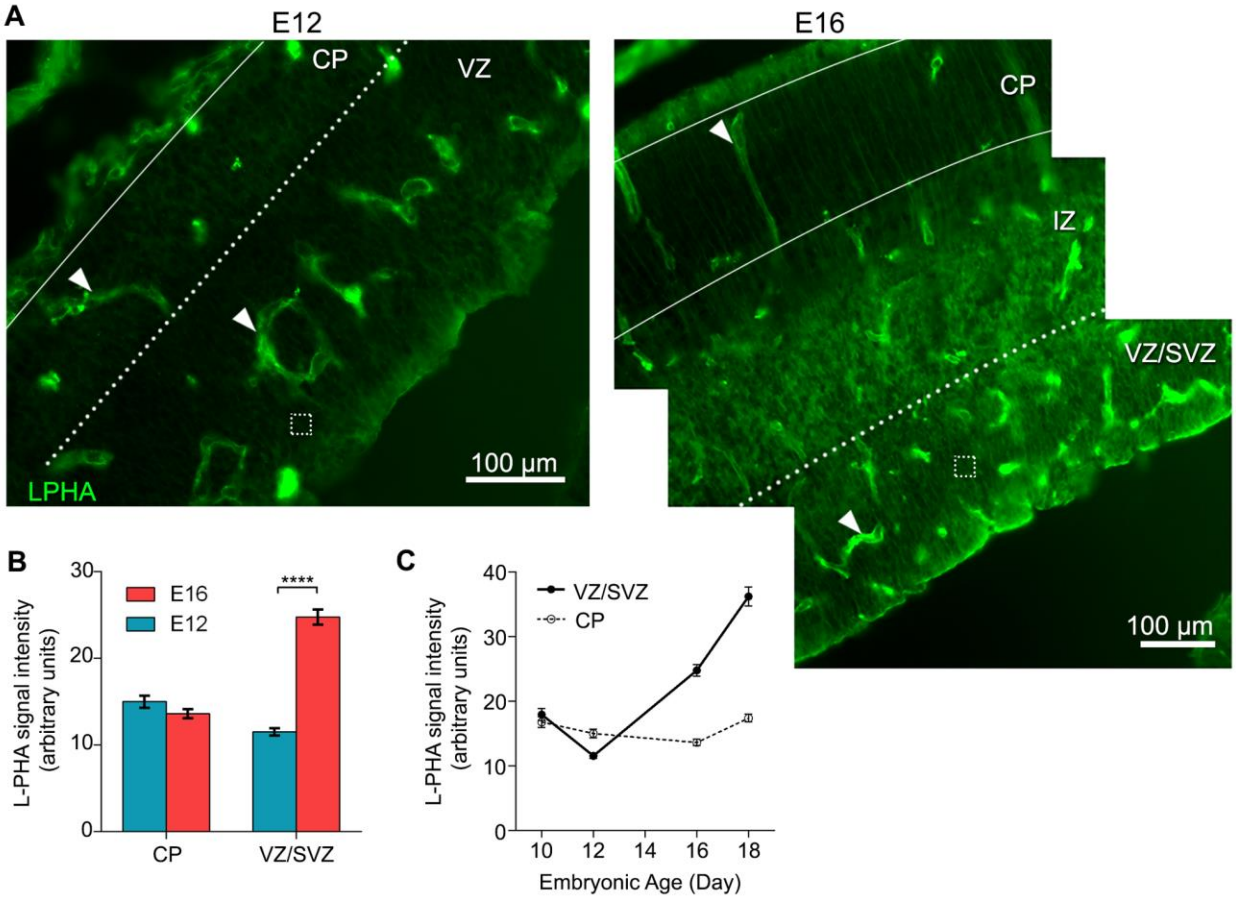

D

Cortical Plate

comparison	p-value	significance
E10 vs. E12	0.2628	ns
E10 vs. E16	0.0046	**
E10 vs. E18	0.9208	ns
E12 vs. E16	0.4619	ns
E12 vs. E18	0.0735	ns
E16 vs. E18	0.0005	***

Ventricular/Sub-ventricular Zone

comparison	p-value	significance
E10 vs. E12	0.0001	***
E10 vs. E16	<0.0001	****
E10 vs. E18	<0.0001	****
E12 vs. E16	<0.0001	****
E12 vs. E18	<0.0001	****
E16 vs. E18	<0.0001	****

Figure 3.3 N-glycan branching in the stem cell niche is high during astrogenic developmental stages *in vivo*. (A) Lectin L-PHA indicates the presence of highly-branched tetra-antennary N-glycans in sagittal sections of the developing embryonic cerebral cortex at E12 and E16. Arrowheads point to blood vessels, which stain strongly for L-PHA at both E12 and E16 and were excluded from quantitative analysis. Dotted boxes indicate example regions of the tissue that were selected for quantitative analysis (at least 10 boxes were analyzed per region in each section). More intense L-PHA staining is evident in the E16 NSPC niche (VZ/SVZ) than the E12 niche (VZ). (B) Intensity of L-PHA staining is significantly higher in the E16 NSPC niche compared to the E12 niche (VZ/SVZ E12 vs. E16, $p<0.0001$, unpaired Student's t-test). There was no significant difference in the L-PHA intensity in the CP between E12 and E16 (CP E12 vs. E16, $p=0.1041$, unpaired Student's t-test). (C) Analysis of L-PHA intensity in the NSPC niche (VZ/SVZ) over developmental ages spanning from E10 to E18 indicates rising levels of highly-branched N-glycans. There is not a corresponding increase in L-PHA intensity in the CP.

(D) Statistical analysis of the data in C indicates a significant increase in L-PHA intensity in the VZ/SVZ over time ($p<0.0001$, one-way ANOVA, Tukey *post hoc* for multiple comparisons). All error bars represent standard error of the mean. N=3 or more independent biological repeats, (**$p<0.01$, ***$p<0.001$, ****$p<0.0001$).

3.3.4 GlcNAc treatment enhances expression of highly-branched N-glycans on E12 NSPCs and significantly increases membrane capacitance

We tested whether altering highly-branched N-glycans on the surface of E12 NSPCs changes their membrane capacitance values by supplementing the cells with N-acetylglucosamine (GlcNAc), which is readily taken up by cells and raises intracellular UDP-GlcNAc levels. The MGAT4 and MGAT5 branching enzymes are highly sensitive to availability of UDP-GlcNAc, and GlcNAc treatment increases N-glycan branching in a variety of cell types (*31, 39*).. GlcNAc treatment significantly increased highly-branched N-glycans detected by L-PHA on the surface of E12 NSPCs (Fig. 3.4). Increasing cell surface highly-branched N-glycans also caused a significant increase in whole cell membrane capacitance of E12 NSPCs, indicating a role for branched N-glycans in membrane capacitance (Fig. 3.4C).

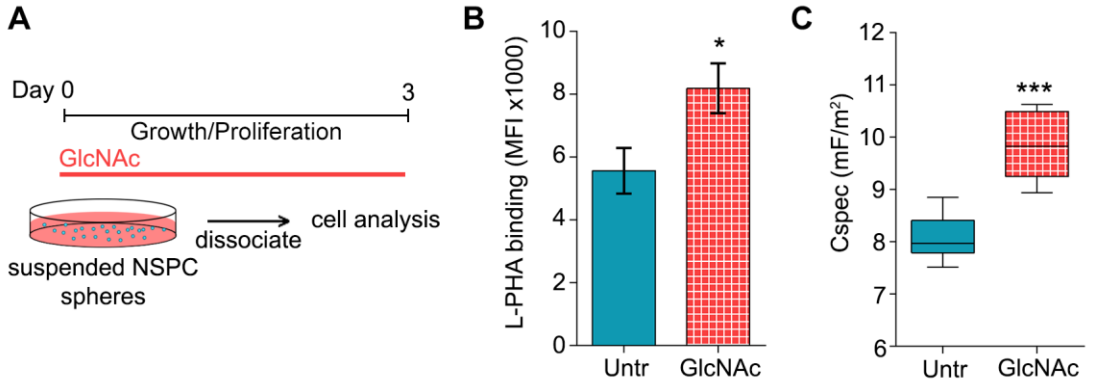

Figure 3.4. Enhancing N-glycan branching on the cell surface increases NSPC membrane capacitance. (A) Experimental design: suspended undifferentiated E12 NSPCs grown in proliferating conditions were supplemented with 80 mM N-acetylglucosamine (GlcNAc) daily for 3 days, at which point the spheres of cells were dissociated for analysis. (B) Flow cytometry analysis with lectin L-PHA indicates significantly more cell surface highly-branched N-glycans on GlcNAc treated cells (GlcNAc) compared to untreated (Untr) control cells ($p=0.0219$, unpaired Student's t-test). Error bars represent standard error of the mean. (C) Analysis of whole cell membrane capacitance by DEP shows a significant increase in capacitance after GlcNAc

treatment of E12 NSPCs ($p=0.001$, unpaired Student's t-test). Box plots depict 25^{th} and 75^{th} quartiles and median and the bars represent min and max values. N=3 or more independent biological repeats, (*$p<0.05$, ***$p<0.001$).

3.3.5 Highly-branched N-glycans restrict neurogenesis without affecting NSPC size, viability, or proliferation

Highly-branched N-glycans may serve as markers of fate or may actively participate in fate decisions since glycosylation controls the function of myriad cell surface receptors, many with identified roles in fate decisions (*40*). To test whether cell surface highly-branched N-glycans affect NSPC fate, we assessed neuronal differentiation of control and GlcNAc treated E12 NSPCs. GlcNAc treatment to induce highly-branched N-glycans led to a significant decrease in neuron formation and this effect was dose-dependent, with significantly lower levels of neurons generated after treatment with 40 or 80 mM GlcNAc (Figs. 3.5A, B). There was no difference in cell size of the control and 80 mM GlcNAc-treated NSPCs (Fig. 3.5C), consistent with the fact that neither NSPCs that differ in fate (E12 and E16) nor astrocyte- and neuron-biased populations enriched from E12 NSPCs differ in size (*9, 10*). GlcNAc supplementation might induce cell death, leading to the loss of cells biased to a particular fate from the population. Yet there was no difference in the overall cell viability or percentage of apoptotic cells between control and GlcNAc-treated NSPCs, suggesting cell death does not play a role in the effect of highly-branched N-glycans on fate (Fig. 3.5D). Highly-branched N-glycans could alter cell proliferation, which may lead to a reduction in the percentage neuron-biased cells in the population as other cells expand. However, two measures of cell proliferation (EdU incorporation and phosphorylated histone H3 expression) showed no differences between control and GlcNAc treated NSPCs (Fig. 3.5E). In sum, GlcNAc treatment to induce highly-branched N-

glycans on E12 NSPCs decreases neurogenesis but not by altering cell size, viability, or proliferation.

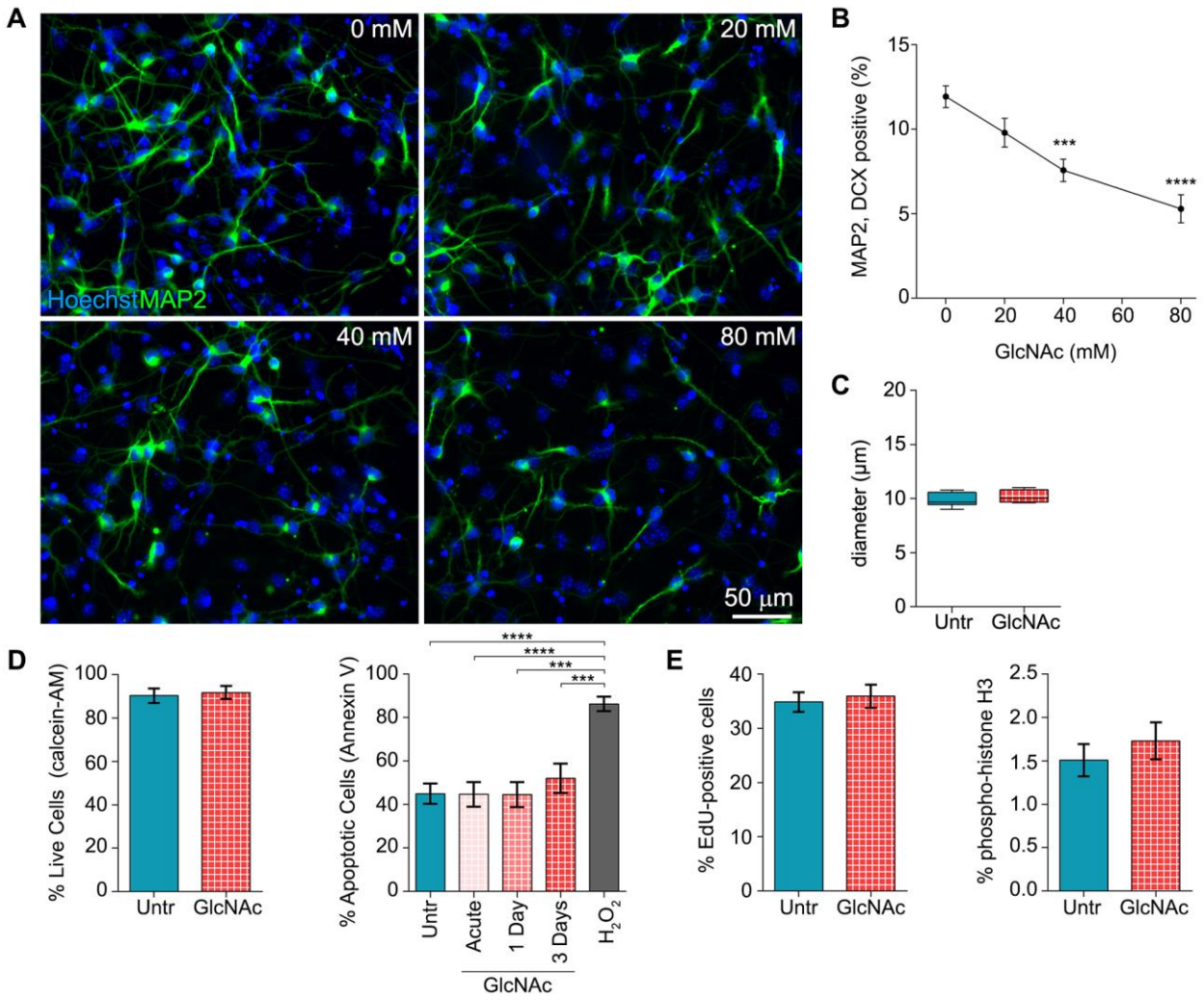

Figure 3.5. NSPCs with enhanced cell surface N-glycan branching form fewer neurons upon differentiation but do not differ in size, viability, or proliferation. (A) E12 NSPCs treated with 0-80 mM GlcNAc during 3 days as undifferentiated cells and for an additional 3 days during differentiation show a dose-dependent decrease in neuron formation (MAP2). All nuclei were labeled with Hoechst. (B) The percentage of MAP2/doublecortin (DCX) double-positive neurons formed from E12 NSPCs decreases with increasing GlcNAc concentration (one-way ANOVA, $p<0.0001$). *Post hoc* analysis by Dunnett's test: untreated E12 NSPCs vs. 40 mM ($p=0.0002$) and 80 mM ($p<0.0001$) GlcNAc treated cells. (C) Treatment with GlcNAc did not alter cell diameters of E12 NSPCs ($p=0.3985$, unpaired Student's t-test). (D) Cell viability assessed by a calcein-AM cell stain and flow cytometry denotes no effect of GlcNAc treatment on the percentage of live E12 NSPCs ($p=0.7569$, unpaired Student's t-test). Annexin V flow cytometry indicated no difference in apoptosis acutely (~3-6 hours post treatment), 1 day, or 3 days after GlcNAc supplementation. As a positive control, cells were treated with 200 µM H_2O_2 for 3 hours to induce apoptosis. (E) NSPC proliferation as measured by EdU incorporation (cells

in S-phase) and phospho-histone H3 staining (cells in M-phase) was not affected by GlcNAc treatment (EdU analysis p=0.7023, phospho-histone H3 analysis p=0.4354, unpaired Student's t-tests). All error bars represent standard error of the mean. N=3 or more independent biological repeats, (***p<0.001, ****p<0.0001).

3.3.6 Enhancing highly-branched N-glycans on undifferentiated NSPCs leads to the formation of more astrocytes at the expense of neurons

We expanded analysis of the impact of GlcNAc treatment on NSPC differentiation to consider the timing of treatment and generation of all the differentiated cell types formed by NSPCs. GlcNAc treatment effects could be due to branched N-glycans on undifferentiated NSPCs, on newly differentiated cells, or a combination of both since GlcNAc treatment spanned proliferation and differentiation stages (Fig. 3.5). Experiments were therefore designed to separate these effects by treating cells (1) when in the undifferentiated state (NSPCs in proliferation medium), (2) as cells were undergoing differentiation (cells in differentiation medium), or (3) during both stages (throughout) (Fig. 3.6A).

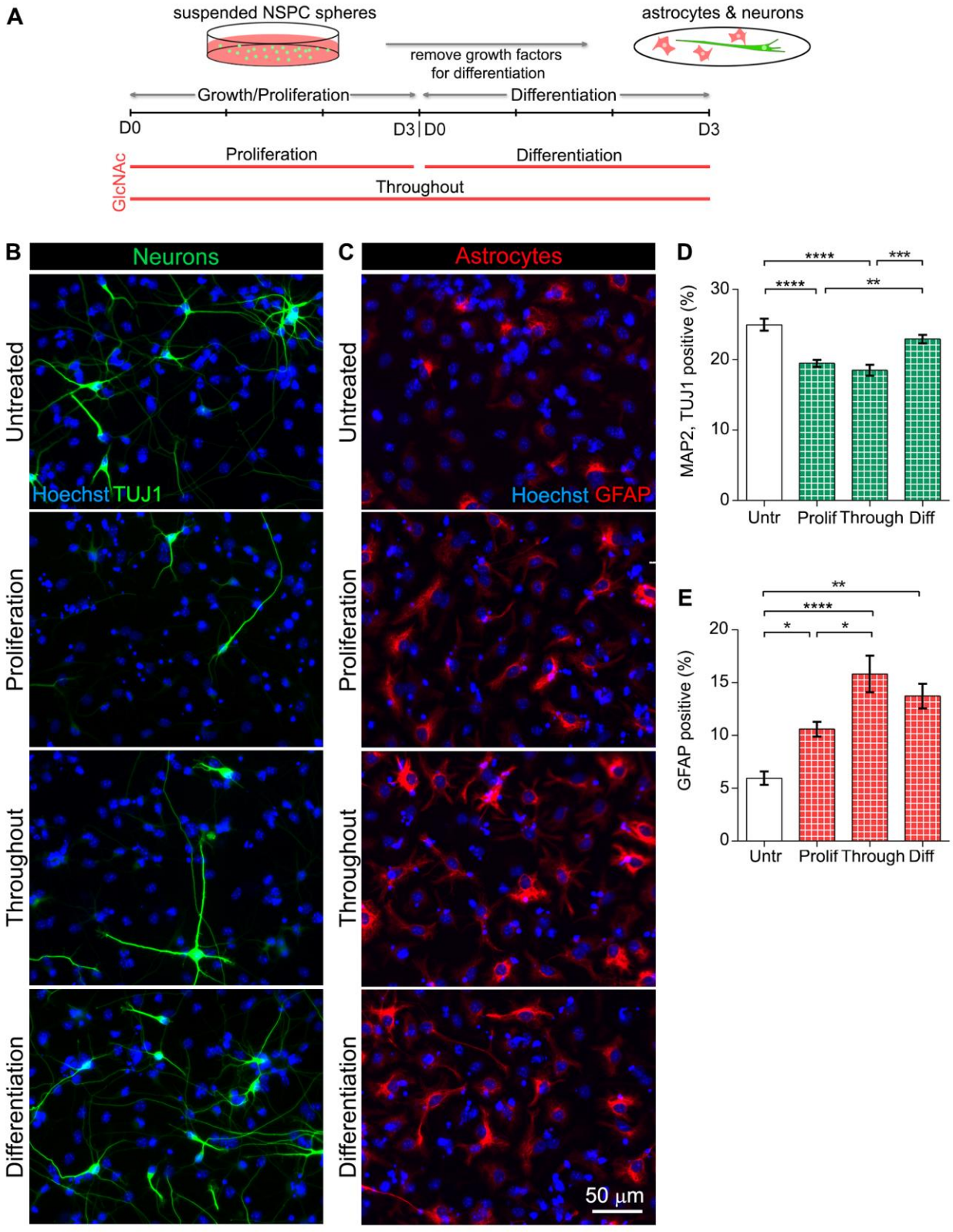
A
suspended NSPC spheres
astrocytes & neurons
remove growth factors
for differentiation
Growth/Proliferation
Differentiation
D0
D3 | D0
D3
GlcNAc
Proliferation
Differentiation
Throughout
B
Neurons
C
Astrocytes
Untreated
Proliferation
Throughout
Differentiation
Hoechst TUJ1
Hoechst GFAP
50 μm
D
MAP2, TUJ1 positive (%)
Untr
Prolif
Through
Diff
E
GFAP positive (%)

Figure 3.6. Increasing NSPC N-glycan branching during the stem/progenitor stage decreases neurogenesis and increases astrogenesis upon differentiation. (A) Experimental design: E12 NSPCs were treated with 80 mM GlcNAc in proliferation media as undifferentiated cells (Proliferation, 3 days treatment), in differentiation media (Differentiation, 3 days treatment), or in both proliferation and differentiation (Throughout, 6 days treatment). Cells were in suspension during the proliferation stage then plated as adherent cells on laminin for differentiation. (B) Fewer neurons formed from NSPCs treated with GlcNAc during proliferation or throughout both stages compared to cells treated during differentiation or untreated controls. No obvious differences in neuronal morphology were noted in the different conditions. (C) More astrocytes were generated from NSPCs treated with GlcNAc than untreated controls (all treatment paradigms). (D) Neuronal quantitation shows a significant reduction in MAP2/TUJ1 double-positive neurons from cells treated with GlcNAc during proliferation (Prolif) or throughout both stages (Through) compared to cells treated during differentiation (Diff) or untreated (Untr) control cells (Untr v Prolif $p<0.0001$, Untr v Through $p<0.0001$, Prolif v Diff $p=0.0042$, Through v Diff $p=0.0002$, one-way ANOVA, Tukey *post hoc* for multiple comparisons). These data indicate an effect of GlcNAc on undifferentiated NSPCs but not on differentiated neurons. (E) The percentage of GFAP-positive astrocytes was significantly increased in all GlcNAc-treated samples, showing effects of N-glycan branching on both undifferentiated NSPCs and differentiated cells (Untr v Prolif $p=0.047$, Untr v Through $p<0.0001$, Untr v Diff $p=0.0018$, Prolif v Through $p=0.0236$, one-way ANOVA, Tukey *post hoc* for multiple comparisons). All error bars represent standard error of the mean. N=3 or more independent biological repeats, (*$p<0.05$, **$p<0.01$, ***$p<0.001$, ****$p<0.0001$).

GlcNAc treatment throughout both proliferation and differentiation stages led to a significant decrease in neuron formation (Fig. 3.6B, D, “throughout”) as seen in our initial experiments of neuron differentiation (Fig. 3.5). Treatment during only the proliferation stage induced a similar decrease in neuron formation, but treatment during the differentiation stage only had no effect on the percentage of neurons (Fig. 3.6B, D, “proliferation”, “differentiation”). These data indicate that increasing cell surface highly-branched N-glycans decreases neurogenic potential of undifferentiated E12 NSPCs rather than affecting differentiated neurons.

Analysis of astrocyte generation from E12 NSPCs treated with GlcNAc at distinct stages revealed effects of highly-branched N-glycans on both undifferentiated and differentiated cells. Astrocyte quantitation was standardized by selecting regions that did not contain dense clusters of cells and cell debris (Fig. 3.S6) since astrocytes can become reactive in response to dying cells and upregulate GFAP expression, which could complicate quantitation. Treatment with GlcNAc

to increase highly-branched N-glycans on undifferentiated NSPCs during the proliferation stage led to a significant increase in the percentage of astrocytes formed after differentiation (Fig. 3.6C, E, “proliferation”). Interestingly, treatment during the differentiation stage also significantly increased astrocyte percentages, suggesting effects of highly-branched N-glycans on the differentiated cells (Fig. 3.6C, E, “differentiation”). The percentage of astrocytes formed when GlcNAc treatment occurred throughout both proliferation and differentiation stages was significantly higher than that of cells treated only during proliferation, suggesting an additive effect on both undifferentiated and differentiated cells (Fig. 3.6C, E, “throughout”). Thus, highly-branched N-glycans impact the formation of astrocytes from NSPCs and also affect differentiated astrocytes.

At E12, cortical NSPCs primarily generate neurons and astrocytes and the number of cells in the cortex capable of making oligodendrocytes is low, in part since very few oligodendrocyte producing cells have migrated from the ganglionic eminence into the cortex at this stage (*28*). However, cortical NSPCs isolated at E12 are able to generate low numbers of oligodendrocytes in culture (*29*). We assessed the effects of GlcNAc on generation of oligodendrocytes from E12 NSPCs and found the percentage of oligodendrocytes was significantly decreased when cells were treated with 80 mM GlcNAc during proliferation or throughout both proliferation and differentiation stages, but not when treated during differentiation only (Fig. 3.S7). Since E12 NSPCs generate few oligodendrocytes, the biological significance of this finding is unclear and further analysis of the role of highly-branched N-glycans in oligodendrocyte maturation should utilize cells isolated from the ganglionic eminence or other sources to assess cells capable of generating higher numbers of oligodendrocytes.

Since GlcNAc is utilized in both N- and O-glycosylation, we tested whether GlcNAc treatment effects were specifically due to incorporation in the N-glycan branching pathway by pretreating cells with kifunensine (Kif). Kif is a highly specific inhibitor of mannosidase I in N-glycosylation, preventing branch formation by blocking the first steps of the N-glycan branching pathway (Fig. 3.2A) (*41*, *42*). E12 NSPCs were pretreated with 0.5 μM Kif for 1 day and maintained in Kif during the 3 days of GlcNAc treatment to prevent GlcNAc incorporation into the branching pathway (Fig. 3.7A). As indicated by L-PHA flow cytometry, Kif effectively blocked the branching pathway since no increase in branched N-glycans occurred with GlcNAc in the presence of Kif (Fig. 3.7B). No significant difference in neuron formation was observed between Kif treated NSPCs and cells treated with both Kif and GlcNAc, indicating Kif blocked the effect of GlcNAc on NSPC neurogenesis (Fig. 3.7C). Similarly, Kif prevented the effect of GlcNAc on astrogenesis since the Kif treated NSPCs did not differ from those treated with both Kif and GlcNAc (Fig. 3.7D). The ability of Kif to block the effects of GlcNAc indicates that GlcNAc influences the fate potential of NSPCs through the formation of branched N-glycans.

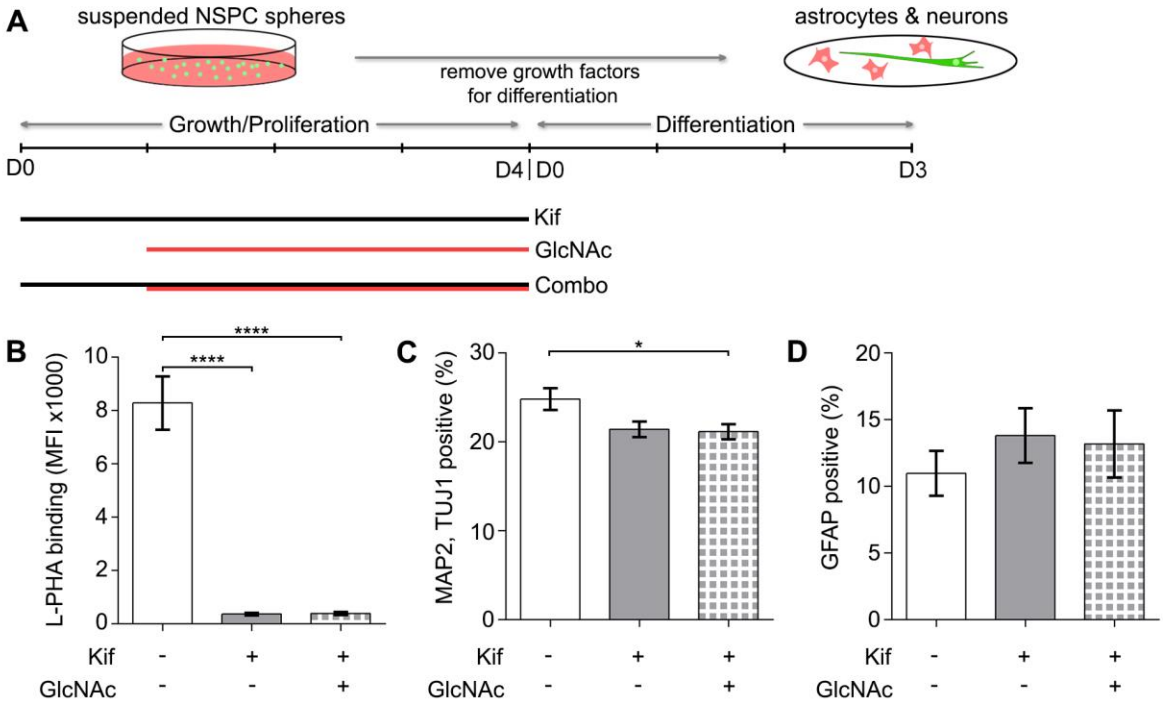

Figure 3.7. Preventing GlcNAc from incorporating into the N-glycan branching pathway blocks GlcNAc effects on fate potential. (A) Experimental design: Undifferentiated E12 NSPCs were treated with either 0.5 µM kifunensine (Kif) for 4 days, 80 mM GlcNAc (GlcNAc) for 3 days, or pre-treated with Kif 1 day prior to an additional 3 days of Kif + GlcNAc supplementation (Combo). Cells were grown in suspension during proliferation and treatment then plated as adherent cells for differentiation. (B) Lectin L-PHA flow cytometry analysis of cells after the 4 days of treatment indicates significantly less cell surface highly-branched N-glycans on Kif and Combo treated cells compared to untreated control cells (untreated v Kif $p<0.0001$, untreated v Combo $p<0.0001$, one-way ANOVA, Tukey *post hoc* for multiple comparisons). (C) Quantitation of neuronal differentiation shows no difference between Kif and Combo treated cells, indicating no effect of GlcNAc in the presence of Kif. Combo treated cells show a slight decrease in neuron formation compared to untreated controls (untreated v combo $p=0.0311$, one-way ANOVA, Tukey *post hoc* for multiple comparisons). (D) When blocked with Kif, GlcNAc has no effect on astrocyte formation since no difference was observed between Kif and Combo treated samples. All error bars represent standard error of the mean. N=3 or more independent biological repeats, (*$p<0.05$, ****$p<0.0001$).

3.4 DISCUSSION

Deciphering the factors regulating NSPC fate bias will lead to better control over differentiation. Here we provide evidence that fate-specific membrane capacitance is linked to

cell surface glycans and altering these sugars affects fate. Neurogenic and astrogenic NSPCs differ in expression of enzymes that lead to the formation of highly-branched N-glycans and these N-glycans increase in the stem cell niche *in vivo* as fate potential shifts from neurogenesis to astrogenesis. NSPCs induced to express more highly-branched N-glycans had significantly increased fate-specific membrane capacitance values, providing a direct link between cell surface glycosylation and this biophysical property. Increasing the levels of NSPC highly-branched N-glycans specifically affected fate choice since GlcNAc treatment lead to the formation of greater percentages of astrocytes at the expense of neurons without affecting cell size, proliferation, or death. These data provide the first evidence that N-glycan branching significantly contributes to fate specific membrane capacitance and identify this glycosylation pathway as an important regulator of fate choice in the neural lineage.

The data presented here establish a significant contribution of cell surface N-glycosylation to membrane capacitance, a label-free measure of cell fate. Glycosylation likely affects whole cell capacitance values of a variety of cell types since reductions in the complexity of the bacteria *C. difficile* S-layer, which is made up of glycoproteins and glycans on the bacterial envelope, induces shifts in membrane capacitance values (*43*). Glycosylation may contribute to membrane capacitance in other stem cell lineages since differentiation of MSCs to adipogenic and osteogenic lineages is associated both with changes in membrane capacitance (*44*) and glycosylation (*45*, *46*). Thus, the interaction of membrane capacitance, cell fate, and cell surface glycosylation may have relevance for many cell types, including those in other stem cell lineages. In the long run, it is likely that a combination of label free measures, such as membrane capacitance, and molecular marker-based approaches will provide the highest degree of sensitivity for detecting subtle differences between living cell subpopulations.

Cell surface glycosylation affects membrane structure and surface area, which are expected to impact whole cell membrane capacitance (*16*). The size of neuron- and astrocyte-biased NSPCs enriched by DEP did not differ (*10*) and there was no difference in the size of untreated and GlcNAc-treated NSPCs in phase contrast microscopy although they differ in both membrane capacitance and fate (e.g. Figs. 3.4-3.6). Cell surface glycosylation affects formation of membrane microdomains such as microvilli and lipid rafts associated with membrane invaginations, and thus could lead to changes in surface area not visible by phase contrast (*19, 20*). Cell surface glycosylation also contributes to the formation of the glycocalyx on the cell surface, which can create thickened regions of membrane that may affect capacitance (*21, 22*). The shift in membrane capacitance of E12 NSPCs due to GlcNAc treatment (untreated: 8.2 +/- 0.2 mF/m^2; GlcNAc treated: 9.8 +/- 0.3 mF/m^2) (Fig. 3.4) is similar to the difference in membrane capacitance values of E12 and E16 NSPCs that differ in fate (E12: 8.2 +/- 0.5 mF/m^2; E16: 10.7 +/- 0.6 mF/m^2) (*9*). Thus, cell surface highly-branched N-glycans could be sufficient to explain the fate-specific differences in capacitance of NSPCs. However, we do not rule out contributions of other types of glycosylation since cell surface proteoglycans containing O-linked sugars play significant roles in development and may affect capacitance. Glycosylation on NSPC cell surfaces likely affects the membrane molecular landscape and morphology to impact membrane capacitance.

The formation of more highly-branched N-glycans on the surface of NSPCs alters their fate potential, leading to the generation of more astrocytes and fewer neurons while not inducing changes in cell proliferation or viability. A direct role for branched N-glycans in NSPC differentiation has not been previously described, although glycosylation patterns shift in the cortex during developmental stages of increased neuron or astrocyte production (*26, 27*).

Deletion of the N-glycan branching enzyme MGAT1 results in failed neural tube closure and embryonic lethality and targeted knockout of MGAT1 in neurons causes premature neuronal death and postnatal lethality (*47-49*). Loss of the enzyme MGAT2 critical for the formation of branched N-glycans causes congenital disease with mental and psychomotor retardation (*30, 50*). The role of branched N-glycans in NSPC differentiation warrants further study.

The effects of highly-branched N-glycans on NSPCs could relate to the interaction of these N-glycans with galectins, which are endogenous N-glycan binding lectins that form complexes with cell surface glycoproteins and glycolipids (*23*). Galectin affinity is proportional to the number of sugar residues available for binding, so is increased when glycans are more branched and elongated from each branch point with N-acetyllactosamine (*23, 39*). Galectins may influence NSPC differentiation since the E12 cortical NSPCs in our study make galectin 1, which induces astrocyte maturation *in vitro* (*51*) and down-regulates neurogenesis in the adult rodent hippocampus (*52*). Galectin 3, but not galectin 1, boosts oligodendrocyte differentiation of cells from newborn mice (*53*); however, our data show E12 cortical NSPCs do not express high levels of galectin 3 (Fig 3.2B) suggesting this pathway may not be as active in these cells. Interaction of galectin 1 with the highly-branched N-glycans induced by GlcNAc may be part of the process leading to more astrocytes but fewer neurons from GlcNAc-treated E12 NSPCs.

N-linked glycosylation regulates multiple receptor classes and is thus well-poised to affect cell differentiation. N-glycan content governs the residence time of plasma membrane receptors on the cell surface and their ligand affinities, affecting integrins that bind ECM (β1, α3, α5, αV), cell-cell adhesion proteins (cadherins), and receptors for growth factors and morphogens (e.g. EGFR, PDGFR, gp130 subunit of CNTFR) (*39, 54-63*). The absence of MGAT5 activity reduces cell responses to EGF, PDGF, bFGF, and IGF (*64*). The N-glycan

branching pathway governs cell proliferation through the regulation of growth-promoting (e.g. EGFR and PDGFR) and growth arrest receptors (e.g. TGFβR) that differ in numbers of N-glycan sites (*39*). Thus, differences in the cell surface glycosylation of neuron- and astrocyte-biased NSPCs may not only contribute to their distinct membrane capacitance values but also specifically regulate multiple types of receptors that guide fate. Future studies will address the roles of these receptors in the control of NSPC fate by N-glycosylation.

Our data suggest the enzyme MGAT5 may be more active in cells that will form astrocytes and MGAT3 in neuron-biased NSPCs, raising the possibility that the balance of these two enzymes affects fate decisions. MGAT3 antagonizes the activity of MGAT5 since the formation of a bisecting N-glycan by MGAT3 prevents further branching by MGAT5 (*65, 66*). The *Mgat5* gene is more highly expressed in both astrogenic-biased E16 and DEP-enriched NSPCs while the levels of *Mgat3* are higher in neurogenic E12 and unsorted NSPCs (Fig. 3.1, 3.2). GlcNAc treatment increases highly-branched N-glycans formed by MGAT5 leading to greater astrogenesis and reduced neurogenesis (Fig. 3.5, 3.6). Pluripotent stem cells that differentiate into neurons upregulate MGAT3 expression and have higher cell surface bisecting N-glycans, whereas differentiated astrocytes retain low levels of bisecting N-glycans (*67, 68*). The balance of MGAT3 and MGAT5 activity regulates several proteins impacting cell function. Overexpression of MGAT5 or loss of MGAT3 induces greater integrin-mediated migration, while high levels of MGAT3 cause reduced migration (*55, 59*). The generation of more bisecting N-glycans on cadherins fosters greater cell-cell adhesion whereas more highly-branched N-glycans decrease cell-cell adhesion (*55, 69-71*). The degree of MGAT3 and MGAT5-modified N-glycans at the cell surface of NSPCs could regulate responses to a variety of extracellular cues and thus alter fate potential.

In summary, we identify the N-glycosylation pathway leading to the formation of highly-branched N-glycans as a regulator of fate choice in the neural lineage and provide links between the expression of N-glycans on the cell surface and membrane capacitance, a novel label free biomarker of cell fate. Since glycosylation controls the function of many cell surface receptors, it is likely that the glycosylation of NSPC receptors will impact their responses to extracellular cues in the transplantation niche, thus affecting fate of transplanted cells.

3.5 EXPERIMENTAL PROCEDURES

NSPC cell culture:

CD-1 mice (Charles River) were purchased, selected randomly, and bred as approved by the University of California, Irvine Institutional Animal Care and Use Committee. Dorsal forebrain cortical tissue was dissected from the cerebral cortices of embryonic day 12.5 (E12) and 16.5 (E16) mice and placed in dissection buffer: PBS, 0.6% glucose, 50 U/mL Pen/Strep. Cortical tissue from multiple embryos within the same litter was pooled, and a subsequent culture from a single litter was considered a biological repeat. The tissue was dissociated using 0.05% Trypsin-EDTA at 37^{o} C for 10 min. Afterward, trypsin was inhibited using soybean trypsin inhibitor (Life Technologies) and dissociated cells were re-suspended in proliferation medium containing DMEM, 1x B27, 1x N2, 1 mM sodium pyruvate, 2 mM L-glutamine, 1 mM N-acetylcysteine, 20 ng/mL EGF, 10 ng/mL bFGF, and 2 µg/mL heparin. Cells were seeded at 150,000 cells/mL into non-tissue culture treated plastic plates and grown as non-adherent spheres. Cell cultures were passaged approximately every 3 days using enzyme-free NeuroCult Chemical Dissociation Kit (Mouse) (StemCell Technologies). All NSPC cultures were passaged at least once prior to experimental use. NSPCs were plated as adherent cultures for

differentiation. HCl-washed German glass coverslips (Assistant/Carolina Biological Supply, Burlington, NC) were pretreated with poly-D-lysine (40 µg/mL in milliQ H_20) for 5 minutes then coated with laminin (20 µg/mL in EMEM) at 37^o C for 24 hours prior to cell adhesion. Whole neurospheres were seeded onto the laminin-coated coverslips in proliferation medium. After 24 hours, proliferation medium was removed and replaced with differentiation medium (same components as proliferation medium but excluding EGF, bFGF, and heparin) to induce differentiation. NSPCs were differentiated into neurons and astrocytes in these conditions for 3 days and oligodendrocytes for 7 days. For 7 day differentiated samples, culture media was replaced after 3 days.

GlcNAc treatment of NSPCs:

A stock solution of 800 mM N-acetylglucosamine (GlcNAc) was prepared in proliferation medium. For dose response experiments, the stock solution was added to E12 NSPC cultures in proliferation medium to create final concentrations ranging from 20 to 80 mM GlcNAc and the same concentration of GlcNAc was maintained in the differentiation medium. The medium was re-supplemented with fresh GlcNAc every 24 hours for 3 days since GlcNAc breaks down over time in aqueous solutions. For some experiments NSPCs were treated with 80 mM GlcNAc for 3 days in proliferation medium then dissociated for analysis. Experiments designed to test the effects of GlcNAc at different stages of cell growth and differentiation used GlcNAc supplementation in either the proliferation medium only (and not the differentiation medium), the differentiation medium only (and not the proliferation medium), or treated throughout proliferation and differentiation so included in both media. When GlcNAc was added to differentiation medium, the GlcNAc stock was also prepared in differentiation medium and GlcNAc was re-supplemented daily in the culture media. Control cells were grown in medium

lacking supplementation with GlcNAc. Kifunensine (0.5 µM) was added to proliferation medium in some experiments to block the incorporation of GlcNAc into highly branched N-glycans. Both kifunensine and GlcNAc were withdrawn during differentiation conditions.

Proliferation Assays

Cells undergoing mitosis were visualized by immunocytochemistry utilizing the primary antibody mouse anti-phospho-histone H3 (Ser10) (6G3) IgG (Cell Signaling Technology 9706S) and the secondary antibody donkey anti-mouse IgG Alexa Fluor 488 (Thermo Fisher Scientific A21202). All cells were counterstained with Hoechst 33342 nuclear dye (Thermo Fisher Scientific). Cells that passed through at least one S-phase were visualized using EdU incorporation (Click-iT EdU Alexa Fluor 555 Imaging Kit, Thermo Fisher Scientific). Proliferation medium of adherent NSPCs was supplemented with 10 µM EdU and cells incubated at 37^{o} C for 4 hours. Afterwards, cells were fixed and permeabilized as described above. After washing with PBS, cells were incubated with the EdU Click-iT reaction cocktail for 30 min at room temperature in the dark and counterstained with Hoechst 33342 nuclear dye (Thermo Fisher Scientific). Cells were analyzed using manual counting software in ImageJ and positively labeled cells were counted as a percentage of all Hoechst-stained cells in 5 randomly selected fields.

Immunocytochemistry and fate potential analysis

After differentiation, adherent cells were fixed with 4% paraformaldehyde (4% paraformaldehyde, 5 mM $MgCl_2$, 10 mM EGTA, 4% sucrose in PBS) for 10 min, and the cell membranes were permeabilized with 0.3% Triton-X 100 in PBS for 5 min. Cells were blocked using 5% BSA in PBS for 1 hour then incubated with the primary antibody for approximately 18 hours at 4^{o} C and the secondary antibody for 2 hours at room temperature in the dark. All cells

were counterstained using a Hoechst 33342 nuclear dye (Thermo Fisher Scientific) and coverslips were mounted onto glass slides using VectaShield mounting medium (Vector Labs). Cells were visualized using a Nikon Eclipse Ti-E fluorescence microscope at 20x magnification, and all images were acquired using NIS Elements AR 4.51 image capturing and analysis software. Antibodies for immunostaining included mouse anti-MAP2 IgG (Sigma M9942) at 1:200, goat anti-DCX (C-18) IgG (Santa Cruz Biotechnology SC8066) at 1:200, rabbit-anti TUJ1 IgG (Sigma T2200) at 1:100, mouse anti-O4 IgM (R&D Systems MAB1326) at 1:100, or mouse anti-GFAP IgG (Sigma G9269) at 1:200 with all antibodies prepared in 1% BSA in PBS. Secondary antibodies donkey anti-mouse IgG Alexa Fluor 555, donkey anti-goat IgG Alexa Fluor 555, donkey-anti rabbit IgG Alexa Fluor 555, donkey anti-mouse IgG Alexa Fluor 488, and goat anti-mouse IgM heavy chain Alexa Fluor 555 (Thermo Fisher Scientific A31570, A21432, A21206, A21202, A21426) were diluted 1:200 in 1% BSA.

For fate analysis, at least 3 independent sets of NSPCs derived from 3 different litters were analyzed using manual counting software built into ImageJ. The percentage of cells that differentiated into double-positive MAP2/DCX or MAP2/TUJ1 neurons with neurite lengths of at least 3 times the length of the soma was calculated from 5 randomly selected fields per experiment with more than 1000 cells counted per experimental group in each of the 3 independent experiments, so over 3000 cells per group. The percentages of GFAP-positive astrocytes were calculated from randomly selected fields of cells adjacent to the sphere attachment site but not from the dense cells within the sphere since cell density and cell death affect astrocyte GFAP reactivity. Cells expressing GFAP in a filamentous cytoskeletal pattern were counted as astrocytes and 3000 or more cells per experimental group were analyzed.

RNA isolation, array, and qRT-PCR analysis

NSPC or E12 cerebral cortex total RNA was isolated using the Aurum total RNA isolation kit (Bio-Rad Laboratories), and cDNA was synthesized using M-MLV reverse transcriptase (Promega) in the S100 Thermal Cycler (Bio-Rad) after which the enzyme was heat inactivated at 95^{o} C for 5 min. cDNA generated from E12 and E16 NSPC total RNA was analyzed using the RT^{2} Profiler PCR Array (Qiagen) for 84 glycosylation-related genes in mouse. Function of glycosylation enzymes is listed in Tables 3.S1, 3.S2, 3.S3(*72*, *73*).

Analysis of glycosylation enzyme expression was performed using TaqMan probe-based gene expression assays with the Taqman universal PCR master mix (Life Technologies 4304437) and commercially available Taqman high specificity probes. Taqman probes used for qRT-PCR analysis included mouse actin (Mm00607939_s1), *18s* (Mm0392899_g1), *Man2a1* (Mm00484781_m1), *Man2a2* (Mm00556618_m1), *Mgat1* (Mm01288784_m1), *Mgat5* (Mm01291751_m1), *Fut8* (Mm00489789_m1), *St6gal1* (Mm00486119_m1), *St8sia2* (Mm0131039_m1), *St8sia4* (Mm01292231_m1) all from Life Technologies. In experiments analyzing astrocyte progenitor marker expression, qRT-PCR was performed using short oligonucleotide DNA primers customized through NCBI's Primer-BLAST (ordered from IDT) (see Table 3.S4) and PowerUp™ SYBR® Green Master Mix (Thermo Fisher Scientific). All qRT-PCR experiments were performed using the ABI Viia7 instrument, and data was exported from the ABI Viia7 software. Data from the PCR arrayTaqman, and SYBR green assays were analyzed by the comparative cycle (C_t) method (*74*). The PCR array C_t experimental data was normalized to internal array controls. The Taqman assay data utilized 18s or actin to normalize the experimental C_t values. The SYBR green assay used GAPDH as the reference gene. Where indicated, gene expression was further normalized to RNA isolated from whole E12 cerebral cortex or *in vitro* NSPC samples as indicated

RNA sequencing and analysis

RNA was isolated from suspended E12 mouse NSPC cultures from three separate litters using the Bio-Rad RNA Isolation Kit (Genicity, Irvine, CA, USA; G00065). Genomic DNA contamination of all RNA samples was assessed by using qRT-PCR for mouse 18S and GAPDH with and without reverse transcriptase and found to be insignificant. cDNA for qRT-PCR was synthesized using M-MLV reverse transcriptase (Promega). Total RNA was further monitored for quality control using the Agilent Bioanalyzer Nano RNA chip and Nanodrop absorbance ratios for 260/280nm and 260/230nm.

RNA library preparation and sequencing was performed at the UCI Genomics Core. Library construction was performed according to the Illumina TruSeq mRNA stranded protocol. The input quantity for total RNA was 250ng and mRNA was enriched using oligo dT magnetic beads. The enriched mRNA was chemically fragmented for five minutes. First strand synthesis used random primers and reverse transcriptase to make cDNA. After second strand synthesis the double-stranded cDNA was cleaned using AMPure XP beads and the cDNA was end repaired and the 3' ends were adenylated. Illumina barcoded adapters were ligated on the ends and the adapter ligated fragments were enriched by nine cycles of PCR. The resulting libraries were validated by qPCR and sized by Agilent Bioanalyzer DNA high sensitivity chip. The concentrations for the libraries were normalized and the libraries were multiplexed together. The concentration for clustering on the flowcell was 12.5 pM. The multiplexed libraries were sequenced on one lane using single read 100 cycles chemistry for the HiSeq 2500. The version of HiSeq control software was HCS 2.2.58 with real time analysis software, RTA 1.18.64.

For sequence mapping and bioinformatic analysis, RNA-Seq data was processed as described previously (*75*). All bioinformatics analyses were conducted using the Galaxy platform

(*76*). Reads were aligned to the mouse NCBI37/mm9 reference genome with the TopHat program (*77*) using most default parameters. Alignments were restricted to uniquely mapping reads with two possible mismatches permitted. RPKM (reads per kilobase pair per million mapped reads) were calculated as described (*78*) for mm9 RefSeq genes using the SeqMonk program (http://www.bioinformatics.babraham.ac.uk/projects/seqmonk/). mRNA RPKMs were derived by counting exonic reads and dividing by mRNA length.

Membrane preparation and MALDI-TOF Mass Spectroscopy

Approximately $7x10^7$ NSPCs were washed with PBS containing 0.6% glucose twice. Cells were suspended in an ice-chilled hypotonic solution (1x PBS diluted 1:10) containing AEBSF and leupeptin protease inhibitors and lysed by freeze-thaw cycling between a dry ice/ethanol bath and 37^o C water bath. The sample was centrifuged at 75 x g for 15 min at 4^o C to remove nuclei, large organelles, and unlysed cells. The supernatant was collected and further centrifuged at 100,000 x g for 1 hour at 4^o C using a Beckman Ultracentrifuge (rotor TL110). The pellet containing the cell membrane fraction was isolated and sent to the Glycotechnology Core Facility of the Glycobiology Research and Training Center at the University of California, San Diego where MALDI-TOF Mass Spectroscopy was performed as described by Lee *et al*. (*79*). Glycan species were obtained from E12 and E16 NSPCs and the total intensity measured for each glycan structure was analyzed. N-glycan species formed by core branching glycosylation enzymes were grouped according to the number of branches emanating from the core structure (1 to 4) and each group compared between E12 and E16 NSPCs. N-glycan species containing sialic acid or fucose residues were grouped to compare sialic acid or fucose containing N-glycans between E12 and E16 NSPCs.

Flow cytometry

Live E12, E16, GlcNAc-treated E12 NSPCs, or DEP sorted cells from E12 NSPCs were dissociated using NeuroCult and washed 3 times with 5% BSA in PBS. For labeling with lectins, 300,000 cells were re-suspended in 20 µg/mL FITC-conjugated lectin *Phaseolus vulgaris* leukagglutinin (L-PHA), 20 µg/mL FITC-conjugated lectin *Lens culinaris* agglutinin (LCA), or 40 µg/mL FITC-conjugated *Sambuca nigra* lectin (SNA) (Vector Labs) in 1% BSA and incubated in the dark at 4^{o} C for 1 hour. After washing 3 times with 1x PBS, cells were re-suspended in PBS containing 3 µM propidium iodide, which was used to exclude non-viable cells for analysis. For antibody labeling, cells were re-suspended in 1% BSA with unconjugated-monoclonal antibody against PSA-NCAM (clone 2-2B, Millipore MAB5324) and incubated at 4^{o} C for 30 min. Following washes in 1% BSA, cells were incubated in the dark at 4^{o} C for 30 min with donkey-anti mouse IgM Alexa Fluor 594 (Jackson ImmunoResearch 715-585-140). Cells were additionally stained using the Zombie Green™ Fixable Viability Kit (BioLegend) to exclude non-viable cells in analysis. All cells were analyzed on a BD LSR II flow cytometer, and the data was collected using the BD FACSDIVA software. All data analysis was performed using FlowJo v10.1.

DEP-based sorting of NSPCs

Mouse NSPCs were dissociated prior to sorting by dielectrophoresis (DEP) with non-enzymatic NeuroCult as described above. Dissociated cells were resuspended in DEP buffer, an iso-osmotic solution consisting of 8.5% (w/v) sucrose, 0.3% (w/v) glucose, and adjusted to a final conductivity of 110 µS/cm via addition of RPMI-1640 medium (*5*, *6*). DEP buffer conductivity was measured with a conductivity meter (Thermo Orion, Beverly, MA). The final cell concentration was adjusted to 1x10^{6} cells/mL for all DEP experiments.

The DEP device used for sorting experiments was fabricated as previously described and appropriate sorting parameters were used so that DEP had no effect on NSPC survival, proliferation or differentiation potential (*5, 11*). Prior to DEP sorting, the DEP multi-well device was sterilized by UV light for 30-45 minutes, followed by washing with 70% EtOH (v/v), mQ H_2O, 0.05% trypsin-EDTA (v/v), and DEP buffer in sequential order in a sterile biosafety cabinet. Dissociated cells resuspended in DEP buffer were added to each well ($60x10^5$ cells per well) followed by a 10 minute incubation to ensure settling of all cells to the bottom of the wells. This was done to make sure the majority of cells were in close proximity to the electrodes. Cells were sorted by applying an AC electric field using a function generator AFG320 (Tektronix, Beaverton, OR) with 3 $V_{peak\text{-}peak}$ at 100 kHz (sorting frequency) for 5 minutes while 3 washes with DEP buffer removed cells not attracted to the electrodes. Control samples include cells exposed to 1 MHz (control frequency) for 5 minutes, since this frequency exposes cells to DEP but does not sort the cells, or cells incubated in DEP buffer without application of the electric field. Cells from these two controls did not differ in any of the analyses. Cells were collected and either processed for RNA analysis or flow cytometry as described above or plated in proliferation medium in 4mm diameter PDMS microwells that were contact bonded to glass coverslips that were subsequently coated with pDL/laminin as previously described (*10*). After 24 hours, the medium on the plated cells was switched to differentiation medium and cells were differentiated for 5 days prior to immunocytochemistry with anti-GFAP as described above.

<u>DEP-based capacitance and cell size measurements</u>

NSPCs were dissociated and suspended in DEP buffer as described above. DEP-based membrane capacitance measurements were obtained using the DEP-Well system, as described previously (*9, 80*). The DEP-Well was observed using a Nikon inverted microscope equipped

with a 1.3 Mpixel video camera, and the change in light intensity across the well over time was determined using a MATLAB (The Mathworks Inc, Natick, MA) script. The well was energized with frequencies ranging from 1 kHz–20 MHz at 5 points per decade. Using MATLAB, light intensity measurements were fit to the single shell model (*81*) and the best-fit model (minimum line correlation coefficient 0.98) was used to determine the specific membrane capacitance (Cspec). Cell diameters were measured using ImageJ to analyze phase contrast microscopy images of trypan blue excluding cells in a hemocytometer.

Brain tissue section analysis:

Developing CD-1 mice embryos were collected at embryonic days E10, E12, E16, and E18. The whole embryo was collected for E10 embryos, the head for E12 embryos, and the brain dissected out at E16 and E18. Tissue was placed in 4% paraformaldehyde (PFA) for approximately 18 hours at 4°C then transferred to 30% sucrose in PBS until the tissue was no longer floating. For some antibodies (Sox1, Sox2), tissue was fixed in 4% PFA, 2% saponin for 2 hours at 4°C. Tissue was quickly frozen in Optimal Cutting Temperature (OCT) compound (Tissue-Tek) and stored at -80°C prior to sectioning. Cryosections (20 µm) were taken along the sagittal plane using a Leica research cryostat (Leica CM3050 S) and mounted on SuperFrost glass slides. Sections were washed with PBS and blocked for 20 min at room temperature with 3% BSA in PBS for lectin histochemistry or 5% donkey serum in PBS for antibody staining, with both solutions containing 0.1% Triton-X 100. For lectin staining, sections were incubated with diluted lectin in blocking solution for 1 hour at room temperature in a humidified chamber. For antibody staining, sections were incubated with primary antibody in blocking solution for 18 hours at 4°C in a humidified chamber then with secondary antibody for 1 hour at room temperature. All sections were counterstained with Hoechst 33342 nuclear dye (Thermo Fisher

Scientific) and mounted using VectaShield (Vector Labs). Lectins included FITC-conjugated lectin *Phaseolus vulgaris* leukagglutinin (L-PHA) at 20 µg/mL (Vector Labs). Primary antibodies included goat anti-Sox1 IgG (Santa Cruz Biotechnology SC17318) at 1:50, goat anti-Sox2 IgG (Santa Cruz Biotechnology SC17320) at 1:200, goat-anti DCX (C-18) IgG (Santa Cruz Biotechnology SC8066) at 1:200, mouse anti-MAP2 IgG (Sigma M9942) at 1:200. Secondary antibodies included donkey anti-mouse Alexa Fluor 555 and donkey anti-goat Alexa Fluor 555 (Thermo Fisher Scientific A31570 and A21432) at 1:500. Images of the developing dorsal forebrain surrounding the lateral ventricle were taken using a Nikon Eclipse Ti-E fluorescent microscope at 20x magnification and the NIS image capturing software. The cortical plate (CP) and ventricular zone/subventricular zone (VZ/SVZ) were distinguished by MAP2/DCX for neurons in the CP and Sox1/Sox2 staining for NSPCs in the VZ/SVZ. A measuring box generated in ImageJ was used to quantify the average signal intensity in 10 randomly selected areas within each of the given regions and lectin-stained blood vessels were excluded from analysis. Maximum and minimum intensity values were recorded for each analyzed box and the minimum value was subtracted from the maximum to control for variations in staining intensity across different staining batches. One brain from a litter represented one biological repeat and at least 3 brains were analyzed for each embryonic stage.

Statistical Analysis:

Statistical analysis used Prism v6 software (GraphPad). Comparison of two samples utilized 2-tailed unpaired Student's t-tests except for qRT-PCR data obtained from E12 NSPCs and sorted cells, which was analyzed by a paired sample t-test since the same sample was measured before and after sorting. Data sets containing more than two samples were analyzed by one-way ANOVA. A Dunnett's *post hoc* correction was applied for the GlcNAc dose response

experiments to compare all GlcNAc treatment groups to the untreated control and a Tukey's *post hoc* correction was applied for all other multiple comparisons.

3.6 AUTHOR CONTRIBUTIONS

LAF, ARY, JLN conceived and designed the experiments. ARY, JLN, KRL, SNA, JA, AYLJ, LPM performed experiments. ARY, JLN, KRL, SNA, JA, GAB analyzed data. APL, ESM, MD provided expert advice. ARY, JLN, LAF wrote the manuscript. LAF supervised, supported the study, and finalized the manuscript.

3.7 ACKNOWLEDGEMENTS

This work was supported in part by NSF CAREER Award IOS-1254060 (LAF), NIH NINDS T32 NS082174 (predoctoral fellowship to AY), CIRM RT1-01074 (LAF) and CIRM Bridges to Stem Cell Research at California State University, Fullerton TB-01181 (SNA), NIH NCRR and NCATS through Grant UL1 TR001414 (Pilot Grant to LAF), a Collaborative Multiple Sclerosis (MS) Research Center Award from the National MS Society (MD), the Sue & Bill Gross Stem Cell Research Center at University of California, Irvine, and a gift by Pearl Tze Hosfiel and Keith Hosfiel.

3.8 SUPPLEMENTAL MATERIAL

3.8.1 Supplemental Figures

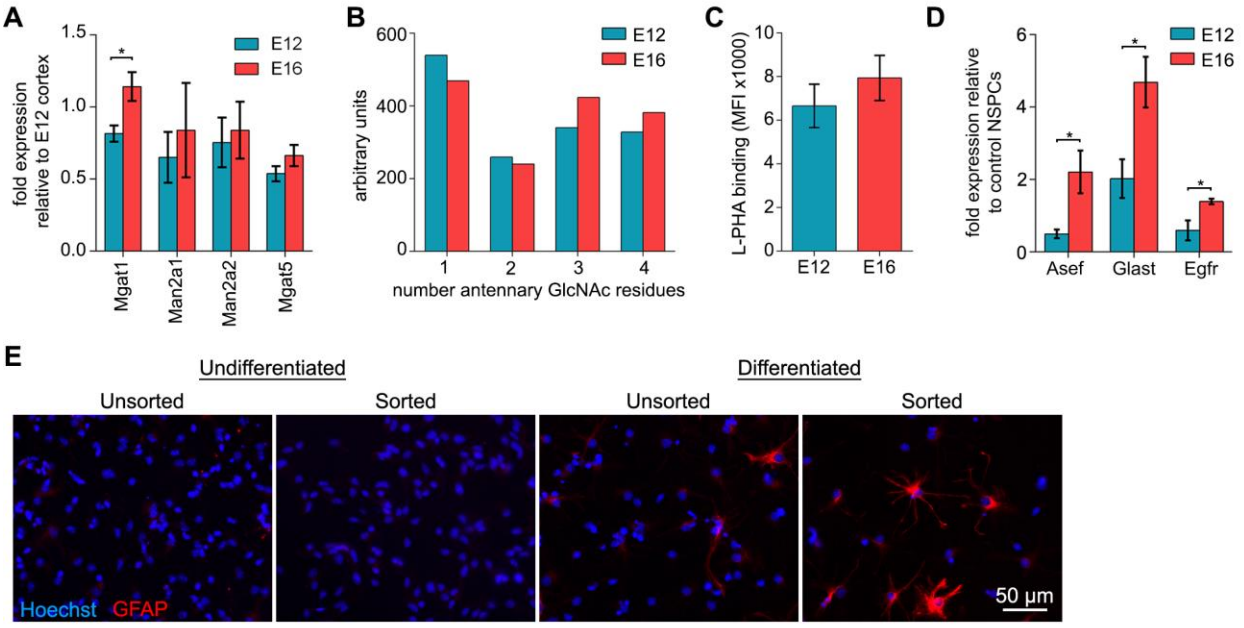

Figure 3.S1. Analysis of E12, E16, and sorted astrocyte-biased NSPCs. (A) Analysis of N-glycan branching enzyme gene expression by qRT-PCR indicates higher levels of expression in E16 compared to E12 NSPCs (*Mgat1*, p=0.015, unpaired Student's t-test). Values for E12 and E16 NSPCs are relative to E12 cortex (see Supplemental Experimental Procedures). (B) Plasma membrane N-glycans of E12 and E16 NSPCs analyzed by MALDI-TOF mass spectrometry reveal differences in numbers of GlcNAc residues attached to the trimannosyl core (referred to here as branches). One branch corresponds to mono-antennary GlcNAc structures and 2 branches to bi-antennary structures. Three branches correspond to either tri-antennary structures or bi-antennary sugars also containing a bisected GlcNAc. Four branches correspond to either tetra-antennary structures or tri-antennary sugars also containing a bisected GlcNAc. E12 NSPCs contain more 1 or 2 branched N-glycans while E16 NSPCs have more with 3 or 4 branches (n=1). (C) Flow cytometry analysis with lectin L-PHA to detect cell surface highly branched N-glycans indicates similar levels of these structures on E12 and E16 NSPCs, with a trend toward higher levels on E16 cells. Data is represented as mean fluorescence intensity (MFI). (D) Analysis of astrocyte progenitor marker expression by qRT-PCR indicates higher levels of expression in E16 compared to E12 NSPCs (*Asef*, p=0.0300; *Glast*, p=0.0234; *Egfr*, p=0.0311; unpaired Student's t-test). Values for E12 and E16 NSPCs are relative to an independent E12 NSPC sample. (E) Unsorted and DEP-sorted E12 NSPCs were immunostained for GFAP. No GFAP expression was observed in undifferentiated unsorted controls or sorted cells. More GFAP-positive cells were observed in the differentiated sorted sample compared to control NSPCs. All error bars represent standard error of the mean. N=3 or more independent biological repeats unless otherwise noted, (*p<0.05).

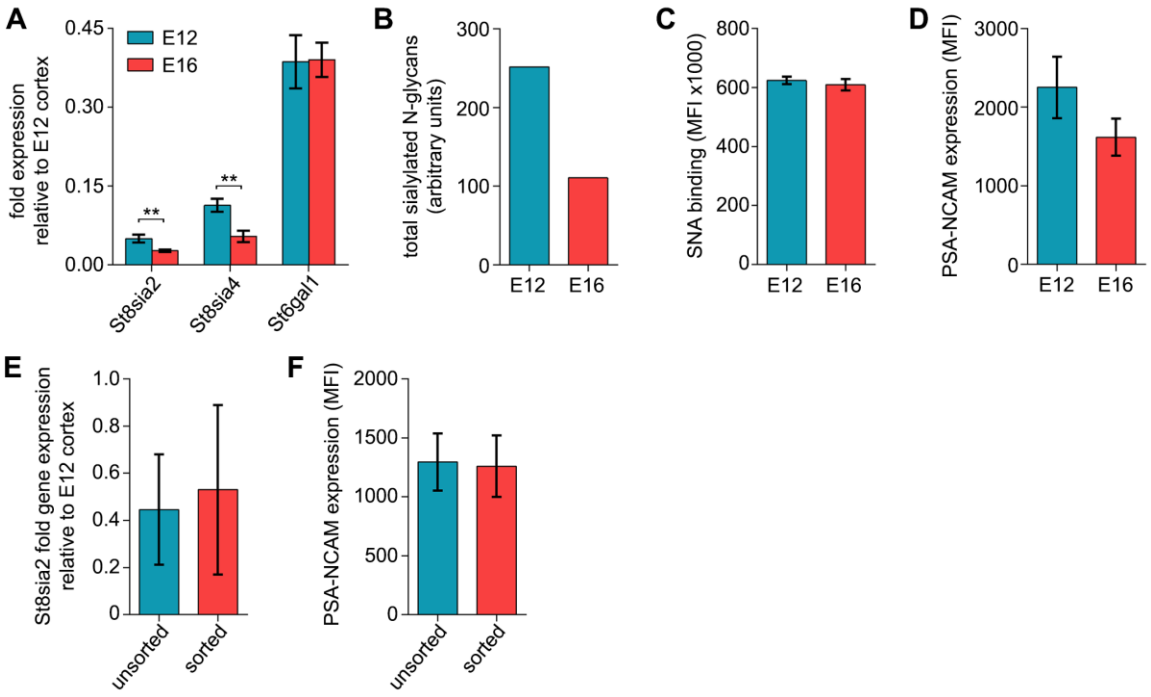

Figure 3.S2. Characterization of NSPC sialic acid. (A) qRT-PCR gene expression analysis of transcripts encoding sialic acid modifying enzymes indicates higher expression of *St8sia2* and *St8sia4* in E12 compared to E16 NSPCs (*St8sia2*, p=0.007, *St8sia4*, p=0.0072, unpaired Student's t-test). There was no difference in *St6gal1* expression between the two cell populations. Values for E12 and E16 NSPCs are relative to those of E12 cortex. (B) Analysis of plasma membrane N-glycans from E12 and E16 NSPCs by MALDI-TOF mass spectrometry shows more sialic acid modified N-glycans on E12 than E16 NSPCs (n=1). (C) Flow cytometry analysis with lectin SNA to detect cell surface sialic acid containing N-glycans modified by ST6GAL1 indicates similar levels of these structures on E12 and E16 NSPCs. Data is represented as mean fluorescence intensity (MFI). (D) Flow cytometry analysis of PSA-NCAM indicates a non-significant lower (p=0.0891) expression of PSA-NCAM on E16 NSPCs compared to E12 NSPCs. Data represented as MFI. (E) Expression of the sialic acid modifying enzyme *St8sia2* analyzed by qRT-PCR indicates similar levels in control and sorted astrocyte-biased NSPCs. Values for E12 NSPCs and sorted cells are relative to those of E12 cortex. (F) Flow cytometry analysis of PSA-NCAM indicates similar levels between control and sorted cells. All error bars represent standard error of the mean. N=3 or more independent biological repeats unless otherwise noted, (**p<0.01).

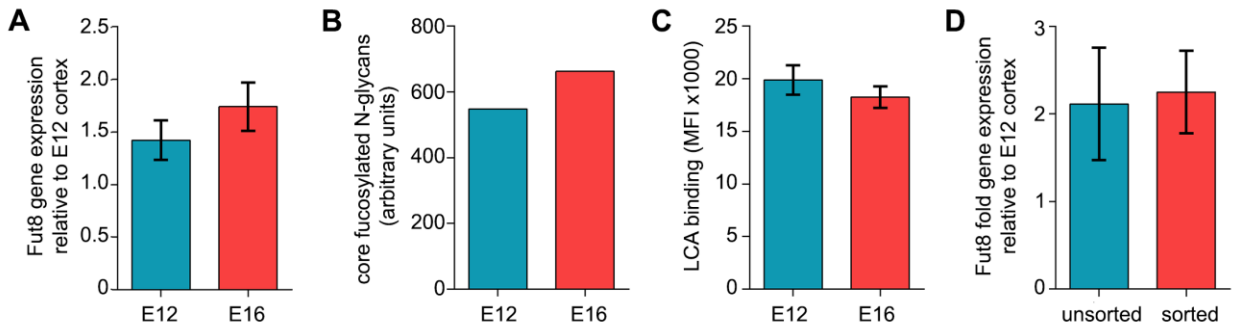

Figure 3.S3. Characterization of NSPC core fucose glycosylation. (A) qRT-PCR gene expression analysis of transcripts encoding the *Fut8* enzyme that adds core fucose indicates similar levels in E12 and E16 NSPCs. Values for E12 and E16 NSPCs are relative to those of E12 cortex. (B) Plasma membrane N-glycans of E12 and E16 NSPCs analyzed by MALDI-TOF mass spectrometry show similar amounts of core fucose modified N-glycans on E12 and E16 NSPCs (n=1). (C) Flow cytometry analysis with lectin LCA to detect cell surface core fucose containing N-glycans indicates similar levels of these structures on E12 and E16 NSPCs. Data is represented as mean fluorescence intensity (MFI). (D) Expression of *Fut8* analyzed by qRT-PCR indicates similar levels in control and sorted E12 NSPCs. Values for E12 NSPCs and sorted cells are relative to those of E12 cortex. All error bars represent standard error of the mean. N=3 or more independent biological repeats unless otherwise noted.

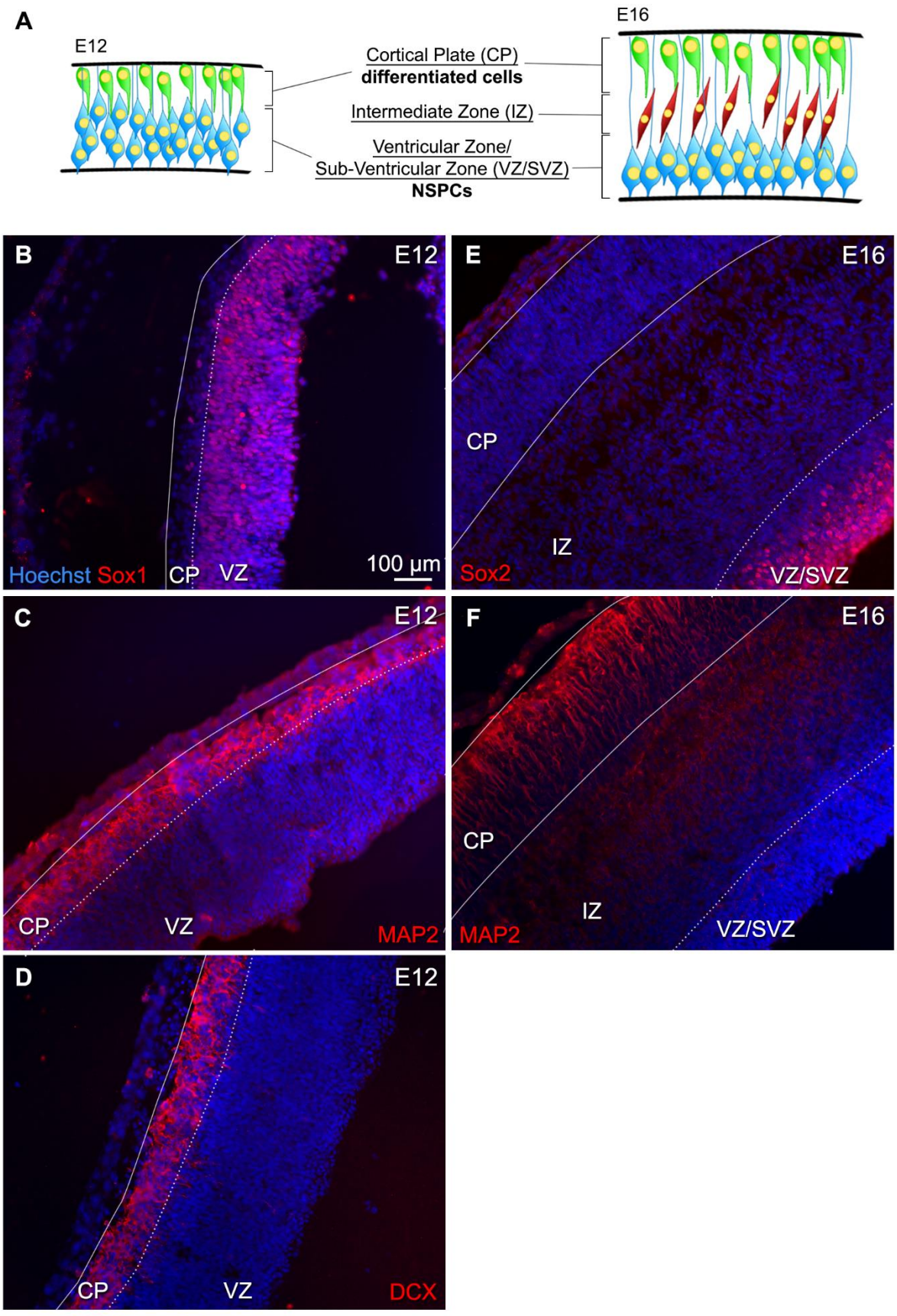
A
E12
E16
Cortical Plate (CP)
differentiated cells
Intermediate Zone (IZ)
Ventricular Zone/
Sub-Ventricular Zone (VZ/SVZ)
NSPCs
B
E12
Hoechst Sox1
CP
VZ
100 µm
E
E16
CP
IZ
Sox2
VZ/SVZ
C
E12
CP
VZ
MAP2
F
E16
CP
IZ
MAP2
VZ/SVZ
D
E12
CP
VZ
DCX

Figure 3.S4. Identification of the VZ/SVZ and CP during embryonic cortical development. **(**A) Schematic representing the layers of the developing cerebral cortex depicts the VZ and CP at E12 and the VZ/SVZ, IZ, and CP at E16. Stem and progenitor cells in the VZ/SVZ are shown in blue, migrating cells in the IZ are in red, and the differentiated cells of the CP are in green. (B) Sagittal sections of the E12 mouse embryonic cortex were stained with antibodies to SOX1 to identify NSPCs and define the borders of the VZ. (C) E12 sagittal sections stained with antibodies to MAP2 to identify differentiated neurons define the borders of the CP. (D) Similarly, DCX antibodies detect differentiated neurons in the E12 CP. (E) Sagittal sections of the E16 mouse embryonic cortex were stained with antibodies to SOX2 to mark the NSPCs of the VZ/SVZ. (F) MAP2 staining of E16 sagittal sections marks the differentiated neurons in the CP; note the intervening IZ between the VZ/SVZ and CP at E16. All cell nuclei were labeled with Hoechst stain.

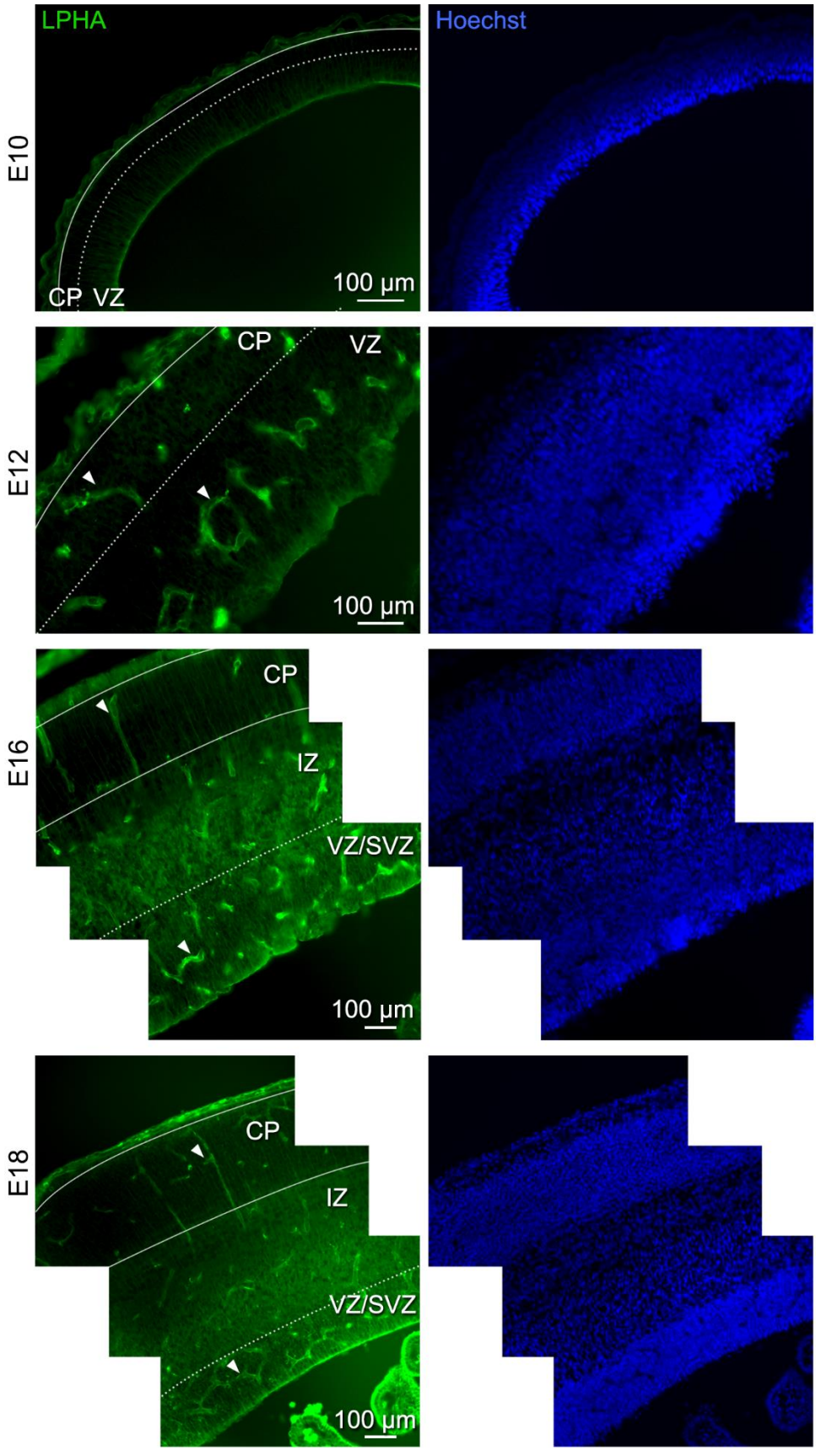
LPHA
Hoechst
E10
CP VZ
100 μm
E12
CP
VZ
100 μm
E16
CP
IZ
VZ/SVZ
100 μm
E18
CP
IZ
VZ/SVZ
100 μm

Figure 3.S5. Labeling of the E10 to E18 developing cerebral cortex with lectin L-PHA to detect highly branched N-glycans. Lectin L-PHA indicates the presence of highly branched tetra-antennary N-glycans in sagittal sections of the developing embryonic cerebral cortex at E10, E12, E16, and E18. Dotted lines denote the boundaries between the NSPC niches (VZ in E12 and VZ/SVZ in E16) and regions containing more differentiated cells, the cortical plate (CP) and migrating progenitors, intermediate zone (IZ). Solid lines indicate the outer boundaries of the CP and IZ. Arrowheads point to blood vessels, which stain strongly for L-PHA and were excluded from quantitative analysis. More intense L-PHA staining is evident in the E16 and E18 NSPC niche (VZ/SVZ) than the E10 or E12 niche (VZ). Right hand panels are corresponding Hoechst stained nuclei for each panel on the left.

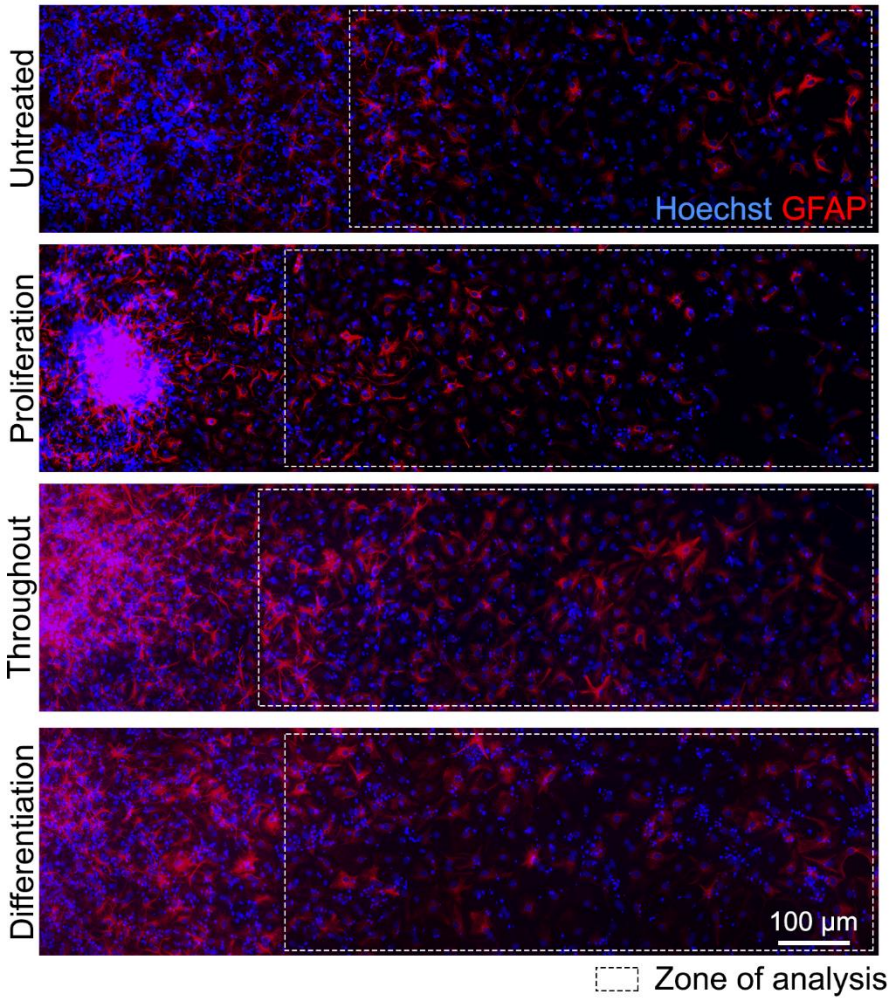

Figure 3.S6. Whole field images of GFAP-positive cells. Images of GFAP-positive astrocytes differentiated from E12 NSPCs indicate the zones of cells used for analysis (dashed boxes) to avoid high cell density regions (left side of each image). Cells were untreated or treated with 80 mM GlcNAc during proliferation, throughout proliferation and differentiation, or during differentiation (see Figure 3.6A). All cell nuclei were labeled with Hoechst.

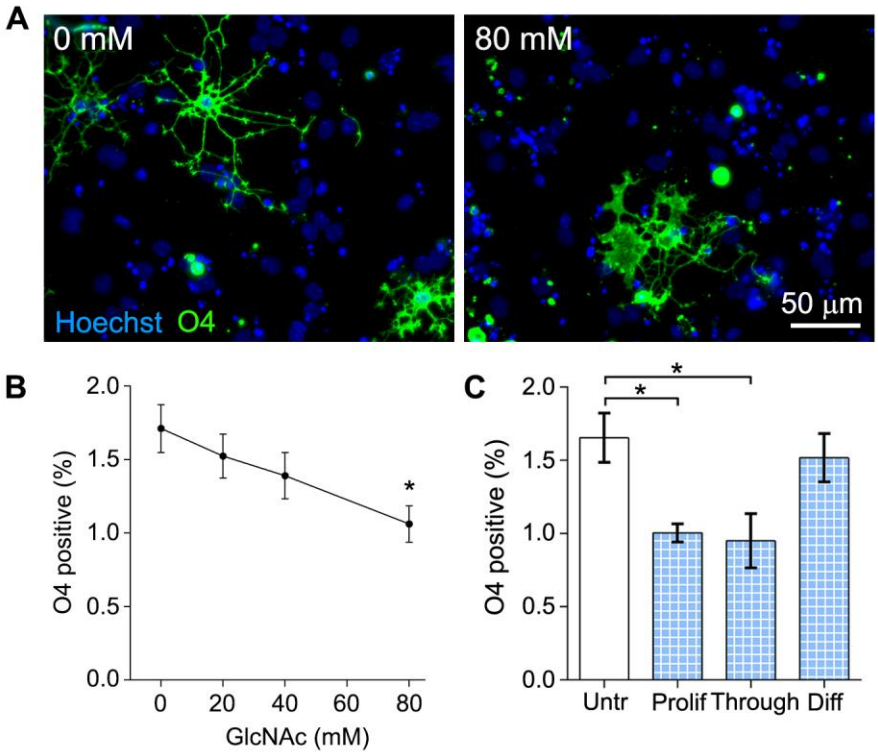

Figure 3.S7. GlcNAc treatment decreases oligodendrocyte formation from E12 mouse NSPCs. (A) E12 NSPCs treated with 80 mM GlcNAc during 3 days as undifferentiated cells and for an additional 7 days during differentiation generated fewer oligodendrocytes stained with O4 (green) than control NSPCs (0 mM, untreated). Some non-specific globular signal was present in all samples and was excluded from analysis. All nuclei were labeled with Hoechst (blue). (B) The percentage of O4-positive oligodendrocytes formed from E12 NSPCs decreases with increasing GlcNAc concentration (one-way ANOVA, p=0.0222). *Post hoc* analysis by Dunnett's test indicates significant decrease in oligodendrocyte formation after supplementation with 80 mM GlcNAc (p=0.0161) compared to untreated E12 NSPCs. (C) E12 NSPCs were treated with 80 mM GlcNAc in the proliferation stage (Prolif, 3 days), throughout both proliferation and differentiation stages (Through, 10 days), or during the differentiation stage (Diff, 7 days). The percentage of O4 positive oligodendrocytes was significantly decreased when NSPCs were treated with GlcNAc during the proliferation stage or throughout both stages (Untr v Prolif p=0.0383, Untr v Through p=0.0144, one-way ANOVA, Tukey *post hoc* for multiple comparisons) but not the differentiation stage, suggesting an effect on undifferentiated NSPCs but not differentiated cells. All error bars represent standard error of the mean. N=3 or more independent biological repeats, (*p<0.05).

3.8.2 Supplemental Tables

Table 3.S1: **N-glycosylation enzymes of E12 and E16 NSPCs**. Bolded enzymes represent expression difference greater than 1.2-fold.

Enzyme	E16 fold over E12	Function
Man2a2	**1.6935**	**Removes mannose from N-glycans to initiate complex branching**
Fut8	**1.5476**	**Adds α1-6 linked fucose to first GlcNAc on N-glycan core**
B3gnt2	**1.5476**	**Involved in the formation of poly-N-acetyllactosamine**
St6gal1	**1.5263**	**Adds α2-6 linked sialic acid to galactose residues**
Man2a1	**1.2924**	**Removes mannose from N-glycans to initiate complex branching**
B4galt5	**1.2483**	**Adds galactose to N-glycans**
Mgat5	**1.2142**	**Adds β1-6 linked GlcNAc on highly-branched N-gycans**
Prkcsh	1.1810	B-subunit of glucosidase II
Mgat1	1.1567	Adds first β1-2 linked GlcNAc to form hybrid and complex N-glycans
Ganab	1.1408	A-subunit of glucosidase II; cleaves glucose from immature N-glycans in the ER
B4galt1	1.0000	Adds galactose to GlcNAc residues on branched N-glycans
St3gal2	1.0000	Adds α2-3 linked sialic acid to galactose
B3gnt4	0.9931	Biosynthesis of poly-N-acetyllactosamine
Mgat2	0.9794	Adds second β1-2 linked GlcNAc to form di-antennary N-glycans
Man1b1	0.9659	Removes mannose from N-glycans
B4galt3	0.9461	Adds first galactose for poly-N-acetyllactosamine chains
Man1a2	0.9395	Removes mannose from N-glycans necessary to initiate biosynthesis of branched N-glycans
Mogs	0.9013	Cleaves glucose from mannose in early N-glycan processing
Mgat4b	0.8888	Adds β1-4 linked GlcNAc on highly-branched N-gycans
Mgat4a	0.8526	Adds β1-4 linked GlcNAc on highly-branched N-gycans
Man1c1	0.8011	Removes mannose from N-glycans
Fut11	**0.7792**	**α1-3 fucosyltransferase**
B4galt2	**0.7423**	**Involved in the formation of poly-N-acetyllactosamine**
St8sia4	**0.5664**	**Also known as PST, biosynthesis of polysialic acid**
Mgat3	**0.5471**	**Adds β1-4 linked GlcNAc to form bisected N-glycans**
St8sia2	**0.2755**	**Also known as STX, biosynthesis of polysialic acid**
B3gnt8	low expr	Elongates branched N-glycans, strong activity toward tetra-antennary N-glycans
Man1a	low expr	Removes mannose from N-glycans necessary to initiate biosynthesis of branched N-glycans
Mgat4c	low expr	Adds β1-4 linked GlcNAc on highly-branched N-gycans
St8sia3	low expr	Biosynthesis of polysialic acid
B3gnt3	not expr	Involved in the formation of poly-N-acetyllactosamine
Man2b1	not expr	Removes mannose from N-glycans

Table 3.S2: O-glycosylation enzymes of E12 and E16 NSPCs. Bolded enzymes represent expression difference greater than 1.2-fold.

Enzyme	E16 fold over E12	Function or possible function based on homology
Galnt7	**1.74**	**Adds galactose to pre-existing O-linked GalNAc on serine/threonine (S/T) residues**
Galnt4	**1.65**	**Adds initial GalNAc onto S/T in mucin-type O-glycans**
Pofut2	**1.37**	**Generates O-fucosylated proteins**
Pomt1	**1.23**	**Works with Pomt2 to generate O-mannose glycans**
Ogt	1.19	Adds initial GlcNAc to S/T to generate cytoplasmic and nuclear O-GlcNAc glycans
B3glct	1.1567	Transfers glucose to O-linked fucosyl glycans
Pomgnt1	1.07	Adds GlcNAc onto O-mannose glycans
Galnt1	1.06	Adds initial GalNAc onto S/T for mucin type O-glycans
St6GalNAc1	1.0479	Adds sialic acid to galactose residues of O-linked sugars
Pomt2	1	Works with Pomt1 to generate O-mannose glycans
Galnt11	0.97	Initiates biosynthesis of O-linked GalNAc glycans
Galnt2	0.97	Initiates biosynthesis of O-linked GalNAc glycans
C1galt1c1	0.97	Chaperone necessary for C1galt1 and core 1 O-glycan synthesis
C1galt1	0.93	Generates the core 1 O-glycan structure
Galnt10	0.87	Adds initial GalNAc onto S/T for mucin type O-glycans
Pofut1	0.85	Adds initial fucose to S/T to generate O-fucosylated proteins
Wbscr17	0.84	Initiates biosynthesis of O-linked GalNAc glycans
Galnt16	0.81	Adds initial GalNAc onto S/T in mucin-type O-glycans
St3gal1	**0.79**	**Adds sialic acid to galactose residues of O-linked sugars**
Galnt13	**0.68**	**Adds initial GalNAc onto S/T in mucin-type O-glycans**
Mgat5b	**0.48**	**Adds GlcNAc to mannose to generate branched O-mannose glycans**
Galnt12	low expr	Initiates biosynthesis of O-linked GalNAc glycans
Galnt14	low expr	Adds initial GalNAc onto S/T in mucin-type O-glycans
Galnt3	low expr	Adds initial GalNAc onto S/T in mucin-type O-glycans
Galnt9	low expr	Adds initial GalNAc on S/T in mucin-type O-glycans
Gcnt1	low expr	Generates the core 2 O-glycan structure
St8sia6	low expr	Biosynthesis of polysialic acid on O-glycans
A4gnt	low expr	Transfers GlcNAc to core 2 O-glycans to form type III mucins
Galnt5	not expr	Adds initial GalNAc onto S/T in mucin-type O-glycans
Galnt6	not expr	Adds initial GalNAc onto S/T in mucin-type O-glycans
Galntl5	not expr	Adds initial GalNAc onto S/T in mucin-type O-glycans
Galntl6	not expr	Adds initial GalNAc onto S/T in mucin-type O-glycans
Gcnt3	not expr	Involved in biosynthesis of core 2 and core 4 O-glycans of mucins

Table 3.S3: Enzymes of E12 and E16 NSPCs involved in endoplasmic reticulum (ER) quality control, targeting of enzymes to lysosomes, or lysosomal degradation of glycans. Bolded enzymes represent expression difference greater than 1.2-fold.

Enzyme	E16 fold over E12	Function
Manba	**1.8921**	**Lysosomal mannosidase**
Hexa	**1.7901**	**A-subunit of lysosomal enzyme that degrades GM2 ganglioside**
Aga	**1.7532**	**Lysosomal enzyme; cleaves GlcNAc-Asn linkage on N-linked glycoproteins**
Fuca1	**1.2924**	**Lysosomal enzyme; degrades fucose containing glycoproteins**
Nagpa	**1.2746**	**Cleaves GlcNAc from mannose; involved in lysosomal enzyme trafficking from Golgi to lysosome**
Uggt1	**1.2142**	**Re-glucosylates N-glycans of misfolded proteins in the ER**
Edem3	1.1567	Participates in ER-associated degradation (ERAD) by cleaving mannose residues from N-glycans
Edem1	1.1408	Participates in ERAD by cleaving mannose residues from N-glycans and targets misfolded glycoproteins for degradation
Uggt2	1.0718	Re-glucosylates N-glycans of misfolded proteins in the ER
Hexb	1.0497	B-subunit of lysosomal enzyme that degrades GM2 ganglioside
Glb1	1.014	Lysosomal enzyme; involved in degradation
Neu3	1.0070	Plasma membrane sialidase
Neu1	0.9862	Lysosomal sialidase
Edem2	0.9461	Participates in ERAD by trimming mannose in the ER
Fuca2	0.9138	Lysosomal enzyme, degrades fucose containing glycoproteins
Gnptg	0.9075	Generates glycans necessary for trafficking lysosomal enzymes to lysosome
Gnptab	0.895	Generates glycans necessary for trafficking lysosomal enzymes to lysosome
Neu4	low expr	Lysosomal sialidase
Neu2	not expr	Cytoplasmic sialidase

Table 3.S4: DNA primers for qRT-PCR.

Gene	Forward Primer (5'→ 3')	Reverse Primer (5' → 3')	Expected length (bp)
Asef (probe 1)	TCTCCAGAGTCTCCGCATCTTC	GTGGCATCCATCACTTCGATG	353
Asef (probe 2)	GAGGAGGTGGAGAGCAACTG	GCGGTAGATGTCCTCGATGTTC	484
Slc1a3 (GLAST)	TTTCTCTCTAGGGGCAGGCT	CAGAAGGGAGGGCCTCTAGT	140
Egfr	TCTTCAAGGATGTGAAGTGTG	TGTACGCTTTCGAACAATGT	145
GAPDH	ATACGGCTACAGCAACAGGG	GCCTCTCTTGCTCAGTGTCC	105

3.9 REFERENCES

1. Q. Cao, R. L. Benton, S. R. Whittemore, Stem cell repair of central nervous system injury. *J Neurosci Res* **68**, 501-510 (2002).
2. P. Gascoyne, R. Pethig, J. Satayavivad, F. Becker, M. Ruchirawat, Dielectrophoretic detection of changes in erythrocyte membranes following malarial infection. *Biochimica Et Biophysica Acta-Biomembranes* **1323**, 240-252 (1997).
3. R. Pethig *et al.*, Dielectrophoretic studies of the activation of human T lymphocytes using a newly developed cell profiling system. *Electrophoresis* **23**, 2057-2063 (2002).
4. M. Cristofanilli *et al.*, Automated electrorotation to reveal dielectric variations related to HER-2/neu overexpression in MCF-7 sublines. *Clinical Cancer Research* **8**, 615-619 (2002).
5. J. Lu *et al.*, Advancing practical usage of microtechnology: a study of the functional consequences of dielectrophoresis on neural stem cells. *Integr Biol (Camb)* **4**, 1223-1236 (2012).
6. L. A. Flanagan *et al.*, Unique dielectric properties distinguish stem cells and their differentiated progeny. *Stem Cells* **26**, 656-665 (2008).
7. J. L. Prieto, J. Lu, J. L. Nourse, L. A. Flanagan, A. P. Lee, Frequency discretization in dielectrophoretic assisted cell sorting arrays to isolate neural cells. *Lab Chip* **12**, 2182-2189 (2012).
8. A. Lee, M. Aghaamoo, T. Adams, L. Flanagan. (Current Stem Cell Reports, 2018), vol. 4, pp. 116-126.
9. F. H. Labeed *et al.*, Biophysical characteristics reveal neural stem cell differentiation potential. *PLoS One* **6**, e25458 (2011).
10. J. L. Nourse *et al.*, Membrane biophysics define neuron and astrocyte progenitors in the neural lineage. *Stem Cells* **32**, 706-716 (2014).
11. M. G. Simon *et al.*, Increasing label-free stem cell sorting capacity to reach transplantation-scale throughput. *Biomicrofluidics* **8**, 064106 (2014).
12. Y. Hirota, M. Hakoda, Relationship between Dielectric Characteristic by DEP Levitation and Differentiation Activity for Stem Cells. *Key Engineering Materials* **459**, 84-91 (2011).
13. E. Gheorghiu, The resting potential in relation to the equivalent complex permittivity of a spherical cell-suspension. *Physics in Medicine and Biology* **38**, 979-988 (1993).
14. M. Stoneman *et al.*, Protein influence on the plasma membrane dielectric properties: In vivo study utilizing dielectric spectroscopy and fluorescence microscopy. *Bioelectrochemistry* **70**, 542-550 (2007).
15. D. Zimmermann *et al.*, Effects on capacitance by overexpression of membrane proteins. *Biochem Biophys Res Commun* **369**, 1022-1026 (2008).
16. X. Wang *et al.*, Changes in friend murine erythroleukemia cell-membranes during induced-differentiation determined by electrorotation. *Biochimica Et Biophysica Acta-Biomembranes* **1193**, 330-344 (1994).
17. M. Muratore, V. Srsen, M. Waterfall, A. Downes, R. Pethig, Biomarker-free dielectrophoretic sorting of differentiating myoblast multipotent progenitor cells and their membrane analysis by Raman spectroscopy. *Biomicrofluidics* **6**, 034113 (2012).
18. S. Desai, M. Vahey, J. Voldman, Electrically Addressable Vesicles: Tools for Dielectrophoresis Metrology. *Langmuir* **25**, 3867-3875 (2009).
19. F. T. Zhao, J. Li, G. X. Shi, Y. Liu, L. P. Zhu, Modification of glycosylation reduces microvilli on rat liver epithelial cells. *Cell Biol Int* **26**, 627-633 (2002).

20. O. B. Garner, L. G. Baum, Galectin-glycan lattices regulate cell-surface glycoprotein organization and signalling. *Biochem Soc Trans* **36**, 1472-1477 (2008).
21. M. J. Paszek *et al.*, The cancer glycocalyx mechanically primes integrin-mediated growth and survival. *Nature* **511**, 319-325 (2014).
22. R. L. Schnaar, R. Gerardy-Schahn, H. Hildebrandt, Sialic acids in the brain: gangliosides and polysialic acid in nervous system development, stability, disease, and regeneration. *Physiol Rev* **94**, 461-518 (2014).
23. I. R. Nabi, J. Shankar, J. W. Dennis, The galectin lattice at a glance. *J Cell Sci* **128**, 2213-2219 (2015).
24. R. S. Haltiwanger, J. B. Lowe, Role of glycosylation in development. *Annu Rev Biochem* **73**, 491-537 (2004).
25. S. Ngamukote, M. Yanagisawa, T. Ariga, S. Ando, R. Yu, Developmental changes of glycosphingolipids and expression of glycogenes in mouse brains. *Journal of Neurochemistry* **103**, 2327-2341 (2007).
26. N. Flaris *et al.*, Developmentally-regulated lectin-binding in the embryonic mouse telencephalon. *Brain Research* **678**, 99-109 (1995).
27. A. Ishii *et al.*, Developmental changes in the expression of glycogenes and the content of N-glycans in the mouse cerebral cortex. *Glycobiology* **17**, 261-276 (2007).
28. W. He, C. Ingraham, L. Rising, S. Goderie, S. Temple, Multipotent stem cells from the mouse basal forebrain contribute GABAergic neurons and oligodendrocytes to the cerebral cortex during embryogenesis. *Journal of Neuroscience* **21**, 8854-8862 (2001).
29. X. Qian *et al.*, Timing of CNS cell generation: a programmed sequence of neuron and glial cell production from isolated murine cortical stem cells. *Neuron* **28**, 69-80 (2000).
30. H. Schachter, Congenital disorders involving defective N-glycosylation of proteins. *Cellular and Molecular Life Sciences* **58**, 1085-1104 (2001).
31. J. W. Dennis, I. R. Nabi, M. Demetriou, Metabolism, cell surface organization, and disease. *Cell* **139**, 1229-1241 (2009).
32. R. D. Cummings, S. Kornfeld, Characterization of the structural determinants required for the high affinity interaction of asparagine-linked oligosaccharides with immobilized Phaseolus vulgaris leukoagglutinating and erythroagglutinating lectins. *J Biol Chem* **257**, 11230-11234 (1982).
33. L. S. Chaboub *et al.*, Temporal Profiling of Astrocyte Precursors Reveals Parallel Roles for Asef during Development and after Injury. *J Neurosci* **36**, 11904-11917 (2016).
34. Y. Sun, S. K. Goderie, S. Temple, Asymmetric distribution of EGFR receptor during mitosis generates diverse CNS progenitor cells. *Neuron* **45**, 873-886 (2005).
35. R. C. Burrows, D. Wancio, P. Levitt, L. Lillien, Response diversity and the timing of progenitor cell maturation are regulated by developmental changes in EGFR expression in the cortex. *Neuron* **19**, 251-267 (1997).
36. E. Hartfuss, R. Galli, N. Heins, M. Götz, Characterization of CNS precursor subtypes and radial glia. *Dev Biol* **229**, 15-30 (2001).
37. P. Gascoyne, R. Pethig, J. Burt, F. Becker, Membrane-changes accompanying the induced-differentiation of friend murine erythroleukemia cells studied by dielectrophoresis. *Biochimica Et Biophysica Acta* **1149**, 119-126 (1993).
38. J. P. Burt, R. Pethig, P. R. Gascoyne, F. F. Becker, Dielectrophoretic characterisation of Friend murine erythroleukaemic cells as a measure of induced differentiation. *Biochim Biophys Acta* **1034**, 93-101 (1990).

39. K. S. Lau *et al.*, Complex N-glycan number and degree of branching cooperate to regulate cell proliferation and differentiation. *Cell* **129**, 123-134 (2007).
40. Y. Y. Zhao *et al.*, Functional roles of N-glycans in cell signaling and cell adhesion in cancer. *Cancer Sci* **99**, 1304-1310 (2008).
41. A. Males, L. Raich, S. J. Williams, C. Rovira, G. J. Davies, Conformational Analysis of the Mannosidase Inhibitor Kifunensine: A Quantum Mechanical and Structural Approach. *Chembiochem* **18**, 1496-1501 (2017).
42. S. W. Mast, K. W. Moremen, Family 47 alpha-mannosidases in N-glycan processing. *Methods Enzymol* **415**, 31-46 (2006).
43. Y. Su, C. Warren, R. Guerrant, N. Swami, Dielectrophoretic Monitoring and Interstrain Separation of Intact Clostridium difficile Based on Their S(Surface)-Layers. *Analytical Chemistry* **86**, 10855-10863 (2014).
44. P. O. Bagnaninchi, N. Drummond, Real-time label-free monitoring of adipose-derived stem cell differentiation with electric cell-substrate impedance sensing. *Proc Natl Acad Sci U S A* **108**, 6462-6467 (2011).
45. A. Heiskanen *et al.*, Glycomics of bone marrow-derived mesenchymal stem cells can be used to evaluate their cellular differentiation stage. *Glycoconjugate Journal* **26**, 367-384 (2009).
46. H. Hamouda *et al.*, N-Glycosylation Profile of Undifferentiated and Adipogenically Differentiated Human Bone Marrow Mesenchymal Stem Cells: Towards a Next Generation of Stem Cell Markers. *Stem Cells and Development* **22**, 3100-3113 (2013).
47. Z. Ye, J. D. Marth, N-glycan branching requirement in neuronal and postnatal viability. *Glycobiology* **14**, 547-558 (2004).
48. E. Ioffe, P. Stanley, Mice lacking N-acetylglucosaminyltransferase I activity die at mid-gestation, revealing an essential role for complex or hybrid N-linked carbohydrates. *Proc Natl Acad Sci U S A* **91**, 728-732 (1994).
49. M. Metzler *et al.*, Complex asparagine-linked oligosaccharides are required for morphogenic events during postimplantation development. *Embo Journal* **13**, 2056-2065 (1994).
50. Y. Wang, H. Schachter, J. D. Marth, Mice with a homozygous deletion of the Mgat2 gene encoding UDP-N-acetylglucosamine:alpha-6-D-mannoside beta1,2-N-acetylglucosaminyltransferase II: a model for congenital disorder of glycosylation type IIa. *Biochim Biophys Acta* **1573**, 301-311 (2002).
51. T. Sasaki, J. Hirabayashi, H. Manya, K. Kasai, T. Endo, Galectin-1 induces astrocyte differentiation, which leads to production of brain-derived neurotrophic factor. *Glycobiology* **14**, 357-363 (2004).
52. Y. Imaizumi *et al.*, Galectin-1 is expressed in early-type neural progenitor cells and down-regulates neurogenesis in the adult hippocampus. *Mol Brain* **4**, 7 (2011).
53. L. A. Pasquini *et al.*, Galectin-3 drives oligodendrocyte differentiation to control myelin integrity and function. *Cell Death Differ* **18**, 1746-1756 (2011).
54. L. J. Slieker, M. D. Lane, Post-translational processing of the epidermal growth factor receptor. Glycosylation-dependent acquisition of ligand-binding capacity. *J Biol Chem* **260**, 687-690 (1985).
55. H. Guo, I. Lee, M. Kamar, S. Akiyama, M. Pierce, Aberrant N-glycosylation of beta(1) integrin causes reduced alpha(5)beta(1) integrin clustering and stimulates cell migration. *Cancer Research* **62**, 6837-6845 (2002).

56. T. Isaji *et al.*, Introduction of bisecting GlcNAc into integrin alpha5beta1 reduces ligand binding and down-regulates cell adhesion and cell migration. *J Biol Chem* **279**, 19747-19754 (2004).
57. T. Isaji, Y. Sato, T. Fukuda, J. Gu, N-glycosylation of the I-like domain of beta1 integrin is essential for beta1 integrin expression and biological function: identification of the minimal N-glycosylation requirement for alpha5beta1. *J Biol Chem* **284**, 12207-12216 (2009).
58. T. Isaji *et al.*, N-glycosylation of the beta-propeller domain of the integrin alpha5 subunit is essential for alpha5beta1 heterodimerization, expression on the cell surface, and its biological function. *J Biol Chem* **281**, 33258-33267 (2006).
59. Y. Zhao *et al.*, N-acetylglucosaminyltransferase III antagonizes the effect of N-acetylglucosaminyltransferase V on alpha 3 beta 1 integrin-mediated cell migration. *Journal of Biological Chemistry* **281**, 32122-32130 (2006).
60. R. Akama *et al.*, N-acetylglucosaminyltransferase III expression is regulated by cell-cell adhesion via the E-cadherin-catenin-actin complex. *Proteomics* **8**, 3221-3228 (2008).
61. M. E. Kremser *et al.*, Characterisation of alpha3beta1 and alpha(v)beta3 integrin N-oligosaccharides in metastatic melanoma WM9 and WM239 cell lines. *Biochim Biophys Acta* **1780**, 1421-1431 (2008).
62. Y. Song, J. A. Aglipay, J. D. Bernstein, S. Goswami, P. Stanley, The bisecting GlcNAc on N-glycans inhibits growth factor signaling and retards mammary tumor progression. *Cancer Res* **70**, 3361-3371 (2010).
63. G. H. Waetzig *et al.*, N-linked glycosylation is essential for the stability but not the signaling function of the interleukin-6 signal transducer glycoprotein 130. *J Biol Chem* **285**, 1781-1789 (2010).
64. E. A. Partridge *et al.*, Regulation of cytokine receptors by Golgi N-glycan processing and endocytosis. *Science* **306**, 120-124 (2004).
65. H. Miwa, Y. Song, R. Alvarez, R. Cummings, P. Stanley, The bisecting GlcNAc in cell growth control and tumor progression. *Glycoconjugate Journal* **29**, 609-618 (2012).
66. I. Brockhausen, S. Narasimhan, H. Schachter, The biosynthesis of highly branched N-glycans - studies on the sequential pathway and functional-role of N-acetylglucosaminyltransferases I, II, III, IV, V AND VI. *Biochimie* **70**, 1521-1533 (1988).
67. M. Terashima, M. Amano, T. Onodera, S. Nishimura, N. Iwasaki, Quantitative glycomics monitoring of induced pluripotent- and embryonic stem cells during neuronal differentiation. *Stem Cell Research* **13**, 454-464 (2014).
68. M. Amano *et al.*, Threshold in Stage-specific Embryonic Glycotypes Uncovered by a Full Portrait of Dynamic N-Glycan Expression during Cell Differentiation. *Molecular & Cellular Proteomics* **9**, 523-537 (2010).
69. S. Pinho *et al.*, The role of N-acetylglucosaminyltransferase III and V in the post-transcriptional modifications of E-cadherin. *Human Molecular Genetics* **18**, 2599-2608 (2009).
70. M. Yoshimura, Y. Ihara, Y. Matsuzawa, N. Taniguchi, Aberrant glycosylation of E-cadherin enhances cell-cell binding to suppress metastasis. *Journal of Biological Chemistry* **271**, 13811-13815 (1996).
71. H. Guo, I. Lee, M. Kamar, M. Pierce, N-acetylglucosaminyltransferase V expression levels regulate cadherin-associated homotypic cell-cell adhesion and intracellular signaling pathways. *Journal of Biological Chemistry* **278**, 52412-52424 (2003).

72. A. Varki, *Essentials of Glycobiology*. (Cold Spring Harbor Laboratory Press, Cold Spring Harbor, New York, ed. 2, 2009).
73. . (Weizmann Institute of Science), vol. 2017.
74. X. Cheng *et al.*, Central roles of the roof plate in telencephalic development and holoprosencephaly. *J Neurosci* **26**, 7640-7649 (2006).
75. M. M. Lissner *et al.*, Age-Related Gene Expression Differences in Monocytes from Human Neonates, Young Adults, and Older Adults. *PLoS One* **10**, e0132061 (2015).
76. J. Goecks, A. Nekrutenko, J. Taylor, G. Team, Galaxy: a comprehensive approach for supporting accessible, reproducible, and transparent computational research in the life sciences. *Genome Biol* **11**, R86 (2010).
77. C. Trapnell *et al.*, Transcript assembly and quantification by RNA-Seq reveals unannotated transcripts and isoform switching during cell differentiation. *Nat Biotechnol* **28**, 511-515 (2010).
78. A. Mortazavi, B. A. Williams, K. McCue, L. Schaeffer, B. Wold, Mapping and quantifying mammalian transcriptomes by RNA-Seq. *Nat Methods* **5**, 621-628 (2008).
79. S. U. Lee *et al.*, N-glycan processing deficiency promotes spontaneous inflammatory demyelination and neurodegeneration. *J Biol Chem* **282**, 33725-33734 (2007).
80. K. F. Hoettges *et al.*, Dielectrophoresis-activated multiwell plate for label-free high-throughput drug assessment. *Anal Chem* **80**, 2063-2068 (2008).
81. L. Broche, F. Labeed, M. Hughes, Extraction of dielectric properties of multiple populations from dielectrophoretic collection spectrum data. *Physics in Medicine and Biology* **50**, 2267-2274 (2005).

CHAPTER 4

Regulation of neural stem cells and neural development by MGAT5-mediated N-glycosylation

Authors: **Andrew R. Yale[1,2,3]**, Estelle Kim[1,2,3], Edwin S. Monuki[3,4], Lisa A. Flanagan[1,2,3,5]

[1]Department of Anatomy & Neurobiology, University of California, Irvine

[2]Department of Neurology, University of California, Irvine

[3]Sue & Bill Gross Stem Cell Research Center, University of California, Irvine

[4]Department of Pathology and Laboratory Medicine, University of California, Irvine

[5]Department of Biomedical Engineering, University of California, Irvine

4.1 ABSTRACT

N-linked glycans attached to cell surface proteins come in a variety of different configurations that impact protein folding, trafficking, and function and can thus alter a cell's behavior and perception of its environment. N-glycans undergo a modification known as "branching" that can directly alter receptor retention at the cell surface as well as modulate ligand affinity. Increasing the expression of highly branched N-glycans on neural stem/progenitor cells (NSPCs) alters fate-specific electrophysiological properties, reduces neurogenesis and increases astrogenesis. However, the specific N-glycan configurations that impact NSPC fate decisions are unknown. We hypothesized that modulating glycosylation enzymes to reduce N-glycan branching would influence NSPC fate potential. We report that blocking an early enzyme in the branching pathway did not alter the differentiation of NSPCs. However, targeting the enzyme that produces the most highly branched N-glycans in mammalian cells, MGAT5, did impact NSPC fate. NSPCs lacking MGAT5 had significantly reduced N-glycan branching and generated more neurons and fewer astrocytes in vitro. MGAT5 plays a significant role in neural development in vivo since mice lacking MGAT5 generated more NeuN-labeled mature neurons, but fewer cells in the cortex overall and less neurons in both upper and deep layers. These data identify MGAT5 as a significant contributor to NSPC fate potential and development in the neural lineage and define a novel role for N-glycosylation branching in neural development and NSPC differentiation.

4.2 INTRODUCTION

Glycosylation is a major post-translational modification in which enzymes attach sugar molecules, known as a glycans, to target conjugates such as proteins or lipids (*1*). Glycosylation patterns expressed across the CNS change during development and impact a variety of different functions such as cell maturation, neuronal migration, axonal targeting, and synapse formation (*1-7*). Defects in N-glycans lead to a variety of diseases termed congenital disorders of glycosylation (CDGs), many of which include neurological symptoms such as psychomotor and mental retardation, seizures, or paralysis (*8-11*).

How N-glycosylation may affect neural stem cells is not fully understood since this process affects a wide variety of signaling modalities across the cell surface. LewisX, a terminal N-glycan modification produced by the glycosylation enzyme FUT9, has been shown to impact human neural stem/progenitor cell (NSPC) proliferation by interacting with the Notch signaling pathway (*12*). The mitogenic activation of adult hippocampal NSPCs by FGF2 is dependent on the N-glycosylated form of the secreted protein cystatin C (CCg), which is secreted by NSPCs, but most predominantly those found within the adult SVZ (*13*). Polysialic acid found on neural cell adhesion molecule (PSA-NCAM) is necessary for proper migration of immature neurons (*2, 3, 14*), but there is some evidence that it could also impact NSPC fate potential. PSA-NCAM deficient NSPCs isolated from embryonic cortices are more susceptible to glial formation when stimulated by PDGF (*15*). On the other hand, degradation of PSA by EndoN from hippocampal adult NSPCs induced neuronal differentiation *in vivo* and *in vitro* (*16*). Galectins, proteins that bind to N-glycan epitopes, have been implicated in astrocyte maturation and suppression of neurogenesis within the adult hippocampus (*17, 18*). Additionally, Galectin-3 has been shown to induce oligodendrocyte differentiation and maturation from local oligodendrocyte progenitor

cells to maintain myelin integrity. Furthermore, galectin-3 deficient adult NSPCs had reduced commitment to the oligodendritic lineage (*19*). A glycomic study revealed astrocytes express less bisected N-glycans compared to neurons when differentiated from pluripotent stem cells suggesting differences in N-glycan branching can potentially reflect the fate potential of NSPCs (*20*).

N-linked glycosylation begins by covalently linking glycans to an asparagine residue of a translated polypeptide in the endoplasmic reticulum. Enzymes in the Golgi add and remodel sugars on proteins that eventually reside on the cell surface or are secreted from cells. N-glycans share a common processing pathway in which additional sugars can be added to form what is known as complex branches (*21-24*). N-glycan branching is essential for proper CNS development since reducing the expression of enzymes that generate branched N-glycans results in severe developmental issues. For example, deficiency of MGAT1 causes failure in neural tube closure and is embryonic lethal (*25, 26*); neuron-specific deletion of MGAT1 results in early postnatal lethality due to spontaneous neuronal apoptosis (*27*). Deletion of MGAT2 in animals mimics symptoms of patients with CDG IIa and causes premature death; symptoms include psychomotor retardation and cognitive deficits (*28*).

We previously reported that increased N-glycan branching induced by N-acetylglucosamine (GlcNAc) treatment causes a shift in NSPC fate potential towards astrogenesis (*29*). Screening for differences in glycosylation enzyme expression revealed higher levels of expressed N-glycan branching related enzymes in astrocyte-biased NSPCs that were either isolated from later stages of cortical development or enriched to contain more astrocyte progenitors in the sample population (*29*). Additionally, we found increased expression of highly branched N-glycans in the ventricular/sub-ventricular zone of the developing embryonic cortices

in vivo (29). Stimulating N-glycan branching by N-acetylglucosamine (GlcNAc) supplementation resulted in a significant shift in membrane capacitance (*29*). Furthermore, we found GlcNAc treatment affected fate potential as NSPCs with increased expression of highly branched N-glycans generated more astrocytes and fewer neurons (*29*). Our studies show N-glycan branching directly impacts NSPC differentiation; however, the specific N-glycan configurations that impact NSPC fate decisions are unknown. Here we identify that NSPCs lacking the N-glycan branching enzyme, MGAT5, generate more neurons and less astrocytes *in vitro*. Furthermore, the loss of MGAT5 spurs increased maturation of neurons early in cortical development. However, this is accompanied by a loss of progenitor cells within the VZ/SVZ resulting in an overall depletion of neuron production seen in both embryonic and postnatal cortices.

4.3 RESULTS

4.3.1 Abolishing N-glycan branching by targeting early enzymes in the branching pathway significantly alters the cell surface N-glycan landscape and does not alter NSPC fate

We previously identified that branched, complex N-glycans significantly impact the fate potential of NSPCs (*29*). N-acetylglucosamine (GlcNAc) stimulates N-glycan branching in NSPCs, causing increased expression of highly branched N-glycans on the cell surface (*29*). Treating NSPCs with GlcNAc induced the formation of more astrocytes at the expense of neurons (*29*). We therefore hypothesized that reducing the formation of branched N-glycans would have the opposite effect. Specifically, we asked whether simple, high-mannose type N-glycans correlated with the formation of neurons.

We utilized the drug Kifunensine (Kif) to selectively inhibit alpha-mannosidase 1 (MAN1) (*30*), which is the enzyme responsible for cleaving excess mannose residues to initiate N-glycan branching. This treatment was chosen to induce high-mannose N-glycans on NSPCs. We treated embryonic day 12 (E12) mouse NSPCs with Kif doses ranging from 0.001 to 10 µM and analyzed N-glycan branching by binding of L-PHA, a lectin used to detect highly branched N-glycans (Supp. Fig. 4.S1A). To prevent potential side effects of Kif at too high a concentration, we chose 0.5 µM Kif as the lowest dose to achieve ~100% reduction in L-PHA reactivity after 4 days of treatment (Supp. Fig. 4.S1B). After 4 days, L-PHA binding was virtually undetectable on E12 NSPCs treated with 0.5 uM Kif (Fig. 4.1A, B, Supp. Fig. 4.S1B) whereas NSPCs treated with 80 mM GlcNAc showed increased L-PHA reactivity relative to controls (Fig. 4.1B). Thus, 4 days of 0.5 µM Kif treatment significantly reduced the expression of highly branched N-glycans on the surfaces of NSPCs.

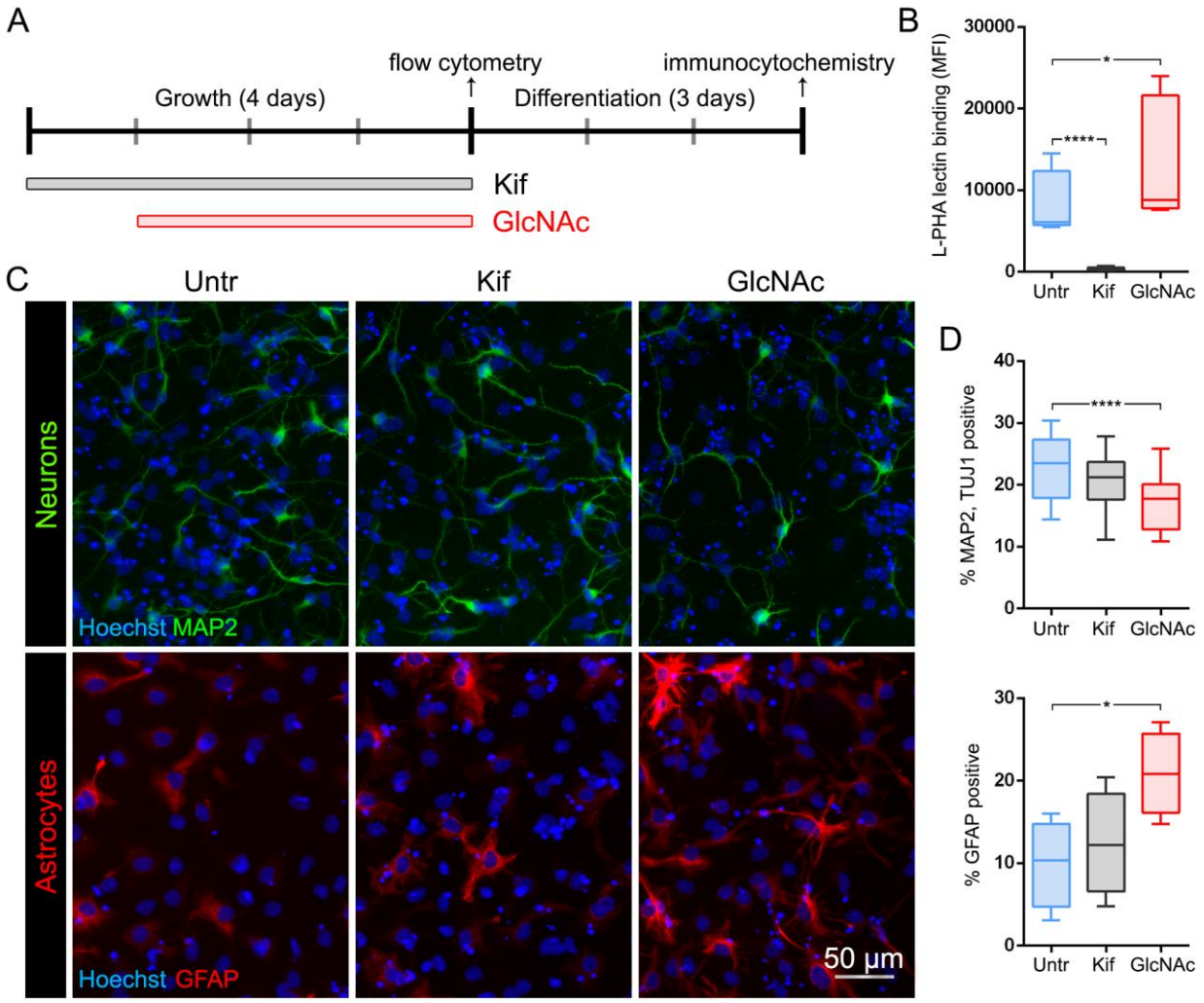

Figure 4.1. Kifunensine treatment abolishes expression of highly branched N-glycans but does not affect neuron and astrocyte differentiation. A) Schematic representing the experimental design. Undifferentiated E12 NSPCs in growth medium were treated with 0.5 µM Kif for 4 days or 80 mM GlcNAc for 3 days. After treatment, cells were either dissociated for lectin analysis by flow cytometry or allowed to differentiate for 3 days and analyzed by immunocytochemistry. B) Flow cytometry with L-PHA lectin (MFI, mean fluorescence intensity) indicated that N-glycan branching was significantly reduced by treatment with Kif ($p<0.0001$) and enhanced by GlcNAc treatment ($p=0.0154$) (one-way ANOVA, Dunnett's *post-hoc*, $N\geq3$, *$p<0.05$, ****$p<0.0001$). C) Control (Untr, untreated), Kif treated and GlcNAc treated E12 NSPCs were differentiated for 3 days and immunostained to detect neuron marker MAP2 or astrocyte marker GFAP. All nuclei were stained with Hoechst. D) Quantitation of cells co-expressing neuron markers MAP2 and TuJ1 indicates GlcNAc treatment significantly reduced formation of neurons ($p<0.0001$) while Kif treatment did not affect neuron formation. Quantitation of GFAP expressing cells indicates GlcNAc treatment significantly increased formation of astrocytes ($p=0.0173$) while Kif treatment did alter astrocyte generation (one-way ANOVA, Tukey's *post hoc*, $N\geq3$, *$p<0.05$, ****$p<0.0001$).

We tested whether Kif treatment affected differentiation of NSPCs by treating undifferentiated E12 mouse NSPCs with Kif for 4 days then removing Kif and allowing the cells to differentiate. As a comparison, we treated undifferentiated NSPCs with 80 mM GlcNAc for 3 days to increase highly branched N-glycans then removed GlcNAc and differentiated the cells. As we found previously, NSPCs treated with GlcNAc differentiated into significantly fewer neurons and more astrocytes compared to untreated controls (Fig 4.1) (*29*). In contrast, Kif-treated NSPCs demonstrated no change in neuron or astrocyte formation (Fig. 4.1, Supp. Fig. 4.S1C), indicating that disruption of MAN1 activity in E12 mouse NSPCs prior to differentiation did not affect generation of neurons or astrocytes.

We next tested whether Kif treatment would affect differentiation of mouse NSPCs from other developmental stages at which more astrocytes are normally formed. During development, NSPCs in the cortex switch from neurogenesis at early embryonic stages to astrogenesis at later stages. This developmental fate switch translates *in vitro* as NSPCs isolated from E12 cortices tend to generate more neurons than astrocytes when compared to NSPCs isolated from more mature developmental stages such as E16 (*31*). NSPCs *in vivo* express more highly branched N-glycans detected by L-PHA at later astrogenic stages, such as E16 and E18, than they do at earlier neurogenic stages, revealing a correlation between expression of highly branched N-glycans and astrogenesis (*29*). We hypothesized that Kif treatment might have a greater impact on cells that express higher levels of the highly branched N-glycans, such as E16 and E18 NSPCs. However, treatment of E16 and E18 NSPCs with 0.5 μM Kif did not significantly impact neuron or astrocyte formation (Supp. Fig. 4.S2). These data indicate that blocking MAN1 in the branching pathway did not affect generation of neurons or astrocytes from NSPCs at several stages of development.

One possibility to Kif treatment not showing any effect in our system could be due to the withdrawal of Kif during the differentiation process resulting in a rapid recovery of N-glycan branching on the cell surface. In another set of experiments, NSPCs were treated with either deoxymannojirimycin (DMJ) to inhibit MAN1 or swainsonine (SW) to block MAN2. NSPCs were treated prior to differentiation and throughout the process of differentiation to ensure disruption of the branching pathway in undifferentiated cells and in cells undergoing differentiation. There was no significant difference in the formation of either neurons or astrocytes from E12 or E16 NSPCs with these treatments (**E12 MAP2**: untreated 16.5% ± 0.8, DMJ 17.2% ± 1.8, SW 14.8% ± 1.0) (**E12 GFAP**: untreated 21.3% ± 3.2, DMJ 22.6% ± 3.3, SW 17.5% ± 3.7) (**E16 MAP2**: untreated 14.4% ± 0.8, DMJ 13.0% ± 1.6, SW 14.5% ± 1.0) (**E16 GFAP**: untreated 27.2% ± 2.6, DMJ 28.0% ± 2.1, SW 28.4% ± 1.4) (N≥3, all variation represent SEM). These data confirm the findings with Kif, showing that blocking enzymes in early steps of the N-glycan branching pathway does not alter NSPC differentiation into neurons or astrocytes *in vitro*.

Several glycosylation enzymes function downstream of MAN1, so we used lectin analysis to determine which N-glycan configurations were altered after Kif treatment. We performed flow cytometry on GlcNAc or Kif-treated E12 NSPCs using a variety of lectins that detect different N-glycan species (Fig. 4.2A). Treatment of E12 NSPCs with 80 mM GlcNAc increased cell surface levels of β1-4 and β1-6 branched N-glycans detected by lectins DSL and L-PHA without changing other N-glycan species (Fig. 4.2B). GlcNAc treatment thus specifically enhanced the formation of highly branched N-glycans generated by the glucosaminyltransferases MGAT4 and MGAT5. In contrast to the specificity of GlcNAc treatment for highly branched N-glycans, Kif treatment induced shifts in 6 out of the 7 N-glycan species analyzed. E12 NSPCs

treated with Kif had reduced levels of β1-4 branches (DSL), β1-6 branches (L-PHA), bisected branches (E-PHA) and core fucose (LCA) and increased levels of high mannose (ConA) and poly-lactosamine (LEA) (Fig. 4.2C). Terminal sialic acid residues (SNA) were not significantly changed (Fig. 4.2C). Kif treatment therefore induces widespread changes to the cell surface N-glycan landscape that includes, but is not limited to, the highly branched N-glycans.

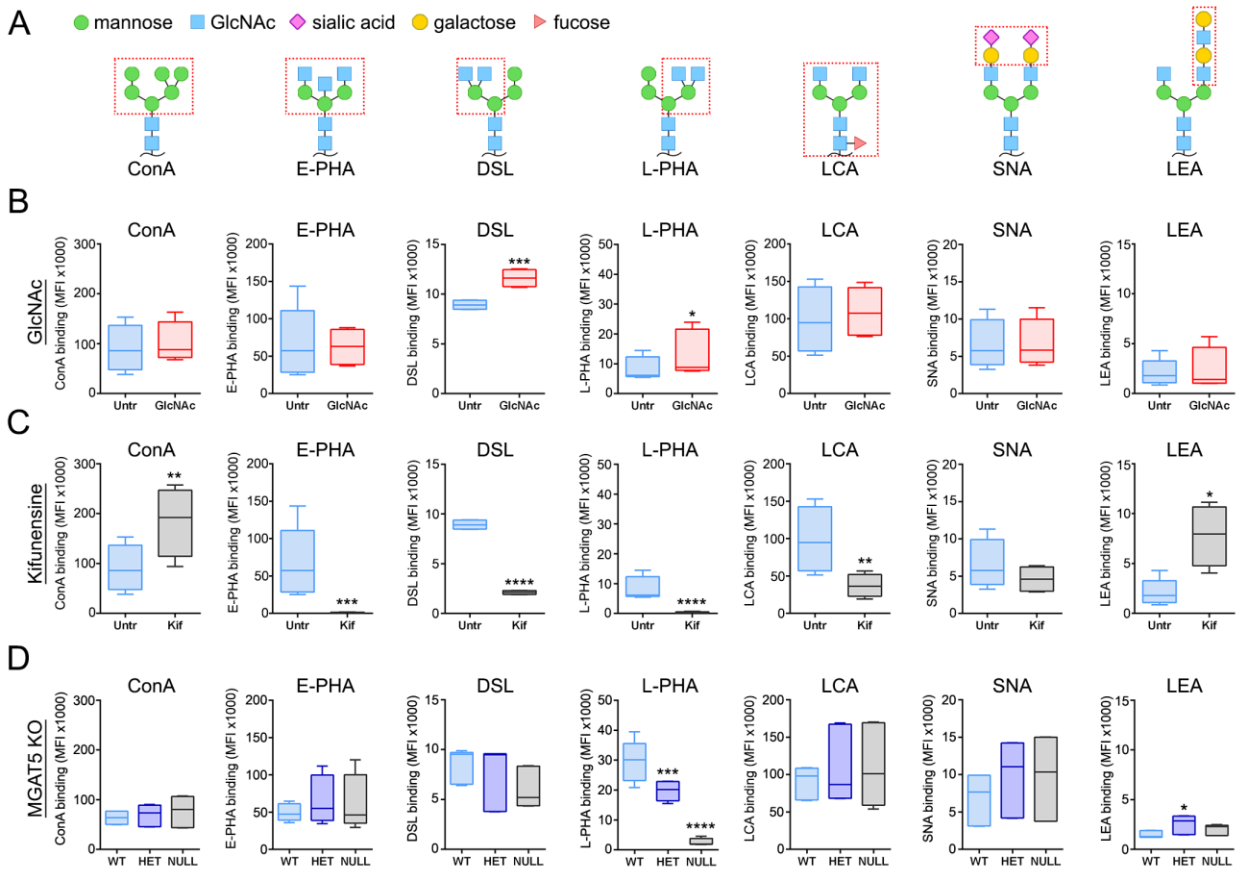

Figure 4.2. Changes to the N-glycan landscape of NSPCs after treatment with GlcNAc, Kifunensine, or genetic disruption of MGAT5. A) Schematic diagrams of N-glycan structures in which symbols denote particular sugar moieties. Boxed regions indicate structures recognized by the listed lectins: concanavalin concanavalin A (ConA), Phaseolus vulgaris erythroagglutinin (E-PHA), Datura stramonium lectin (DSL), Phaseus vulgaris leucoagglutinin (L-PHA), Lens culinaris agglutinin (LCA), Sambucus nigra agglutinin (SNA), Lycopersicon esculentum agglutinin (LEA). B) E12 NSPCs treated with 80 mM GlcNAc expressed significantly more branched N-glycans detected by DSL ($p=0.0001$) and L-PHA ($p=0.0154$) lectins compared to untreated controls (one-way ANOVA followed by Tukey's post hoc test, $N\geq3$, *$p<0.05$, ***$p<0.001$). C) E12 NSPCs treated with 0.5 μM Kif expressed higher levels of N-glycans that

bind to lectins ConA ($p=0.0025$) and LEA ($p=0.04$), but lower levels of those that bind to lectins E-PHA ($p=0.0002$), DSL ($p<0.0001$), L-PHA ($p<0.0001$), and LCA ($p=0.0011$) Comparisons between Untr, GlcNAc, and Kif were carried out by one-way ANOVA followed by Dunnett's post hoc test, $N\geq3$, *$p<0.05$, **$p<0.01$, ***$p<0.001$, ****$p<0001$). D) E12 NSPCs from wild-type (WT), heterozygous (HET) and null (NULL) MGAT5 knockout mice were analyzed by lectin staining. Both heterozygous ($p=0.0004$) and null ($p<0.0001$) NSPCs exhibited lower levels of branched N-glycans detected by L-PHA compared to WT cells. Heterozygous NSPCs showed an increase in polylactosamine detected by LEA ($p=0.0192$) (one-way ANOVA followed by Dunnett's post hoc test, $N\geq3$, *$p<0.05$, ***$p<0.001$, ****$p<0001$).

4.3.2 MGAT5 knockout specifically blocks the production of highly branched N-glycans

Enhanced N-glycan branching drives NSPC differentiation towards astrocytes at the expense of neurons (*29*), but blocking the MAN1 enzyme, which is early in the branching pathway, did not affect NSPC fate potential (Fig. 4.1, Supp. Fig. 4.S2). The balance of highly branched N-glycans and other N-glycan species generated by enzymes downstream of MAN1 may be important for NSPC fate. We previously reported that astrocyte-biased NSPCs expressed higher levels of *Mgat5,* whereas neuron-biased NSPCs have higher levels of *Mgat3* , which produces a bisected N-glycan (*29*). Furthermore, bisected N-glycans were upregulated on neurons and downregulated on astrocytes differentiated from neural stem cells derived from pluripotent stem cells (*20*). Taken together, a balance between branched N-glycans and bisected N-glycans may impact fate decisions made by NSPCs. It may be that Kif treatment does not change NSPC fate because intermediate structures such as the bisected N-glycan produced by MGAT3, are lost with Kif disruption of MAN1 (Fig. 4.2C). Therefore, we sought an alternative model to reduce N-glycan branching without changing the activity of other N-glycan remodeling enzymes.

We obtained a genetic mouse model containing a *lacZ* gene insert within the *Mgat5* coding region (*32*). This mutation disrupts generation of the functional MGAT5 enzyme, which is responsible for the addition of a β1-6 modified GlcNAc branch to the tri-mannosyl core of an

N-glycan. The activity of this enzyme is selectively upregulated in the presence of excess GlcNAc (*21*), causing an increase in highly branched tetra-antennary N-glycans (*21, 29*). We mated heterozygous (having only one disrupted *Mgat5* allele) animals to generate wild type (WT), heterozygous (het) and null (lacking both *Mgat5* alleles) littermates, genotyped each embryo, and isolated E12 cortical NSPCs from the forebrain of each embryo.

We analyzed E12 MGAT5 WT and mutant NSPCs with lectins to assess any changes to the cell surface N-glycan landscape. Binding of L-PHA, which detects the β1-6 N-glycan branch, was reduced in the het cells and virtually abolished in the MGAT5 null NSPCs (Fig. 4.2D). There was a slight increase in poly-lactosamine, detected by lectin LEA, on het NSPCs (Fig. 4.2D). Binding of the other lectins to WT, het, and null NSPCs was relatively similar (Fig. 4.2D). These data indicate that the main change to the N-glycan landscape of the MGAT5 mutant NSPCs is reduced N-glycan branching with few changes to other N-glycan configurations. Thus, the MGAT5 knockout model provides an opportunity to decipher the contributions of highly branched N-glycans to NSPC fate without confounding changes to other N-glycan structures.

4.3.3. MGAT5 deficiency *in vivo* alters embryonic cortical neurogenesis

Changes in glycosylation patterns occur during brain development (*7*), and we found that N-glycan branching increases between E12 and E18 in the VZ/SVZ, where NSPCs reside (*29*). MGAT5 null animals appear grossly normal (*24*, *32*), but exhibit behavioral abnormalities, including failure to nurture pups (*24*) and decreased depressive-like behaviors (*33, 34*). MGAT5 knockout animals may have altered neural development that leads to later behavioral deficits. We investigated whether MGAT5 deficiency decreases highly-branched N-glycans in the mouse brain. We stained E16 brain sections with L-PHA lectin and found a decrease in signal intensity

in the het brain and a marked reduction in signal in null animals (Supp. Fig. 4.S3). These data, coupled with the lectin analysis of NSPCs from WT, het, and null animals, confirm that loss of MGAT5 causes a specific and significant decrease in highly branched N-glycans in the brain.

Since increasing highly branched N-glycans with GlcNAc treatment of NSPCs lead to a decrease in neuron formation (*29*), we tested whether loss of highly branched N-glycans might alter neuron generation in the brain. We analyzed neurons in embryonic (E16) coronal brain sections by immunostaining for class III beta tubulin (TuJ1, detects all neurons) or NeuN (detects mature neurons). There was a notable increase in class III beta tubulin and NeuN expression in MGAT5 null cortex (Fig. 4.3A, B). We quantified NeuN-positive cells in the cortical plate, where differentiated neurons reside, of WT and null animals and found a significant increase in the percentage of NeuN-positive cells at 3 locations across the cortex: medial, dorsal, and lateral (Fig. 4.3C, D). There was a significant increase in the number of NeuN-positive cells per mm^2 in the dorsal cortical plate (Fig. 4.3D). We tested whether there might be a defect in neuronal migration by measuring NeuN signal in the intermediate zone (IZ), which contains newly born and migrating neurons, and VZ/SVZ, which is the NSPC niche. Very few NeuN-positive cells were detected in the IZ and VZ/SVZ and there was no difference across the genotypes, indicating that MGAT5 depletion did not alter neuronal migration (Supp, Fig. 4.4). Our data show that a higher proportion of cells in the cortical plate express the mature neuronal marker NeuN in MGAT5 null animals.

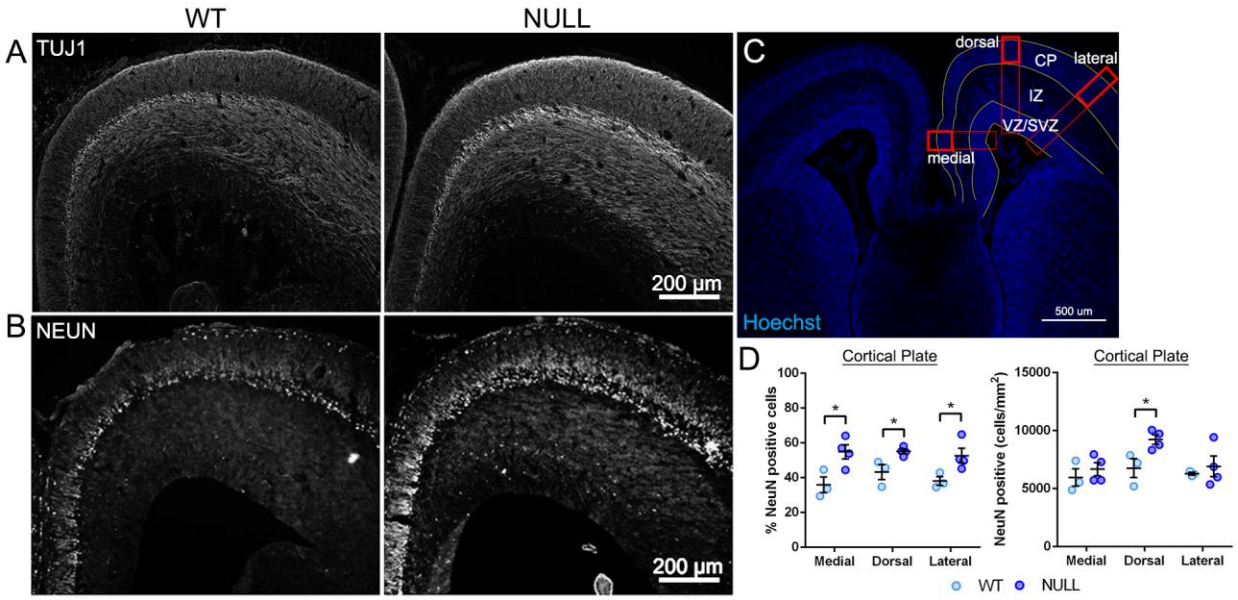

Figure 4.3. MGAT5 deficiency leads to enhanced neuron production in the developing embryonic cerebral cortex. A) E16 coronal sections of wild-type (WT) and homozygous null brains were immunostained with TuJ1 to detect the neuronal marker class III beta tubulin. Greater TuJ1 signal was evident in the null brain compared to the WT brain. B) E16 coronal sections of WT and NULL brains were immunostained to detect the mature neuronal marker NeuN. NeuN expression is be enhanced in the cortical plate (CP) of the MGAT5 null brain. C) Quantification paradigm schematized on a WT E16 coronal section of dorsal forebrain stained with Hoechst. Yellow lines indicate the separation of cortical plate (CP), intermediate zone (IZ), and ventricular zone/sub-ventricular zone (VZ/SVZ) regions. The red boxes indicate slices from medial, dorsal, and lateral regions of the cortex and the bolded red boxes show cortical plate regions for analysis. D) NeuN signal was quantified in E16 brain sections as either the percentage of NeuN expressing cells or the number of NeuN expressing cells per mm^2 in the cortical plate. MGAT5 null brains displayed a significant increase in the percentage of NeuN positive cells in the cortical plate compared to WT brains in medial, dorsal, and lateral regions (Student's t-test WT vs. null; medial, p=0.027; dorsal, p=0.0291; lateral, p=0.049). Similarly, MGAT5 null cortices displayed significantly increased NeuN cells per mm^2 in the dorsal cortical plate (two-tailed Student's t-test WT vs. null, p=0.0310) (N≥3) (*p<0.05)

We analyzed the number of cells and thickness of the embryonic cortex to determine whether the increase in NeuN-positive cells in MGAT5 null animals changed either of these measures. Analysis of the cortex as a whole, which included the cortical plate (CP), IZ, and VZ/SVZ, indicated that there were decreases in the cells/mm^2 in lateral cortex, decreases in thickness of lateral and dorsal cortex, and decreases in the total number of cells in lateral and dorsal cortex in MGAT5 null animals (Fig. 4.4). In the CP, loss of MGAT5 caused decreases in

cells/mm^2 in lateral and medial CP, decreases in thickness of lateral and dorsal CP, and decreases in the total number of cells in lateral, dorsal, and medial CP (Fig. 4.4). The IZ of MGAT5 null animals had decreased cells/mm^2 in lateral IZ but an increase in medial IZ, decreased thickness of lateral and dorsal IZ, and decreased total number of cells in lateral IZ (Fig. 4.4). Lastly, analysis of the VZ/SVZ indicated decreases in cells/mm^2 in lateral and dorsal VZ/SVZ, no change in thickness, and decreases in the total number of cells in lateral and dorsal VZ/SVZ (Fig. 4.4). Overall, the number of cells and thickness is decreased in the MGAT5 null brain compared to the WT brain. These data suggest that the increase in NeuN-positive cells could be due to a more rapid neuronal differentiation into neurons expressing mature markers that does not lead to an overall increase in neuron numbers. We assessed this further by analyzing markers of neuronal layers in the embryonic cortex.

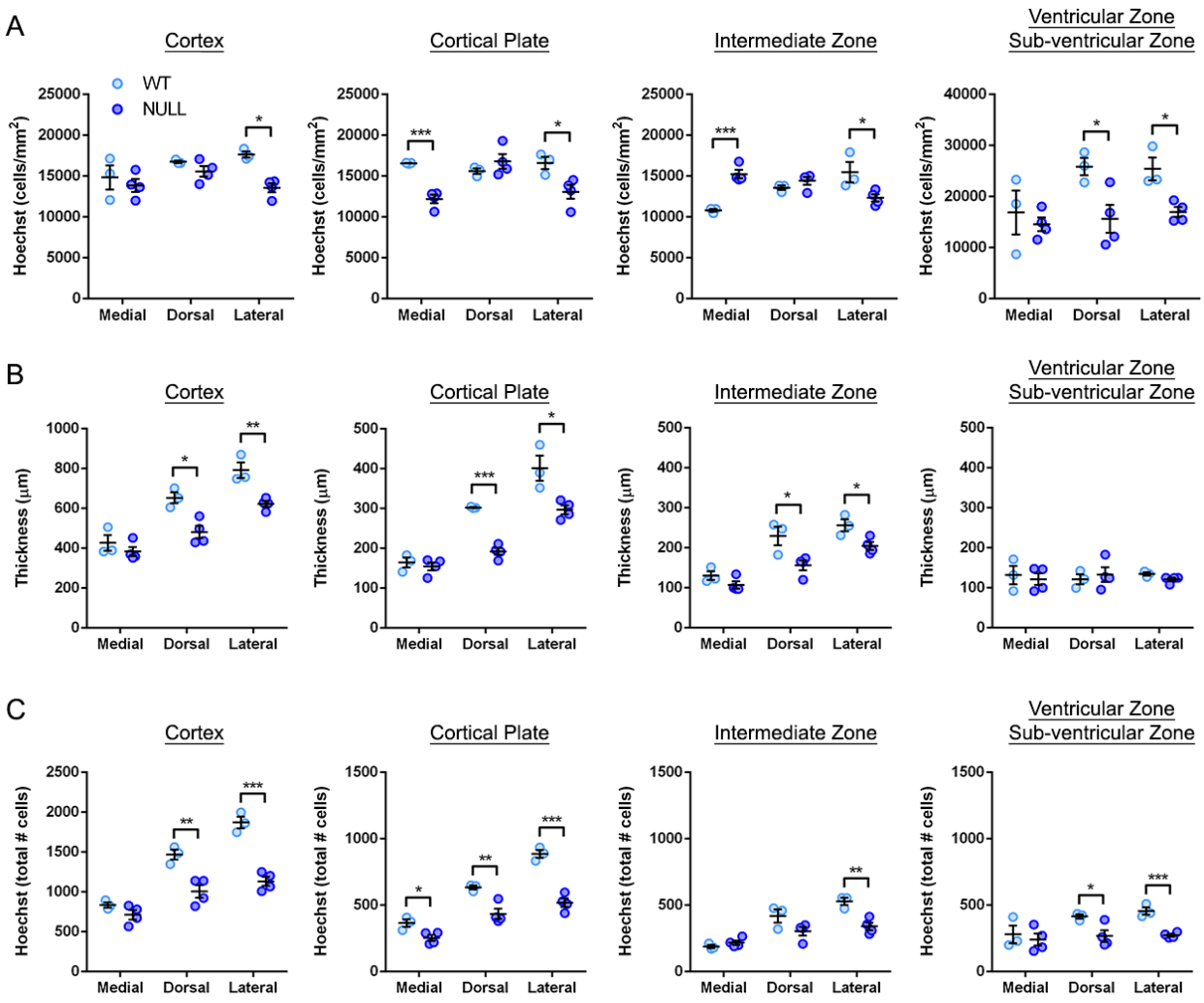

Figure 4.4. Embryonic MGAT5 null brains display decreased cell numbers and cortical thickness. A) The number of cells per mm^2 detected by Hoechst staining was quantified across the total cortex (combined CP, IZ, and VZ/SVZ) and in the CP, IZ, and VZ/SVZ individually. The number of cells per mm^2 was significantly decreased in the null lateral cortex (p=0.0025), medial (p=0.0009) and lateral (p=0.0318) CP, lateral (p=0.0442) IZ, and dorsal (p=0.0343) and lateral (p=0.0119) VZ/SVZ compared to WT. In contrast, MGAT5 null medial (p=0.0009) IZ shows higher cell density than WT. All data were analyzed by two-tailed Student's t-test WT vs. null, N≥3, *p<0.05, **p<0.01, ***p<0.001. B) The thickness of the total cortex (combined CP, IZ, and VZ/SVZ) and the CP, IZ, and VZ/SVZ individually was measured. The MGAT5 null brains were reduced in thickness across the dorsal (p=0.0105) and lateral (p=0.0062) total cortex, the dorsal (p=0. 0.0001) and lateral (p=0.0172) CP, and the dorsal (p=0.0300) and lateral (p=0.0286) IZ compared to WT. No change in VZ/SVZ thickness was observed between WT and null brains. All data were analyzed by two-tailed Student's t-test WT vs. null, N≥3, *p<0.05, **p<0.01, ***p<0.001. C) The total cell number was quantified as the total number of Hoechst-stained cells in the cortex (combined CP, IZ, and VZ/SVZ) and in the CP, IZ, and VZ/SVZ individually. The total number of cells was significantly reduced in the MGAT5 null dorsal (p=0.0081) and lateral (p=0.0004) total cortex, medial (p=0.0246), dorsal (p=0.0083), and lateral

(p=0.0005) CP, lateral (p=0.0058) IZ, and dorsal (p=0.0369) and lateral (p=0.0009) VZ/SVZ compared to WT. All data were analyzed by two-tailed Student's t-test WT vs. null, N≥3, *p<0.05, **p<0.01, ***p<0.001.

4.3.4 Embryonic neuronal layers in MGAT5 deficient cortices

The cortex is composed of intricately patterned layers of neurons. During development, the deep neuronal layers are formed first and the upper layers follow. Perturbations to early developmental processes can alter the formation of cortical layers. We investigated whether neuronal layering was impacted by staining E16 brains for the upper layer marker BRN2 and deep layer markers CTIP2 and TBR1 (Fig. 4.5A). Neurogenesis occurs in a gradient during development with maturation beginning laterally and moving to dorsal then medial regions. Since the medial region could include the newly developing hippocampus, we focused analyses on dorsal and lateral regions. BRN2-positive neurons were not present laterally at E16 so we focused on dorsal regions to assess upper layers and found no significant difference in the number of BRN2-positive cells per mm^2 in MGAT5 null CP (Fig. 4.5B). There was not a significant difference in the deep layer marker CTIP2 in dorsal or lateral regions, but TBR1-positive deep layer neurons were significantly decreased in the MGAT5 null CP (Fig. 4.5B, Supp. Fig. 4.5). The reduction in TBR1-neurons was consistent with the decrease in the total number of cells observed in the MGAT5 null CP (Fig. 4.4). Since TBR1 labels some of the earliest born neurons, further analysis of neuronal layers would best be carried out at a later developmental stage, such as P7. The reduction of cells in the cortical plate and the decreases in TBR1-positive neurons could be due to a change in progenitor cells in the VZ/SVZ.

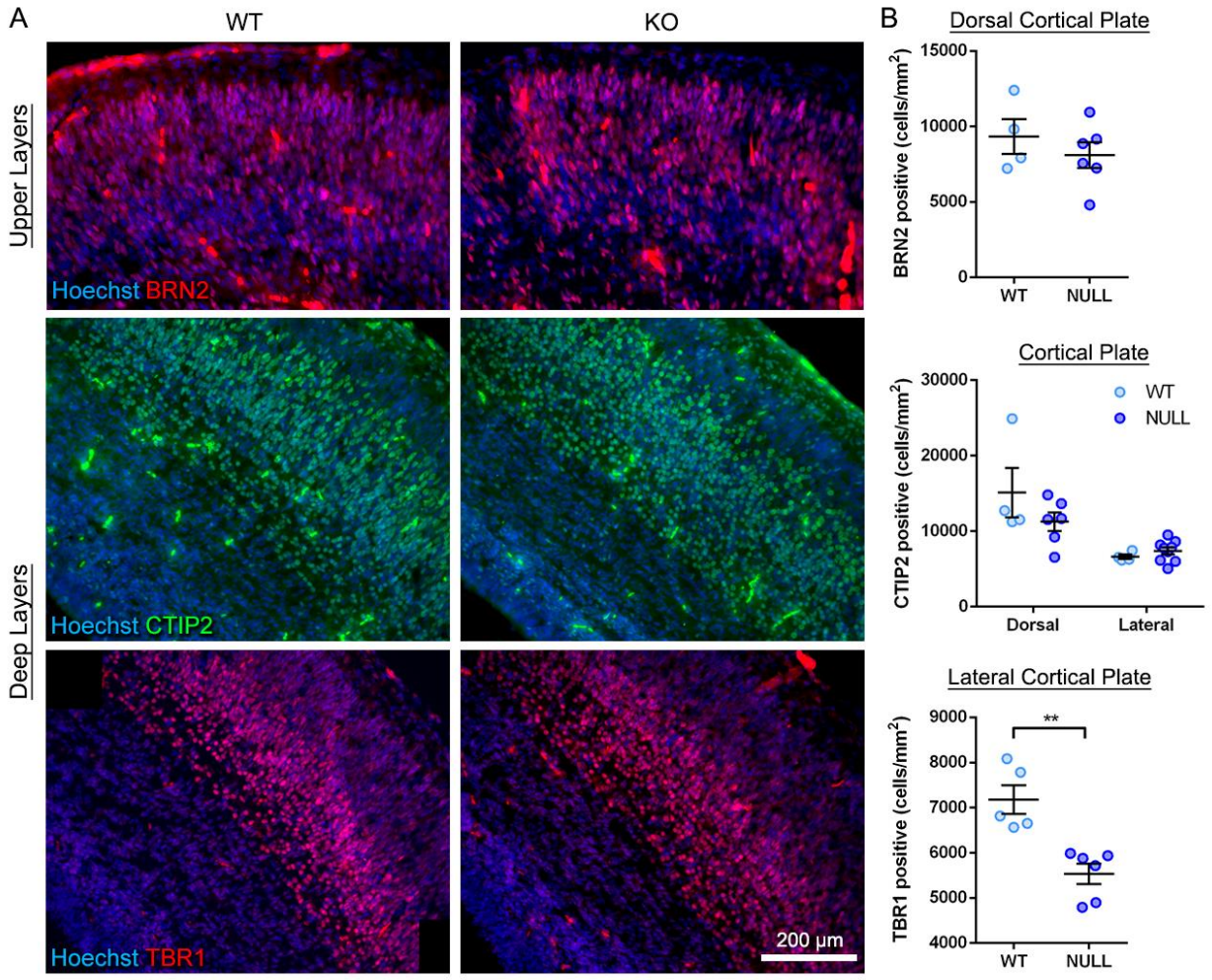

Figure 4.5. Loss of MGAT5 causes a decrease in deep layer neurons that is visible at embryonic stages. A) E16 brain cortices were immunostained to detect upper layer neuron marker BRN2 in the dorsal cortex and deep layer neuron markers CTIP2 (layers 5/6) and TBR1 (layer 6) in the lateral cortex. All nuclei counterstained with Hoechst. B) There was no significant difference in the upper layer marker BRN2 or the deep layer 5/6 marker CTIP2 in the cortical plate between WT and null brains. However, TBR1-positive layer 6 neurons were significantly reduced ($p=0.0018$) in the MGAT5 null cortical plate. All data were analyzed by two-tailed Student's t-test WT vs. null, $N \geq 3$, $^{**}p<0.01$.

4.3.5 MGAT5 deficiency depletes a subset of neural progenitors in the embryonic VZ/SVZ

We identified significant decreases in cell numbers in the MGAT5 null cortex, including a significant reduction in cells in the VZ/SVZ (Fig. 4.4). These data could suggest a depletion of NSPCs in the VZ/SVZ. In order to test whether the reduced cells in the VZ/SVZ could be due to lower levels of proliferation in MGAT5 null animals, we measured levels of Ki67-positive

proliferating cells in E16 VZ/SVZ. We found no difference in Ki67 expression in the WT and null VZ/SVZ (Fig. 4.6A), indicating that lower cell numbers were not due to a decrease in proliferation. We assessed progenitors in the VZ/SVZ using three markers: SOX2, a neural stem cell and progenitor cell marker, TBR2, a neuron progenitor marker, and BRN2, a marker of upper layer neuron progenitors. SOX2 labeled cells along the VZ and showed no significant differences between WT and null animals (Fig. 4.6B). TBR2-positive cells were less likely to be adjacent to the ventricle and there was no difference in these cells between WT and null brains (Fig. 4.6C). BRN2 is expressed by progenitor cells in the VZ/SVZ and is critical for instructing upper layer neuron identity (*35*). There was a significant decrease in the percentage of BRN2-positive cells and in the total number of BRN2-positive cells in the VZ/SVZ of MGAT5 null animals (Fig. 4.6D). The progenitor cell data suggest that MGAT5 deficiency does not alter NSPC proliferation but may decrease some progenitors. This could reflect depletion of the progenitor pool that could cause a reduction in neuron numbers in the cortex. Since TBR1-positive deep layer neurons and BRN2-positive progenitors were reduced in MGAT5 null brains at E16, we assessed upper and deep layer neurons at postnatal stages after neurogenesis is complete.

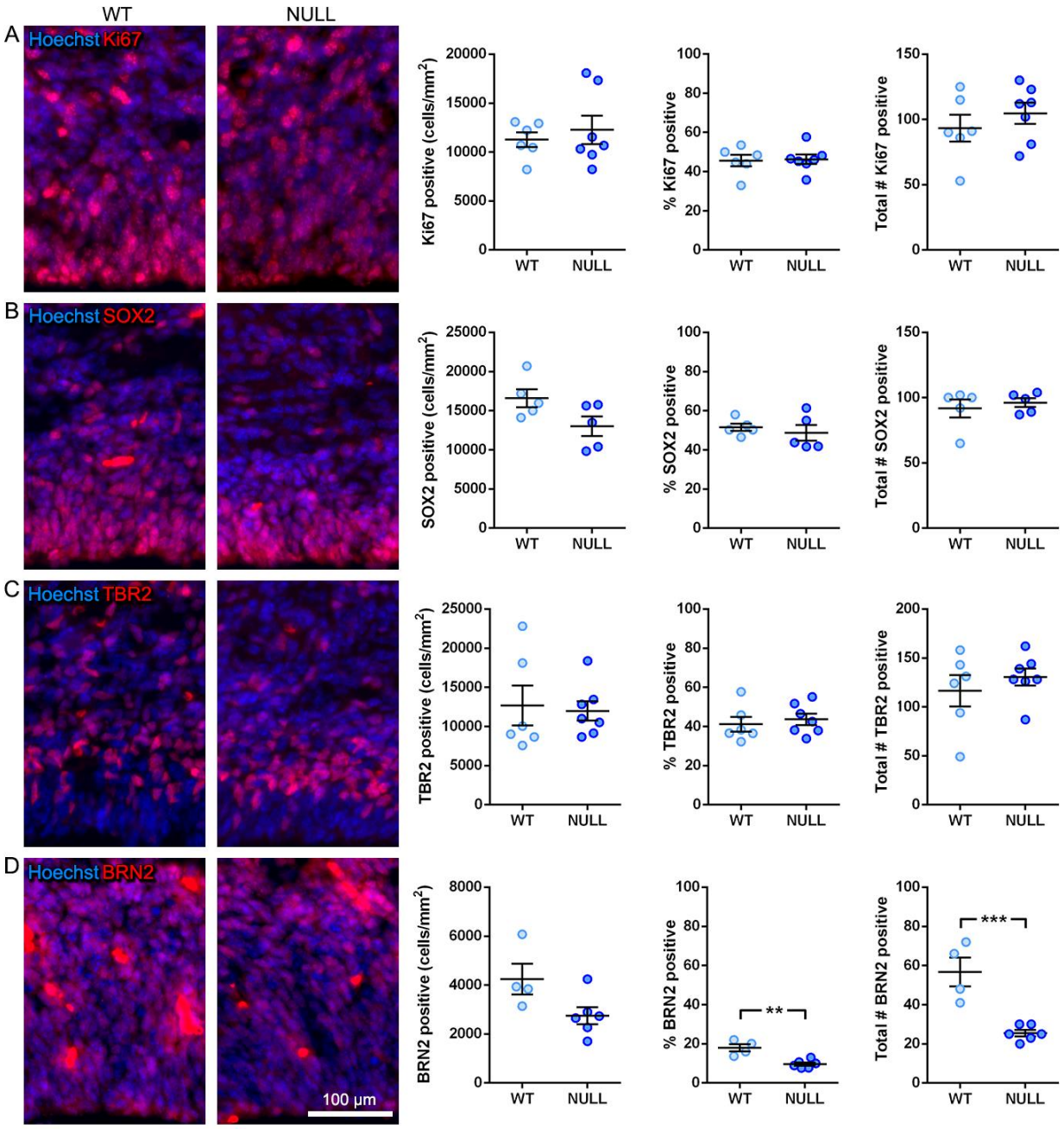

Figure 4.6. MGAT5 deficiency does not affect proliferation of progenitors in the VZ/SVZ at embryonic stages but does cause a decrease in certain progenitor populations. A) MGAT5 WT and null E16 brains were immunostained to detect Ki67, a marker of proliferating cells. Quantitation of signal in the lateral cortical region showed no difference in Ki67 labeling in the VZ/SVZ between WT and null brains. B) SOX2 immunostaining of E16 WT and null brains showed a slight but non-significant decrease (p=0.0693) in density of SOX2-positive cells in the VZ/SVZ and no difference in the percentage or total number of SOX2-positive cells between the samples. C) Analysis of TBR2, an intermediate progenitor marker, indicated no difference in TBR2-positive cells between WT and MGAT5 null VZ/SVZ regions. D) Immunostaining to detect BRN2, a marker of upper layer neuron progenitors, showed a non-significant decrease

($p=0.0537$) in cells/mm^2, a significant decrease in percentage of positive cells ($p=0.0019$) and in total number of positive cells ($p=0.0009$) in the VZ/SVZ. All nuclei were counter-stained with Hoechst and all data were analyzed by were two-tailed Student's t-test WT vs. null, $N\geq3$, $^{**}p<0.01$, $^{***}p<0.001$.

4.3.6 Neuronal layering and architecture are altered in postnatal MGAT5 deficient brains

We assessed neurons in the WT and MGAT5 null postnatal (P7) brain using a pan-neuronal marker of mature neurons, NeuN, and markers for upper (BRN2) and deep (CTIP2) layer neurons. There was a non-significant increase in the percentage and number of NeuN-positive cells in the MGAT5 null cortical plate compared to WT, suggesting that neuronal maturation in the WT animals is catching up to that of the null animals at this stage (Fig. 4.7A, B). Analysis of BRN2 staining revealed that MGAT5 null animals have a significant reduction in the number of upper layer neurons at P7 (Fig. 4.7 C, D). The deep layer marker CTIP2 showed a similar significant decrease in deep layer neurons in MGAT5 null animals when compared to WT (Fig. 4.7 C, D). We wondered whether upper and deep layers were equally impacted by the loss of MGAT5. To test whether there might be a difference relative to each other, we generated a ratio of the number of deep to upper layer neurons for WT and MGAT5 null brains. There was a significant increase in the CTIP2:BRN2 ratio in null animals compared to WT, suggesting that upper layer neurons were disproportionately affected during development of MGAT5 null brains (Fig. 4.7E).

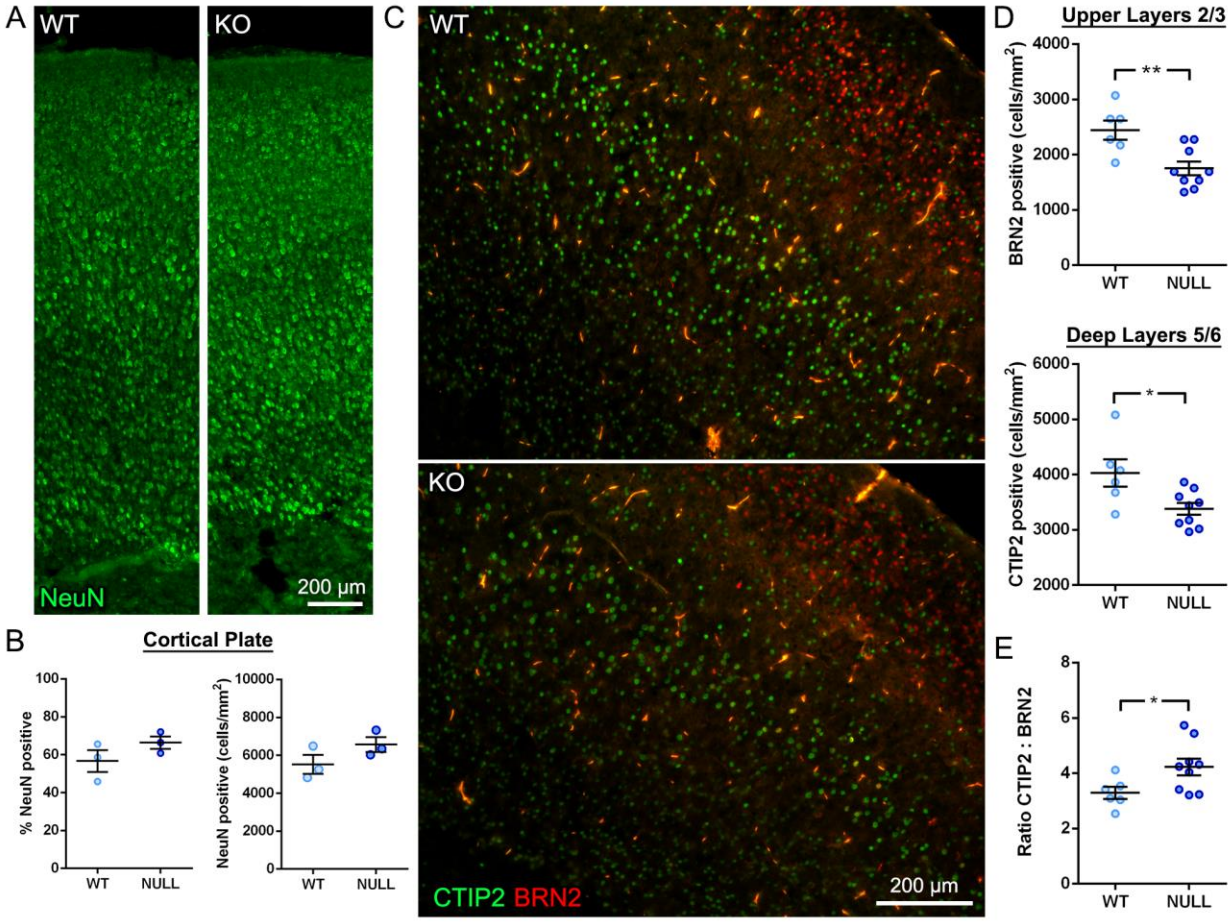

Figure 4.7. At postnatal stages, mature neurons are similar in WT and MGAT5 null brains, but decreases in upper and deep layer neurons are evident in animals lacking MGAT5. A) P7 coronal sections of WT and MGAT5 null brains were immunostained to detect NeuN. Sections are from lateral cortical regions, somatosensory cortex in the anterior portion of the forebrain, and show the cortical plate. B) The percentage of NeuN expressing cells and number of NeuN positive cells per mm^2 showed a non-significant increase in MGAT5 null cortical plate compared to WT. C) Coronal sections of P7 WT and MGAT5 null brains were immunostained to detect the upper layer neuron marker BRN2 and the deep layer neuron marker CTIP2 to assess cortical layers in the postnatal brain. D) BRN2-positive upper layer neurons were significantly reduced ($p=0.0053$) in MGAT5 null cortical plate at P7 compared to WT. Deep layer neurons detected by CTIP2 labeling were also significantly reduced ($p=0.0187$) in the MGAT5 null brain compared to WT. E) The ratio of CTIP2:BRN2 indicates that upper layer neurons were more affected than deep layer neurons in MGAT5 null brains. There was a significant increase ($p=0.0408$) in the ratio of CTIP2:BRN2 in the MGAT5 null brain compared to WT. All data were analyzed by two-tailed Student's t-test WT vs. null, N=3, *$p<0.05$, **$p<0.01$.

We analyzed cell numbers and thickness of the P7 WT and MGAT5 null cortical plate.

The number of cells per mm^2 in upper (layers 2/3) and deep (layers 5/6) cortical layers were

significantly lower in MGAT5 null animals compared to WT (Fig. 4.8A). We analyzed cortical plate thickness from the pia surface to the corpus callosum and found significantly reduced thickness in MGAT5 null brains (Fig. 4.8B). Analysis of layer thickness revealed that layer 2/3 and 4 thickness did not differ between WT and null but there was a significant decrease in the thickness of layer 5/6 in the MGAT5 null brain compared to WT (Fig. 4.8B). The reduction in cell numbers in MGAT5 null compared to WT is consistent with the reduction in BRN2 and CTIP2 upper and lower neuronal layer markers (Fig. 4.7). Collectively, the data suggest that loss of MGAT5 leads to earlier neuronal differentiation but an overall reduction in the number of neurons in the cortex.

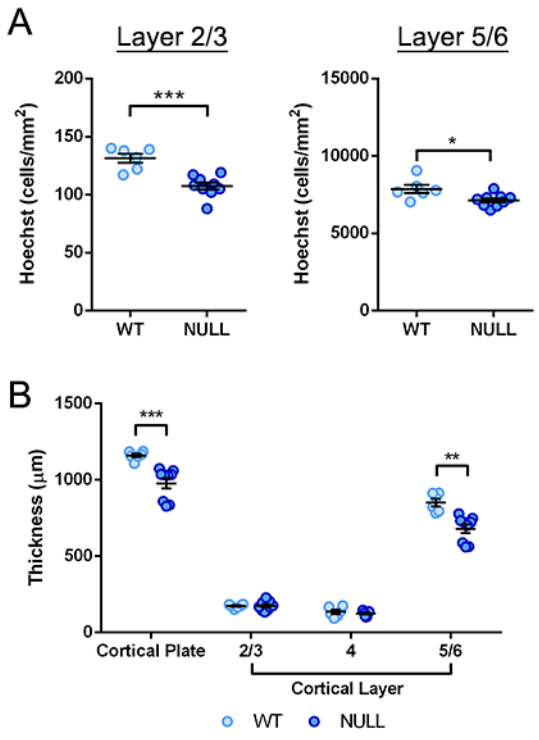

Figure 4.8. The postnatal MGAT5 null cortical plate has lower cell density and reduced cortical thickness. A) The number of cells per mm^2 were significantly reduced in layers 2/3 ($p=0.0003$) and layers 5/6 ($p=0.0189$) in MGAT5 null cortical plate compared to WT. B) Cortical plate thickness, measured from the pial surface to the corpus callosum and encompassing all cortical layers, was significantly reduced ($p=0.011$) in the MGAT5 null brain.

The reduction in thickness is primarily due to significantly reduced ($p=0.0009$) thickness in layers 5/6 rather than a change in layers 2/3 or layer 4. All data were analyzed by two-tailed Student's t-test WT vs. null, N=3, *$p<0.05$, **$p<0.01$, ***$p<0.001$)

Generation of neurons during development impacts neuron number in the cortex, but this measure is also regulated by pruning mechanisms in which unnecessary neurons undergo apoptosis to ensure correct neuron number and neuronal connectivity throughout the cortex. We tested whether the reduced number of neurons in the MGAT5 null cortex could be due to neuronal apoptosis by staining for cleaved Caspase-3. There was no difference in the number of cells labeled with cleaved Caspase-3 between WT and null brains (Supp. Fig. 4.S6) and the distribution of labeled cells in the cortical layers was also similar (data not shown). These data indicate that the reduced neuron numbers in the postnatal MGAT5 null cortex are not due to increased neuronal apoptosis.

We found in previous studies that enhancing highly branched N-glycans on NSPCs lead to increased generation of GFAP-positive astrocytes in culture (*29*). Therefore, we hypothesized that loss of branching in MGAT5 null mice may cause a decrease in GFAP-positive astrocytes in the brain. GFAP labels astrocytes in the CNS that are more mature or are reactive and GFAP-positive astrocytes were not present in E16 or P1 brain tissue (data not shown). GFAP-positive cells were detected in P7 brains and were mostly restricted to regions near the pial surface of the medial, cingulate cortex and the white matter tracts of the external capsule, cingulum, and corpus callosum (Supp. Fig. 4.S7A). We quantified GFAP-positive signal near the pial surface of the cingulate cortex along the midline (Supp Fig. 4.7B) and found a non-significant reduction in GFAP-positive cells in the MGAT5 null brain (Supp. Fig. 4.S7C).

4.3.7 NSPCs deficient in MGAT5 differentiate into more neurons and fewer astrocytes *in vitro*

In order to more specifically assess the effects of MGAT5 on NSPCs, we established cultures of these cells from WT, het and null embryonic (E12) cerebral cortices. We found previously that enhanced N-glycan branching induced by GlcNAc reduces generation of neurons from E12 NSPCs and boosts astrocyte formation (*29*). We differentiated MGAT5 WT, het and null NSPCs and used neuronal and glial markers to assess cell phenotype. E12 MGAT5 het and null cells formed significantly more neurons expressing MAP2 and TuJ1 compared to WT NSPCs (Fig. 4.9A, B). MGAT5 null NSPCs generated significantly fewer GFAP-positive astrocytes compared to WT cells (Fig. 4.9A, B). We assessed oligodendrocyte generation although NSPCs isolated from the developing E12 cortex generate few oligodendrocytes *in vitro* and most cortical oligodendrocytes derive from the ganglionic eminence (*29, 36, 37*). There was no difference in the formation of O4-positive oligodendrocytes among WT, het and null NSPCs (Supp. Fig. 4.S8). The NSPC culture experiments show that loss of MGAT5 leads to enhanced neuron differentiation and reduction in the formation of GFAP-positive astrocytes.

We assessed whether MGAT5 WT, het and null NSPCs differed in cell viability or proliferation since these could impact differentiation into neurons or astrocytes. There was no difference in cell viability of WT, het and null NSPCs (Fig. 4.9C). NSPC proliferation was analyzed by multiple assays. Ki67 labels all cycling cells and we found no difference in Ki67 labeling of control and mutant cells (Fig. 4.9D), which was consistent with the fact that we saw no difference in Ki67 *in vivo* labeling between WT and null brains (Fig. 4.6A). We utilized EdU incorporation to measure cells in S-phase and found a significant increase in labeling of null cells compared to WT or het NSPCs (Fig. 4.9D). We assessed cells in M-phase by measuring the

percentage of cells expressing phosphorylated histone H3 (phospho-histone H3) and found no difference among WT, het and null cells (Fig. 4.9D). Since there was a difference in one marker of proliferation in the null cells but not others, we performed cell cycle analysis by flow cytometry utilizing propidium iodide labeling of nuclear content to measure all stages of the cell cycle in the same population of cells. There was no significant differences in the percentages of cells in G_0/G_1, S, or G_2/M phases across genotype (Fig. 4.9E). Taken together, these data suggest that the viability and proliferative ability of MGAT5 deficient cells are similar to those of their WT counterparts.

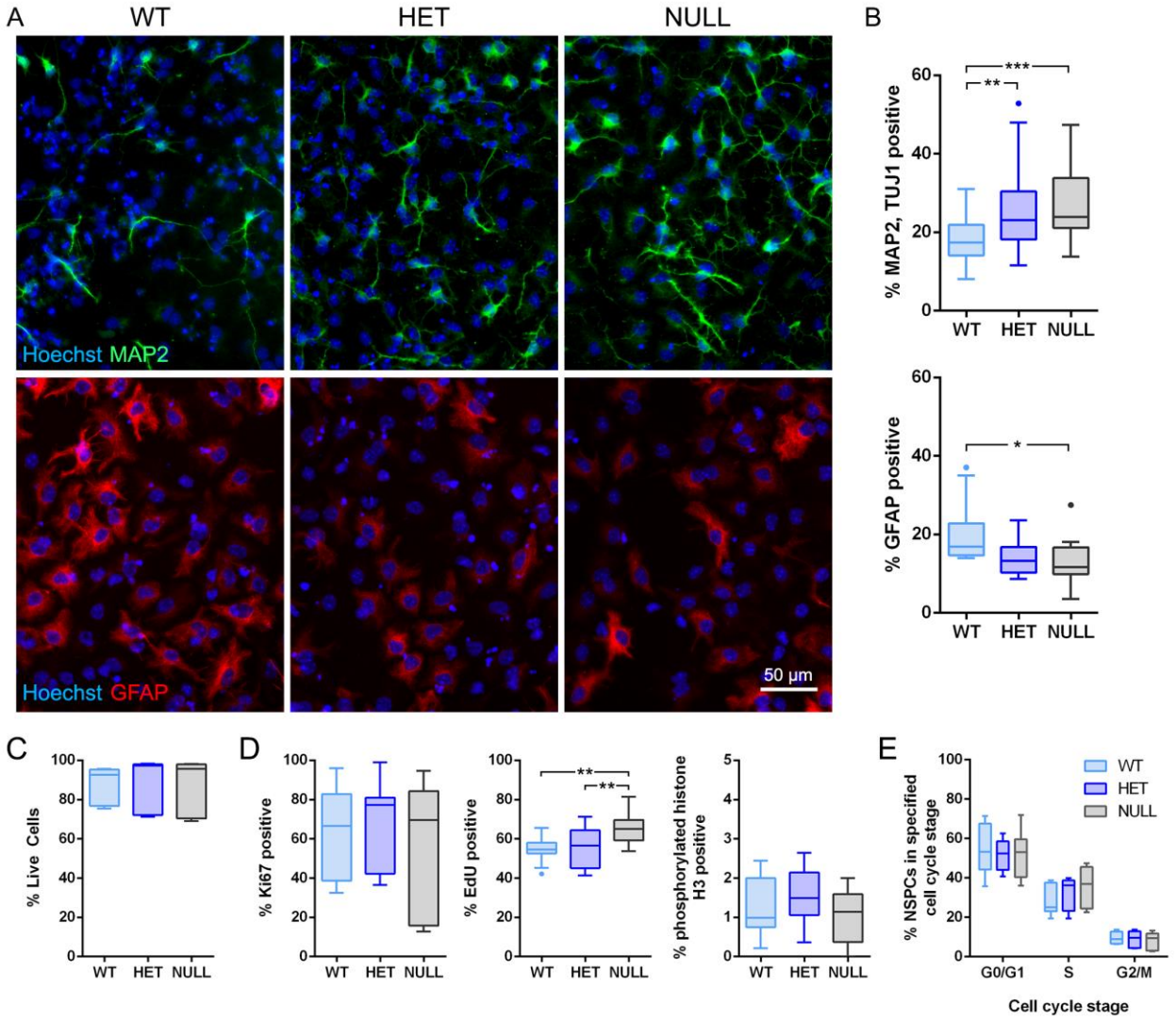

Figure 4.9. E12 NSPCs lacking MGAT5 generate more neurons and fewer GFAP-positive astrocytes *in vitro* and retain cell viability and proliferative ability. A) E12 NSPCs isolated from MGAT5 WT, het, and null cerebral cortices were differentiated and immunostained to detect neuron marker MAP2 or astrocyte marker GFAP. More MAP2-positive neurons formed in the het and null cell populations compared to WT while GFAP-positive cells were reduced in both the het and null cell populations. B) Quantitation of MAP2/TuJ1 co-expressing neurons shows a significant increase in neuron production from both het (p=0.0075) and null (p=0.00009) NSPCs compared to WT. The percentage of GFAP-positive astrocytes formed by null NSPCs was significantly reduced (p=0.0267) compared to WT NSPCs. C) Cellular viability was assessed by co-staining NSPCs with propidium iodide and calcein-AM and analyzing labeled cells by flow cytometry. No change in cell viability was detected between the WT and MGAT5 deficient het and null NSPCs. D) NSPC proliferation was measured by Ki67 (cells actively cycling, not in G_0), EdU (cells in S-phase), or phosphorylated histone H3 (cells in M-phase). No difference was observed among the NSPCs by Ki67 or phosphorylated histone H3 labeling. However, MGAT5 null NSPCs had significantly increased EdU incorporation compared to both WT and het NSPCs (null vs. WT, p=0.0021; null vs. het, p=0.0058). E) Cell cycle analysis by

propidium iodide labeling and flow cytometry revealed no difference in the proportion of cells in G_0/G_1, S, or G_2/M phase among WT, het, and null NSPCs. All data were analyzed by one-way ANOVA followed by Tukey's *post hoc* test, N≥3, *p<0.05, **p<0.01, ***p<0.001.

4.4 DISCUSSION

We identify the enzyme MGAT5 and the production of highly branched N-glycans as critical determinants of differentiation in the neural lineage. Enhancing expression of highly branched N-glycans with GlcNAc pushed NSPCs toward a more astrogenic bias while reducing neurogenesis (*29*) (Fig. 4.1); however, blocking branched N-glycans by treating NSPCs with Kif to disrupt MAN1 activity did not alter fate potential (Fig. 4.1, Supp. Fig. 4.S2). These data suggest that 1) increased levels of high-mannose, simple N-glycans are not sufficient to increase neurogenesis *in vitro*, and 2) other enzymes downstream of MAN1 may be responsible for the GlcNAc-induced changes in fate potential.

Treating NSPCs with Kif completely blocked the production of branched N-glycans but did not impact fate potential. Kif treatment induced significant changes to the cell surface N-glycan landscape beyond affecting highly branched N-glycans. The central nervous system is rich in bisected N-glycans (*38*), and glycomic studies of the differentiation of pluripotent stem cells into neurons or astrocytes revealed that neurons, but not astrocytes, up-regulate expression of bisected N-glycans produced by MGAT3 (*20*). Furthermore, we found that astrocyte-biased NSPCs express more *Mgat5* and less *Mgat3 (29)*. Since MGAT3 acts as a molecular brake for N-glycan branching and indirectly opposes the function of MGAT5, there might exist a balance of bisected and highly branched N-glycans that regulate the fate potential of NSPCs. In our study, Kif treatment did not just block the production of branched N-glycans – as indicated by diminished DSL and L-PHA signal by flow cytometry – but also abrogated the production of bisected N-glycans as detected by the lectin E-PHA (Fig. 4.2B). In contrast, GlcNAc treatment

primarily stimulates the production of outer N-glycan branches produced by MGAT4 and MGAT5 since GlcNAc is the limiting substrate for these enzymes (*22*). NSPCs lacking functional MGAT5 show selective reduction in N-glycan branching without affecting bisected N-glycans (Fig. 4.2D). Kif treatment thus may disrupt processes influencing both neurogenesis and astrogenesis, making the knockout of MGAT5 a more direct means to test the effects of N-glycan branching on NSPC fate potential.

Loss of MGAT5 leads to the generation of a higher proportion of neurons expressing NeuN but a loss in cell density in both the developing embryonic and postnatal cerebral cortex. Studies involving defects to N-glycan branching within the CNS have demonstrated the importance of N-glycan processing and its indispensability to normal CNS development (*1, 9, 11, 25-27, 39*). These studies highlight the importance of N-glycan branching for the normal development of the CNS, but they do not identify an impact to NSPCs during cortical development. Loss of MGAT5 causes an increase in the proportion of mature neurons occupying the CP at E16 (Fig. 4.3). However, this is accompanied by a decrease in cell density and cortical thickness throughout the cortex (Fig. 4.4). Additionally, there is a decrease in a subset of progenitors and reduced numbers of cells in the VZ/SVZ at E16 (Fig. 4.6). Taken together, we hypothesize two effects that may be occurring due to the lack of functional MGAT5 within the CNS: 1) neuronal differentiation is accelerated leading to an increased percentage of mature NeuN-positive cells in the CP early in development, and 2) the lower numbers of neurons in the CP and cells in the VZ/SVZ could be due to a depletion of NSPCs that accompanies the accelerated neuronal differentiation (Fig. 4.10A).

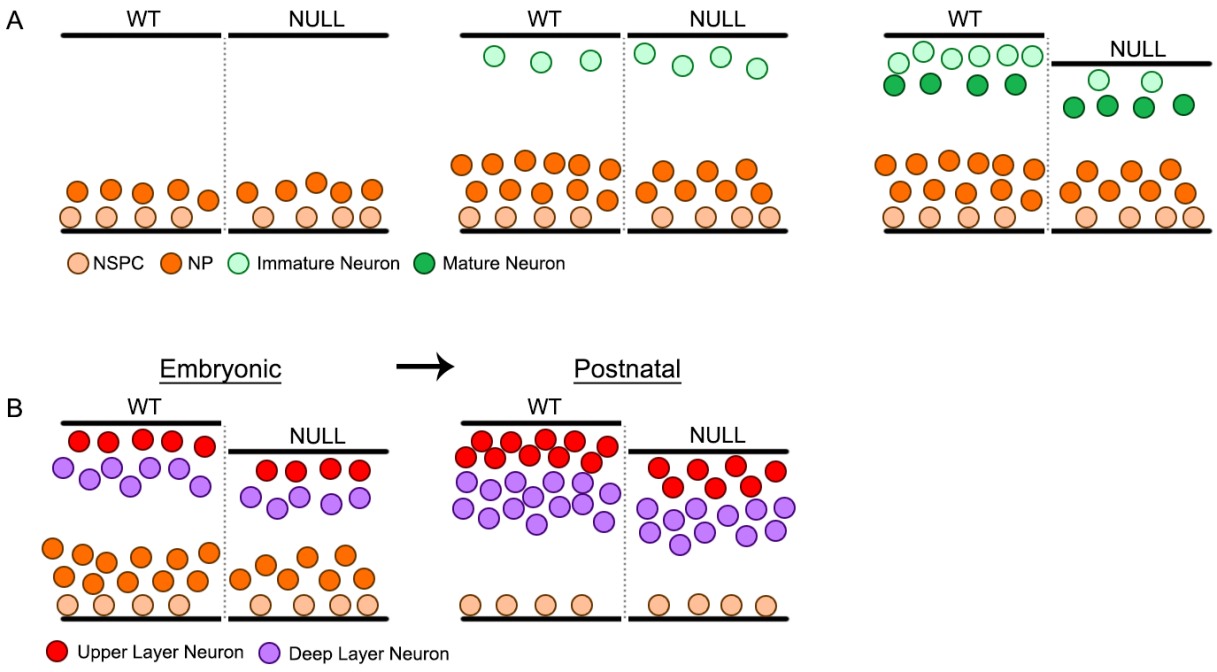

Figure 4.10. Model of neurogenesis during cortical development in the MGAT5 null brain. A) Schematic illustration of neuron formation in the WT and MGAT5 null brain. Our data suggest a model for cortical development in the MGAT5 null brain in which NSPCs form neuron progenitors (NP) that rapidly transition to immature then mature neurons, which express NeuN. This leads to an increase in the percentage and number of NeuN-expressing cells in the cortical plate at embryonic stages (E16). Similarly, cultured MGAT5 null NSPCs from embryonic ages generate higher percentages of neurons than their WT counterparts. Our data also showed that at E16, the total number of cells in null animals was reduced in the cortical plate, so there were fewer neurons overall. Animals lacking MGAT5 also had reduced numbers of cells in VZ/SVZ at E16 and reduced numbers of progenitors, particularly those destined to form upper layer neurons. The lower numbers of cells correlated with a reduced thickness of the cortex at E16 in animals lacking MGAT5. At postnatal stages (P7), there was a reduction in upper and deep layer neurons in animals lacking MGAT5 and, as observed at embryonic stages, a reduction in cell number and thickness of the cortex. Collectively, the data suggest that loss of MGAT5 leads to a more rapid production of mature neurons expressing NeuN in the cortical plate that depletes progenitors in the VZ/SVZ, resulting in an overall lower production of neurons in the cortex, reduced cell numbers, and reduced cortical thickness. B) Schematic illustration of neuronal layering as development progresses from embryonic to postnatal stages. At embryonic stages (E16), our data showed a reduction in both BRN2-positive progenitors destined to form upper layer neurons and in TBR1-positive deep layer neurons in animals lacking MGAT5. Postnatally, MGAT5 null animals had reduced neuron numbers in both upper (2/3) and deep layers (5/6), reduced cell numbers overall in those layers, and reduced thickness of deep layers. Layers formed relatively normally in MGAT5 null animals, but with reduced cell numbers and a shift in the ratio of deep to upper layer neurons, suggesting that upper layers that form later in development were more affected than deep layers. Overall, these data suggest that loss of MGAT5 leads to more rapid neuron generation that depletes progenitors, reducing the number of neurons in all layers with more of an impact on later formed upper layer neurons.

Early, subtle abnormalities that occur during CNS development can have long lasting impacts on behavior. For example, mutations in *disheveled*, which is an important protein in the Wnt/β-catenin pathway, cause abnormal expansion of deep layer cortical neurons due to rampant neuron progenitor cell expansion and premature differentiation. The brain appears normal in adults, but mutant animals exhibit abnormal social interactions and repetitive behaviors (*40*). Similarly, adult MGAT5 deficient animals appear grossly normal but fail to nurture pups and have altered depression-like behavior (*24, 33, 34*). Generalized N-glycosylation has been shown to be important for cerebellar development. A reduction in N-glycosylation of cerebellar progenitors leads to ectopic cell clustering and defects to migration and adhesion of maturing neurons (*41*). Our novel findings indicate that there is a significant decrease to the amount of upper and deep layer neurons produced in the postnatal P7 MGAT5 null mouse brain when compared to the WT (Fig. 4.7) including a change to cortical thickness, particularly in layers 5/6 (Fig. 4.8). These postnatal layer abnormalities appear to originate during embryonic stages as there is a decrease in the amount of BRN2-positive progenitors in the VZ/SVZ and TBR1-positive deep layer neurons in the CP at E16 (Fig. 4.5) This is accompanied by an overall decrease in the number of total cells found throughout the cortex in both embryonic and postnatal stages (Fig. 4.4, Fig. 4.8). We not only hypothesize that there is a change to neuronal production and maturation, but also that cortical layering is significantly impacted (Fig. 4.10B). Specifically, by the time upper layer neuron production normally occurs, BRN2-positive progenitors are depleted (Fig. 4.6) leading to a significant decrease in BRN2-positive neurons in the postnatal brain when compared to the WT brain (Fig. 4.7).

We isolated NSPCs from MGAT5 null brains, grew them in culture, and found that NSPCs lacking MGAT5 and thus incapable of generating highly branched N-glycans generate more neurons at the expense of astrocytes *in vitro* (Fig. 4.9). The molecular mechanisms by which N-glycan branching impacts NSPC fate are not currently known. N-glycan branching can modulate cell surface receptor function multiple ways, including cell surface residence time and ligand affinity. A multitude of cell surface proteins are regulated by branching, including cell adhesion molecules, ion channels, and growth factor receptors that could affect the differentiation of NSPCs. Loss of MGAT5 within T-cells or breast cancer cells desensitizes them to growth factors such as EGF, PDG, bFGF, and IGF (*21, 42*). This is likely due to increased endocytosis and recycling of the receptors, since N-glycan branching opposes endocytosis by locking retention of proteins at the cell surface (*21, 43*). Overexpression of MGAT5 leads to increased integrin-mediated cell migration and reduced cell adhesion (*44-49*). The gene *Srd5a3* encodes the enzyme that synthesizes dolichol, the lipid carrier for all N-glycans prior to their transfer to a peptide. When *Srd5a3* is knocked out in the cerebellum, IgSF-CAMs fail to be glycosylated properly resulting in decreased expression of a variety of cell adhesion molecules. Cerebellar size is reduced and ectopic neuronal clusters are formed due to defects in neurite outgrowth and neuronal migration in the cerebellum (*41*). Thus, the cell surface proteome or a cell's response to extracellular cues may change depending on N-glycan patterns present on the cell surface. These may affect NSPC fate decisions and CNS development.

4.5 MATERIALS AND METHODS

Animals and Tissue Collection

The CD-1 mice (Charles River) and Mgat5-deficient mice (gift from Dr. Michael Demetriou) were purchased, selected randomly, bred, and tissue was collected in accordance to protocols approved by the University of California, Irvine Institutional Animal Care and Use Committee. Heterozygote Mgat5-deficient mice (HET, $Mgat5^{+/-}$), as previously described, were maintained and bred together to generate pups containing either wild type (WT, $Mgat5^{+/+}$), heterozygous, and homozygous (KO, $Mgat5^{-/-}$) knockout of Mgat5.

To collect cells, dorsal forebrain cortical tissue was dissected from the cerebral cortices of embryonic day 12.5 (E12), E16.5, or E18.5 mice and placed in dissection buffer: PBS, 0.6% glucose, 50 U/mL Pen/Strep. Cortical tissue from multiple embryos within the same litter was pooled, and a subsequent culture from a single litter was considered a biological repeat. The tissue was dissociated using 0.05% Trypsin-EDTA at 37o C for 10 min. Afterward, trypsin was inhibited using soybean trypsin inhibitor (Life Technologies) and dissociated cells were re-suspended in proliferation medium containing DMEM, 1x B27, 1x N2, 1 mM sodium pyruvate, 2 mM L-glutamine, 1 mM N-acetylcysteine, 20 ng/mL EGF, 10 ng/mL bFGF, and 2 µg/mL heparin. Cells were seeded at 150,000 cells/mL into non-tissue culture treated plastic plates and grown as nonadherent spheres.

To collect brain tissue, whole brain was dissected from embryos on development stages E12, E16, P1, and P7. Whole brain was drop fixed in 4% paraformaldehyde (PFA) for approximately 18 hours at 4C then transferred to 30% sucrose in 1x PBS until the tissue was no longer floating. Tissue was quickly frozen in Optimal Cutting Temperature (OCT) compound (Tissue-Tek) and stored at -80°C prior to sectioning.

Genotyping

Animals with Mgat5-deficiency have a *lacZ* gene insertion that disrupts the coding portion of exon 1 as described previously (Granovsky, 2000, Nat. Medicine). All animals and tissue samples were genotyped for Mgat5-deficiency using standard PCR and utilizing the following primers for Mgat5 (forward: 5' - GCC AAG GGA ATG GTA CAT TGC – 3'; reverse: 5' - GGA GTC GAC ACT CAG GAA TG – 3') and LacZ (forward: 5' - CCC ATC TAC ACC AAC GTA ACC – 3'; reverse: 5' - CCT TCT AGT CCT ATA CAC CGC – 3'). A single band about 400 bp amplicon signifies expression of the wild type Mgat5 allele; a single 300 bp amplicon signifies complete knockout of Mgat5; and both bands in a single sample indicate heterozygous knockout of Mgat5.

Cell Culture, Differentiation, and Fate Analysis

Cell cultures were passaged and maintained in proliferation medium (as described above) approximately every 3 days using enzyme-free NeuroCult Chemical Dissociation Kit (Mouse) (StemCell Technologies). All NSPC cultures were passaged at least once after dissection prior to experimental use. NSPCs were plated as adherent cultures for differentiation. HCl-washed German glass coverslips (Assistant/Carolina Biological Supply, Burlington, NC) were pretreated with poly-D-lysine (40 µg/mL in milliQ H20) for 5 minutes then coated with laminin (20 µg/mL in EMEM) at 37o C for 24 hours prior to cell adhesion. Whole neurospheres were seeded onto the laminin-coated coverslips in proliferation medium. After 24 hours, proliferation medium was removed and replaced with differentiation medium (same components as proliferation medium but excluding EGF, bFGF, and heparin) to induce differentiation. NSPCs were differentiated into neurons and astrocytes in these conditions for 3 days and oligodendrocytes for 7 days. For 7 day differentiated samples, culture media was replaced after 3 days.

For fate analysis, at least 3 independent sets of NSPCs derived from 3 different litters were analyzed using manual counting software built into ImageJ. The percentage of cells that differentiated into double-positive MAP2/TUJ1 neurons with neurite lengths of at least 3 times the length of the soma was calculated from 5 randomly selected fields per experiment with more than 1000 cells counted per experimental group in each of the 3 independent experiments, so over 3000 cells per group. The percentages of GFAP-positive astrocytes were calculated from randomly selected fields of cells adjacent to the sphere attachment site but not from the dense cells within the sphere since cell density and cell death affect astrocyte GFAP reactivity. Cells expressing GFAP in a filamentous cytoskeletal pattern were counted as astrocytes and 3000 or more cells per experimental group were analyzed.

Cell Treatment

A stock solution of 800 mM N-acetylglucosamine (GlcNAc,Thermo Fisher Scientific, 1079) was prepared in proliferation medium. To stimulate the N-glycan branching pathway, the stock GlcNAc solution was diluted to 80 mM in proliferation medium. The medium was re-supplemented with fresh GlcNAc every 24 hours since GlcNAc breaks down over time in aqueous solutions. A stock 1mg/ml solution of kifunensine (Sigma-Aldrich, K1150) in H_2O was diluted to 0.5 µM in the proliferation medium to block the N-glycan branching pathway. Both kifunensine and GlcNAc were withdrawn during differentiation.

Lectin Flow cytometry

Live NSPCs were dissociated using the NeuroCult dissociation kit and re-suspended in 1x PBS with 5% BSA. Cells were incubated with various fluorescein-conjugated lectins for 1 hour on ice in the dark. All cells were counter-stained with propidium iodide (Thermo Fisher, P3566) for 5 minutes prior to being analyzed. Cell samples were analyzed on a BD LSR II flow

cytometer, and the data was collected using the BD FACSDIVA software. All data analysis was performed using FlowJo v10.1. See Table 4.1 for lectins and concentrations.

Immunocytochemistry

Cell culture samples were fixed with 4% paraformaldehyde (4% paraformaldehyde, 5 mM MgCl2, 10 mM EGTA, 4% sucrose in PBS) for 10 min, and the cell membranes were permeabilized with 0.3% Triton-X 100 in PBS for 5 min. Cells were blocked using 5% BSA in PBS for 1 hour then incubated with the primary antibody for approximately 18 hours at 4º C and the secondary antibody for 2 hours at room temperature in the dark. Primary antibodies were diluted in 1% BSA in 1x PBS; secondary antibodies were diluted in 1x PBS. All cells were counterstained using a Hoechst 33342 nuclear dye (Thermo Fisher Scientific) and coverslips were mounted onto glass slides using ProLong Gold Antifade Mountant medium (Thermo Fisher Scientific). Cells were visualized using a Nikon Eclipse Ti-E fluorescence microscope at 20x magnification, and all images were acquired using NIS Elements AR 4.51 image capturing and analysis software. See Table 4.1 for antibodies and concentrations.

Immunohistochemistry

All frozen tissue samples were sectioned into 12 µm thick slices using a Leica research cryostat (Leica CM3050 S) and mounted on SuperFrost glass slides. OCT was dissolved by submerging slides in 1x PBS for 5 min. For tissue samples stained for Ki67, TBR1, TBR2, CTIP2, BRN2, and cleaved Caspase-3, sections were subjected to antigen retrieval in a sodium citrate buffer (10 mM sodium citrate, 0.05% Tween 20, adjusted for pH 6.0) for 1 hour in a pressure cooker prior to blocking. Sections were blocked for 20 min. using a solution containing 1x PBS, 0.1% Triton X detergent (PBST), and 5% donkey serum (DS). Primary antibody was diluted in PBST with 5% DS and the sections were incubated with the primary antibody

overnight at 4°C. After washing, sections were incubated with secondary antibody diluted in PBST with 5% DS for 1 hour at room temperature. All sections were counter stained with Hoechst 33342 nuclear dye and mounted using ProLong Gold Antifade Mountant medium (Thermo Fisher Scientific). Sections were visualized using a Nikon Eclipse Ti-E fluorescence microscope, and all images were acquired using NIS Elements AR 4.51 image capturing and analysis software. See Table 4.1 for antibodies and concentrations.

Proliferation Assays

Cells actively cycling were visualized utilizing immunostaining of the Ki67 proliferation marker using an anti-Ki67 antibody (Leica Biosystems, KI67P-CE). Cells undergoing mitosis were visualized by immunocytochemistry utilizing the primary antibody mouse anti-phospho-histone H3 (Ser10) (6G3) IgG (Cell Signaling Technology 9706S). All cells were counterstained with Hoechst 33342 nuclear dye (Thermo Fisher Scientific). Cells that passed through at least one S-phase were visualized using EdU incorporation (Click-iT EdU Alexa Fluor 555 Imaging Kit, Thermo Fisher Scientific). Proliferation medium of adherent NSPCs was supplemented with 10 µM EdU and cells incubated at 37o C for 4 hours. Afterwards, cells were fixed and permeabilized as described above. After washing with PBS, cells were incubated with the EdU Click-iT reaction cocktail for 30 min at room temperature in the dark and counterstained with Hoechst 33342 nuclear dye (Thermo Fisher Scientific). Cells were analyzed using manual counting software in ImageJ and positively labeled cells were counted as a percentage of all Hoechst-stained cells in 5 randomly selected fields.

Cell cycle analysis by flow cytometry was performed by dissociating NSPCs and fixing suspended cells using cold 70% ethanol for 30 min. at 4° C. Fixed cells were incubated with ribonuclease (Thermo Fisher, EN0531) for 45 min at 37° C. Cells were then incubated in

propidium iodide (final concentration 2.5 µg/mL) for 30 min. on ice. Afterwards, volume was increased to 500 µL using PBS. All cells were analyzed on a BD LSR II flow cytometer, and the data was collected using the BD FACSDIVA software. Cell cycle data analysis was performed using the built-in program within FlowJo v10.1.

Table 4.1 Antibodies and lectins used to label cell markers and glycans

Item	Vendor	Catalogue #	Dilution
Mouse anti-MAP2 IgG	Sigma	M9942	ICC: 1:200
Rabbit anti-TUJ1 IgG	Sigma	T2200	ICC: 1:100 IHC: 1:200
Rabbit anti-GFAP IgG	Sigma	G9269	ICC: 1:200 IHC: 1:200
Mouse anti-O4 IgM	R&D Systems	MAB1326	ICC: 1:100
Rabbit anti-NeuN	EMD Millipore	ABN78	IHC: 1:100
Mouse anti-phospho-Histone H3 (Ser10) (6G3) IgG	Cell Signaling Technology	9706S	ICC: 1:200
Rabbit anti-Ki67	Leica Biosystems	KI67P-CE	ICC: 1:200 IHC: 1:500
Mouse anti-Brn2 (B-2)	Santa Cruz Biotechnology	Sc-393324	IHC: 1:1000
Rat anti-Ctip2 (25B6)	Abcam	Ab18465	IHC: 1:1000
Rabbit anti-Tbr1	Abcam	Ab31940	IHC: 1:500
Rabbit anti-Tbr2	Abcam	Ab23345	IHC: 1:500
Rabbit anti-Caspase-3	Cell Signaling Technologies	9661S	IHC: 1:1000
Alexa Fluor 594 donkey anti-rabbit IgG	Jackson ImmunoResearch	711-585-152	ICC: 1:200 IHC: 1:200
Alexa Fluor 488 donkey anti-mouse IgG	Jackson ImmunoResearch	715-545-151	ICC: 1:200
L-PHA	Vector Labs	FL-1111	Flow: 20 µg/ml IHC: 1:100
E-PHA	Vector Labs	FL-1121	Flow: 20 µg/ml
DSL	Vector Labs	FL-1181	Flow: 20 µg/ml
ConA	Vector Labs	FL-1001	Flow: 20 µg/ml
SNA	Vector Labs	FL-1301	Flow: 40 µg/ml
LEA	Vector Labs	FL-1171	Flow: 50 µg/ml
LCA	Vector Labs	FL-1041	Flow: 20 µg/ml

4.6 ACKNOWLEDGEMENTS

The authors gratefully acknowledge Dr. Michael Demetriou for the MGAT5 knockout mice. This work was supported in part by NSF CAREER Award IOS-1254060 (LAF), NIH NINDS T32 NS082174 (predoctoral fellowship to AY), CIRM RT1-01074 (LAF), NIH NCRR and NCATS through Grant UL1 TR001414 (Pilot Grant to LAF), the Sue & Bill Gross Stem Cell Research Center at University of California, Irvine, and a gift by Pearl Tze Hosfiel and Keith Hosfiel.

4.7 SUPPLEMENTAL MATERIAL

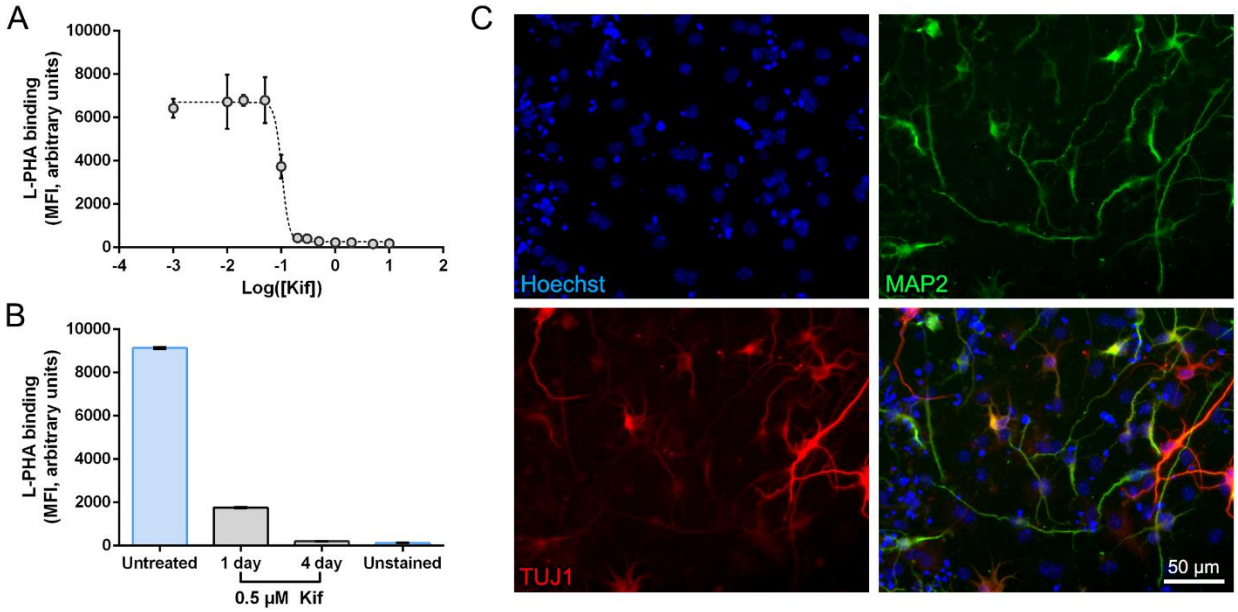

Figure 4.S1. Kifunensine dose response and *in vitro* neuron detection. E12 NSPCs were treated for 4 days with varying dose of Kifunensine (µM): 0, 0.001, 0.01, 0.02, 0.05, 0.1, 0.2, 0.3, 0.5, 1, 2, 5, 10. At the conclusion of Kif treatment, NSPCs were labeled with L-PHA to detect highly branched N-glycans and analyzed by flow cytometry. A dosage of 0.5 µM was chosen to disrupt formation of highly branched N-glycans. (N=3). B) E12 NSPCs were treated with 0.5 µM Kif for 1 or 4 days and highly branched N-glycans analyzed by flow cytometry with L-PHA. Treatment for 4 days resulted in a greater decrease than treatment for 1 day. (N=1) C) Differentiated E12 NSPCs were co-stained for neuronal markers MAP2 and TUJ1. Quantitation in Figures 4.1, 4.9 and Supplemental Figure 4.2 was based on co-labeling with both markers.

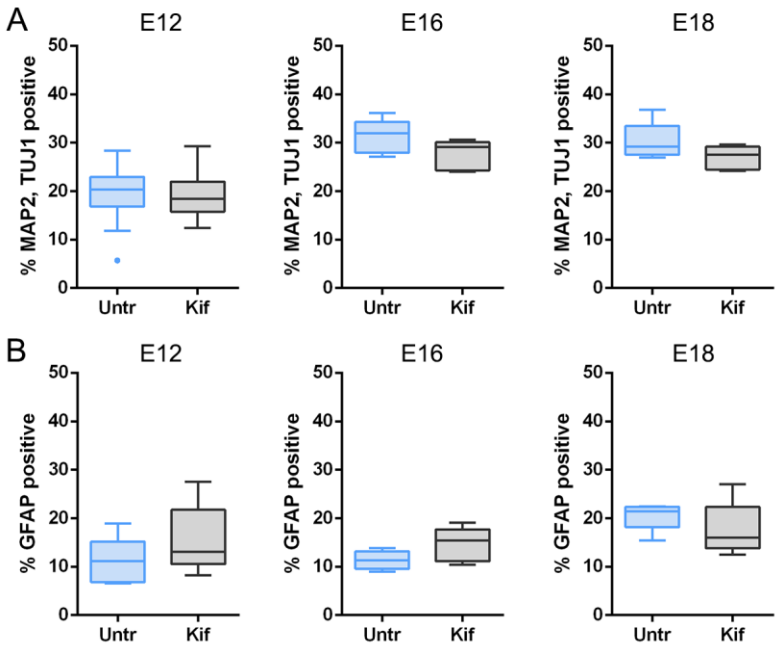

Figure 4.S2. Differentiation of Kif-treated NSPCs from embryonic ages E12, E16, and E18. NSPCs isolated from E12, E16, and E18 embryonic cortices were treated with 0.5 µM Kif for 4 days then differentiated for 3 days and immunostained for markers of neurons or astrocytes. A) There was no significant difference in the generation of MAP2/TuJ1-positive neurons between untreated control (Untr) and Kif-treated NSPCs from any of the embryonic ages. (N=3) B) There was no significant difference in the generation of GFAP-positive astrocytes between untreated control (Untr) and Kif-treated NSPCs from any of the embryonic ages. (N=3)

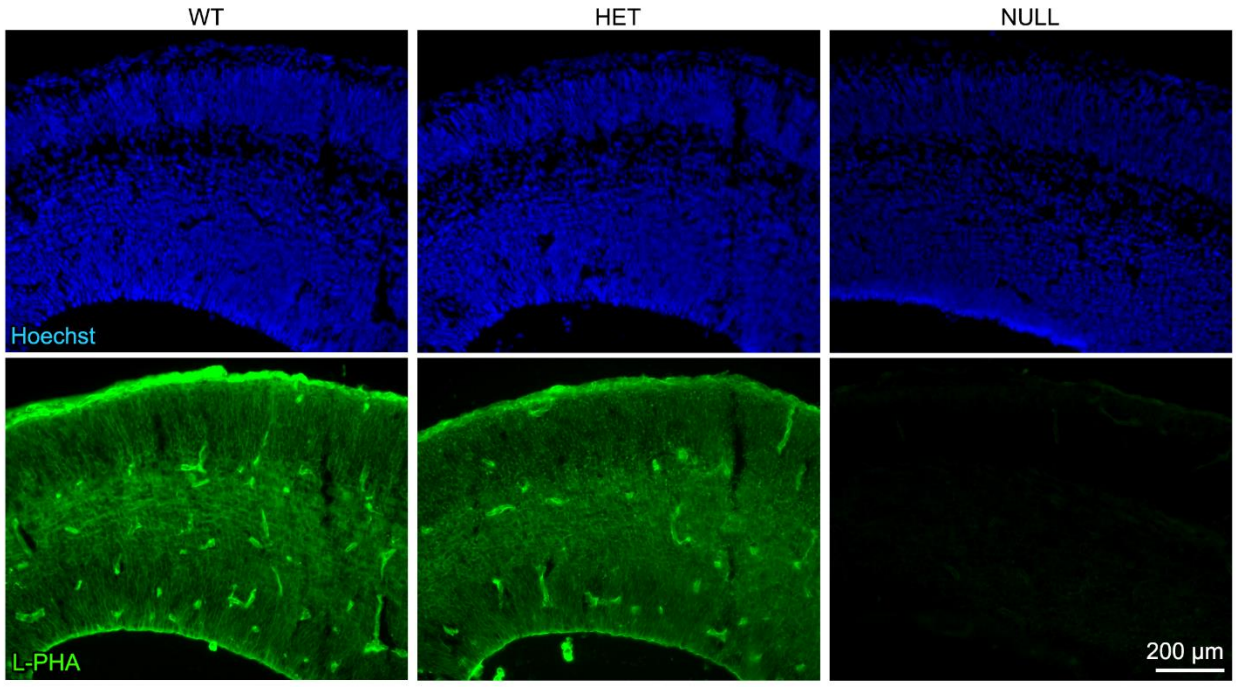

Figure 4.S3. L-PHA labeling is reduced in the cerebral cortices of MGAT5 knockout animals. Coronal sections of E16 brain cerebral cortices were labeled with L-PHA, a lectin binding to highly-branched N-glycans modified by MGAT5. Compared to WT, L-PHA signal intensity is reduced in the MGAT5 heterozygous knockout brain and totally abolished in the MGAT5 homozygous null brain.

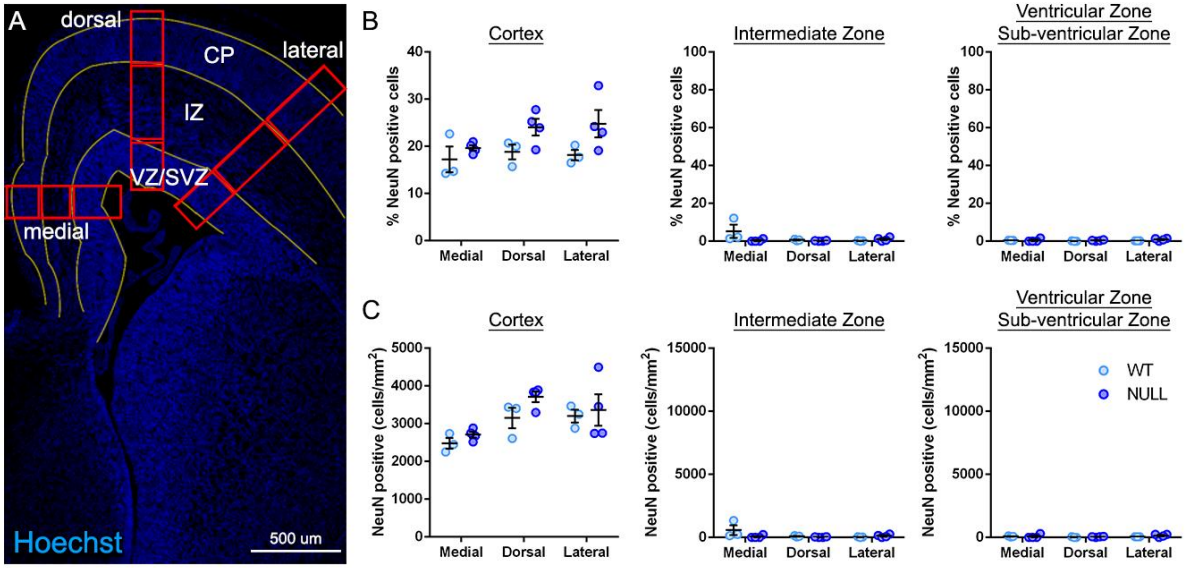

Figure 4.S4. NeuN quantitation in the developing WT and MGAT5 null E16 cortex. A) Quantification paradigm schematized on a WT E16 coronal section of dorsal forebrain stained with Hoechst. Yellow lines indicate the separation of cortical plate (CP), intermediate zone (IZ), and ventricular zone/sub-ventricular zone (VZ/SVZ) regions. The red boxes indicate slices from medial, dorsal, and lateral regions of the cortex divided into CP, IZ, and VZ/SVZ. The total cortex values are a summation of CP, IZ and VZ/SVZ while the values for IZ and VZ/SVZ are for only those regions. The values for CP are shown in Figure 4.3D) NeuN signal was quantified as a percentage of the cells either within the total cortex (combined CP, IZ, and VZ/SVZ) or within the IZ or VZ/SVZ. There was a non-significant increase in the percentage of NeuN expressing cells in null brains compared to WT in the medial, dorsal, and lateral regions. Very few NeuN-positive cells were present in the IZ or VZ/SVZ, and there was no difference between WT and null brains in the percentage of NeuN expressing cells in these regions. (N≥3)**.** C) The number of NeuN-positive cells per area (cells/ mm^2) showed a non-significant increase in null brains compared to WT brains. No differences were observed in the IZ or VZ/SVZ. (N≥3). Comparisons between WT and null data utilized two-tailed Student's t-tests.

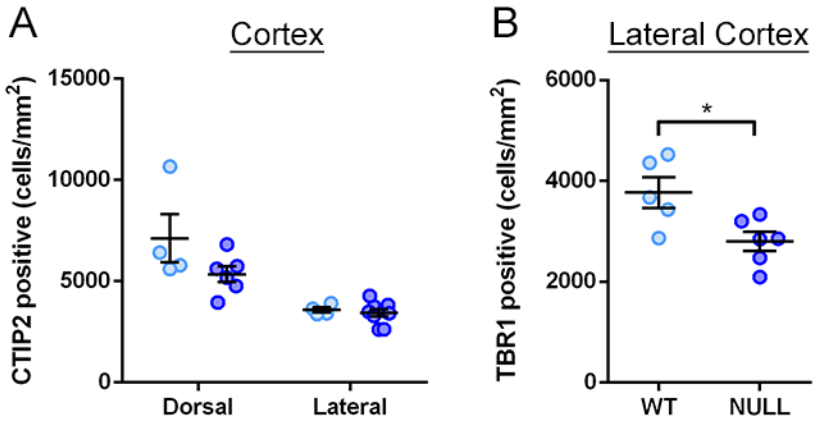

Figure 4.S5. Quantitation of deep layer neuron markers across the total cortex at embryonic stages. A) E16 brain cortices were immunostained to detect deep layer neuron markers CTIP2 and TBR1. Marker expression was quantified across the total cortex (combined CP, IZ, and VZ/SVZ) in either dorsal or lateral regions. B) No significant difference in the amount of CTIP2 positive cells was observed across the total cortex between WT and null brains in both dorsal and lateral regions. C) TBR1 positive cells were significantly reduced (p=0.0203) in the MGAT5 null lateral cortex compared to WT. All comparisons two-tailed Student's t-test WT vs. null, N≥3, (*p<0.05).

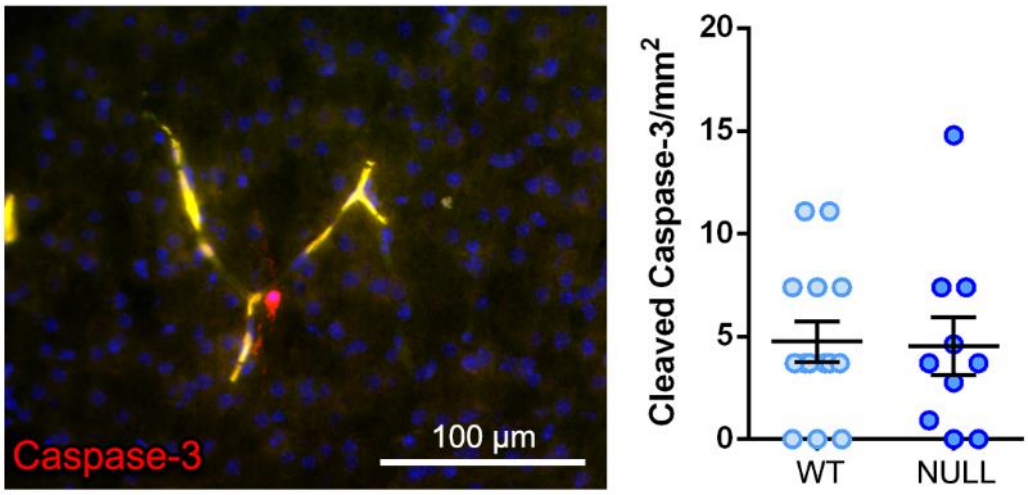

Figure 4.S6. No difference in cell death in postnatal WT and MGAT5 null brain. P7 brain cortices were immunostained to detect cleaved Caspase-3 to assess apoptotic cell death in the cortex. The was no difference in the number of cells per mm^2 positive for cleaved Caspase-3 between WT and null brains. All data were analyzed by two-tailed Student's t-test WT vs. null, N=3.

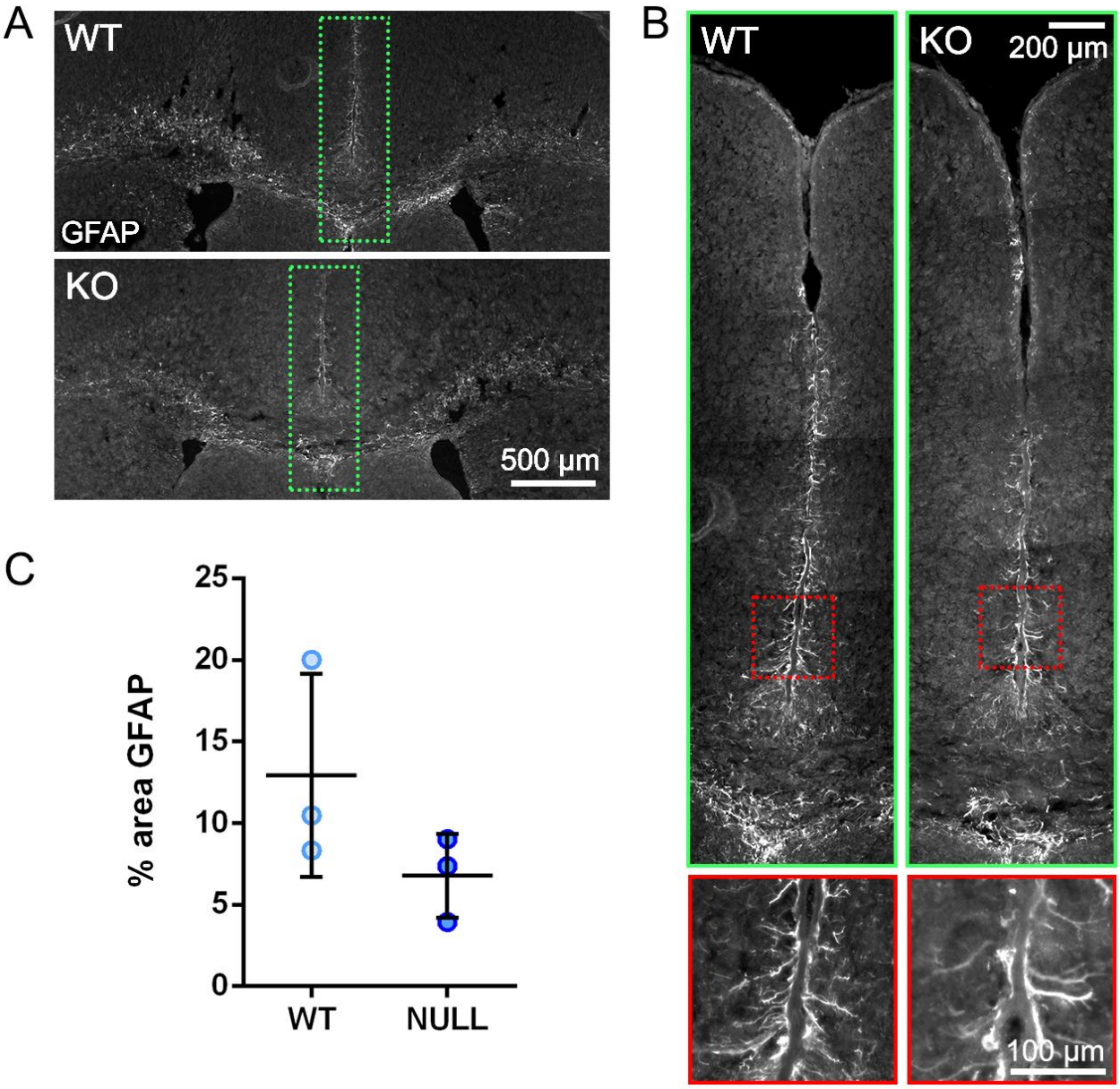

Figure 4.S7. GFAP labeling in the P7 brain did not significantly differ between WT and MGAT5 null brains. A) Coronal sections from P7 WT and MGAT5 null brains were immunostained to detect GFAP. GFAP labeling was primarily restricted at P7 to white matter tracts and cortical areas along the pial surface at the midline. Dashed green boxes indicate areas magnified in (B). B) Magnified images of the midline region show further detail of GFAP-positive cells in WT and MGAT5 null brains. Dashed red boxes indicate areas further magnified in the lower panel red-bordered boxes. C) GFAP expression was quantified as the percent GFAP-positive area in the midline region, such as shown by the dotted red boxes indicated in B. There was a non-significant decrease in GFAP-positive area in MGAT5 null cortex compared to WT. (N=3)

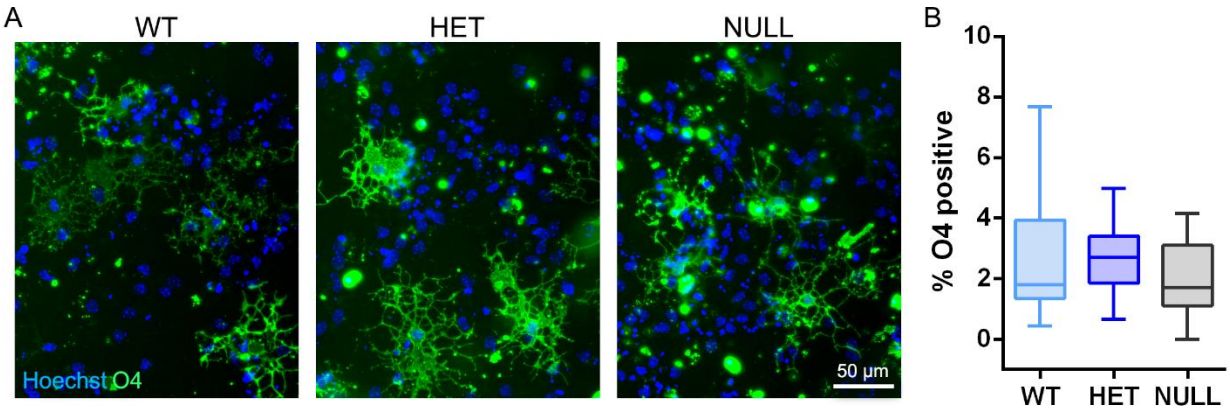

Figure 4.S8. Oligodendrocyte formation from cultured E12 NSPCs did not significantly differ between WT and MGAT5 mutants. A) WT, MGAT5 het, and MGAT5 null E12 NSPCs were differentiated for 7 days and immunostained for oligodendrocyte marker O2. Nuclei were stained with Hoechst. B) Quantitation of cells expressing O4 indicates no change in the formation of oligodendrocytes. (N=3)

4.8 REFERENCES

1. K. Ohtsubo, J. D. Marth, Glycosylation in cellular mechanisms of health and disease. *Cell* **126**, 855-867 (2006).
2. H. Scott, V. M. Panin, N-glycosylation in regulation of the nervous system. *Adv Neurobiol* **9**, 367-394 (2014).
3. H. Scott, V. M. Panin, The role of protein N-glycosylation in neural transmission. *Glycobiology* **24**, 407-417 (2014).
4. A. Kelly, A. O'Malley, M. Redha, G. W. O'Keeffe, D. S. Barry, The distribution of the proteoglycan FORSE-1 in the developing mouse central nervous system. *J Anat* **234**, 216-226 (2019).
5. R. S. Haltiwanger, J. B. Lowe, Role of glycosylation in development. *Annu Rev Biochem* **73**, 491-537 (2004).
6. N. Flaris *et al.*, Developmentally-regulated lectin-binding in the embryonic mouse telencephalon. *Brain Research* **678**, 99-109 (1995).
7. A. Ishii *et al.*, Developmental changes in the expression of glycogenes and the content of N-glycans in the mouse cerebral cortex. *Glycobiology* **17**, 261-276 (2007).
8. R. Kleene, M. Schachner, Glycans and neural cell interactions. *Nat Rev Neurosci* **5**, 195-208 (2004).
9. H. Schachter, The clinical relevance of glycobiology. *Journal of Clinical Investigation* **108**, 1579-1582 (2001).
10. A. Varki, J. B. Lowe, in *Essentials of Glycobiology*, nd *et al.*, Eds. (Cold Spring Harbor (NY), 2009).
11. P. Stanley, What Have We Learned from Glycosyltransferase Knockouts in Mice? *J Mol Biol* **428**, 3166-3182 (2016).
12. H. Yagi, T. Saito, M. Yanagisawa, R. K. Yu, K. Kato, Lewis X-carrying N-glycans regulate the proliferation of mouse embryonic neural stem cells via the Notch signaling pathway. *J Biol Chem* **287**, 24356-24364 (2012).
13. P. Taupin *et al.*, FGF-2-responsive neural stem cell proliferation requires CCg, a novel autocrine/paracrine cofactor. *Neuron* **28**, 385-397 (2000).
14. R. L. Schnaar, R. Gerardy-Schahn, H. Hildebrandt, Sialic acids in the brain: gangliosides and polysialic acid in nervous system development, stability, disease, and regeneration. *Physiol Rev* **94**, 461-518 (2014).
15. K. Angata, M. Fukuda, Roles of polysialic acid in migration and differentiation of neural stem cells. *Methods Enzymol* **479**, 25-36 (2010).
16. A. Burgess *et al.*, Polysialic acid regulates the clustering, migration, and neuronal differentiation of progenitor cells in the adult hippocampus. *Dev Neurobiol* **68**, 1580-1590 (2008).
17. T. Sasaki, J. Hirabayashi, H. Manya, K. Kasai, T. Endo, Galectin-1 induces astrocyte differentiation, which leads to production of brain-derived neurotrophic factor. *Glycobiology* **14**, 357-363 (2004).
18. Y. Imaizumi *et al.*, Galectin-1 is expressed in early-type neural progenitor cells and down-regulates neurogenesis in the adult hippocampus. *Mol Brain* **4**, 7 (2011).
19. L. A. Pasquini *et al.*, Galectin-3 drives oligodendrocyte differentiation to control myelin integrity and function. *Cell Death Differ* **18**, 1746-1756 (2011).

20. M. Terashima, M. Amano, T. Onodera, S. Nishimura, N. Iwasaki, Quantitative glycomics monitoring of induced pluripotent- and embryonic stem cells during neuronal differentiation. *Stem Cell Research* **13**, 454-464 (2014).
21. K. S. Lau *et al.*, Complex N-glycan number and degree of branching cooperate to regulate cell proliferation and differentiation. *Cell* **129**, 123-134 (2007).
22. J. W. Dennis, I. R. Nabi, M. Demetriou, Metabolism, cell surface organization, and disease. *Cell* **139**, 1229-1241 (2009).
23. M. Demetriou, M. Granovsky, S. Quaggin, J. Dennis, Negative regulation of T-cell activation and autoimmunity by Mgat5 N-glycosylation. *Nature* **409**, 733-739 (2001).
24. J. W. Dennis, J. Pawling, P. Cheung, E. Partridge, M. Demetriou, UDP-N-acetylglucosamine:alpha-6-D-mannoside beta1,6 N-acetylglucosaminyltransferase V (Mgat5) deficient mice. *Biochim Biophys Acta* **1573**, 414-422 (2002).
25. E. Ioffe, P. Stanley, Mice lacking N-acetylglucosaminyltransferase I activity die at mid-gestation, revealing an essential role for complex or hybrid N-linked carbohydrates. *Proc Natl Acad Sci U S A* **91**, 728-732 (1994).
26. M. Metzler *et al.*, Complex asparagine-linked oligosaccharides are required for morphogenic events during postimplantation development. *Embo Journal* **13**, 2056-2065 (1994).
27. Z. Ye, J. D. Marth, N-glycan branching requirement in neuronal and postnatal viability. *Glycobiology* **14**, 547-558 (2004).
28. Y. Wang, H. Schachter, J. D. Marth, Mice with a homozygous deletion of the Mgat2 gene encoding UDP-N-acetylglucosamine:alpha-6-D-mannoside beta1,2-N-acetylglucosaminyltransferase II: a model for congenital disorder of glycosylation type IIa. *Biochim Biophys Acta* **1573**, 301-311 (2002).
29. A. R. Yale *et al.*, Cell Surface N-Glycans Influence Electrophysiological Properties and Fate Potential of Neural Stem Cells. *Stem Cell Reports* **11**, 869-882 (2018).
30. A. Males, L. Raich, S. J. Williams, C. Rovira, G. J. Davies, Conformational Analysis of the Mannosidase Inhibitor Kifunensine: A Quantum Mechanical and Structural Approach. *Chembiochem* **18**, 1496-1501 (2017).
31. F. H. Labeed *et al.*, Biophysical characteristics reveal neural stem cell differentiation potential. *PLoS One* **6**, e25458 (2011).
32. M. Granovsky *et al.*, Suppression of tumor growth and metastasis in Mgat5-deficient mice. *Nat Med* **6**, 306-312 (2000).
33. L. Feldcamp *et al.*, Mgat5 modulates the effect of early life stress on adult behavior and physical health in mice. *Behav Brain Res* **312**, 253-264 (2016).
34. L. Soleimani, J. C. Roder, J. W. Dennis, T. Lipina, Beta N-acetylglucosaminyltransferase V (Mgat5) deficiency reduces the depression-like phenotype in mice. *Genes Brain Behav* **7**, 334-343 (2008).
35. M. H. Dominguez, A. E. Ayoub, P. Rakic, POU-III transcription factors (Brn1, Brn2, and Oct6) influence neurogenesis, molecular identity, and migratory destination of upper-layer cells of the cerebral cortex. *Cereb Cortex* **23**, 2632-2643 (2013).
36. X. Qian *et al.*, Timing of CNS cell generation: a programmed sequence of neuron and glial cell production from isolated murine cortical stem cells. *Neuron* **28**, 69-80 (2000).
37. W. He, C. Ingraham, L. Rising, S. Goderie, S. Temple, Multipotent stem cells from the mouse basal forebrain contribute GABAergic neurons and oligodendrocytes to the cerebral cortex during embryogenesis. *Journal of Neuroscience* **21**, 8854-8862 (2001).

38. Y. Kizuka, N. Taniguchi, Neural functions of bisecting GlcNAc. *Glycoconj J* **35**, 345-351 (2018).
39. H. Schachter, Congenital disorders involving defective N-glycosylation of proteins. *Cellular and Molecular Life Sciences* **58**, 1085-1104 (2001).
40. H. Belinson *et al.*, Prenatal beta-catenin/Brn2/Tbr2 transcriptional cascade regulates adult social and stereotypic behaviors. *Mol Psychiatry* **21**, 1417-1433 (2016).
41. D. Medina-Cano *et al.*, High N-glycan multiplicity is critical for neuronal adhesion and sensitizes the developing cerebellum to N-glycosylation defect. *Elife* **7**, (2018).
42. E. A. Partridge *et al.*, Regulation of cytokine receptors by Golgi N-glycan processing and endocytosis. *Science* **306**, 120-124 (2004).
43. K. S. Lau, J. W. Dennis, N-Glycans in cancer progression. *Glycobiology* **18**, 750-760 (2008).
44. H. Guo, I. Lee, M. Kamar, S. Akiyama, M. Pierce, Aberrant N-glycosylation of beta(1) integrin causes reduced alpha(5)beta(1) integrin clustering and stimulates cell migration. *Cancer Research* **62**, 6837-6845 (2002).
45. H. Guo, I. Lee, M. Kamar, M. Pierce, N-acetylglucosaminyltransferase V expression levels regulate cadherin-associated homotypic cell-cell adhesion and intracellular signaling pathways. *Journal of Biological Chemistry* **278**, 52412-52424 (2003).
46. R. Guo *et al.*, Glycogenes mediate the invasive properties and chemosensitivity of human hepatocarcinoma cells. *Int J Biochem Cell Biol* **45**, 347-358 (2013).
47. S. S. Pinho *et al.*, E-cadherin and adherens-junctions stability in gastric carcinoma: functional implications of glycosyltransferases involving N-glycan branching biosynthesis, N-acetylglucosaminyltransferases III and V. *Biochim Biophys Acta* **1830**, 2690-2700 (2013).
48. Y. Zhao *et al.*, N-acetylglucosaminyltransferase III antagonizes the effect of N-acetylglucosaminyltransferase V on alpha 3 beta 1 integrin-mediated cell migration. *Journal of Biological Chemistry* **281**, 32122-32130 (2006).
49. Y. Y. Zhao *et al.*, Functional roles of N-glycans in cell signaling and cell adhesion in cancer. *Cancer Sci* **99**, 1304-1310 (2008).

CHAPTER 5

N-glycosylation branching regulates NSPC adhesion

Authors: **Andrew R. Yale[1,2,3]**, Lakshay Verma[2,3], Craig Reeves[2,6], Chloe Thangavelu[2,3], Loise Cho[2,3], Paul D. Gershon[5], Lisa A. Flanagan[1,2,3,4]

[1]Department of Anatomy & Neurobiology, University of California, Irvine

[2]Department of Neurology, University of California, Irvine

[3]Sue & Bill Gross Stem Cell Research Center, University of California, Irvine

[4]Department of Biomedical Engineering, University of California, Irvine

[5]Department of Molecular Biology and Biochemistry, University of California, Irvine

[6]College of Natural Sciences and Mathematics – Biology, California State University, Fullerton

5.1 INTRODUCTION

Neural stem and progenitor cells (NSPCs) have the ability to differentiate into neurons, astrocytes, or oligodendrocytes as they mature. Central nervous system (CNS) tissue does not regenerate efficiently; thus, transplantation of NSPCs has the potential to be used as a clinical therapeutic for the restoration of damaged tissue in patients suffering from neurodegenerative diseases and traumatic injuries to the CNS. However, current methods to characterize and predict the behavior of NSPCs are insufficient and give variable results. In order to have a more efficient and consistent cell transplantation-based therapeutic for humans, it is essential to gain a better understanding of mechanisms that control NSPC behavior and cellular responses to their surroundings.

Our lab determined that membrane capacitance, or the cell membrane's ability to store charge, is a unique physiological signature that distinguishes fate-biased progenitors in a heterogenous population of NSPCs (*1-8*). Experiments to decipher the molecular components underlying membrane capacitance determined a significant relationship between fate-specific membrane capacitance and glycosylation patterns (*1*). Specifically, experiments showed that altering N-glycosylation complexity by adding sugars to proteins on the cell surface changed both membrane capacitance and fate bias of NSPCs (*1*). The complexity of N-glycosylation is dependent on the number of N-acetylglucosamine (GlcNAc) 'branches' that are added to the N-glycan core. Almost all N-glycans undergo a process known as N-glycan branching. N-glycan branches generate structures to which sialic acid or galactose residues can be added to to form the vast diversity of N-glycans expressed on the cell surface. Since N-glycan branching complexity can significantly alter the function of many cell membrane proteins, it can control and coordinate the function of proteins that detect environmental cues and therefore dictate a

cell's response to its surroundings. Identifying which cell responses are most susceptible to changes in glycosylation patterns on the surface will be key to understanding how N-glycosylation can direct NSPC behavior.

The molecular mechanisms by which N-glycosylation can impact NSPC fate are not currently known. Changes to N-glycan branching impact ligand-receptor sensitivity to a number of growth factors such as EGF, PDGF, bFGF, and IGF (*9, 10*). Additionally, N-glycan branching regulates the metastatic potential of cancer cells by regulating cellular adhesion and migration through modifying functional activity of cadherins and integrins, which are cell-cell and cell-extracellular matrix (ECM) binding proteins (*11-18*). The objective of these studies was to investigate how N-glycosylation patterns may specifically regulate NSPC cell surface proteins and cell function.

5.2 RESULTS

5.2.1 Unbiased screen of cell surface proteome

N-glycan branching impacts NSPC fate potential (see Chapter 3), but the molecular mechanisms and signaling cascades that mediate this process are not well understood. Since glycosylation controls multiple different types of proteins on the cell surface, we performed an unbiased screen of all cell surface proteins by mass spectrometry (MS). We isolated the plasma membranes of GlcNAc-treated and control mouse NSPCs by ultracentrifugation-based fractionation. By comparing the relative protein abundance between GlcNAc-treated and control NSPCs using MS, we found that a large number of proteins that regulate cell adhesion were less abundant on GlcNAc-treated NSPCs than controls. GlcNAc-treated cells expressed lower cell surface levels of the cell-cell adhesion proteins neural cell adhesion molecule (NCAM), N-

cadherin, and accessory proteins that link cadherins to the actin cytoskeleton: α-catenin and δ-catenin/p120. Our screen also identified proteins critical for cell-extracellular matrix (ECM) adhesion since GlcNAc-treated cells had lower cell surface expression of integrin subunits αV and β1. Based on the proteins identified in our screen, we assessed whether N-glycan branching functionally impacted cell adhesion.

5.2.2 N-glycan branching impacts cell-cell adhesion

We first tested whether NSPC cell-cell adhesion is affected by the N-glycan branching pathway. We treated E12 NSPCs with the sugar supplement N-acetylglucosamine (GlcNAc) to enhance N-glycan branching on the cell surface (*1*) (Chapter 3) and found GlcNAc-treated NSPC neurospheres to be significantly smaller compared to untreated NSPC neurospheres (Fig. 5.1AB). Interestingly, the number of spheres in the GlcNAc-treated sample was more than double that of the untreated sample (Fig. 5.1C). Neurosphere formation is initiated by either one or a cluster of NSPCs that bind to each other and proliferate to form their own micro-niche. This data seems to suggest that the initial clustering of GlcNAc-treated NSPCs was diminished, resulting in smaller neurospheres compared to the untreated control, but more in number. It is also possible that this could be due to proliferative differences or cell death, but we previously did not find that GlcNAc treatment affected both properties (*1*).

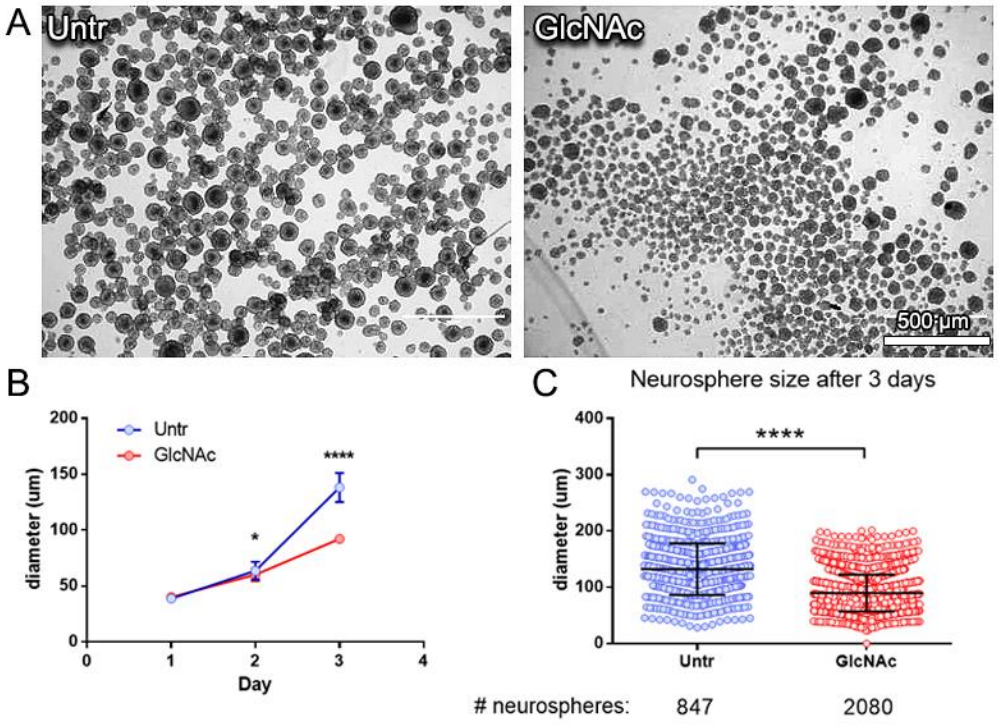

Figure 5.1. GlcNAc treatment reduces neurosphere size. A) Phase contrast images show neurospheres formed by untreated and GlcNAc-treated NSPCs. Scale bar represents 1000 µm. B) Neurosphere diameter of GlcNAc treated E12 NSPCs significantly differed from controls by 2 and 3 days of growth in suspension. C) Neurosphere diameters at day 3 depicted as a dot plot. The total number of neurospheres in the GlcNAc-treated NSPC group was more than 2-fold greater than the number of neurospheres in the untreated group. (n=3; *p<0.05, ****p<0.0001)

Although we did not observe a change in proliferation or cell death in the GlcNAc-treated NSPCs, the neurosphere assay is not specific to cell adhesion. We therefore utilized a second adhesion assay to isolate the interaction of cells adhering to one another. We developed a monolayer adhesion assay where single cells could be seeded onto an existing monolayer of cells. The number of cells attached after a period of time could then be quantified. Through this process, we can control the number of live cells being seeded. Additionally, seeding would only occur for a short period of time prior to being fixed, not allowing cells enough time to proliferate. Thus, this monolayer adhesion enables the direct assessment of cell-cell adhesion without confounding variables such as proliferation or cell death. In this study, fluorescently

labeled dissociated NSPCs were seeded onto a glycosylation-matched monolayer of cells – control NSPCs on a control, untreated monolayer; GlcNAc-treated NSPCs on a GlcNAc-treated monolayer. Unbound cells were washed away and the number of fluorescently labeled cells remaining on the monolayer was quantified. Within the GlcNAc-treated sample, NSPCs showed reduced binding to the monolayer compared to the controls (Fig. 5.2).

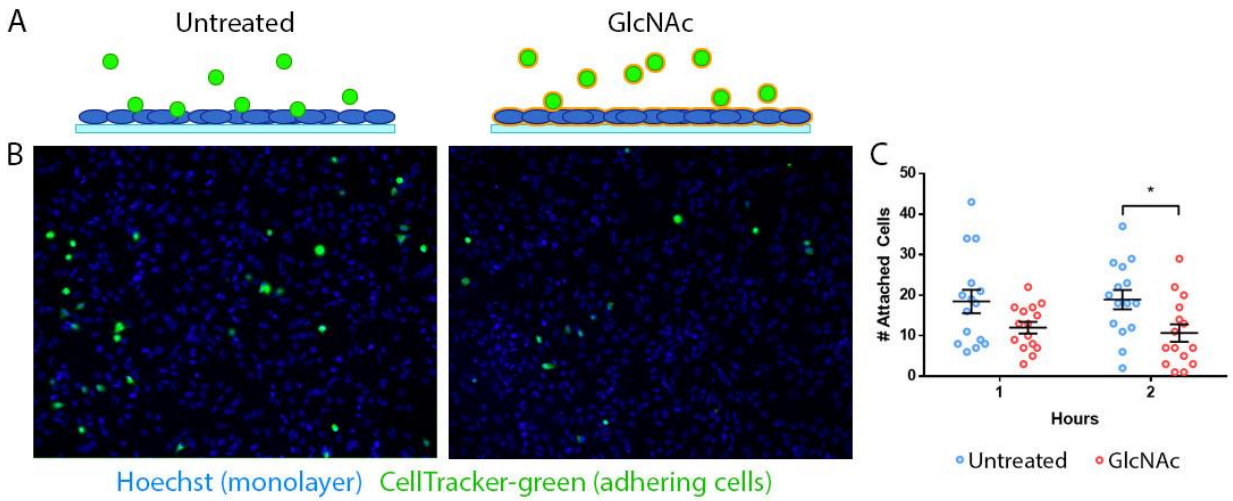

Figure 5.2. GlcNAc-treated NSPCs have diminished cell-cell adhesion. A) Cartoon diagram depicting the monolayer adhesion assay. NSPCs were grown as a monolayer (blue) on glass coverslips. Dissociated cells, either control or GlcNAc-treated (orange outline), were labeled with CellTracker green fixable fluorescent dye (green) and seeded onto the confluent monolayer. Cells not attached were washed away, and the remaining cells adhered to the monolayer were quantified. B) Example fluorescence images depict fewer GlcNAc-treated NSPCs (green) bound to the monolayer (Hoechst) compared to the control untreated cells. C) Quantitation of the number of cells attached to the monolayer. GlcNAc-treated NSPCs had reduced adherent cells. (n=3; *$p<0.05$).

One of the proteins that showed low expression in GlcNAc-treated cells in the proteomic screen was N-cadherin. N-cadherins are critical for the structural maintenance of all organs (*19*) and are indispensable for early nervous system development as they stabilize the structure, shape, and closure of the neural tube (*20*). Their normal expression throughout embryonic development allow NSPCs *in vivo* to retain apical-basal polarity (*21*), and compromised

expression results in precocious neurogenesis and randomization of the cortical lamina during development (*22-25*). However, N-cadherin expression has not been linked to NSPC fate choice along the neuron-astrocyte axis. Immunostaining for N-cadherin in untreated and GlcNAc-treated NSPC monolayers suggest reduction of N-cadherin links at the cell-cell junction within GlcNAc-treated NSPCs when compared to untreated control cells (Fig. 5.3). Taken together, these data suggest that cell-cell adhesion is significantly reduced when N-glycan branching is enhanced. This effect is partially mediated by either the diminished expression or binding of N-cadherin receptors across two cells.

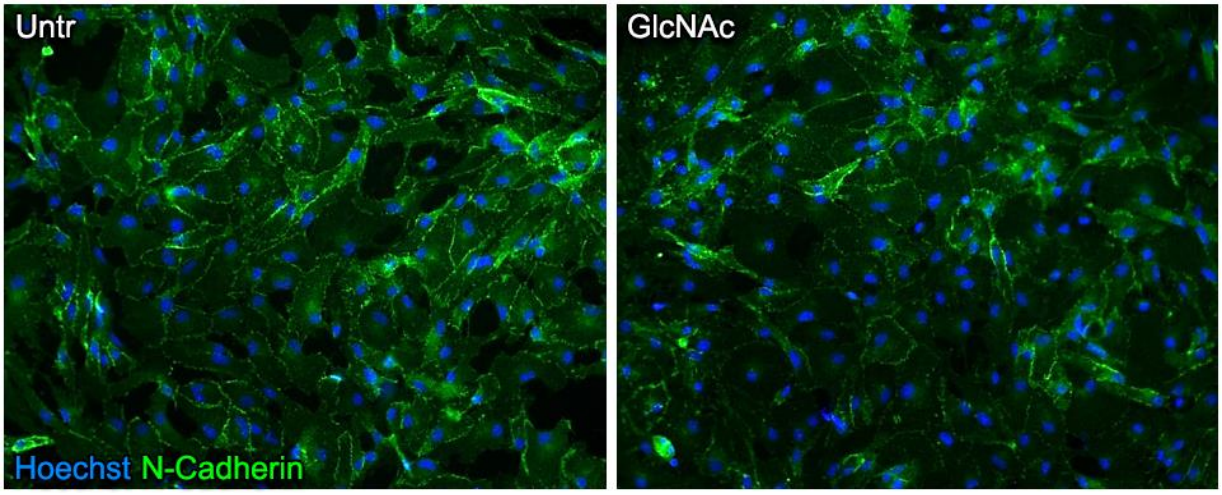

Figure 5.3. N-cadherin expression is disrupted in GlcNAc-treated cells. Fluorescence images showing the change in expression of N-cadherin with GlcNAc treatment of E12 mouse NSPCs grown as a monolayer. N-cadherin "tracks" appear disrupted in the GlcNAc-treated sample, and N-cadherin labeling was less evident at cell-cell borders.

5.2.3 N-glycan branching alters NSPC adhesion and migration on different ECM substrates

In addition to proteins that regulate cell-cell adhesion, the cell surface expression of cell-ECM interacting proteins such as integrins was also reduced on GlcNAC-treated NSPCs.

Integrins are a family of ECM-binding proteins that form heterodimers with α and β subunits; the type of ECM bound is determined by the particular α and β subunits in the heterodimer. Integrins allow for adhesion to and migration along a variety of different substrates. Integrin expression and their interaction with the extracellular environment plays a substantial role in neural development *in vivo* and *in vitro* (*26*) including NSPC fate decisions in vitro (*27, 28*). Our MS analysis indicated that αV and β1 integrins were down-regulated on mouse NSPCs after GlcNAc treatment, and analysis of GlcNAc treated human cells showed that αV, α2, α5, α6, α7, β1, β8 were all reduced on treated cells.

We tested whether these changes to integrin expression impact cell-ECM binding and adhesion. We first performed a static adhesion assay. Dissociated control and GlcNAc-treated E12 NSPCs were seeded onto fibronectin-coated glass coverslips. After 30, 90, and 180 minutes, cells were gently washed and the remaining cells were quantified. GlcNAc-treated NSPCs had significantly fewer cells remaining on the fibronectin substrate after 90 and 180 minutes when compared to untreated NSPCs (Fig. 5.4A). This assay is challenging due to the varied rate and force of washing in static conditions. To better control for the forces that are meant to dislodge loosely attached cells, we developed a microfluidic assay where we can control the flow rate that is pushing against the attached cells. Control and GlcNAc-treated NSPCs were thus seeded into a fibronectin-coated microfluidic channel and subjected to an increasing flow rate. Similar to our static well assay, GlcNAc-treated NSPCs were less resilient to an increasing flow rate and significantly more cells were dislodged compared to the untreated NSPCs (Fig. 5.4B). Taken together, these data indicate that N-glycan branching reduces cell-ECM adhesion to fibronectin.

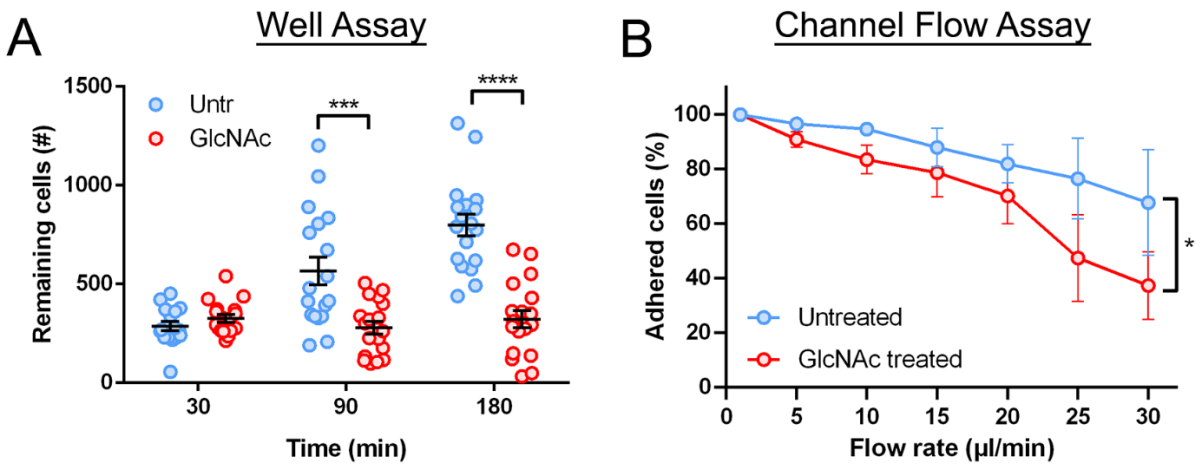

Figure 5.4. N-glycan branching reduces NSPC adhesion to fibronectin. Control and GlcNAc-treated NSPCs were dissociated and seeded onto fibronectin-coated glass. After 3 hours, non-adherent cells were washed. GlcNAc-treated NSPCs bound less tightly to fibronectin than the untreated cells at the 90 min (two-tailed Student's t-test, p=0.0006) and 180 min timepoints (p<0.0001). B) Cells seeded into a microchannel coated with fibronectin were subjected to increasing amounts of flow to induce shear stress. GlcNAc-treated NSPCs were able to be dislodged significantly more often than untreated NSPCs at increasing flow rates (linear regression, p=0.0373). (N=3, *p<0.05, ***p<0.001, ****p<0.0001)

Integrins are also invariably linked to cell migration and their function is important for patterning in a number of different organs (*29*). N-linked glycosylation has been reported to alter the functional activity of integrins. For instance, integrins with increased N-glycan branching, generated by the enzyme MGAT5 (see Chapter 4), promote cellular migration and metastatic behavior in cancer-derived cells *in vitro* (*30*). Whether a similar behavior is seen in NSPCs has yet to be elucidated. We tested whether migration on different substrates is impacted by N-glycan branching by seeding whole neurospheres on either laminin or fibronectin-coated glass coverslips and allowing the cells to spread for 24 hours (Fig. 5.5A). The distance traveled by the radially migrating cells was indistinguishable between the control and GlcNAc-treated NSPCs on laminin. However, GlcNAc-treated NSPCs on fibronectin migrated further than the untreated NSPCs (Fig. 5.5B). These data suggest that one role of glycosylation may be to selectively alter the interaction of specific integrin heterodimers with particular components of the ECM.

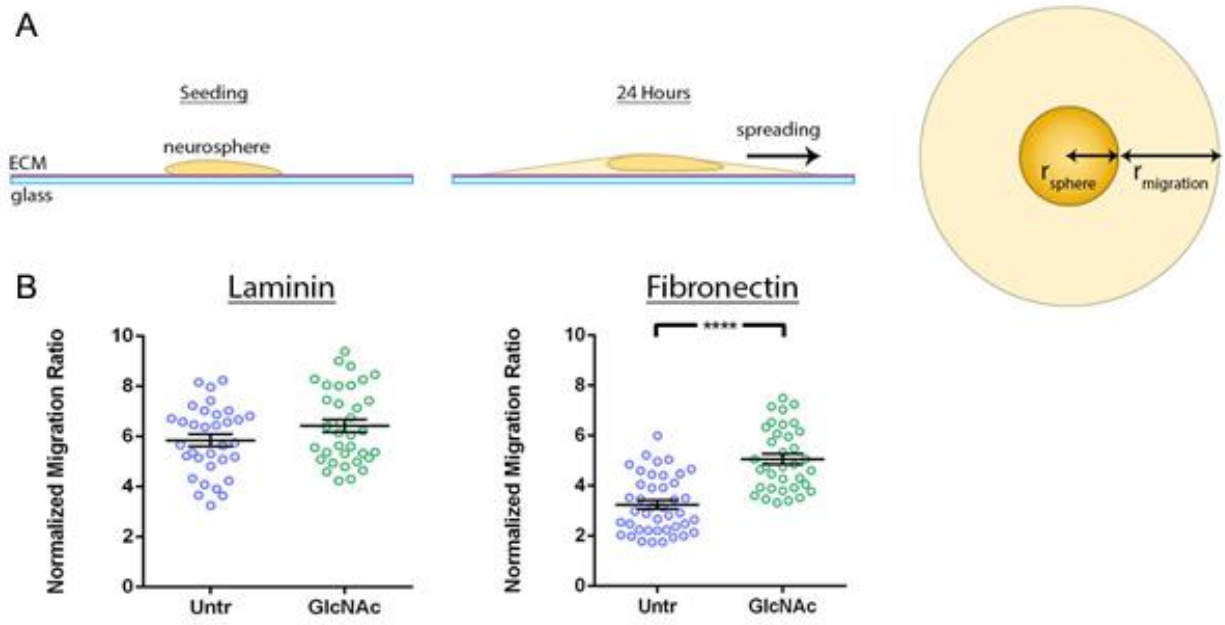

Figure 5.5. GlcNAc-treatment increases NSPC migration on fibronectin. A) Cartoon schematic indicating neurosphere spreading after being seeded onto ECM-coated glass. After 24 hours, individual NSPCs migrated away from the site of neurosphere attachment. The distance (μm) was measured from the edge of the original sphere to the edge of the expanded region ($r_{migration}$). Distance was normalized to radius of the sphere (r_{sphere}) to generate a ratio (normalized migration ratio) to account for variability in sphere size. B) NSPCs seeded onto fibronectin but not laminin, exhibited enhanced migration after treatment with GlcNAc. (n=3; ***p<0.001, ****p<0.0001)

Integrins and their associated ECM binding partners impact NSPC fate potential in vitro. We found previously that GlcNAc-treated NSPCs on laminin form more astrocytes and fewer neurons upon differentiation (*1*). Since αV and β1 integrins were altered after GlcNAc treatment and heterodimers of these integrins bind fibronectin, we tested whether increasing N-glycan branching with GlcNAc treatment altered NSPC differentiation on fibronectin. Compared to controls, GlcNAc-treated NSPCs on fibronectin formed more neurons while astrocyte differentiation was unchanged (Fig. 5.6). These data could show that highly-branched N-glycans induce differential responses to distinct ECM molecules, such that an increase in highly branched

N-glycans on integrins leads to more astrocytes in an environment rich in laminin but more neurons in the presence of fibronectin.

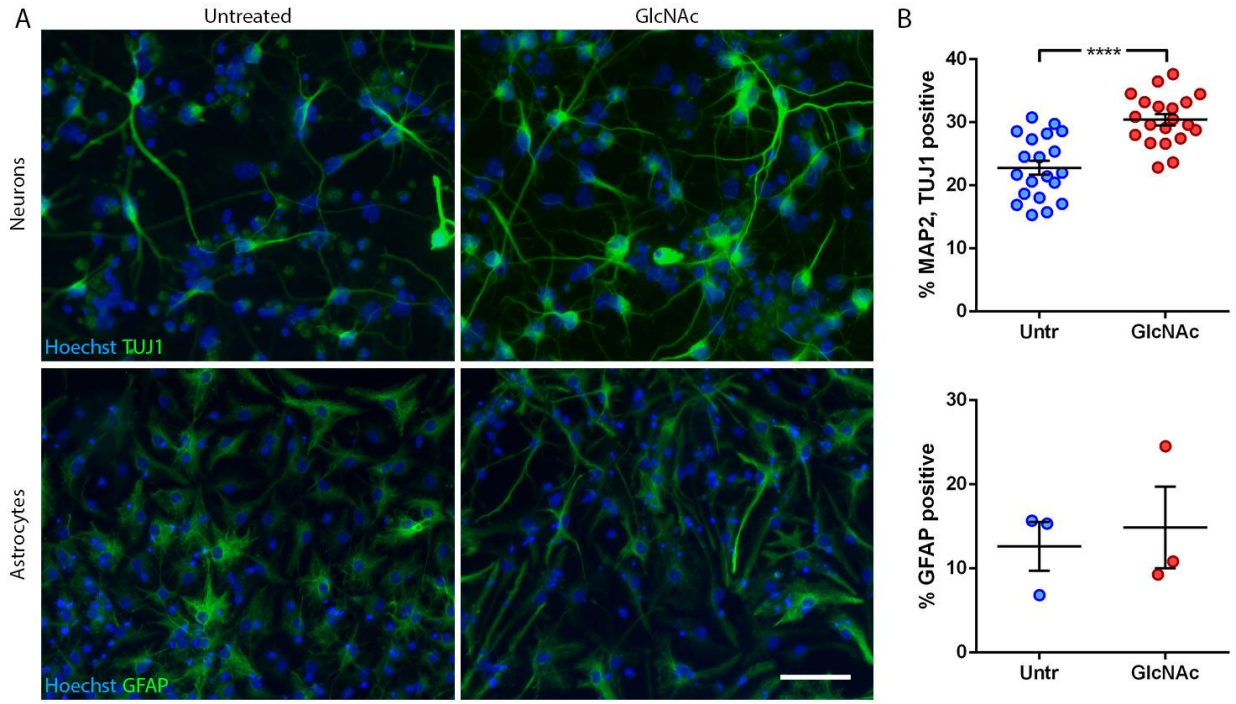

Figure 5.6. GlcNAc-treatment affects NSPC differentiation on fibronectin. A) E12 NSPCs were treated with GlcNAc and differentiated on fibronectin for 72 hours. Neurons were labeled with TUJ1 (green). Astrocytes were stained for GFAP (green). All cells were counterstained with Hoechst nuclear dye (blue). There appeared to be more TUJ1-positive neurons in the GlcNAc sample. Astrocyte numbers were not observed to be different; however, morphology appeared changed. Astrocytes derived from control NSPCs appeared to have a flatter morphology compared to those derived from GlcNAc-treated NSPCs, which exhibited extended processes and a more stellate shape. B) Significantly more MAP2/TUJ1-positive neurons were formed from GlcNAc treated NSPCs. The percentage of GFAP-positive cells was not different for control and GlcNAc treated NSPCs. (n=3, ****p<0.0001)

5.2.4 Changes to N-glycan branching alters Yap nuclear localization

An important signaling pathway downstream of cell adhesion is the Hippo signaling pathway, which has been linked to the control of organ size during development (*31, 32*). The major downstream effectors of the Hippo pathway are the two co-nuclear factors Yap and Taz.

Yap/Taz can be found either within the nucleus or the cytoplasm. When activated, Yap/Taz are redistributed into the nucleus and they regulate growth and proliferation. Yap activity has been linked to mechanotransduction through sensing stretch or tensile forces at the cell membrane (*33, 34*) and could be transmitted through actin remodeling in the cytoskeleton (*35-37*). Both cadherins and integrins are linked to the cytoskeleton and can affect actin filament remodeling (*32, 38-40*). Despite the relationship of Yap/Taz and cellular adhesion being clear, the links between N-glycosylation, cellular adhesion, and Hippo signaling remain undescribed. We stained control and GlcNAc-treated E12 NSPCs for the Yap protein to assess subcellular localization. We found Yap was strongly redistributed to the nucleus of NSPCs compared to the untreated NSPCs. Since GlcNAc-treated NSPCs exhibit reduced cell adhesion (Fig. 5.1, Fig. 5.2, Fig. 5.3), the proteins mediating the differences in adhesion may transduce mechanosensory signals and affect NSPC fate potential through the Hippo signaling pathway.

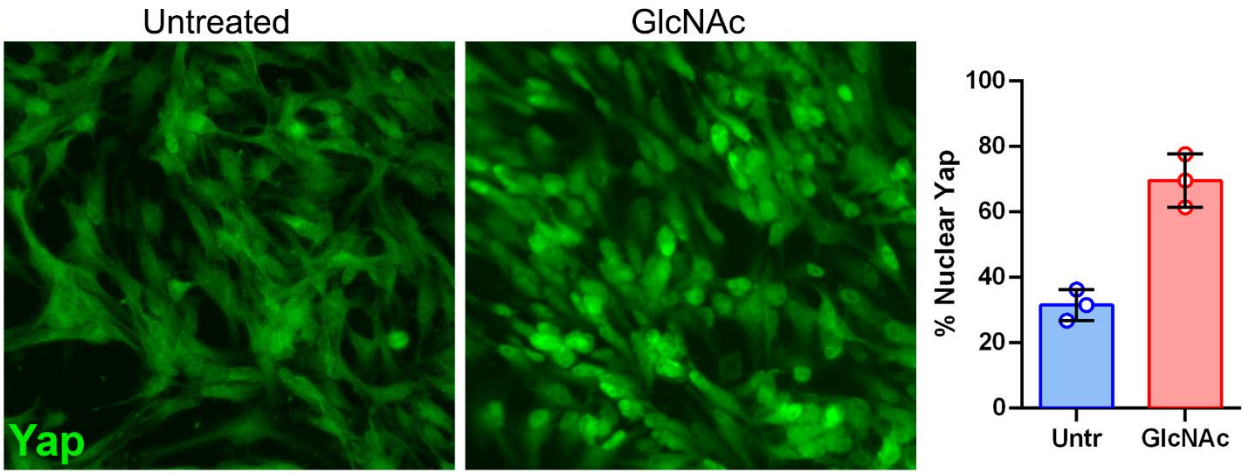

Figure 5.7. Yap is predominantly localized to the nucleus in GlcNAc-treated NSPCs. Yap immunostaining of E12 NSPCs. Quantitation of the proportion of Yap within the nucleus indicate that GlcNAc-treatment redistributes Yap out of the cytoplasm (n=1).

5.3 DISCUSSION

We identify the N-glycosylation branching pathway as a regulatory system for NSPC adhesion. Our preliminary mass spectrometry analysis indicated a reduction in both cell-cell and cell-ECM proteins expressed within the GlcNAc-treated NSPCs compared to untreated cells. Consequently, we found direct cell-cell adhesion was reduced in GlcNAc-treated NSPCs when analyzed by both a neurosphere formation assay and a monolayer adhesion assay. Enhanced N-glycan branching also correlated with a decrease in N-cadherin labeling in a monolayer of NSPCs. Concomitantly, GlcNAc treatment reduces NSPC adhesion to fibronectin substrates, but also enhances their migration on the ECM substrate. Interestingly, when testing differentiation of GlcNAc-treated NSPCs on fibronectin, we observed the opposite effect to that observed on laminin (*1*). GlcNAc treatment enhanced neuron formation, but had no change in astrocyte formation on fibronectin. Lastly, GlcNAc treatment enhanced Yap nuclear localization, potentially identifying a novel mechanism by which cell surface glycosylation impacts cell adhesion receptors, leading to a change in Yap/Taz signaling that impacts NSPC fate potential. Taken together, these data suggest the different glycosylation patterns that exist on neurogenic or astrogenic progenitors may regulate cell surface proteins that guide or restrict their fate potential.

The expression of a variety of cell adhesion proteins at the cell surface is less abundant on GlcNAc-treated sample compared to control. The data we present suggest decreased cellular adhesion to a number of substrates including other cells and the extracellular matrix. A proteomics study between wild type (WT) and *Srd5a3* mutant cerebellar cells found differences in IgSF-CAM expression (*41*). *Srd5a3* encodes the enzyme that synthesizes dolichol, the lipid carrier for all N-glycans prior to their transfer to a peptide within the ER. Since IgSF-CAMs are a family of cell adhesion molecules that include neural cell adhesion molecule (NCAM), a highly

expressed protein in the nervous system that carries the glycan polysialic acid (PSA), it is possible that cell adhesion in neural progenitor cells throughout the CNS is most impacted by changes in N-glycosylation.

NSPC cell-cell adhesion is reduced when N-glycosylation branching is enhanced, potentially by a reduction in N-cadherin expression and binding at the cell surface. In the cancer field, strong ties between cadherins and glycosylation have been outlined. Aberrant glycosylation of E-cadherin results in malignant proliferation and metastatic invasiveness of tumorigenic cells (*13, 17, 42-44*). Similarly, N-glycosylation exerts a similar control over N-cadherin. Reduced N-glycan branching increased N-cadherin-mediated contacts, stabilized adhesion junctions, and reduced cellular migration (*15, 45*). N-cadherin is highly expressed by NSPCs in the VZ/SVZ or neurogenic niche during early embryonic development (*46, 47*), is meant to stabilize the architecture of the nervous system (*46, 48*), and is highly expressed in the apical domain of an NSPC to maintain apical to basal polarity (*49-51*). Downregulation of N-cadherin in the neuron-forming daughter cell during asymmetric division, that is the formation of an NSPC and a neuron, is necessary for apical detachment, cell cycle exit, and migration toward the cortical plate (*52, 53*). Thus N-cadherin promotes NSPC self-renewal and maintenance of the neurogenic niche, and its downregulation induces neurogenesis (*52-54*).

How glycosylation might regulate N-cadherin function in NSPCs is not known. Highly-branched N-glycans are increasingly expressed during late cortical development within the mouse (*1*), coinciding with the switch from neurogenesis to gliagenesis. Furthermore, MGAT5 deficiency causes decreased neuron formation within the developing cortex (see Chapter 4). Thus, it is possible that loss of MGAT5 in NSPCs during development could cause persistent N-cadherin expression and functional adhesion even during neurogenesis, thus preventing neuronal

progenitors from forming neurons normally *in vivo*. Conversely, enhancing N-glycan branching by GlcNAc supplementation could reduce N-cadherin-mediated cell adhesion and cause precocious differentiation of cells *in vitro*, thus forming more astrocytes than neurons due to loss of neuronal progenitor maintenance (*1*). Taken together, our data links N-glycosylation branching to the control of cell-cell adhesion in NSPCs, and potentially provides a mechanism through which N-glycan branching could impact NSPC differentiation through the modulation of N-cadherin.

Our preliminary mass spectrometry study identified multiple integrin subunits that were downregulated due to enhanced N-glycan branching, including laminin and fibronectin-binding integrins. The binding and interaction to different ECM proteins expressed throughout neural development change over time (*55, 56*) and is dependent on the integrins being expressed on the cell surface. β1 subunit-containing integrins are the most ubiquitously expressed throughout the developing central nervous system, and specific integrin heterodimers such as α6β1, α3β1, and αvβ1 are important for NSPC maintenance and cortical layer formation *in vivo* (*57-60*). While these integrin heterodimers confer strong affinity toward laminin, suppression of β1 *in vitro* does not impact fibronectin binding suggesting expression of other integrin heterodimers, including αvβ5 or αvβ8, may regulate binding and interaction to other matrix molecules (*60, 61*). Adhesion to fibronectin is weakened when N-glycan branching is enhanced (Fig. 5.4), but migration along the substrate is increased (Fig. 5.5). Cell spreading and attachment to fibronectin is reduced in mammary epithelial tumor cells with an MGAT5 genetic knockout (*16, 62*). MGAT5 overexpression, which is similar to GlcNAc supplementation, in cancer cells does not affect fibronectin-binding integrin subunit (α5 and β1) expression, but rather reduces integrin clustering along the cell surface, resulting in less adhesion but more migration on fibronectin (*16*).

Interestingly, the same study showed that MGAT5-mediated N-glycan remodeling was specific to the β1 integrin subunit and not the α5 subunit suggesting a protein dependent effect of N-glycan branching (*16*). This may explain why the effect on cellular migration appears to be most prominent on fibronectin instead of laminin.

The integrins expressed on the cell surface could dictate or modulate how a cell interacts with the ECM. Human NSPCs exhibited enhanced growth and differentiation when grown on laminin as opposed to fibronectin (*28*). These cells expressed high levels of laminin-binding integrin subunits (*28*). The differentiation potential of GlcNAc-treated NSPCs on fibronectin was opposite to what we had previously observed when the cells were differentiated on laminin (*1*). This was unexpected since integrins that bind to both fibronectin and laminin were decreased within the GlcNAc-treated NSPC sample. It is possible that different subunits of integrins are differentially affected by a change in N-glycosylation. Alternatively, there could be a difference in integrin and growth factor receptor crosstalk (*63-66*) that is somehow altered by changes in N-glycosylation. Overexpression of β4 integrin subunit induces NSPC differentiation, an effect that is dependent on FGFR2 signaling (*67*). N-glycosylation could also impact the receptors of other signaling systems (eg. EGFR, PDGFR, FGFR, IGFR, etc.), and there is some evidence that N-glycosylation alters crosstalk between integrin α5 and EGFR signaling (*68, 69*). A similar mechanism could be occurring here with the GlcNAc-treated NSPCs, although more experiments are necessary to understand the underlying signaling cascades.

We found the transcription factor Yap is redistributed to the nucleus in GlcNAc-treated NSPCs (Fig. 5.6). The Hippo signaling pathway and cellular adhesion are well described regulators of organ size during development (*70-72*). Hippo downstream effectors, Yap and Taz are crucial components of mechanotransduction systems (*33, 73*) and their activation is linked to

cell adhesion and the state of the actin cytoskeleton (*37*). The role of Yap signaling is now being looked at more closely in the neural lineage. Yap activation is linked to the stretch-activated ion channel Piezo1, which regulates NSPC differentiation (*33*). During retinal development, Yap signaling promotes proliferation of progenitor cells while inhibition induces differentiation (*74*). Yap was previously detailed to be selectively expressed by neocortical NSPCs and astrocytes *in vivo* and *in vitro* (*75-77*). Isolated Yap-deficient E14.5 NSPCs grown in culture displayed no change to neuron formation but a significant decrease to astrocyte production *in vitro* (*75*) Furthermore, conditional knockout of Yap in nestin-positive cells resulted in decreased BLBP- and Aldolase C-positive astrocytes throughout the cortex but not the hippocampus (*75*). In another study, viral infusion and local expression of a constitutively active Yap in the VZ/SVZ of embryonic cortices reduced Sox2 expression and formed ectopic clusters at E18.5; this effect was not seen when activated Yap was expressed earlier at E13.5 suggesting molecular mechanisms that enable Yap sensitivity are not turned on until late stage cortical development (*78*). GlcNAc-treatment induced redistribution of Yap into the nucleus (Fig. 5.6) and increased formation of GFAP-expressing cells *in vitro* (*1*). We have potentially identified a novel mechanism that links N-glycosylation branching, cell adhesion receptors, and Yap/Taz signaling in the regulation of NSPC fate potential.

5.4 FUTURE DIRECTIONS

This study utilized various assays to assess the functional impacts of enhanced N-glycan branching on both cell-cell and cell-ECM adhesion. We find that the ability for cells to adhere to one another and to the ECM, specifically fibronectin, was significantly diminished in the GlcNAc-treated samples. The adhesion proteins impacted by the changing glycosylation patterns

remain to be determined. Our proteomic analysis identified decreased expression of cell adhesion proteins on the membranes of GlcNAc treated NSPCs. Future work will utilize antibodies to confirm the expression of the different proteins by flow cytometry. Lastly, we identified a significant redistribution of the YAP transcription factor into the nucleus when cells were treated with GlcNAc. While YAP signaling is known to be intertwined with cellular adhesion (both cell-cell and cell-ECM), it is unknown how N-glycan branching could affect this process. We will utilize models of reduced N-glycan branching (kifunensine treatment, MGAT5-NULL NSPCs) to determine whether loss of N-glycan branching has an impact on NSPC subcellular localization of YAP. Future studies involving the disruption of cellular adhesion and downstream effectors of either cadherin or integrin-mediated signaling will help us understand how N-glycan branching could modulate NSPC differentiation through the YAP signaling pathway.

5.5 MATERIALS AND METHODS

NSPC cell culture:

CD-1 mice (Charles River) were purchased, selected randomly, and bred as approved by the University of California, Irvine Institutional Animal Care and Use Committee. Dorsal forebrain cortical tissue was dissected from the cerebral cortices of embryonic day 12.5 (E12) and 16.5 (E16) mice and placed in dissection buffer: PBS, 0.6% glucose, 50 U/mL Pen/Strep. Cortical tissue from multiple embryos within the same litter was pooled, and a subsequent culture from a single litter was considered a biological repeat. The tissue was dissociated using 0.05% Trypsin-EDTA at 37^{o} C for 10 min. Afterward, trypsin was inhibited using soybean trypsin inhibitor (Life Technologies) and dissociated cells were re-suspended in proliferation medium containing DMEM, 1x B27, 1x N2, 1 mM sodium pyruvate, 2 mM L-glutamine, 1 mM

N-acetylcysteine, 20 ng/mL EGF, 10 ng/mL bFGF, and 2 µg/mL heparin. Cells were seeded at 150,000 cells/mL into non-tissue culture treated plastic plates and grown as non-adherent spheres. Cell cultures were passaged approximately every 3 days using enzyme-free NeuroCult Chemical Dissociation Kit (Mouse) (StemCell Technologies). All NSPC cultures were passaged at least once prior to experimental use. NSPCs were plated as adherent cultures for differentiation. HCl-washed German glass coverslips (Assistant/Carolina Biological Supply, Burlington, NC) were pretreated with poly-D-lysine (40 µg/mL in milliQ H_20) for 5 minutes then coated with laminin (20 µg/mL in EMEM) at 37^o C for 24 hours prior to cell adhesion. Whole neurospheres were seeded onto the laminin-coated coverslips in proliferation medium. After 24 hours, proliferation medium was removed and replaced with differentiation medium (same components as proliferation medium but excluding EGF, bFGF, and heparin) to induce differentiation. NSPCs were differentiated into neurons and astrocytes in these conditions for 3 days.

GlcNAc treatment of NSPCs:

A stock solution of 800 mM N-acetylglucosamine (GlcNAc) was prepared in proliferation medium. For dose response experiments, the stock solution was added to E12 NSPC cultures in proliferation medium to create final concentrations ranging from 20 to 80 mM GlcNAc and the same concentration of GlcNAc was maintained in the differentiation medium. The medium was re-supplemented with fresh GlcNAc every 24 hours for 3 days since GlcNAc breaks down over time in aqueous solutions. For some experiments NSPCs were treated with 80 mM GlcNAc for 3 days in proliferation medium then dissociated for analysis. Experiments designed to test the effects of GlcNAc at different stages of cell growth and differentiation used GlcNAc supplementation in either the proliferation medium only (and not the differentiation

medium), the differentiation medium only (and not the proliferation medium), or treated throughout proliferation and differentiation so included in both media. When GlcNAc was added to differentiation medium, the GlcNAc stock was also prepared in differentiation medium and GlcNAc was re-supplemented daily in the culture media. Control cells were grown in medium lacking supplementation with GlcNAc. GlcNAc was withdrawn during differentiation conditions.

Mass spectrometry of NSPC proteins

Approximately $2x10^7$ NSPCs were washed with PBS containing 0.6% glucose twice. Cells were suspended in an ice-chilled hypotonic solution (1x PBS diluted 1:10) containing AEBSF and leupeptin protease inhibitors and lysed by freeze-thaw cycling between a dry ice/ethanol bath and 37° C water bath. The sample was centrifuged at 100 x g for 15 min at 4° C to remove nuclei, large organelles, and unlysed cells. The supernatant was collected and further centrifuged at 100,000 x g for 1 hour at 4° C using a Beckman Ultracentrifuge (rotor SW41). The supernatant containing cytoplasmic proteins was discarded, and the pellet containing the cell membrane fraction was isolated and sent to Dr. Paul Gershon's lab at the University of California, Irvine for peptide degradation and mass spectrometry analysis.

Nano-liquid chromatography-tandem mass spectrometry (nanoLC-MS/MS) was carried out at the UCI Proteomics MS Facility to determine the membrane proteomes of E12, GlcNAc-treated E12, and E16 NSPCs. Samples of cells to be compared (E12 vs. E12 GlcNAC-treated, E12 vs. E16) underwent stable isotopic labeling of trypsin-digested preparations prior to mix-back and nanoLC-MS/MS, using area-under-the peak quantitation of precursor spectral segments exhibiting the appropriate mass split to indicate isotopically labeled peptide pairs from the 2

samples (*79*). Protein identification and quantification used Mascot Distiller software and in-house code written by Dr. Gershon.

Fate analysis

For fate analysis, at least 3 independent sets of NSPCs derived from 3 different litters were analyzed using manual counting software built into ImageJ. The percentage of cells that differentiated into double-positive MAP2/TUJ1 neurons with neurite lengths of at least 3 times the length of the soma was calculated from 5 randomly selected fields per experiment with more than 1000 cells counted per experimental group in each of the 3 independent experiments, so over 3000 cells per group. The percentages of GFAP-positive astrocytes were calculated from randomly selected fields of cells adjacent to the sphere attachment site but not from the dense cells within the sphere since cell density and cell death affect astrocyte GFAP reactivity. Cells expressing GFAP in a filamentous cytoskeletal pattern were counted as astrocytes and 3000 or more cells per experimental group were analyzed.

Immunocytochemistry

Cell culture samples were fixed with 4% paraformaldehyde (4% paraformaldehyde, 5 mM MgCl2, 10 mM EGTA, 4% sucrose in PBS) for 10 min, and the cell membranes were permeabilized with 0.3% Triton-X 100 in PBS for 5 min. Cells were blocked using 5% BSA in PBS for 1 hour then incubated with the primary antibody for approximately 18 hours at 4º C and the secondary antibody for 2 hours at room temperature in the dark. Primary antibodies were diluted in 1% BSA in 1x PBS; secondary antibodies were diluted in 1x PBS. All cells were counterstained using a Hoechst 33342 nuclear dye (Thermo Fisher Scientific) and coverslips were mounted onto glass slides using ProLong Gold Antifade Mountant medium (Thermo Fisher Scientific). Cells were visualized using a Nikon Eclipse Ti-E fluorescence microscope at 20x

magnification, and all images were acquired using NIS Elements AR 4.51 image capturing and analysis software. See table below for antibodies and concentrations.

Table 5.1 Antibodies and dilutions

Item	Vendor	Catalogue #	Dilution
Mouse anti-NCADH IgG	BioLegend	844702	ICC: 1:100
Rabbit anti-TUJ1 IgG	Sigma	T2200	ICC: 1:100
Mouse anti-MAP2 IgG	Sigma	M9942	ICC: 1:200
Rabbit anti-GFAP IgG	Sigma	G9269	ICC: 1:200
Mouse anti-YAP IgG	Santa Cruz Biotech	Sc-101199	ICC: 1:200

NSPC migration assay

E12 NSPCs control or GlcNAc-treated were grown in suspension for 3 days. Neurospheres were then seeded onto laminin (20 ug/ul) or fibronectin coated glass coverslips (40 ug/ul). The glass used were 12 mm German glass with a photo etched grid (Bellco, SKU: 1916-91012). Phase contrast images were taken of random spheres after 15 minutes to ensure attachment. Using the photo etched grid to align, the same spheres were imaged after 24 hours. A circle was drawn around the original placement and shape of neurosphere attachment, r_{sphere}. An approximate circle was drawn around the maximal edge of the cells migrating outward, $r_{migration}$. A migration ratio was factored by $(r_{migration}-r_{sphere})/r_{sphere}$.

Monolayer adhesion assay

A monolayer of E12 NSPCs were grown on laminin-coated glass coverslips until confluency of 90% or more was accomplished. These monolayers were either control or GlcNAc-treated (80 mM). Suspended E12 NSPCs, either control or 3-day 80mM GlcNAc-treated, were dissociated and stained using CellTracker Green (ThermoFisher Scientific; C925). Cells were then seeded onto the monolayer at a concentration of 50,000 cells/ml. After 1 or 2 hours, cells were gently washed and fixed using 4% PFA. All cells were counterstained using a

Hoechst 33342 nuclear dye (Thermo Fisher Scientific) and coverslips were mounted onto glass slides using ProLong Gold Antifade Mountant medium (Thermo Fisher Scientific). Cells were visualized using a Nikon Eclipse Ti-E fluorescence microscope at 20x magnification, and all images were acquired using NIS Elements AR 4.51 image capturing and analysis software.

Static ECM adhesion assay

Dissociated E12 NSPCs, either control or 80 mM GlcNAc-treated, were seeded onto fibronectin-coated glass coverslips at a concentration of 25,000 cells/ml. After 30, 90, or 180 minutes, cells were gently washed, and the number of cells remaining were quantified.

Flow-based ECM adhesion assay

For this assay, we used a modified microfluidic channel, the LCEA device (*2*), that contained no printed electrodes. The microfluidic channel was coated with fibronectin (10 ug/ul) overnight by flowing in a fibronectin-containing wash solution by syringe pump. Afterwards, the channel was washed with 1x PBS, and dissociated E12 NSPCs were seeded into the channel. Cells were allowed to attach for 1 hour. Afterwards, an increasing flow rate starting at 5 ul/min and stepping up by increments of 5 ul/min was applied to the attached cells. A video feed attached to a microscope enabled visualization within the microfluidic channel. Each flow rate step was applied for 10 minutes. The remaining number of cells attached to the channel were quantified.

5.6 REFERENCES

1. A. R. Yale *et al.*, Cell Surface N-Glycans Influence Electrophysiological Properties and Fate Potential of Neural Stem Cells. *Stem Cell Reports* **11**, 869-882 (2018).
2. M. G. Simon *et al.*, Increasing label-free stem cell sorting capacity to reach transplantation-scale throughput. *Biomicrofluidics* **8**, 064106 (2014).
3. J. L. Nourse *et al.*, Membrane biophysics define neuron and astrocyte progenitors in the neural lineage. *Stem Cells* **32**, 706-716 (2014).
4. Y. Liu *et al.*, Identification of neural stem and progenitor cell subpopulations using DC insulator-based dielectrophoresis. *Analyst* **144**, 4066-4072 (2019).
5. F. H. Labeed *et al.*, Biophysical characteristics reveal neural stem cell differentiation potential. *PLoS One* **6**, e25458 (2011).
6. A. Y. L. Jiang *et al.*, High-throughput continuous dielectrophoretic separation of neural stem cells. *Biomicrofluidics* **13**, 064111 (2019).
7. L. A. Flanagan *et al.*, Unique dielectric properties distinguish stem cells and their differentiated progeny. *Stem Cells* **26**, 656-665 (2008).
8. T. N. G. Adams, A. Y. L. Jiang, P. D. Vyas, L. A. Flanagan, Separation of neural stem cells by whole cell membrane capacitance using dielectrophoresis. *Methods* **133**, 91-103 (2018).
9. K. S. Lau *et al.*, Complex N-glycan number and degree of branching cooperate to regulate cell proliferation and differentiation. *Cell* **129**, 123-134 (2007).
10. E. A. Partridge *et al.*, Regulation of cytokine receptors by Golgi N-glycan processing and endocytosis. *Science* **306**, 120-124 (2004).
11. C. Boscher *et al.*, Galectin-3 Protein Regulates Mobility of N-cadherin and GM1 Ganglioside at Cell-Cell Junctions of Mammary Carcinoma Cells. *Journal of Biological Chemistry* **287**, 32940-32952 (2012).
12. C. Boscher, I. Nabi, Galectin-3 and phospho-caveolin-1 promote integrin-dependent EGF activation of RhoA, circular dorsal ruffles and matrix remodeling. *Molecular Biology of the Cell* **23**, (2012).
13. S. S. Pinho *et al.*, E-cadherin and adherens-junctions stability in gastric carcinoma: functional implications of glycosyltransferases involving N-glycan branching biosynthesis, N-acetylglucosaminyltransferases III and V. *Biochim Biophys Acta* **1830**, 2690-2700 (2013).
14. R. Guo *et al.*, Glycogenes mediate the invasive properties and chemosensitivity of human hepatocarcinoma cells. *Int J Biochem Cell Biol* **45**, 347-358 (2013).
15. H. Guo, I. Lee, M. Kamar, M. Pierce, N-acetylglucosaminyltransferase V expression levels regulate cadherin-associated homotypic cell-cell adhesion and intracellular signaling pathways. *Journal of Biological Chemistry* **278**, 52412-52424 (2003).
16. H. Guo, I. Lee, M. Kamar, S. Akiyama, M. Pierce, Aberrant N-glycosylation of beta(1) integrin causes reduced alpha(5)beta(1) integrin clustering and stimulates cell migration. *Cancer Research* **62**, 6837-6845 (2002).
17. Y. Y. Zhao *et al.*, Functional roles of N-glycans in cell signaling and cell adhesion in cancer. *Cancer Sci* **99**, 1304-1310 (2008).
18. Y. Zhao *et al.*, N-acetylglucosaminyltransferase III antagonizes the effect of N-acetylglucosaminyltransferase V on alpha 3 beta 1 integrin-mediated cell migration. *Journal of Biological Chemistry* **281**, 32122-32130 (2006).

19. D. E. Leckband, J. de Rooij, Cadherin adhesion and mechanotransduction. *Annu Rev Cell Dev Biol* **30**, 291-315 (2014).
20. A. F. Paulson, M. S. Prasad, A. H. Thuringer, P. Manzerra, Regulation of cadherin expression in nervous system development. *Cell Adh Migr* **8**, 19-28 (2014).
21. S. Hirano, M. Takeichi, Cadherins in brain morphogenesis and wiring. *Physiol Rev* **92**, 597-634 (2012).
22. M. Kadowaki *et al.*, N-cadherin mediates cortical organization in the mouse brain. *Dev Biol* **304**, 22-33 (2007).
23. M. M. Guerra *et al.*, Cell Junction Pathology of Neural Stem Cells Is Associated With Ventricular Zone Disruption, Hydrocephalus, and Abnormal Neurogenesis. *J Neuropathol Exp Neurol* **74**, 653-671 (2015).
24. Y. Jossin *et al.*, Llgl1 Connects Cell Polarity with Cell-Cell Adhesion in Embryonic Neural Stem Cells. *Dev Cell* **41**, 481-495 e485 (2017).
25. E. Taverna, M. Gotz, W. B. Huttner, The cell biology of neurogenesis: toward an understanding of the development and evolution of the neocortex. *Annu Rev Cell Dev Biol* **30**, 465-502 (2014).
26. K. R. Long, W. B. Huttner, How the extracellular matrix shapes neural development. *Open Biol* **9**, 180216 (2019).
27. J. Arulmoli *et al.*, Static stretch affects neural stem cell differentiation in an extracellular matrix-dependent manner. *Sci Rep* **5**, 8499 (2015).
28. L. A. Flanagan, L. M. Rebaza, S. Derzic, P. H. Schwartz, E. S. Monuki, Regulation of human neural precursor cells by laminin and integrins. *J Neurosci Res* **83**, 845-856 (2006).
29. A. B. Prowse, F. Chong, P. P. Gray, T. P. Munro, Stem cell integrins: implications for ex-vivo culture and cellular therapies. *Stem Cell Res* **6**, 1-12 (2011).
30. J. Gu, N. Taniguchi, Roles of N-glycans on integrin-mediated signaling. *Glycobiology* **14**, 1062-1062 (2004).
31. B. C. Low *et al.*, YAP/TAZ as mechanosensors and mechanotransducers in regulating organ size and tumor growth. *FEBS Lett* **588**, 2663-2670 (2014).
32. F. X. Yu, B. Zhao, K. L. Guan, Hippo Pathway in Organ Size Control, Tissue Homeostasis, and Cancer. *Cell* **163**, 811-828 (2015).
33. M. M. Pathak *et al.*, Stretch-activated ion channel Piezo1 directs lineage choice in human neural stem cells. *Proc Natl Acad Sci U S A* **111**, 16148-16153 (2014).
34. A. Das, R. S. Fischer, D. Pan, C. M. Waterman, YAP Nuclear Localization in the Absence of Cell-Cell Contact Is Mediated by a Filamentous Actin-dependent, Myosin II- and Phospho-YAP-independent Pathway during Extracellular Matrix Mechanosensing. *J Biol Chem* **291**, 6096-6110 (2016).
35. D. E. Mason *et al.*, YAP and TAZ limit cytoskeletal and focal adhesion maturation to enable persistent cell motility. *J Cell Biol* **218**, 1369-1389 (2019).
36. M. Bush *et al.*, An ensemble of flexible conformations underlies mechanotransduction by the cadherin-catenin adhesion complex. *Proc Natl Acad Sci U S A* **116**, 21545-21555 (2019).
37. B. M. Gumbiner, N. G. Kim, The Hippo-YAP signaling pathway and contact inhibition of growth. *J Cell Sci* **127**, 709-717 (2014).
38. T. Sakai *et al.*, Integrin-linked kinase (ILK) is required for polarizing the epiblast, cell adhesion, and controlling actin accumulation. *Genes Dev* **17**, 926-940 (2003).

39. B. D. Hoffman, C. Grashoff, M. A. Schwartz, Dynamic molecular processes mediate cellular mechanotransduction. *Nature* **475**, 316-323 (2011).
40. R. Saffary, Z. Xie, FMRP regulates the transition from radial glial cells to intermediate progenitor cells during neocortical development. *J Neurosci* **31**, 1427-1439 (2011).
41. D. Medina-Cano *et al.*, High N-glycan multiplicity is critical for neuronal adhesion and sensitizes the developing cerebellum to N-glycosylation defect. *Elife* **7**, (2018).
42. J. C. de Freitas Junior *et al.*, Inhibition of N-linked glycosylation by tunicamycin induces E-cadherin-mediated cell-cell adhesion and inhibits cell proliferation in undifferentiated human colon cancer cells. *Cancer Chemother Pharmacol* **68**, 227-238 (2011).
43. F. Geng, B. Z. Shi, Y. F. Yuan, X. Z. Wu, The expression of core fucosylated E-cadherin in cancer cells and lung cancer patients: prognostic implications. *Cell Res* **14**, 423-433 (2004).
44. S. S. Pinho, C. A. Reis, Glycosylation in cancer: mechanisms and clinical implications. *Nat Rev Cancer* **15**, 540-555 (2015).
45. H. B. Guo, H. Johnson, M. Randolph, M. Pierce, Regulation of homotypic cell-cell adhesion by branched N-glycosylation of N-cadherin extracellular EC2 and EC3 domains. *J Biol Chem* **284**, 34986-34997 (2009).
46. K. Hatta, M. Takeichi, Expression of N-cadherin adhesion molecules associated with early morphogenetic events in chick development. *Nature* **320**, 447-449 (1986).
47. A. Dady, C. Blavet, J. L. Duband, Timing and kinetics of E- to N-cadherin switch during neurulation in the avian embryo. *Dev Dyn* **241**, 1333-1349 (2012).
48. I. Masai *et al.*, N-cadherin mediates retinal lamination, maintenance of forebrain compartments and patterning of retinal neurites. *Development* **130**, 2479-2494 (2003).
49. H. Inuzuka, C. Redies, M. Takeichi, Differential expression of R- and N-cadherin in neural and mesodermal tissues during early chicken development. *Development* **113**, 959-967 (1991).
50. F. Sakane, Y. Miyamoto, N-cadherin regulates the proliferation and differentiation of ventral midbrain dopaminergic progenitors. *Dev Neurobiol* **73**, 518-529 (2013).
51. A. Shitamukai, D. Konno, F. Matsuzaki, Oblique radial glial divisions in the developing mouse neocortex induce self-renewing progenitors outside the germinal zone that resemble primate outer subventricular zone progenitors. *J Neurosci* **31**, 3683-3695 (2011).
52. D. L. Rousso *et al.*, Foxp-mediated suppression of N-cadherin regulates neuroepithelial character and progenitor maintenance in the CNS. *Neuron* **74**, 314-330 (2012).
53. R. M. Das, K. G. Storey, Apical abscission alters cell polarity and dismantles the primary cilium during neurogenesis. *Science* **343**, 200-204 (2014).
54. G. K. Wong, M. L. Baudet, C. Norden, L. Leung, W. A. Harris, Slit1b-Robo3 signaling and N-cadherin regulate apical process retraction in developing retinal ganglion cells. *J Neurosci* **32**, 223-228 (2012).
55. J. D. Lathia, M. S. Rao, M. P. Mattson, C. Ffrench-Constant, The microenvironment of the embryonic neural stem cell: lessons from adult niches? *Dev Dyn* **236**, 3267-3282 (2007).
56. E. Georges-Labouesse, M. Mark, N. Messaddeq, A. Gansmuller, Essential role of alpha 6 integrins in cortical and retinal lamination. *Curr Biol* **8**, 983-986 (1998).
57. Q. Shen *et al.*, Adult SVZ stem cells lie in a vascular niche: a quantitative analysis of niche cell-cell interactions. *Cell Stem Cell* **3**, 289-300 (2008).

58. L. S. Campos *et al.*, Beta1 integrins activate a MAPK signalling pathway in neural stem cells that contributes to their maintenance. *Development* **131**, 3433-3444 (2004).
59. E. S. Anton, J. A. Kreidberg, P. Rakic, Distinct functions of alpha3 and alpha(v) integrin receptors in neuronal migration and laminar organization of the cerebral cortex. *Neuron* **22**, 277-289 (1999).
60. T. S. Jacques *et al.*, Neural precursor cell chain migration and division are regulated through different beta1 integrins. *Development* **125**, 3167-3177 (1998).
61. P. E. Hall, J. D. Lathia, N. G. Miller, M. A. Caldwell, C. ffrench-Constant, Integrins are markers of human neural stem cells. *Stem Cells* **24**, 2078-2084 (2006).
62. A. Lagana *et al.*, Galectin binding to Mgat5-modified N-glycans regulates fibronectin matrix remodeling in tumor cells. *Mol Cell Biol* **26**, 3181-3193 (2006).
63. R. A. Streuli, The making of an internist: an European view. *Vnitr Lek* **45**, 253-257 (1999).
64. M. W. Renshaw, L. S. Price, M. A. Schwartz, Focal adhesion kinase mediates the integrin signaling requirement for growth factor activation of MAP kinase. *J Cell Biol* **147**, 611-618 (1999).
65. T. V. Byzova *et al.*, A mechanism for modulation of cellular responses to VEGF: activation of the integrins. *Mol Cell* **6**, 851-860 (2000).
66. K. M. Yamada, S. Even-Ram, Integrin regulation of growth factor receptors. *Nat Cell Biol* **4**, E75-76 (2002).
67. L. Su *et al.*, Neural stem cell differentiation is mediated by integrin beta4 in vitro. *Int J Biochem Cell Biol* **41**, 916-924 (2009).
68. Q. Hang *et al.*, Integrin alpha5 Suppresses the Phosphorylation of Epidermal Growth Factor Receptor and Its Cellular Signaling of Cell Proliferation via N-Glycosylation. *J Biol Chem* **290**, 29345-29360 (2015).
69. Q. Hang *et al.*, N-Glycosylation of integrin alpha5 acts as a switch for EGFR-mediated complex formation of integrin alpha5beta1 to alpha6beta4. *Sci Rep* **6**, 33507 (2016).
70. C. G. Hansen, T. Moroishi, K. L. Guan, YAP and TAZ: a nexus for Hippo signaling and beyond. *Trends Cell Biol* **25**, 499-513 (2015).
71. R. Karaman, G. Halder, Cell Junctions in Hippo Signaling. *Cold Spring Harb Perspect Biol* **10**, (2018).
72. A. Fulford, N. Tapon, P. S. Ribeiro, Upstairs, downstairs: spatial regulation of Hippo signalling. *Curr Opin Cell Biol* **51**, 22-32 (2018).
73. S. Dupont *et al.*, Role of YAP/TAZ in mechanotransduction. *Nature* **474**, 179-183 (2011).
74. H. Zhang, M. Deo, R. C. Thompson, M. D. Uhler, D. L. Turner, Negative regulation of Yap during neuronal differentiation. *Dev Biol* **361**, 103-115 (2012).
75. Z. Huang *et al.*, YAP stabilizes SMAD1 and promotes BMP2-induced neocortical astrocytic differentiation. *Development* **143**, 2398-2409 (2016).
76. Z. Huang *et al.*, Neogenin Promotes BMP2 Activation of YAP and Smad1 and Enhances Astrocytic Differentiation in Developing Mouse Neocortex. *J Neurosci* **36**, 5833-5849 (2016).
77. Z. Huang, W. C. Xiong, Neogenin-YAP signaling in neocortical astrocytic differentiation. *Neurogenesis (Austin)* **3**, e1248735 (2016).

78. D. Han, M. Kwon, S. M. Lee, S. J. Pleasure, K. Yoon, Non-cell autonomous promotion of astrogenesis at late embryonic stages by constitutive YAP activation. *Sci Rep* **10**, 7041 (2020).
79. W. Chou, T. Ngo, P. D. Gershon, An overview of the vaccinia virus infectome: a survey of the proteins of the poxvirus-infected cell. *J Virol* **86**, 1487-1499 (2012).

CHAPTER 6

Conclusions and Future Directions

6.1 SUMMARY

Neural stem/progenitor cells (NSPCs) have shown great promise as a potential cure for neurodegenerative diseases and trauma, especially since the innate regenerative capacity of the central nervous system (CNS) is insufficient for damaged tissue restoration and functional recovery. However, we currently lack needed cellular characterization to predict cell behavior, leading to inconsistent results in transplantation therapies. Therefore, it is essential to gain a better understanding of the mechanisms that control NSPC development and their response to the environment to develop new brain repair strategies. In the work presented here, we used the application of a novel biophysical signature, membrane capacitance, to identify NSPCs biased toward either neuronal or glial fates, linked membrane capacitance to the N-glycan branching pathway, showed that branching directly impacts fate, found that the MGAT5 branching enzymes regulates NSPC differentiation in vitro and in vivo, and identified molecular mechanisms linking branching to regulation of NSPC function.

Development of the brain is highly regulated temporally and spatially (*1*), and NSPCs are responsible for sequentially generating all neurons, astrocytes, and oligodendrocytes in the brain. Identifying cell fate potential and differentiation bias, for example whether an NSPC will become a neuron or astrocyte, is a highly researched topic. Unfortunately, traditional cell surface markers used to detect NSPC fate bias, such as PSA-NCAM, have considerable overlap across cells biased to different fates and are thus insufficient for identifying differentiation bias. New

methods to characterize the differences between neuron or astrocyte-biased NSPCs will guide the field into generating new concepts for NSPC fate potential.

Prior to the work presented here, our lab pioneered the use of label-free, biophysical markers to discern fate bias in populations of human and rodent NSPCs (*2-11*). In particular, the electrophysiological property membrane capacitance, or the ability of the plasma membrane to store charge, is sufficient to discern neuron-biased and astrocyte-biased NSPCs (*2, 3, 5, 7-11*). Cells can be sorted on the basis of membrane capacitance using dielectrophoresis (DEP), which is the application of a non-uniform electric field that induces cell movement(*2, 3, 5, 9, 11*). As part of my thesis work, we developed new cell sorting devices that couple DEP and microfluidics to rapidly and continuously separate neuron-biased and astrocyte-biased NSPCs (*2, 9*) (Chapters 2 and 3). Future research can combine label-free and marker-based sorting to tailor stem cell-based therapies for neurological disease treatment.

The molecular basis of membrane capacitance has not been well understood. We hypothesized that N-glycosylation may contribute since the process forms large, charged sugars on the cell surface. We found that inhibition of N-glycosylation shifted the behavior of NSPCs within DEP (*5*). To fully understand the contribution of glycosylation to membrane capacitance, we first wanted to identify differences in glycosylation patterns that may underly differences to astrocyte-biased and neuron-biased cells. Since NSPCs in cortical development generate neurons first and later astrocytes (*1*), we isolated NSPCs from either E12 (neurogenic stage) or E16 (astrogenic stage) cortices. We found the N-linked glycosylation branching pathway to be of particular interest since a large number of enzymes involved were differentially expressed (*2*) (Chapter 3). Enhancing N-glycan branching by supplementing cells with N-acetylglucosamine (GlcNAc), a core modification of all N-glycans, was sufficient to shift membrane capacitance (*2*)

(Chapter 3). Additionally, changes to N-glycan branching accounts for nearly the entire difference in membrane capacitance between neuron or astrocyte-biased NSPCs (*2*) (Chapter 3). Lastly, we found that enhancing N-glycan branching significantly shifts the fate potential of NSPCs (*2*) (Chapter 3). This study revealed a novel link between fate-specific membrane capacitance, N-linked glycosylation, and NSPC fate potential.

Most studies detail N-glycosylation as a regulatory element for neuron axon targeting and synaptic maturation (*12, 13*). Its role in neurogenesis or NSPC fate potential was poorly described. Since we found that N-glycan branching was a significant regulator to NSPC fate potential *in vitro* (*2*) (Chapter 3), we sought to identify the relevant enzymes that process N-glycan branches and explore the impact N-glycan branching has on cortical development (Chapter 4). Since the enzyme MGAT5 is the primary enzyme for the highly-branched N-glycan synthesis, we utilized a transgenic mouse model deficient of MGAT5 to study the function of its activity in NSPCs. *In vitro*, NSPCs lacking MGAT5 produced more neurons and fewer astrocytes, showing that N-glycan branching can regulate NSPC fate (Chapter 4). During cortical development, loss of MGAT5 accelerated neuronal differentiation and depleted the NSPC pool (Chapter 4). Specifically, BRN2 progenitors in the VZ/SVZ were reduced (Chapter 4); these cells are responsible for generating upper layer neurons. These observations in the embryo were reflected postnatally as well as we found a significant reduction to both upper and deep layer neurons within the postnatal cortical plate along with significant cortical thinning in layers 5/6 (Chapter 4). Defects in glycosylation have been linked to various neurological diseases (*14*). Further studies into N-glycosylation and brain development may reveal new insights into characterizing NSPC fate potential and potentially new modalities to treat various CNS-related injuries and disorders.

N-glycosylation regulates the function of many cell surface proteins, impacting signaling pathways in cells (*15*). N-glycosylation can therefore affect how a cell perceives and translates the myriad extracellular cues it experiences. We performed an unbiased proteomic screen to determine which cell surface proteins were most changed by N-glycan branching and identified a variety of cell adhesion molecules that were downregulated when N-glycan branching increased (Chapter 5). We found that enhancing N-glycan branching significantly reduced NSPC both cell-cell and cell-ECM adhesion (Chapter 5). Furthermore, N-glycan branching significantly altered Yap localization in NSPCs (Chapter 5). Yap signaling is intricately tied to cell adhesion (*16*) and has been recently linked to the production of astrocytes both *in vitro and in vivo* (*17, 18*). However, the relationship between N-glycan branching, cellular adhesion, and Yap signaling in NSPCs has not been previously described. The studies in Chapter 5 potentially reveal a novel mechanism where N-glycosylation branching controls NSPC fate potential through cell adhesion-mediated Yap signaling.

6.2 DIRECTIONS FOR FURTHER RESEARCH

The work described in this thesis encompasses several fields, such as biomedical engineering, neural development and neural stem cell biology. Our studies present novel findings that can aid in the development of engineering tools to study cell biology. Additionally, our findings improve understanding of the critical role glycosylation plays in neural development, an under-researched area. As such, this work serves as a platform to expand upon these concepts, presenting new opportunities to expand our knowledge of stem cell biology and CNS development.

Do other glycans contribute to membrane capacitance and fate potential in NSPCs?

In Chapter 3, we focused on the N-glycosylation branching pathway since we discovered multiple enzymes of this pathway were differential expressed by neuron or astrocyte-biased NSPCs. However, a large portion of the cell surface glycocalyx contains highly-charged glycans such as glycosaminoglycans (GAGs), e.g. heparan sulfate (HS) and chondroitin sulfate (CS). The large charge differential of these sugars could hypothetically impact membrane capacitance. Previous studies show HS regulates neurogenesis by modulating FGF signaling. Understanding the contribution of GAGs to membrane capacitance and their relationship to NSPC fate potential will help us further elucidate the biological components that underly membrane capacitance.

What is the mechanism that drives neuronal depletion in the MGAT5-deficient model?

In Chapter 4, we described a model in which MGAT5 deficiency increases neuronal differentiation and decreases the progenitor pool, resulting in lower neuron numbers in the MGAT5 null cortex. Further research into the mechanism by which MGAT5 impacts neural development would be bolstered by a conditional knockout mouse model. *In vitro*, we found EdU labeling increased in the MGAT5-deficient NSPCs but failed to find additional evidence of altered proliferation in the MGAT5 null. Studies involving either cell-specific or acute knockdown of MGAT5 both *in vitro* and *in vivo* would help deepen our understanding of how MGAT5 and N-glycan branching impacts neural development.

Does N-glycan branching regulate astrogenesis during cortical development?

As Chapter 4 also describes, MGAT5-deficiency resulted in the generation of more neurons and fewer GFAP-positive astrocytes *in vitro*. We found a non-significant decrease in GFAP-expressing cells in the white matter tracts and the midline near the pial surface in MGAT5 null brains. However, most gray matter astrocytes express little GFAP and are thus unaccounted

for in our study. Future studies identifying astrocytes with more universal markers, such as ALDH1L1, could shed light on whether N-glycan branching affects both neuron and astrocyte formation during development.

Is the relationship between Yap localization and N-glycan branching correlative or causative?

In Chapter 5, we present evidence that Yap nuclear localization increases in GlcNAc-treated NSPCs. The mechanism underlying this shift is not fully understood. We hypothesize that decreased cellular adhesion contributes to the redistribution of Yap. Since Yap signaling is also a readout of mechanotransduction, future research into adhesive or other mechanosensory proteins on the cell membrane and their regulation via N-glycosylation would shed new light on how N-glycan branching controls NSPC fate potential.

6.3 BROADER IMPLICATIONS

The findings throughout this work could have broader implications for research regarding the identification of new markers that could potentially label fate-biased NSPCs. For instance, N-glycan modification by poly-sialic acid (PSA), which is predominately found on neural cell adhesion molecule (NCAM), was originally used to isolate NSPCs from both embryonic and fetal brain tissue (*19*). This particular sugar's role in differentiation bias is not well described, although our data indicates it may not be sufficient to resolve the differences between neuron and astrocyte-biased NSPCs (*2*) (Chapter 3). The glycan LewisX (LeX), or stage-specific embryonic antigen 1 (SSEA-1), is expressed by neural progenitors (*20-22*), and differences in LeX glycan substructure could identify distinct subpopulations of neural progenitors (*22*). More research is

needed to determine the phenotypic differences in subpopulations identified by unique LeX structures.

Our data identify the N-glycan branching pathway as a significant regulator of NSPC fate, and future studies will lead to a deeper understanding of the role glycosylation plays in stem cell differentiation. Immature astrocytes treated with the lectin DSL, which also binds to highly-branched N-glycans, formed mature GFAP-expressing and morphologically stellate astrocytes (*23*). A similar effect was seen when these cells were treated with Galectin-1 (*24*), a protein that binds to the galactose residues found on branched N-glycans. Furthermore, Galectin-1 is thought to suppress neurogenesis of neural progenitors found within the adult hippocampus (*25*). While the role for N-glycan branching in NSPC fate potential is not well described, we provide new evidence that N-glycan branching is a significant regulator of differentiation bias. In particular, increased N-glycan branching pushes NSPCs to generate more astrocytes (*2*) (Chapter 3). Conversely, we show that reduced N-glycan branching confers enhanced neurogenic potential (Chapter 4). These changes in NSPC fate potential specifically correlate with the binding affinity of the lectin L-PHA to branched N-glycans. Furthermore, E-PHA, a lectin that binds to N-glycans modified with a bisected GlcNAc residue known to halt N-glycan branching (see Chapter 4, Fig. 4.2), has been utilized to isolate NSPCs from both embryonic and adult rodent brains (*26*). A glycomics study revealed a selective upregulation of bisected N-glycans when pluripotent stem cells undergo neuronal differentiation (*27*). We present data showing the differential expression of MGAT3 and MGAT5 in neuron-biased and astrocyte-biased NSPCs, respectively (*2*) (Chapter 3). Highly-branched N-glycans may serve as markers for NSPC fate potential bias prior to differentiation.

Cell surface glycans linked to NSPC fate bias could enable the discovery of new proteins involved in specifying fate. The identification of LeX on the surface of NSPCs led to the finding that NSPCs express tenascin-C, phosphacan, L1-CAM, various integrins, Thy-1, LAMP-1, and CD24 at the plasma membrane (*22, 28*). In addition, a proteomic study involving LeX-mediated protein enrichment from NSPCs enabled the finding that LRP1 is necessary for NSPC differentiation into the oligodendrocyte lineage (*28*). Other studies utilized an azide-modified sialic acid that could be taken in by NSPCs and incorporated into sialic acid-containing glycans. The azide modification enabled a biotin and streptavidin-mediated protein enrichment process. Following mass spectrometry, IGSF8 was identified as a sialo-glycoprotein predominately expressed by TBR2-positive neuron progenitors in the sub-ventricular zone (*29*). We present evidence that increased N-glycan branching resulted in decreased abundance of cell adhesion proteins on the cell surface of NSPCs (Chapter 5). More specific methods to isolate N-glycan modified proteins from NSPCs would allow higher fidelity screening to identify more proteins that could impact NSPC fate potential.

Lastly, we provide evidence that MGAT5 and the production of highly-branched N-glycans play a significant role in cortical development (Chapter 4). We show that MGAT5-deficiency enhances the production NeuN-expressing mature neurons but simultaneously depletes all cells throughout the developing dorsal cortex, including upper and deep layer neurons (Chapter 4). The MGAT5-deficient mouse model exhibits several neurological phenotypes, including sensory and motor deficits, decrease in startle response, decrease in depression-like behavior, and a decrease in nurturing (*30, 31*). How MGAT5 stimulation of neurogenesis during neural development (Chapter 4) affects cortical connectivity and brain circuitry is largely unknown. MGAT5 is expressed in the VZ/SVZ (*32*) of the early developing

cortex (E9.5-E10.5), and throughout the intermediate zone at later stages (E11.5-E17.5) (*32*) where active cell migration and axon growth and targeting is occurring. Overexpression of MGAT5 in PC12 cells enhances NGF signaling through TrkA, most likely through opposition of endocytic recycling of the protein receptor, resulting in increased neurite outgrowth (*33*). Analysis of dendritic spine density in pyramidal neurons of the frontal cortex in the MGAT5 knockout mouse revealed remarkable sex differences. Male MGAT5-null mice exhibited increased spine density, whereas female MGAT5-null mice showed decreased spine density when compared to wild type littermate controls (*30*). Lastly, the function of the serotonin transporter (*34*), GABA transporter (*35*), and adrenergic receptors (*36*) are impacted by N-glycosylation. Neurons that utilize these proteins for neurotransmission are involved in the circuitry modulating stress related and/or depressive-like behavior (*36*, *37*). More work will be necessary to understand the developmental impacts of N-glycan branching on neurodevelopment and brain circuitry.

6.4 CLOSING STATEMENTS

The work presented throughout is due to extensive collaborative efforts across the fields of engineering and biology, and highlights two major novel findings. N-glycosylation and the complex remodeling of its branches are a significant molecular component that underlies the biophysical property, membrane capacitance. Secondly, N-glycan branching plays a significant role in NSPC fate potential and neurogenesis during cortical development. These findings will help identify new methods to characterize NSPCs, and aid in the discovery of new mechanisms that control differentiation with the prospect of utilizing NSPCs as a therapeutic for neurodegenerative disease and trauma.

6.5 REFERENCES

1. H. Okano, S. Temple, Cell types to order: temporal specification of CNS stem cells. *Curr Opin Neurobiol* **19**, 112-119 (2009).
2. A. R. Yale *et al.*, Cell Surface N-Glycans Influence Electrophysiological Properties and Fate Potential of Neural Stem Cells. *Stem Cell Reports* **11**, 869-882 (2018).
3. M. G. Simon *et al.*, Increasing label-free stem cell sorting capacity to reach transplantation-scale throughput. *Biomicrofluidics* **8**, 064106 (2014).
4. J. L. Prieto, J. Lu, J. L. Nourse, L. A. Flanagan, A. P. Lee, Frequency discretization in dielectrophoretic assisted cell sorting arrays to isolate neural cells. *Lab Chip* **12**, 2182-2189 (2012).
5. J. L. Nourse *et al.*, Membrane biophysics define neuron and astrocyte progenitors in the neural lineage. *Stem Cells* **32**, 706-716 (2014).
6. J. Lu *et al.*, Advancing practical usage of microtechnology: a study of the functional consequences of dielectrophoresis on neural stem cells. *Integr Biol (Camb)* **4**, 1223-1236 (2012).
7. Y. Liu *et al.*, Identification of neural stem and progenitor cell subpopulations using DC insulator-based dielectrophoresis. *Analyst* **144**, 4066-4072 (2019).
8. F. H. Labeed *et al.*, Biophysical characteristics reveal neural stem cell differentiation potential. *PLoS One* **6**, e25458 (2011).
9. A. Y. L. Jiang *et al.*, High-throughput continuous dielectrophoretic separation of neural stem cells. *Biomicrofluidics* **13**, 064111 (2019).
10. L. A. Flanagan *et al.*, Unique dielectric properties distinguish stem cells and their differentiated progeny. *Stem Cells* **26**, 656-665 (2008).
11. T. N. G. Adams, A. Y. L. Jiang, P. D. Vyas, L. A. Flanagan, Separation of neural stem cells by whole cell membrane capacitance using dielectrophoresis. *Methods* **133**, 91-103 (2018).
12. H. Scott, V. M. Panin, N-glycosylation in regulation of the nervous system. *Adv Neurobiol* **9**, 367-394 (2014).
13. H. Scott, V. M. Panin, The role of protein N-glycosylation in neural transmission. *Glycobiology* **24**, 407-417 (2014).
14. H. H. Freeze, E. A. Eklund, B. G. Ng, M. C. Patterson, Neurology of inherited glycosylation disorders. *Lancet Neurol* **11**, 453-466 (2012).
15. J. W. Dennis, I. R. Nabi, M. Demetriou, Metabolism, cell surface organization, and disease. *Cell* **139**, 1229-1241 (2009).
16. B. M. Gumbiner, N. G. Kim, The Hippo-YAP signaling pathway and contact inhibition of growth. *J Cell Sci* **127**, 709-717 (2014).
17. Z. Huang *et al.*, YAP stabilizes SMAD1 and promotes BMP2-induced neocortical astrocytic differentiation. *Development* **143**, 2398-2409 (2016).
18. Z. Han *et al.*, YAP/TEAD3 signal mediates cardiac lineage commitment of human-induced pluripotent stem cells. *J Cell Physiol* **235**, 2753-2760 (2020).
19. S. Pennartz *et al.*, Purification of neuronal precursors from the adult mouse brain: comprehensive gene expression analysis provides new insights into the control of cell migration, differentiation, and homeostasis. *Mol Cell Neurosci* **25**, 692-706 (2004).

20. A. Capela, S. Temple, LeX is expressed by principle progenitor cells in the embryonic nervous system, is secreted into their environment and binds Wnt-1. *Dev Biol* **291**, 300-313 (2006).
21. A. Capela, S. Temple, LeX/ssea-1 is expressed by adult mouse CNS stem cells, identifying them as nonependymal. *Neuron* **35**, 865-875 (2002).
22. E. Hennen, T. Czopka, A. Faissner, Structurally distinct LewisX glycans distinguish subpopulations of neural stem/progenitor cells. *J Biol Chem* **286**, 16321-16331 (2011).
23. T. Sasaki, T. Endo, Both cell-surface carbohydrates and protein tyrosine phosphatase are involved in the differentiation of astrocytes in vitro. *Glia* **32**, 60-70 (2000).
24. T. Sasaki, J. Hirabayashi, H. Manya, K. Kasai, T. Endo, Galectin-1 induces astrocyte differentiation, which leads to production of brain-derived neurotrophic factor. *Glycobiology* **14**, 357-363 (2004).
25. Y. Imaizumi *et al.*, Galectin-1 is expressed in early-type neural progenitor cells and down-regulates neurogenesis in the adult hippocampus. *Mol Brain* **4**, 7 (2011).
26. M. Hamanoue *et al.*, Cell surface N-glycans mediated isolation of mouse neural stem cells. *J Neurochem* **110**, 1575-1584 (2009).
27. M. Terashima, M. Amano, T. Onodera, S. Nishimura, N. Iwasaki, Quantitative glycomics monitoring of induced pluripotent- and embryonic stem cells during neuronal differentiation. *Stem Cell Research* **13**, 454-464 (2014).
28. E. Hennen *et al.*, A LewisX glycoprotein screen identifies the low density lipoprotein receptor-related protein 1 (LRP1) as a modulator of oligodendrogenesis in mice. *J Biol Chem* **288**, 16538-16545 (2013).
29. Q. R. Bai, L. Dong, Y. Hao, X. Chen, Q. Shen, Metabolic glycan labeling-assisted discovery of cell-surface markers for primary neural stem and progenitor cells. *Chem Commun (Camb)* **54**, 5486-5489 (2018).
30. L. Feldcamp *et al.*, Mgat5 modulates the effect of early life stress on adult behavior and physical health in mice. *Behav Brain Res* **312**, 253-264 (2016).
31. L. Soleimani, J. C. Roder, J. W. Dennis, T. Lipina, Beta N-acetylglucosaminyltransferase V (Mgat5) deficiency reduces the depression-like phenotype in mice. *Genes Brain Behav* **7**, 334-343 (2008).
32. M. Granovsky *et al.*, GlcNAc-transferase V and core 2 GlcNAc-transferase expression in the developing mouse embryo. *Glycobiology* **5**, 797-806 (1995).
33. X. Yang, J. Li, M. Geng, N-acetylglucosaminyltransferase V modifies TrKA protein, regulates the receptor function. *Cell Mol Neurobiol* **28**, 663-670 (2008).
34. A. Cooper, D. Woulfe, F. Kilic, Post-translational modifications of serotonin transporter. *Pharmacol Res* **140**, 7-13 (2019).
35. G. Cai *et al.*, The role of N-glycosylation in the stability, trafficking and GABA-uptake of GABA-transporter 1. Terminal N-glycans facilitate efficient GABA-uptake activity of the GABA transporter. *FEBS J* **272**, 1625-1638 (2005).
36. X. Li, M. Zhou, W. Huang, H. Yang, N-glycosylation of the beta2 adrenergic receptor regulates receptor function by modulating dimerization. *FEBS J* **284**, 2004-2018 (2017).
37. J. Haller *et al.*, Behavioral responses to social stress in noradrenaline transporter knockout mice: effects on social behavior and depression. *Brain Res Bull* **58**, 279-284 (2002).

APPENDIX A

Nanofibrous carbon multifunctional smart scaffolds for simultaneous cell differentiation and dopamine detection

Authors: *Alexandra Perebikovsky[1], *Alexander T. Hwu[2], **Andrew R. Yale[3]**, Maziar Ghazinejad[4,5], Marc Madou[1,4]

[1]Department of Physics and Astronomy, University of California, Irvine

[2]Department of Chemical and Biomolecular Engineering, University of California, Irvine

[3]Department of Anatomy and Neurobiology, University of California, Irvine

[4]Department of Mechanical and Aerospace Engineering, University of California, Irvine

[5]Department of Mechanical and Aerospace Engineering, University of California, San Diego

*Co-first authors

The attached article is an extra body of work performed during my dissertation. My contribution to the project included the derivation and maintenance of the NSPCs used within this study as well as the development of assays encompassing the growth, differentiation, and immunocytochemical labeling of the NSPCs on the nanofibrous carbon film.

Please see the supplemental files for the full article and associated supplemental material.

Reprinted with permission from:

A. Perebikovsky, A.T. Hwu, A.R. Yale, M. Ghazinejad, M. Madou, Nanofibrous multifunctional smart scaffolds for simultaneous cell differentiation and dopamine detection. *ACS Biomater. Sci. Eng.* **2020,** 6: 225-234.